THE UNIVERSITY OF SHEFFIELD

DOCTORAL THESIS

Higgs boson mass measurement and study of anomalous quartic gauge-couplings in the four-lepton final state using Large Hadron Collider proton-proton collisions at $\sqrt{s} = 13$ TeV recorded by the ATLAS detector at CERN

Author:
Kamal A. SAOUCHA

Supervisor:
Dr. Christos ANASTOPOULOS

A thesis submitted in fulfillment of the requirements for the degree of Doctor of Philosophy

in the

Sheffield ATLAS Group
Department of Physics and Astronomy

July 15, 2022

THE UNIVERSITY OF SHEFFIELD

Abstract

Science Faculty
Department of Physics and Astronomy

Doctor of Philosophy

Higgs boson mass measurement and study of anomalous quartic gauge-couplings in the four-lepton final state using Large Hadron Collider proton-proton collisions at $\sqrt{s} = 13$ TeV recorded by the ATLAS detector at CERN

by Kamal A. SAOUCHA

In this thesis, three main analyses are presented. First, a short study on the rejection of background for genuine electrons (from prompt decays) is presented, in the context of the ATLAS electron reconstruction and identification. As the main goal of this thesis, a measurement of the Higgs boson mass is presented in the $H \to ZZ \to 4l^{\pm}$ decay channels using Run-2 proton-proton collision data at the Large Hadron Collider corresponding to an integrated luminosity of 139 fb^{-1} at 13 TeV centre-of-mass energy collected by the ATLAS detector. The mass is found to be $m_H = 124.99 \pm 0.18$ (stat.) ± 0.04 (syst.) GeV. Also, a combined measurement with the ATLAS Run-1 data is performed, corresponding to approximately 5 fb^{-1} at 7 TeV and 20 fb^{-1} at 8 TeV, where $m_H = 124.94 \pm 0.17$ (stat.) ± 0.03 (syst.) GeV. These results were published and can be found in [1]. Finally, a Monte Carlo simulation study is presented, where BSM contributions from anomalous quartic gauge-couplings to $\gamma\gamma \to 4l^{\pm}$ production are investigated. Assuming a Standard Model only hypothesis, expected upper limits corresponding to a 95% confidence level are set on effective couplings sensitive to quartic gauge-couplings.

AUTHOR CONTRIBUTION

Background rejection study for electron reconstruction and identification using $\sqrt{s} = 13$ TeV proton-proton collision events recorded by the ATLAS detector

The electron background rejection study was entirely performed by the author, which consisted of producing the relevant simulation and data samples, the analysis of the latter datasets, and the extraction of the results. This study was fulfilled in order to qualify for the ATLAS authorship, which is obtained by making a substantial contribution to the ATLAS performance tasks. This study was supervised by Dr. Philip Sommer and Dr. Christos Anastopoulos.

Measurement of the Higgs boson mass in the $H \to ZZ^* \to 4\ell$ decay channel using $\sqrt{s} = 13$ TeV proton-proton collision events recorded by the ATLAS detector

The Higgs boson mass measurement was the achievement of team work. The author was involved in different tasks, namely, the production of data and simulation samples, a generator-dependence study for the background estimation, performance studies for the Higgs boson mass fit model, but mainly the development of a correction method for the calibration of the muon track covariance matrix, which was necessary to rectify the agreement between data and simulation of the estimated Higgs boson mass uncertainty and the invariant mass of di-muon events after the kinematic Z-mass constraint fit. This measurement was supervised by Dr. Christos Anastopoulos.

Study of Effective Field Theory operators sensitive to electroweak quartic gauge couplings in $\gamma\gamma \to 4\ell$ events using $\sqrt{s} = 13$ TeV proton-proton collision events recorded by the ATLAS detector

The Effective Field Theory study was entirely conducted by the author, which consisted of analysing the simulation samples, and the extraction of the results. This study was supervised by Dr. Philip Sommer and Dr. Christos Anastopoulos.

Acknowledgements

I would like to express my deepest gratitude and appreciation to all people who contributed to my ability of writing this thesis, directly and indirectly, especially to,

Dr. Quentin Python for the brilliant and intuitive introduction to experimental particle physics back when I was a bachelor/master student,

Prof. Dr. Freya Blekman for allowing me to take part in experimental particle physics research at the CMS experiment and beyond, for giving me the motivation to pursue a career in the field, for her excellent supervision and golden advice,

Dr. Thierry Gys and Dr. Maarten Van Dijk for an exciting, inspiring and fruitful summer internship at CERN working on the novel TORCH detector for the LHCb experiment,

Dr. Kristin Lohwasser for her kindness, help, support and encouragement in taking part in exciting projects and opportunities,

Dr. Jack MacDonald for the fascinating and ingenious discussions, help in my written and spoken language and the brilliant comments on the content of this thesis,

Dr. Philip Sommer, for the relentless help, great support, excellent guidance and supervision in two analyses in this thesis, but also for his endless patience and the countless times he came to the rescue in critical moments

Dr. Christos Anastopoulos for the unparalleled help and support during good and challenging times, invaluable experience, insightful guidance, constructive advice, brilliant supervision, but also for allowing me to take part in various projects within the ATLAS experiment and beyond; this work wouldn't have been possible without you!

Prof. Dr. Vitaly Kudryavtsev and Prof. Dr. Iacopo Vivarelli for taking the time to read my thesis meticulously and providing precious feedback on the content

but above all, to the most important and special person in my life, my mother, who has been my primary source of inspiration and motivation for years, words can't describe how important you have been, I simply couldn't have done this without you!

Contents

List of Abbreviations

SM	**S**tandard **M**odel
BSM	**B**eyond **S**tandard **M**odel
QFT	**Q**uantum **F**ield **T**heory
EFT	**E**ffective **F**ield **T**heory
MC	**M**onte **C**arlo
CR	**C**ontrol **R**egion
SR	**S**ignal **R**egion
GeV	**G**iga **e**lectron **V**olt
ZMC	**Z**-**M**ass **C**onstraint
LHC	**L**arge **H**adron **C**ollider
ATLAS	**A** **T**oroidal **L**HC **A**pparatu**S**
CERN	**C**onseil **E**uropéen pour la **R**echerche **N**ucléaire
QED	**Q**uantum **E**lectro**d**ynamics
QCD	**Q**uantum **C**hromo**d**ynamics
CMS	**C**ompact **M**uon **S**olenoid
NLO	**N**ext-to-**L**eading **O**rder
PDF	**P**arton/**P**robability **D**istribution **F**unction
EM	**E**lectro**m**agnetic
ID	**I**nner **D**etector
MS	**M**uon **S**pectrometer
SFOS	**S**ame-lepton **F**lavour **O**pposite-charge **S**ign
CDF	**C**umulative **D**istribution **F**unction
ECDF	**E**mpirical **C**umulative **D**istribution **F**unction
SMEFT	**S**tandard **M**odel **E**ffective **F**ield **T**heory

To my mother,

my late father,

and my late grandparents,
who I lost while writing this thesis . . .

Introduction

Curiosity, a blessing or a curse? Something we all inherited naturally since the first human being. From the first time we open our eyes in this fascinating world, we *wonder*. Insatiable creatures that never get enough from *knowledge*. After every answer, there is always another question awaiting, there is always a *what*, a *why* or a *how*. An endless spiral that knows no limit. While curiosity is manifested in many contexts, one of the purest and deepest forms is found among the society of universe explorers, the so-called *particle physicists*, a.k.a. scientists that crave for scrutiny. No single detail is taken lightly. A hunt with the absolute goal for a *theory of everything*. Every process in this universe is required to be understood, or the search won't stop!

Over are the times where breakthrough discoveries could be made in university labs, with an experiment devised by a handful of scientists, using a set of relatively simple equipment. Since the birth of our non-intuitive understanding of quantum mechanics [2], the theory describing the behaviour of non-relativistic (sub)atomic particles, our understanding of physics became more complicated, requiring more complex theories and experimental instruments. Ironically, the size of these experiments is constantly increasing, while physicists are looking for the smallest, indivisible constituents of the universe, the so-called *fundamental elementary particles*. Since the discovery of the first subatomic particle in 1897, the electron [4], many other particles have been discovered thanks to particle physics experiments. In recent decades, *high energy* particle physics is the trend, requiring enormous instruments to produce high energy interactions, which are studied in the hope to probe the architecture of the universe. These machines accelerate and collide well-known particles to break them down to even smaller constituents or cause the creation of rare, short-lived particles.

One of these particle colliders is the *Large Hadron Collider* [3] located at *CERN*. It has been a key instrument for many physics measurements. The latest major discovery was made in 2012, where the last piece of the *Standard Model theory* [5] (currently our best understanding for describing the fundamental particles) was discovered, the so-called *Higgs boson* [9] [10] [11]. The Standard Model has been very successful for many years, having predicted many particles and processes that were verified with astonishing precision. However it is well-known today that it cannot be a theory of everything. It fails when it comes to answer certain questions, such as the origin of *dark matter* [12] or describing *gravity* on a quantum level. Nevertheless, physicists have not given up the hunt for physics Beyond the Standard Model. Currently, a

lot of new physics models are being proposed by theorists and tested on the other hand by experimentalists. What might be the first crack in the Standard Model is still to be discovered, but it will surely be a monumental event. One thing is certain, particle physicists at the LHC are determined to find these fissures in the current theory until it crumbles to make space for a new theory, bringing us a step closer to the understanding of this wonderful world.

Chapter 1

The Standard Model of Elementary Particles and beyond

In *particle physics*, one is looking for answers to the deepest questions about our surroundings. What is the universe made of? What are the fundamental building blocks? How do these elements interact with each other? These questions are not new to human beings, and answers have been proposed in all different time eras. In ancient times, when everything was practically in a natural state, air, water, earth and fire were thought to be fundamental. After manipulation of different kinds of substances, such as metals, one started classifying different materials according to their properties in appearance. What made their building blocks different was unknown, speculation about their shape and/or size were hanging around, but there were no indications to prove it. For a long time, human progress in this matter was relatively slow, until the discovery of the *electron* [4] in 1897, which accelerated and caused a cascade of discoveries in the understanding of matter, where the milestone achievement of the atomic model was formulated. Since then, a lot of breakthrough findings have been made which gave birth to the *Standard Model of Elementary Particles* [5] [6] [7] [8] (SM). The SM is so far our best understanding of the building blocks of the universe. In a nutshell, it describes the world around us with different kinds of *fields*, which are spread in every corner of the universe. Just like a string, in a completely empty space, these fields are switched off, while vibrations on these fields are associated to physical particles we can (or not) observe. There are two kinds of fields associated to two kinds of particles; ones that constitute matter, and others that are responsible for interactions among the different fields. In the next section, a brief introduction to the SM is given, with a glance on the particle content and the involved fundamental interactions. Thereafter, an overview of the quantum field theory of the SM is presented, which is essential to explain the role of the Higgs boson in the generation of fundamental masses of SM particles. In the third section, the link to experimental particle physics is discussed, followed by an introduction to some properties of the Higgs boson. The phenomenology of proton-proton collisions at the Large Hadron Collider is briefly touched on in the fifth section. Finally, a coup d'œil at the Effective Field Theory approach is given, providing indirect predictions of physics beyond the SM.

1.1 Glimpse of the Standard Model of elementary particles

The SM of elementary particles is an elegant mathematical description of the known[1] fundamental particles. According to this theory, there are 12 fundamental types of building blocks of matter, which are referred to as *fermions*. These latter particles can interact with each other through the exchange of, again, particles which act as force-carriers, called *bosons*. The main difference between fermions and bosons is in their intrinsic angular momentum, known as the *spin quantum number*, where the former particles have half-integer spin and the latter integer-spin. This difference is at the origin why fermions make up matter and take up space; the laws of quantum mechanics do not allow identical fermions to pile up in the same place, while bosons can.

1.1.1 Fermions

Within fermions and bosons, particles are further classified according to their properties. In the case of fermions, one distinguishes the *quarks* and *leptons*. The common property they share is that they both can interact through the so-called *weak force*, while quarks can also interact through the so-called *strong force*, which is not the case for leptons. There are further two types of leptons; electrically charged and neutral leptons. The charged leptons are electron-like particles that interact on top of the weak force also with the *electromagnetic force*. Apart from the electron, there are two other charged leptons, namely the *muon* and the *tau lepton*. The only known difference in properties between the three types is the mass, where the *muon* is approximately 200 times heavier than the electron, while the *tau lepton* is 3500 times heavier. The electrically neutral leptons are called *neutrinos*, and they also exist in three generations, namely the *electron neutrino*, *muon neutrino* and *tau neutrino*. In the SM, the mass of particles is a free parameter that has to be determined empirically. Since neutrinos interact only weakly and have a very small mass, their exact mass remains unknown to-date, only upper limits on the possible neutrino masses are available.

On the other hand, quarks feel the three previously stated fundamental forces. There are 6 flavours of quarks, which all have different masses. Similarly to leptons, quarks are grouped in three generations. The first generation corresponds to the lightest pair of quarks, the *up* and *down-quark*, which have, apart from the mass difference, also a different electric charge. In contrast to charged leptons, their charge is fractional, and is respectively +2/3 and -1/3 of the elementary charge (e). The two other generations can be similarily grouped in a pair as the first generation, with the only exception that their mass is a few orders of magnitude higher compared to the first generation quarks. The two up-like quark particles are the *charm* and the *top-quark*, while the down-like quarks are the *strange* and *bottom-quark*. Table 1.1 summarises

[1] proven to exist, directly or indirectly.

TABLE 1.1: The SM fermions and their properties. Leptons and quarks are classified in generations according to their mass [5].

	Fermions					
	Leptons			Quarks		
	Particle	Charge (e)	Mass (GeV)	Particle	Charge (e)	Mass (GeV)
1^{st} gen.	electron (e)	-1	0.0005	down-quark (d)	-1/3	0.003
	e-neutrino (ν_e)	0	$< 10^{-9}$	up-quark (u)	+2/3	0.003
2^{nd} gen.	muon (μ)	-1	0.106	strange-quark (s)	-1/3	0.1
	μ-neutrino (ν_μ)	0	$< 10^{-9}$	charm-quark (c)	+2/3	1.3
3^{rd} gen.	tau (τ)	-1	1.78	bottom-quark (b)	-1/3	4.5
	τ-neutrino (ν_τ)	0	$< 10^{-9}$	top-quark (t)	+2/3	174

the fermions and some of their properties described in the SM. From all these particles, only the electron, the up and the down-quark make up the ordinary[2] matter in the universe. Different materials are mixtures of different arrangements of these particles in the form of bound states called *atoms*. They all have the same structure; a dense nucleus in the core made of bound states of the up and down-quark called protons (two up-quarks and one down-quark) and neutrons (two down-quarks and one up-quark), and a number of electrons surrounding the nucleus.

1.1.2 Bosons

In the SM, the elementary particles interact with each other by mediating a boson. The theory includes the three interactions mentioned in the previous section, for which bosons can be associated. The most familiar interaction is the electromagnetic force[3], which is responsible for most of the terrestrial processes. This force is mediated by the massless light particles, called *photons*. Electrically charged particles repel each other if they are like-charged and attract each other if they are opposite-charged by exchanging photons. The second force responsible for holding the nucleus together, despite the positively charged protons that would repel each, is the strong force. As its name suggests, it is the strongest fundamental force in the SM, which is strong enough to overcome the electromagnetic force in the nucleus while holding the quarks in the protons and neutrons together. The force mediating particles for this interaction are massless *gluons*. Finally, the last interaction is the weak force, which is less of a force in the commonly used meaning of a force, i.e. pulling and pushing objects. A familiar application of this interaction is the process of radioactive decays, such as the beta-decay, where a neutron decays into a proton, an electron and an electron-neutrino. If one takes a closer look at subatomic level in the beta-decay, it is a down-quark in the neutron that is turned to an up-quark, which results in a proton. This flavour change is due to the weak force, which happens by mediating this time a massive boson. Unlike the other interactions, there are two types of bosons responsible for the weak interaction, namely the W and the *Z-boson*, with the former having an electric charge, while the latter is electrically neutral.

[2] which is visible to us and is relatively stable over time.
[3] Forces and interactions are used interchangeably in particle physics.

TABLE 1.2: The SM force-carrying bosons and their mass. An order of magnitude of the relative strength of each force is also shown for two fundamental particles being at a distance of the size of a nucleus [5].

The Standard Model bosons

Boson	Associated fundamental interaction	Relative strength	Mass (GeV)
Gluon g	Strong force	1	0
Photon γ	Electromagnetic force	10^{-3}	0
W-boson	Weak force	10^{-8}	80.4
Z-boson			91.2

The previously stated bosons are what we conventionally know as force-carriers. However, there is one last boson in the SM that is somehow different, in the sense that it does not fit in the picture of a force-carrier, but its presence is essential to explain the empirical measurements. Before its discovery in 2012, the *Higgs boson* was elegantly predicted in the SM. Its existence was crucial, otherwise the SM would not make sense, i.e. it would be in contradiction with the experimental measurements. Without the Higgs boson, all SM particles would be massless. Moreover, all particles would travel at the speed of light and it would not be possible to distinguish the three generations of fermions from each other, since their difference is manifested in their mass. To understand how the Higgs boson attributes mass to fermions and the weak bosons, one has to introduce the concept of a field, which is discussed in section 1.2. A summary of the SM bosons and their properties can be found in Table 1.2. An order of magnitude of the relative strength of each force is also shown for two fundamental particles being at a distance of the size of a nucleus. It should be noted that this strength depends on the energy scale and the distance between particles. Another difference among the forces is that the weak and strong force are short-range forces, unlike the electromagnetic force which is extended on larger distances, which is the reason why electromagnetism is dominant in the universe.

1.1.3 Anti-particles

So far, only the flavour of the SM particles has been discussed. In reality, every particle with some conserved physical charge has a twin particle with the same mass but with a different charge, called an anti-particle. In the SM, every particle has a set of conserved quantum numbers, such as the electric charge or the flavour number. In the case of an electrically charged particle, the anti-particle has the same charge value but with reversed sign. For example, a negatively charged electron has an anti-particle, historically called a *positron*, which has the same mass but has a charge $+|e|$. Similarly, the W-boson comes with two possible charges, W^+ with a charge $+|e|$ and W^- with $-|e|$. Up-like quarks have anti-particles with a charge $-\frac{2}{3}|e|$ and down-like quarks with $+\frac{1}{3}|e|$.

Analogously to the electric charge, which arises from the electromagnetic interaction, the strong force has also an associated charge, called the *colour charge*[4]. Since quarks interact strongly, they do carry the colour charge. There are three colour charges; *red*, *green* and *blue*. On top of the fractional electric charge, each quark exists in one of the different colour charges. For example, the blue up-quark has an anti-blue anti-quark as its anti-particle, that has a an electric charge of $-\frac{2}{3}|e|$. Depending on the colour charge of the quarks, when a strong interaction takes place, 8 different types of gluons can be exchanged. These gluons carry a combination of colours and anti-colours, known as the colour octet, that are mediated by quarks with the corresponding colours and anti-colours.

Finally, neutral bosons (the photon, the Z-boson and the Higgs boson) are their own anti-particles, while neutrinos have anti-particles with a different lepton number, which is one of the conserved quantum numbers in the SM. In this thesis, no distinction is made between particles and anti-particles unless stated, e.g. an electron would refer to both the negatively and the positively charged electron.

1.1.4 Shortcomings of the Standard Model

Despite the elegance in which the SM describes fermions and bosons, it cannot not be a theory of everything. As it could be sensed in the previous section, there is one familiar force missing in the picture of the SM, *gravity*. This latter force is hard to reconcile with the SM and remains a mystery on quantum level. Similarly to the three fundamental forces, a hypothetical massless boson is associated to gravity, called the *graviton* [13], which is expected to be the force-carrying particle. Even though the effects of gravity are obvious on macroscopic scales, its impact on quantum level is negligible. This is the reason why it is so hard to detect gravity experimentally, and consequently the SM predictions are confirmed with high precision without including gravity. Compared to the relative strength of the three other forces (Table 1.2), gravity would be of the order of 10^{-37}, which is outrageously small.

Gravity is certainly not the only shortcoming of the SM. A priori, in combination with a theory of gravity (elegantly described as a geometric theory, the so-called *General Relativity* [14]), the SM is sufficient to describe the world within the solar system. However, beyond this scale there are clear hints that the laws of physics are not complete; a significant fraction of the universe mass seems to be hidden in the form of an undetectable substance, called *dark matter* [12]. One of the most direct pieces of evidence of dark matter is the contradictory orbit velocity distribution of stars in galaxies. So far, there is no evidence that constituents of this type of matter can interact with the SM particles. Apart from dark matter, there are other open questions which are not solved considering only the SM, e.g. the origin of the matter

[4]The colour is used as a tag, but has nothing to do with the intrinsic meaning of a colour, i.e. particles having the colour charge are not coloured.

anti-matter asymmetry in the universe, the relatively large number of free parameters in the SM or the reason behind the very small mass of neutrinos.

1.1.5 Potential beyond the Standard Model theories

While particle physics experimentalists are digging in the available data in the hope of finding deviations from the SM predictions, which would hint the direction in which the laws of physics have to be rewritten, theorists have proposed many ideas that could potentially answer some of the questions beyond the SM. A few famous theories are; *supersymmerty* [15], *string theory* [16], *grand unification theory* [17] and *extra dimensions* [18].

Nevertheless, the SM is believed to be an incomplete theory rather than being wrong due to the astonishing precision with which many predictions have been confirmed, e.g. the electron magnetic moment is measured to be in agreement with the SM with a precision of the order of 10^{-13} [19]. An important tool that supports this assumption while providing a systematic way of constructing new theories based on the current SM theory, is the so-called *effective field theory* (EFT) approach [20]. EFT is a concept that has been used many times throughout the history of prediction making. The basic concept behind this formalism is the assumption that relevance of physics theories depends on the considered length or energy scale, while effects that can be prominent at shorter distances or higher energies become irrelevant. For example, one does not need special relativity [21] to calculate whether a car breached the speed limit, the difference between the Lorentz factor and unity would be negligibly small to matter. Or, one does not need the SM to make predictions in chemistry with a satisfying accuracy. Based on this idea, the SM is assumed to be an effective theory that is valid at relatively low energy scales, where beyond the SM processes are diluted at low scales, and therefore cannot be easily observed.

1.2 The Standard Model as a quantum field theory

In the previous section, a general summary of the content of the SM was presented. However, to emphasise the importance of the Higgs boson, one has to cover the principles of the SM in a certain level of detail. The following content is inspired from the following literature [5] [6] [7] [8] [24]. As previously stated, the SM is a field theory describing the elementary particles and how they interact via three fundamental interactions, the weak, the strong and the electromagnetic interaction. To understand why particles are linked to fields, one has to refer back to *quantum mechanics*, where the wave-particle duality is introduced, implying that matter has a wave-like nature, for which a wavelength can be associated that is inversely proportional to the momentum, the so-called *de Broglie equation*. This was verified in the famous double split experiment [22], where electrons showed clear wave-patterns. On the other hand, the photoelectric effect experiment [23] revealed the quantum

nature of light, which together with former experiments suggested that electrons and photons a fundamentally quite similar. But the question can be asked, what is more fundamental; the particle or the wave-like nature?

In the SM, describing the elementary particles as waves, which are special configurations of a field, is found to be more useful. Among other reasons, the fact that elementary particles are exact copies of each other, it is somehow more acceptable to think of a single field stretched in space-time, where ripples of it appear as identical particles. Another motivation is, the fact that particles can be created and annihilated, which is a process that is easier to picture using the wave-like nature. However, in order to reconcile the concept of a field with particles, the introduction of field quantisation is essential, which is achieved by promoting the fields to operators. In other words, the SM is a *quantum field theory* (QFT), where the dynamics of the fields are described. These can be derived from the *Standard Model Lagrangian*, which encodes the properties and interactions of the fields. In QFT, the *Lagrangian density* is used in order to satisfy the Lorentz invariance of the action (essential for deriving the equations of motion), defined as,

$$S = \int \mathscr{L}\, d^4x \qquad \text{with } L(t) = \int \mathscr{L}(\phi, \partial_\mu \phi) d^3x, \tag{1.1}$$

where the Lagrangian density $\mathscr{L}$ is a function of the field ϕ and its derivatives. An important feature in the use of the Lagrangian is that one can derive conservation laws from its symmetry properties, inspired by the famous *Noether's theorem*. In general, when the true theory is missing, the exploitation of symmetries[5] in a systematic way can be very powerful to derive the characteristics of the theory. In fact, the SM is constructed from the assumption that it is invariant under specific symmetry groups from which the fundamental interactions arise. These symmetries are mathematically well defined in *group theory* [30]. In the following sections, the quantum field theories that provide a description of the fundamental interactions are briefly discussed.

1.2.1 Gauge invariant theories

Looking back in classical mechanics, the equations of motion of, say, a particle, are derived from the Euler-Lagrange equation, where the Lagrangian L could be obtained from the kinetic energy T and the potential energy U of the particle as follows,

$$L = T - U. \tag{1.2}$$

A particle is naturally localised in space, therefore the Lagrangian is a function of its coordinates and their time derivatives. On the other hand, a field occupies a region in space. In a relativistic field theory, the Lagrangian is expressed in terms

[5] a set of operations that can be applied to system while leaving it invariant under the operations.

of fields, and their derivatives in each space-time coordinate (since in a relativistic theory space and time coordinates are treated on equal footing). In contrary to the classical case, the Lagrangian density $\mathscr{L}$ (from now on referred to as simply the Lagrangian) in QFT has to be somehow invented. One typically starts from a guess, which is gradually modified to construct a robust theory. Moreover, the Lagrangian for a specific system is often not unique, one can multiply or add a constant to it without affecting the derived field equations.

This is the case in *quantum electrodynamics* (QED), the theory where charged particles interacting electromagnetically are described. QED is constructed starting from the so-called *Dirac Lagrangian*, describing a half-spin particle (fermion) with mass m,

$$\mathscr{L}_{Dirac} = i\bar{\psi}\gamma^{\mu}\partial_{\mu}\psi - m\bar{\psi}\psi, \tag{1.3}$$

where ψ is the *Dirac spinor* (a four-component[6] wave-function satisfying the Dirac equation), γ^{μ} the *Dirac gamma matrices*, and $\bar{\psi}$ the adjoint Dirac spinor defined as

$$\bar{\psi} = \psi^{\dagger}\gamma^{0}, \qquad \text{with } \psi^{\dagger}\text{the Hermititian conjugate of } \psi.$$

The first term represents the kinetic term of the fermion field and the last the mass term. It can be shown that this Lagrangian is invariant under the *global* phase transformation,

$$\psi(x) \longrightarrow \psi'(x) = e^{i\theta}\psi(x), \qquad \text{with } \theta \in \mathbb{R} \tag{1.4}$$

If θ is not a constant in different points of space-time, i.e. $\theta(x)$, the Lagrangian is no longer invariant under these transformations. In other words, the Lagrangian varies under *local* phase transformations. A crucial step in this formalism comes when one requires the Lagrangian to be invariant under such local phase transformations. To achieve this, the extra term after performing the local transformation has to vanish,

$$\mathscr{L}'_{Dirac} = \mathscr{L}_{Dirac} - \bar{\psi}\gamma^{\mu}(\partial_{\mu}\theta(x))\psi. \tag{1.5}$$

The difference between the global and local phase transformations arises from the calculation of derivatives of the field. To counter this difference, the so-called *covariant derivative* is introduced,

$$D_{\mu} = \partial_{\mu} + iqA_{\mu}, \tag{1.6}$$

where A_{μ} is some new vector field transforming as,

$$A_{\mu} \longrightarrow A'_{\mu} = A_{\mu} + \frac{1}{q}\partial_{\mu}\theta(x), \tag{1.7}$$

to ensure the cancellation of the unwanted term. Substituting ∂_{μ} with D_{μ} in the initial Lagrangian restores the desired invariance under local phase transformations.

[6] Although it has four-components, it is not a four-vector, i.e. it does not transform as one

This comes with a price, the introduced vector field is consequently coupled to ψ with a strength q in the updated Dirac Lagrangian,

$$\mathscr{L}_{Dirac} = i\bar{\psi}\gamma^{\mu}\partial_{\mu}\psi - q\bar{\psi}\gamma^{\mu}A_{\mu}\psi - m\bar{\psi}\psi. \tag{1.8}$$

This vector field is nothing but the electromagnetic field, and the new term describes the interaction of fermions and photons with a coupling strength q. This is not the full picture, physically a photon must be able to propagate freely, therefore the Lagrangian must include a free term for A_{μ}. The Lagrangian for a vector spin-1 field with mass m_A is given by the *Proca Lagrangian*,

$$\mathscr{L}_{Proca} = -\frac{1}{4}F^{\mu\nu}F_{\mu\nu} + \frac{1}{2}m_A^2 A^{\mu}A_{\mu}, \tag{1.9}$$

where the electromagnetic field strength tensor $F^{\mu\nu} = \partial^{\mu}A^{\nu} - \partial^{\nu}A^{\mu}$. It should be noted that the last term in not invariant under local phase transformations. This is naturally solved, since the photon is found massless, which drops the last term. Adding the remaining term, which is nothing but the *Maxwell Lagrangian* for a free propagating photon, to the updated Dirac Lagrangian eq. 1.8, the QED Lagrangian reads,

$$\mathscr{L}_{QED} = i\bar{\psi}\gamma^{\mu}\partial_{\mu}\psi - q\bar{\psi}\gamma^{\mu}A_{\mu}\psi - m\bar{\psi}\psi - \frac{1}{4}F^{\mu\nu}F_{\mu\nu}. \tag{1.10}$$

Thus, by imposing local phase invariance on the Dirac Lagrangian, initially describing a free fermion field, one introduces a massless vector field with a specific transformation rule, that could be identified as the massless photon field. Invariance under transformation rules such as eq. 1.7, known as a *gauge transformation*, is said to be a *gauge invariance*, corresponding to a *gauge field* A_{μ}. Moreover, the transformation eq. 1.4 can be generalised in the form,

$$\psi \longrightarrow \psi' = U\psi, \qquad \text{with } U^{\dagger}U = 1, \tag{1.11}$$

where U is a unitary 1×1 matrix. Such matrices are elements of the group $U(1)$, and therefore symmetries of this kind are referred to as $U(1)$ *gauge invariant symmetries*. Thus QED is an abelian[7] $U(1)$ gauge theory.

In fact, the local gauge principle requirement is at the heart of the SM formulation. It serves as the machinery for developing the theory of the interactions and their couplings in a systematic way. Analogously, one can extend the strategy to construct the weak and the strong interaction Lagrangian, where this time the invariance is required under respectively $SU(2)$[8] and $SU(3)$ local phase transformations. The derivation of the Lagrangian can be found in the previously mentioned literature. For the strong interaction, analogously to QED, *quantum chromodynamics* (QCD) is the theory describing quarks interacting strongly with gluons. As opposed to the

[7] An Abelian group is a group in which the elements commute, as is the case with $U = e^{i\theta}$

[8] A SU(n) group refers to the collection of unitary n×n matrices with determinant equal to 1.

single QED electric charge, characterising the coupling strength of charged particles with the photon, in QCD one counts three charges, the previously mentioned colour charges. The QCD Lagrangian reads,

$$\mathscr{L}_{QCD} = \bar{q}(i\gamma^\mu \partial_\mu - m)q - g(\bar{q}\gamma^\mu T_j q)\mathscr{G}^j_\mu - \frac{1}{4}G^j_{\mu\nu}G^{\mu\nu}_j, \tag{1.12}$$

where $q(x)$ is the quark field, T_j represent the *generators* of the SU(3) group given by 3×3 so-called *Gell-Mann matrices* with j running from 1 to 8, g the coupling strength of the quarks to the gluon fields $\mathscr{G}^j_\mu$, and $G^j_{\mu\nu}$ is the gluon field strength tensor, which in contrast with the electromagnetic field strength tensor, has an extra term arising from non-commuting generators. This Lagrangian is as desired invariant under local $SU(3)$ gauge transformations and describes quarks in three colours with eight massless gluon fields.

The local gauge invariance principle works fine as long as the resulting gauge fields are found to be massless, which is not a problem in the case of QED and QCD with the massless photon and gluon. However this does not hold in the case of the weak interaction, where the Z and W-bosons are measured to be massive. More specifically, if one adds a mass term to the weak interaction Lagrangian, the local invariance would not be satisfied in a similar way as in the case of the Proca Lagrangian eq. 1.9 , where the last mass term is not invariant under local phase transformations. In fact, this issue is also apparent in the case of fermions, where the mass term would violate the weak interaction $SU(2)$ gauge invariance .

It is at this specific point where the importance of the Higgs boson appears. As mentioned in the last section, the Higgs field is responsible for the generation of the mass of the elementary particles. This is achieved through a process, called *spontaneous symmetry breaking*, where massless particles interacting with the Higgs field gain mass.

1.2.2 Spontaneous symmetry breaking

To understand the Higgs mechanism, it is useful to consider the following simple Lagrangian,

$$\mathscr{L} = \mathscr{T} - \mathscr{U}, \tag{1.13}$$

where $\mathscr{T}$ and $\mathscr{U}$ are the kinetic and potential terms of a real scalar field ϕ given by,

$$\mathscr{T} = \frac{1}{2}(\partial_\mu \phi)(\partial^\mu \phi),$$

$$\mathscr{U} = \frac{1}{2}\mu^2\phi^2 + \frac{1}{4}\lambda\phi^4.$$

At first glance, the potential term appears to be composed of a mass and a self-interaction term. Considering the lowest energy state of ϕ (vacuum state), λ has to

be positive in order to ensure a finite minimum potential. Consequently, there are two cases depending on the value of μ^2; either it is positive in which case ϕ_{min}=0, or it is negative and thus $\phi_{min}=\pm\sqrt{-\mu^2/\lambda}$. Figure 1.1 shows the potential term of Lagrangian eq. 1.13 as a function of the real scalar field ϕ.

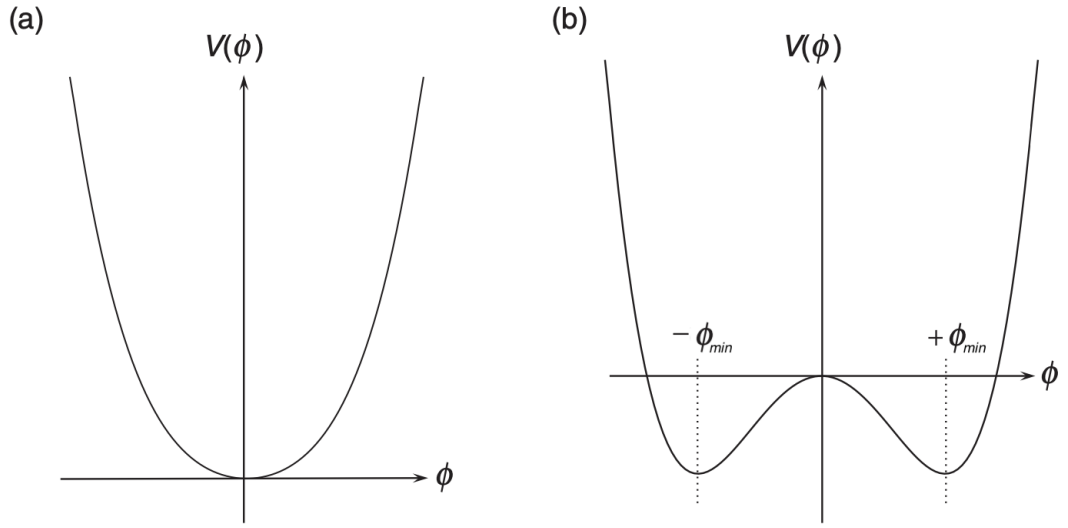

FIGURE 1.1: The potential term of Lagrangian eq. 1.13 as a function of the *real* scalar field ϕ. (a) shows the case for $\mu^2 > 0$, and (b) for $\mu^2 < 0$.

In the first case, the interpretation of the mass term holds, while in the second case the mass would become imaginary. Moreover, in the latter case, since the minimum potential is not at zero, the expectation value of the field in vacuum is non-zero. To identify the mass term in this latter case, one has to express the Lagrangian in terms of a deviation from the vacuum state (=lowest energy state), which describes the particle states. The perturbation of ϕ about the non-zero vacuum state can be written as,

$$\phi(x) = \phi_{min} + \eta(x), \qquad \text{with } \phi_{min} = \text{constant}. \tag{1.14}$$

where the Lagrangian becomes,

$$\mathscr{L} = \frac{1}{2}(\partial_\mu\eta)(\partial^\mu\eta) - \frac{1}{2}\mu^2(\phi_{min}+\eta)^2 + \frac{1}{4}\lambda(\phi_{min}+\eta)^4$$

or (since μ^2=$-\phi^2_{min}/\lambda$),

$$\mathscr{L} = \frac{1}{2}(\partial_\mu\eta)(\partial^\mu\eta) - \lambda\phi^2_{min}\eta^2 - \lambda\phi_{min}\eta^3 - \frac{1}{4}\lambda\eta^4 + \frac{1}{4}\lambda\phi^4_{min}. \tag{1.15}$$

This is the exact same initial Lagrangian eq. 1.13, but re-expressed in terms of the deviation 1.14, where this time the mass term is well defined (i.e. $m = \lambda\phi^2_{min} \in \mathbb{R}$). The third and fourth terms can be interpreted as self-interaction terms, while the last term is constant and has no effect on the derived field equations. However there

is an important difference between eq. 1.13 and eq. 1.15. The initial Lagrangian is invariant under parity transformations of the field ϕ, i.e. $\mathscr{L}(\phi) = \mathscr{L}(-\phi)$, but in the re-expressed version eq. 1.15 the *symmetry is broken*. The laws of physics from both Lagrangians are still invariant, but as soon as the vacuum state is chosen (here $+|\phi_{min}|$ or $-|\phi_{min}|$), one speaks of *spontaneous symmetry breaking*[9].

The scalar field considered in thipecrts example was real, where the broken symmetry was discrete (two possible vacuum states). This can be generalised by considering a complex field,

$$\phi = \frac{1}{\sqrt{2}}(\phi_1 - i\phi_2), \tag{1.16}$$

whereby the Lagrangian eq. 1.13 becomes,

$$\mathscr{L} = (\partial_\mu \phi)^*(\partial^\mu \phi) - \mu^2 \phi^* \phi + \lambda(\phi^* \phi)^2 \tag{1.17}$$

or in terms of ϕ_1 and ϕ_2,

$$\mathscr{L} = \frac{1}{2}(\partial_\mu \phi_1)(\partial^\mu \phi_1) + \frac{1}{2}(\partial_\mu \phi_2)(\partial^\mu \phi_2) - \frac{1}{2}\mu^2(\phi_1^2 + \phi_2^2)^2 - \frac{1}{4}\lambda(\phi_1^2 + \phi_2^2)^2, \tag{1.18}$$

where the condition $\lambda > 0$ is still required to ensure a finite vacuum potential. Furthermore, the Lagrangian has the same QED global $U(1)$ symmetry (eq. 1.4), with the exception that the fields are scalar fields instead of spinors. Analogously to the previous example, there are two cases depending on the sign of μ^2. Figure 1.2 shows the potential term of Lagrangian eq. 1.18 as a function of the components of the complex field ϕ. In the positive case, the potential has a paraboloid shape, with the vacuum state at zero, while in the negative case, the potential has a form referred to as the *Mexican hat*, with a full circle of minima defined by,

$$\phi_1^2 + \phi_2^2 = \frac{-\mu^2}{\lambda} = \phi_{min}^2. \tag{1.19}$$

This time the vacuum state can take an infinite number of minima, while breaking the $U(1)$ global symmetry. In a similar way to the real scalar field case, the Lagrangian is re-expressed in terms of a deviation from one of the vacuum states. Choosing the state along the positive real axis, $(\phi_1, \phi_2) = (\phi_{min}, 0)$, without loss of generality (eq. 1.19), one can expand the scalar field as,

$$\phi = \frac{1}{\sqrt{2}}(\phi_1 + i\phi_2) = \frac{1}{\sqrt{2}}(\eta + \phi_{min} + i\xi), \tag{1.20}$$

in which case the Lagrangian 1.18 reads (while substituting $\mu^2 = -\lambda\phi_{min}^2$),

$$\mathscr{L} = \frac{1}{2}(\partial_\mu \eta)(\partial^\mu \eta) - \lambda\phi_{min}^2\eta^2 + \frac{1}{2}(\partial_\mu \xi)(\partial^\mu \xi) - V(\eta, \xi), \tag{1.21}$$

[9] An example of symmetry breaking: in the middle of the ocean no direction is preferred, until a compass is looked at, which breaks the isotropic symmetry.

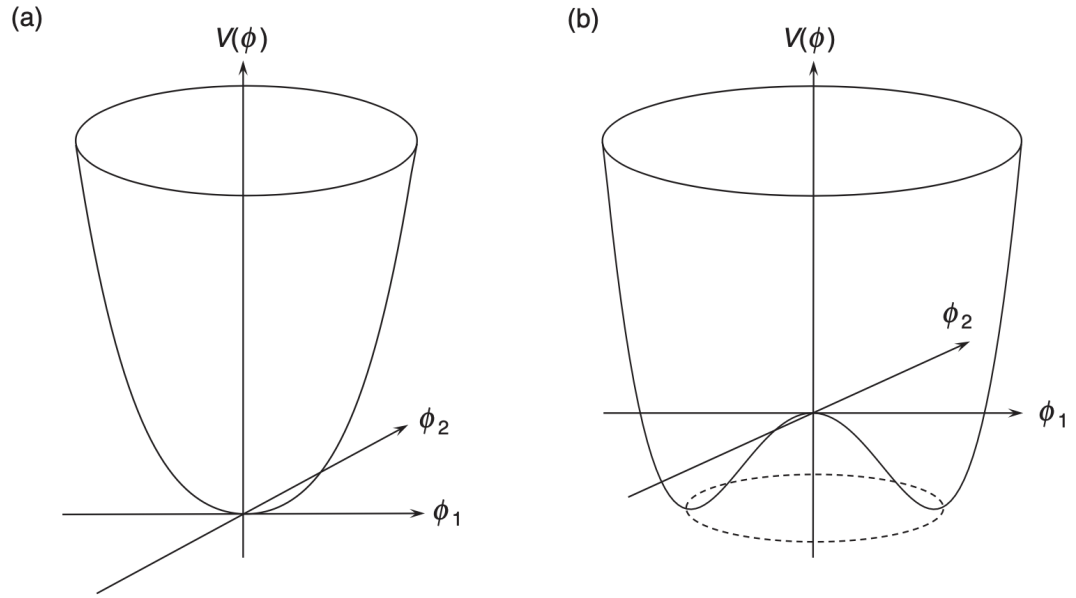

FIGURE 1.2: The potential term of Lagrangian eq. 1.13 as a function of the *complex* scalar field ϕ. (a) shows the case for $\mu^2 > 0$, and (B) for $\mu^2 < 0$.

with the interaction term,

$$V(\eta, \xi) = \lambda \phi_{min} \eta^3 + \frac{1}{4}\lambda(\eta^4 + \xi^4) + \lambda \phi_{min} \eta \xi^2 + \lambda \eta^2 \xi^2. \tag{1.22}$$

Analysing eq. 1.21, respectively, one can identify a kinetic and a mass term for the field $\eta(x)$, and a kinetic term for the massless field $\xi(x)$. The former terms constitute the so-called *Klein-Gordon Lagrangian*, describing a free spin-0 scalar boson field with mass $m = \phi_{min}\sqrt{2\lambda}$. Compared to the previous example, where a discrete symmetry was broken, spontaneously breaking a continuous global symmetry implies the existence of a massless scalar field $\xi(x)$, which is referred to as the *Goldstone field*.

1.2.3 The Higgs Mechanism

The last two sections have demonstrated powerful tools on which the SM is based, and how to formulate the relevant theories to describe the elementary particles and interactions in a field theory. The importance of the last piece of the SM, the Higgs field, will be shown in this section.

As mentioned before, the Lagrangian eq. 1.18 is invariant under a global $U(1)$ symmetry of the form eq. 1.4, and analogously to the QED case, it is possible to make it invariant under local gauge transformations while introducing a gauge field, that is required to be massless. Considering the case where the vacuum state is degenerate, the now gauge invariant Lagrangian can be similarly re-expressed as shown in

section 1.2.2,

$$\begin{aligned}\mathscr{L} =& \frac{1}{2}(\partial_\mu \eta)(\partial^\mu \eta) - \lambda \phi_{min}^2 \eta^2 + \frac{1}{2}(\partial_\mu \xi)(\partial^\mu \xi) - \frac{1}{4}F^{\mu\nu}F_{\mu\nu} \\ &+ \frac{1}{2}g^2\phi_{min}^2 B_\mu B^\mu + g\phi_{min}B_\mu(\partial^\mu \xi) - V(\eta, \xi, B).\end{aligned} \tag{1.23}$$

As shown before, the Lagrangian includes a massive Klein-Gordon field η and a massless Goldstone field ξ, originating from the spontaneous symmetry breaking, and a gauge field B from the gauge invariance, *but this time it is massive!* The marriage of gauge invariance and spontaneous symmetry breaking resulted in a gauge field with a mass term. The interaction terms are grouped in the potential term $V(\eta, \xi, A)$. Moreover, before symmetry breaking the gauge field has two degrees of freedom from the transverse polarisation states, but when it acquired a mass, a third degree of freedom for the longitudinal polarisation state was acquired in the form of a Goldstone field ξ. To see this, one can perform the appropriate gauge transformation to absorb the Goldstone field into the gauge field,

$$B_\mu \longrightarrow B'_\mu = B_\mu + \frac{1}{g\phi_{min}}\partial_\mu \xi(x), \tag{1.24}$$

and since the Lagrangian 1.23 is gauge invariant, the derived equations of motion remain unchanged. Finally, in this specific gauge transformation eq. 1.23 reads (while rewriting $\eta(x) = h(x)$ and $\phi_{min} = v$),

$$\boxed{\mathscr{L} = \frac{1}{2}(\partial_\mu h)(\partial^\mu h) - \lambda v^2 h^2 - \frac{1}{4}F^{\mu\nu}F_{\mu\nu} + \frac{1}{2}g^2 v^2 B_\mu B^\mu + V_{int}(B, h)} \tag{1.25}$$

with,

$$\boxed{V_{int}(B, h) = g^2 v B_\mu B^\mu h - \frac{1}{2}g^2 v B_\mu B^\mu h^2 - \lambda v h^3 - \frac{1}{4}\lambda h^4}$$

which is the Lagrangian describing the Higgs scalar field h with a mass

$$\boxed{m_H = v\sqrt{2\lambda}}$$

and a massive gauge field B of mass $m_B = gv$, proportional to the *Higgs vacuum expectation value*. The potential term $V_{int}(B, h)$ includes the interaction terms, where the first two terms describe the interaction between the Higgs field h and the gauge field B, while the last two are the Higgs self-interaction terms. It is important to note that throughout the procedure the Lagrangians were equivalent, i.e. the derived equations of motion remain the same. By exploiting the symmetries under which the Lagrangian is invariant, one could extract the actors in the theory.

1.2.4 Mass acquisition of electroweak bosons

That W bosons are electrically charged is not a coincidence. In fact the electromagnetic and weak interactions can be unified in a single theory, called the *electroweak theory*. This can be formulated with an $SU(2) \times U(1)$ gauge group, where the generators of the $SU(2)$ and the $U(1)$ are known as the *weak isospin* and *hypercharge* respectively. There are four corresponding gauge fields involved, namely the *weak isospin fields* W_1, W_2, W_3, and the *hypercharge field* B, which are initially massless fields before the Higgs mechanism. In the previous section, the mass generation for a gauge field emerging from a $U(1)$ gauge symmetry was shown. Similarly, in the SM the three massive weak bosons and the photon are produced while spontaneously breaking the electroweak $SU(2) \times U(1)$ symmetry.

The minimal Higgs model required for generating the mass and the additional longitudinal degrees of freedom (in the form of Goldstone fields) of the Z and W bosons is constructed from a two state complex scalar field configuration, referred to as the weak isospin doublet, given by,

$$\phi = \begin{pmatrix} \phi^0 \\ \phi^+ \end{pmatrix} = \frac{1}{\sqrt{2}} \begin{pmatrix} \phi_1 + i\phi_2 \\ \phi_3 + i\phi_4 \end{pmatrix}, \tag{1.26}$$

with ϕ^0 a neutral scalar field and ϕ^+ charged such that $(\phi^+)^\dagger = \phi^-$, ensuring the longitudinal degrees of freedom for respectively the Z^0, W^+ and W^- bosons. Considering Lagrangian 1.17, but this time the fields are doublets (thus $\phi^* \rightarrow \phi^\dagger$), the same Higgs mechanism procedure described in the previous section can be repeated, which can be found in this reference . As a result, the physical gauge fields A, $W^\pm$ and Z corresponding to the electroweak bosons are found to be linear combinations of the massless boson fields from the local $SU(2) \times U(1)$ gauge symmetry before symmetry breaking,

$$A_\mu = cos\theta_W B_\mu + sin\theta_W W_\mu^{(3)} \qquad \text{with } m_A = 0, \tag{1.27}$$

$$Z_\mu = -sin\theta_W B_\mu + cos\theta_W W_\mu^{(3)} \qquad \text{with } m_Z = \frac{1}{2}\frac{g_W}{cos\theta_W} v, \tag{1.28}$$

$$W_\mu^\pm = \frac{1}{\sqrt{2}}(W_\mu^{(1)} \mp iW_\mu^{(2)}) \qquad \text{with } m_W = \frac{1}{2} g_W v, \tag{1.29}$$

where θ_W is the so-called *weak mixing angle*, and g_W the *weak coupling constant*. Analogously to the previous case, the mass of the massive gauge bosons is proportional to the vacuum expectation value of the Higgs field. In summary, the mass of the SM weak bosons are generated through the $SU(2) \times U(1)$ electroweak symmetry breaking, known as the Higgs mechanism. Finally, it can also be shown how fermions acquire their mass through the Higgs mechanism, where the Higgs-fermion interaction is proportional to the so-called *Yukawa coupling* [9] [10] [11].

1.3 Experimental predictions of quantum field theories

In the previous section, discussions about the nature of the interaction terms were omitted to avoid distraction from the main purpose, which was the demonstration of mass acquisition in the SM. In fact, these interaction terms are crucial to verify the credibility of the SM. As previously stated, the Lagrangian formalism is a powerful tool to derive the equations of motion and provides an elegant mathematical description of the SM in a QFT. For instance, it led to the ability of making predictions such as the existence of the Higgs boson. Moreover, knowing the nature of SM interactions, it is possible to calculate quantum amplitudes of particle scattering, from which probabilities of these interactions to occur can be computed. QFT models such as the SM are often tested by measuring *cross sections* of particle scatterings, which are measures of quantum mechanical probability amplitudes of these interactions. These can be predicted from quantum mechanical transition matrix elements which include a factor of the coupling strength of the interaction vertex in question. On the other hand, cross sections can be measured from counting scattering events in collider experiments.

The derivation of cross sections starting from Lagrangians is not trivial; one has to derive the associated *Hamiltonian*, which is used to determine the time evolution operator from initial time t_i to final time t_f as,

$$U(t_f, t_i) = \mathrm{T}\left[\left(-i\int_{t_f}^{t_i} H_{int}dt\right)\right], \tag{1.30}$$

with H_{int} the interaction Hamiltonian and T the time ordering operator. This latter can then be used to define the scattering matrix (*S-matrix*),

$$S \equiv \lim_{\mathrm{t}\to\infty} U(t, -t), \tag{1.31}$$

from which scattering amplitudes encoding the transition rate from the initial to final state can be calculated as,

$$\mathscr{M}_{i\to f} = \langle \text{final state}|S|\text{initial state}\rangle, \tag{1.32}$$

with $|\mathscr{M}_{i\to f}|^2$ the probability density of the interaction occurrence. From this quantity, cross section of processes can be derived. The differential cross section of any given two particle interaction can be expressed as,

$$d\sigma = \frac{|\mathscr{M}_{i\to f}|^2}{\Phi_i} dL \tag{1.33}$$

with dL a Lorentz invariant phase space element and Φ_i the incident flux. In reality, the transition amplitude is usually calculated from a perturbation expansion (if the coupling strength of the interaction is small enough). The corresponding transition

matrix element is an infinite sum of terms, where each term can be interpreted as a specific process, which can be visualised using a pictorial representation, a so-called *Feynman diagram*. This depiction of the particle's interaction describes transitions between initial and final states. These diagrams are constructed from propagators for the exchange of virtual particles[10] and vertices as interaction points between the particles.

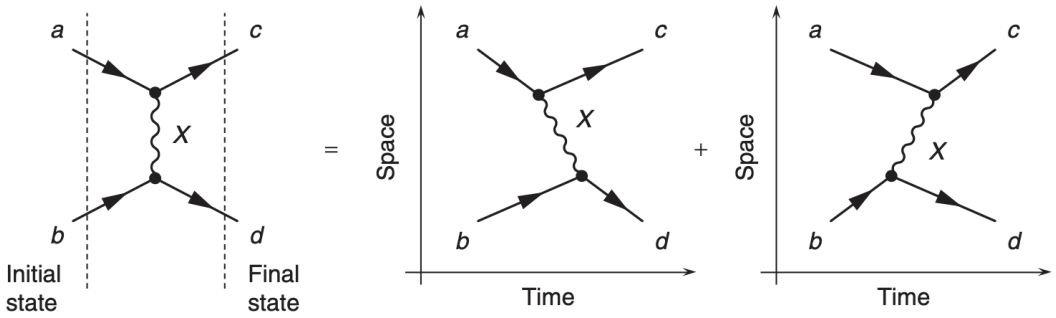

FIGURE 1.3: Feynman diagram of a simple interaction between two particles with initial states a and b, exchanging a propagator X, resulting in final states c and d. The Feynman diagram (left) represents all possible time-orderings of the interaction process.

If two particles, in initial states a and b, interact via the exchange of a propagator X, which results in two final states c and d, one can summarise the process with a Feynman diagram, Figure 1.3, that represents the time evolution of this process, including the incoming and outgoing particles and all vertices of interaction. A Feynman diagram is in fact the representation of all possible time-orderings of the interaction. In general, deriving the transition matrix element of some interaction process from the first principles of QFT can be inconvenient and time consuming. Luckily, from the QFT a simple set of rules can be derived that allow to construct the matrix element for any Feynman diagram, the so-called *Feynman rules*. Furthermore, these rules allow to determine whether a process can exist according to the assumed theory (such as the SM), i.e. if the Feynman diagram represents a an allowed interaction or not. For example, in Figure 1.3 the two incoming particles could be negatively charged electrons, where the Feynman diagram would represent an electron-electron scattering through the exchange of a photon. This process is allowed in the SM, since electrons carry the electric charge to couple with the photon, which for example would not hold if the incoming particles were neutrinos.

In general one can use these diagrams to construct any kind of interactions and predict its cross section, i.e. the probability for such an interaction to occur. For instance, if the diagram in Figure 1.3 is rotated by $\pi/2$, it would describe an annihilation process, where particle a and c annihilate to create the propagator X, which

[10] Virtual particles are short-lived mediators of interactions that cannot be detected.

further decays[11] to b and d. Moreover, since the transition matrix element is calculated from a perturbation expansion, an infinite number of Feynman diagrams can be drawn for the same initial and final states, where each diagram contributes to the matrix element. For example, the diagram in Figure 1.3 would have to be extended, where between the initial and final particles, multiple interactions can occur, resulting in more vertices but with same outcome. The lowest order diagram, with the least number of vertices, is known as the *leading order diagram* (if no loops of particles are included also referred to as the *tree diagram*), while diagrams involving more vertices are referred to as *loop diagrams*. In this thesis, tree level diagrams are always used to demonstrate a process.

Furthermore, the nature of an interaction can be deduced from the Lagrangian of the theory. In the case of QED, the interaction (second) term in Lagrangian 1.10 involves two fermion spinors and a photon field, suggesting that QED interactions happen through three vertices, such as diagram Figure 1.3. Considering the $SU(1)$ Higgs Lagrangian eq. 1.25, four different interaction terms can be distinguished. Figure 1.4 shows the vertices associated to the interaction terms, the first two represent tri- and quartic vertices between two massive gauge bosons and two Higgs bosons, and the last two terms, tri- and quartic self-interaction vertices of the Higgs boson. Also the coupling strength associated to the interaction vertices is shown, which corresponds to the coefficient of each interaction term in the Lagrangian.

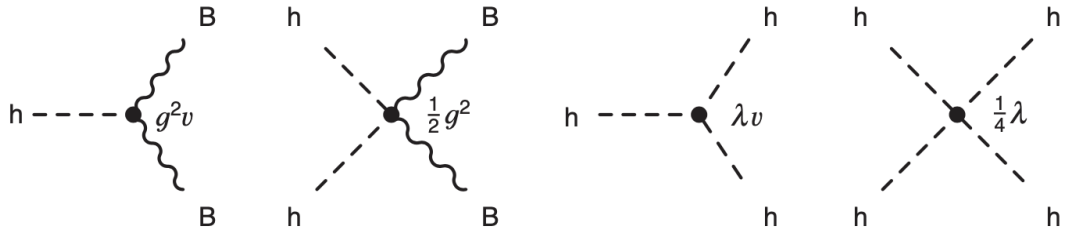

FIGURE 1.4: The interaction vertices associated to the interaction terms in the Higgs Lagrangian eq. 1.25. Also the coupling strength associated to each interaction vertex is shown.

1.4 The Standard Model Higgs boson properties

As mentioned before, the scalar Higgs field is expected to have a non-zero vacuum expectation value, a consequence of the spontaneous symmetry breaking. The associated particle is the Higgs boson, which is a spinless massive particle. According to the SM electroweak theory, the Higgs boson can interact with all fermions and weak bosons through three vertices as shown in Figure 1.5. The coupling strength with each of the vertices is proportional to the mass of the particle. This suggests that

[11] For each SM particle, if there is a particle with a smaller rest mass, the heavier particle will always decay to the latter if there exists a valid Feynman diagram for the process in the SM theory.

the heavier the particle, the stronger the coupling to the Higgs boson, i.e. the more likely the interaction. Therefore, it is more likely that the production and the decay of the Higgs boson happens through heavier particles.

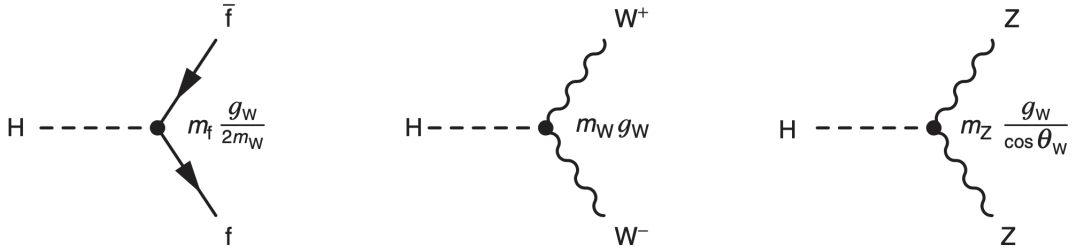

FIGURE 1.5: The interaction vertices of the Higgs boson with fermions and weak bosons. Also the coupling strength associated to each interaction vertex is shown.

As previously stated, the SM Lagrangian includes free parameters, such as the masses of the elementary particles and the weak mixing angle, that to the best of knowledge have to be measured empirically. These parameters are essential in order to test the SM predictions, which depend on the value of the free parameters. For example, the Higgs boson production cross section and the rate at which it decays to specific particles are direct probes to test the SM predictions, but these depend on the value of the Higgs boson mass. Figure 1.7 (A) shows the relative frequency of Higgs boson decays to different SM particles, the so-called *branching ratio*, as a function of its mass.

The Higgs boson was discovered in July 2012 by the ATLAS [31] and CMS [44] experiments at CERN, and was found to have a mass consistent with 125 GeV. Its vacuum expectation value is consistent with 246 GeV, which is known from its relation to Fermi constant [26], $v = (\sqrt{2}G_F)^{-1/2}$. Typically, unstable particles have an intrinsic uncertainty on their mass, a consequence of the *Heisenberg uncertainty principle*, which is proportional to the inverse of the particle's lifetime. This natural width provides a range of masses at which the particle could be observed. For the Higgs boson, this width is approximately 4 MeV [83], which is relatively narrow. Furthermore, the Higgs boson mass value sets the branching ratios for Higgs decays (vertical line on Figure 1.7 (B)) which can be measured. The initial condition for the Higgs boson to decay to a pair, is that the sum of the particles mass has to be smaller than the Higgs boson's mass itself, i.e. $m_H > 2m_i$. The heaviest particle in the SM is the top quark, and since the Higgs boson is lighter, it cannot decay to it. The second heaviest fermion is much lighter than the Higgs boson and therefore the $H \to b\bar{b}$ decay channel is allowed, which has a branching ratio of 57.8% being the largest. Despite the fact a pair of weak bosons is heavier than the Higgs mass, the decay channels $H \to WW$ and $H \to ZZ$ are possible, where one of the bosons in the pair

is virtual off-mass shell[12]. The respective branching ratios are 21.6% and 2.7%. This difference appears in the amplitude calculation of the matrix element [87] . Furthermore, despite the fact that the Higgs boson does not couple to massless particles, the decay modes $H \to \gamma\gamma$ and $H \to gg$ can happen indirectly through so-called top quark and W boson loops. Figure 1.6 shows the Feynman diagrams of interaction vertices of the Higgs boson with the massless bosons.

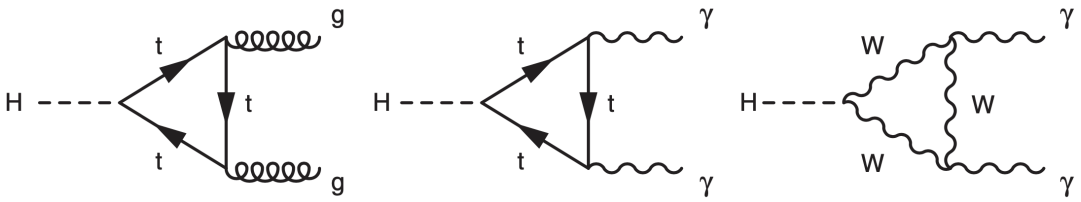

FIGURE 1.6: Feynman diagrams of interaction vertices of the Higgs boson with massless bosons through top quark and W boson loops.

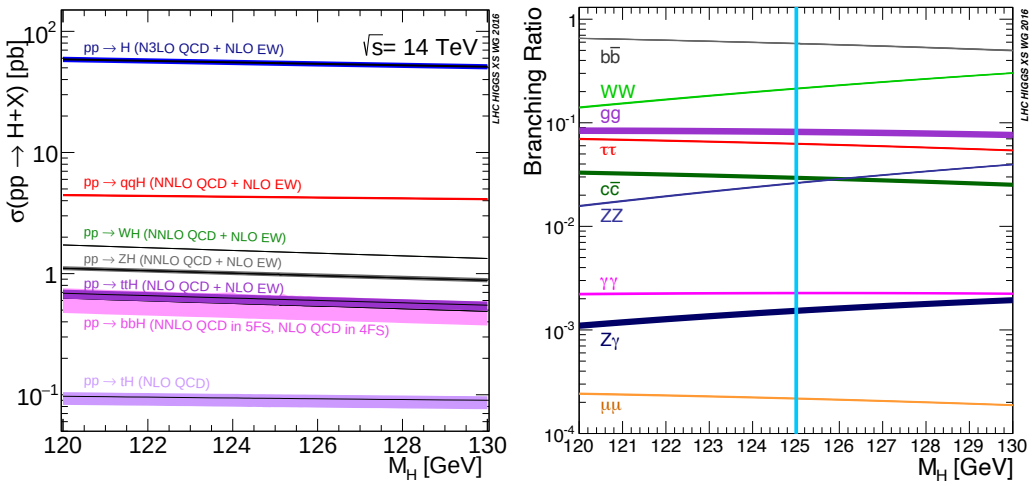

(A) (B)

FIGURE 1.7: Standard Model Higgs boson production cross sections at the LHC (A) and its branching ratios (B) as a function of the Higgs boson mass [25]. The Feynman diagrams of the different production modes are given in decreasing order of cross section in Figure 1.8.

In general, the Feynman diagrams described above can be rotated to form any scenario; in current time-order (from left to right), Figure 1.6 and 1.5 can be interpreted as decay processes of the Higgs boson. If one rotates the diagrams over π, they would describe Higgs boson creation processes. In Figure 1.5, one can even rotate the diagrams over $4/3\pi$ to describe a *Higgs strahlung* process, where a Higgs boson

[12]Virtual particles do not satisfy the energy-momentum equation $E^2 = \vec{p}^2 + m^2$ and therefore their mass does not correspond to the real mass of particles they represent. Virtual particles are only allowed as internal propagators in Feynman diagrams

is radiated by a fermion or a weak vector boson. Using the Feynman rules, one can predict the likelihood of such processes to happen. Unlike decay scenarios, where the Higgs boson decays naturally, producing the Higgs boson comes with an extra challenge, which is providing enough energy for its creation. So far, the Higgs boson has only been successfully produced and observed with the Large Hadron Collider, where protons are collided at high energies.

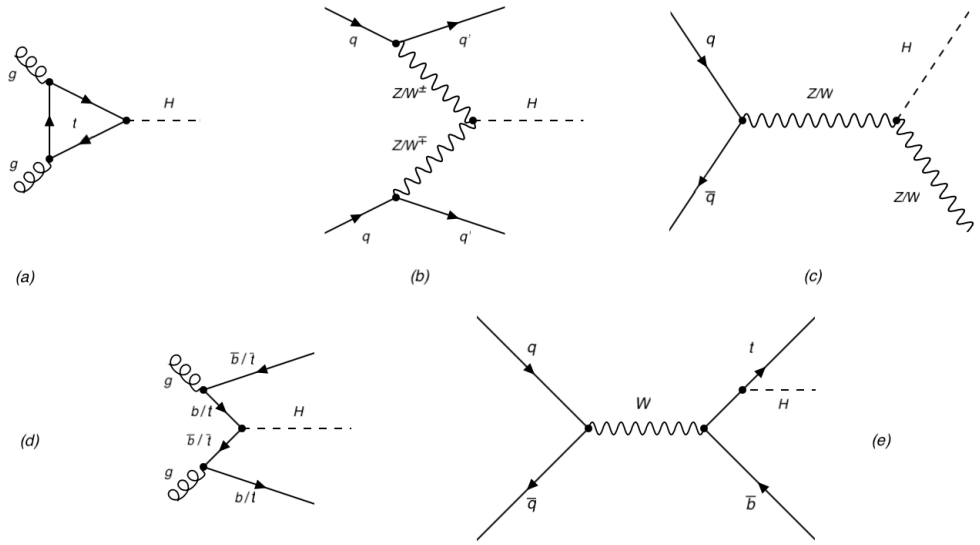

FIGURE 1.8: Feynman diagrams of the dominant Standard Model Higgs boson production modes in proton-proton collision events.

In the latter experimental setup (discussed in), the expected Higgs boson production cross sections are fixed by its mass value. Figure 1.7 (B) shows the Higgs boson production cross section of the leading processes as a function of its mass, and Figure 1.8 the Feynman diagrams of these production modes. The first blue curve corresponds to the cross section of a proton collision producing a Higgs boson ($pp \to H$) through a *gluon-gluon fusion* (a), which is the most dominant process. The gluons are radiated from quarks inside the protons, which produce a Higgs boson through a virtual top quark loop. Since the top quark mass is orders of magnitude higher than any other quark, which corresponds to a larger coupling to the Higgs boson, even the contribution of bottom quark loops is negligible in this process. The second leading process is the *vector boson fusion* (b), where quarks radiate like weak bosons that couple directly to the Higgs boson. The cross section of this latter process corresponds to the red curve, denoted by $pp \to qqH$, which is approximately an order of magnitude lower than the dominant gluon fusion process. The third and fourth are respectively $pp \to WH$ and $pp \to ZH$, which are referred to as *vector boson associated productions* (c), where a produced W and a Z boson radiate a Higgs boson. Two gluons can decay to a pair of top (or bottom) quarks, where the particle and anti-particle of each pair can fuse to give rise to a Higgs boson (d). These are denoted

as $pp \to t\bar{t}H(b\bar{b}H)$. Finally, in a single top quark production, a Higgs boson can be radiated by the massive quark ($pp \to tH$), which is the rarest process of all.

1.5 Proton colliders phenomenology

As discussed in section 1.4, the Higgs boson has been observed so far only in proton-proton collision events at the LHC. Protons are complex objects that are not simply bound states of three quarks (uud), but also contain a sea of virtual gluons, which themselves produce virtual quark and gluon pairs all the time [88]. Since protons are composed of *partons* (i.e. quarks and gluons), proton-proton interactions at sufficiently high energies take place between these fundamental particles, which are quasi unbound, a consequence of the QCD running coupling[13] and asymptotic freedom[14] [89]. In this case, each parton carries a fraction of the proton's momentum, and can interact with partons from another proton. In such inelastic collision events, the protons are broken up, and particles can be created from hard scatter events with new hadronic bound states emerging from the remaining partons. Figure 1.9 shows a diagram with an example of a proton-proton collision event showing the different partons involved in the hard scatter interaction.

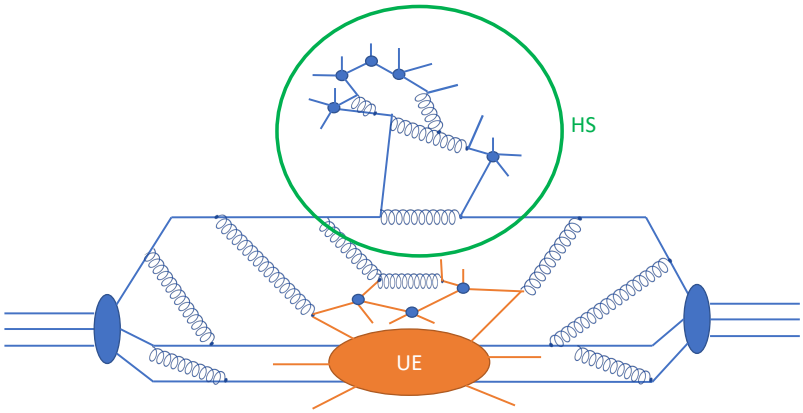

FIGURE 1.9: An example diagram of a proton-proton collision event showing the different partons involved in the hard scatter process (HS) interaction and the underlying event (UE).

In reality, modelling the distribution of partons inside the proton is very difficult. These are in fact extracted from data of collider experiments, where the *parton distribution function*, $f_q(x, Q^2)$, is extracted, which represents the probability density to find a certain type of parton with a momentum fraction x given a four-momentum transfer squared Q^2. As this function is dependent on the energy scale Q of the operating experiment, Figure 1.10 shows the difference in the parton distribution functions of the various partons inside a proton at relatively low energy (Q^2 = 10

[13] The dependence of the QCD coupling on the energy scale is referred to as running coupling.
[14] Parton interactions become asymptotically weaker as the energy scale increases.

GeV^2) versus at high Q ($Q^2 = 10^4$ GeV^2). At a relatively high energy scale, gluons tend to carry most of the proton's momentum, while at lower energies quarks dominate.

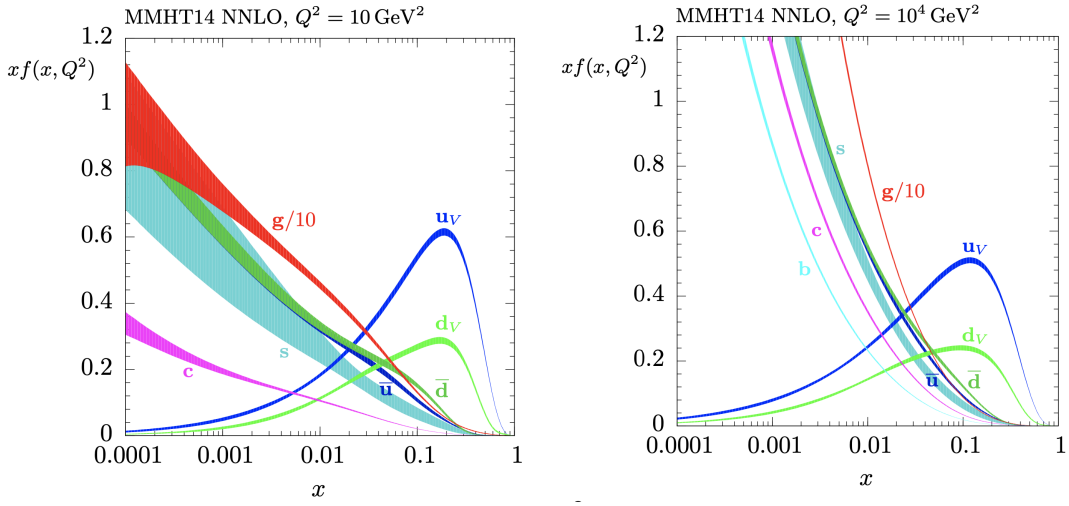

FIGURE 1.10: The parton distribution function of the various partons inside a proton at relatively low energy scale (left) and at high energy (right) [27].

Due to this complex structure of the proton, cross sections of physics processes occurring from high energy proton-proton collisions depend on the inelastic parton interaction cross section as well as the probability of finding the involved partons inside a proton,

$$d\sigma_{p_1p_2\to X} = \int dx_1 dx_2 \sum_{q_1q_2} f_{q_1}(x_1, Q^2) \times f_{q_2}(x_2, Q^2) \times d\sigma_{q_1q_2\to X}(\alpha, Q^2), \tag{1.34}$$

with X a specific final state, $\sigma_{q_1q_2\to X}(\alpha, Q^2)$ the inelastic cross section of the $q_1q_2 \to X$ process depending on the coupling strength of the interaction α and the energy scale Q. Proton-proton interactions are predominantly dependent on the QCD coupling α_s, which is not small and thus the use of perturbation theory does not hold (divergent series). Since this last parameter becomes smaller at higher energies, $\alpha_s(Q^2) \to 0$ with larger Q^2 (asymptotic freedom), $d\sigma_{q_1q_2\to X}(\alpha, Q^2)$ can be calculated perturbatively as,

$$d\sigma_{q_1q_2\to X} = \sum_{m=0}^{\infty} \alpha_s^{m+k} d\hat{\sigma}_{q_1q_2\to X}$$

where each higher order term in m can be regarded as a higher order Feynman diagram, while k represents the number of strong vertices at $m = 0$. Typically, theoretical predictions of cross sections are presented with the accuracy at which the computation was performed; e.g. including only the first order corresponds to the *leading order* (LO) diagram, while the *next-to-leading order* (NLO) is followed by the *next-to-next-to-leading order* (NNLO), and so on up to N^{m}LO. Figure 1.11 shows a

summary example of several predicted and measured SM total cross sections of processes emerging from proton-proton collision events at relatively high *centre-of-mass energies*[15], $\sqrt{s}$, which can be expressed as[16],

$$s = \left(\sum_{i=1}^{2} E_i\right)^2 - \left(\sum_{i=1}^{2} \overrightarrow{p_i}\right)^2, \tag{1.35}$$

where E_i is the energy of the i-th particle in the collision, and $\overrightarrow{p_i}$ its three-momentum vector. The measurements were performed using the ATLAS detector (discussed in section 2.4) and are compatible with the theoretical expectations, which were all calculated at NLO or higher.

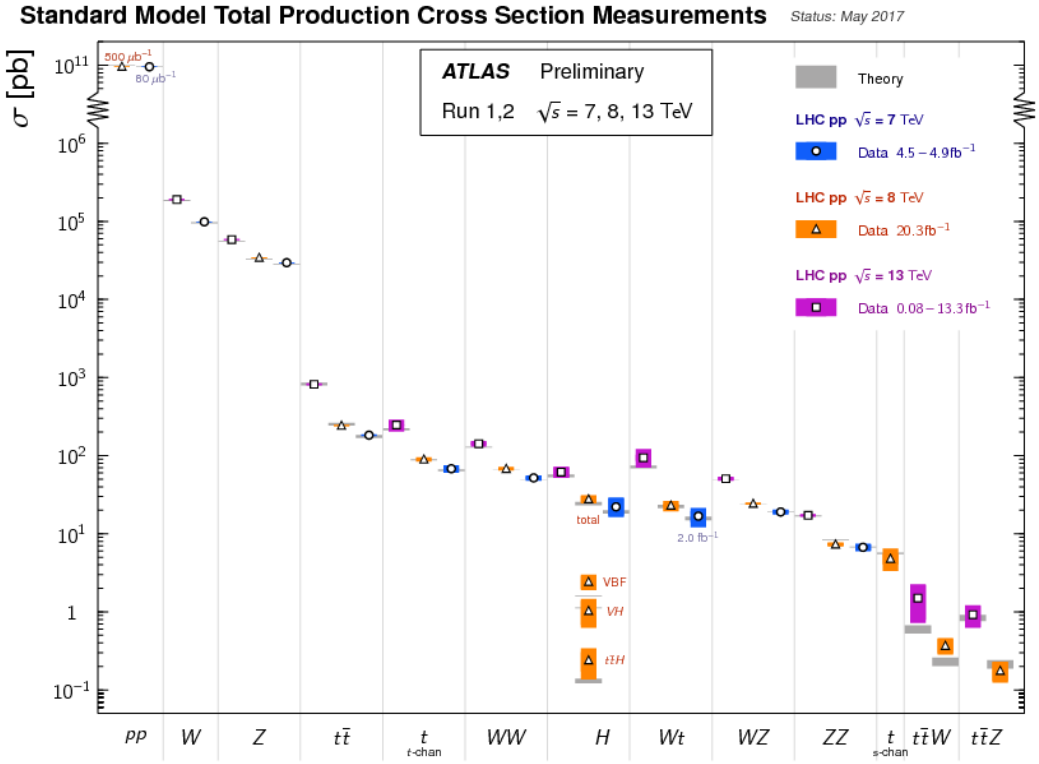

FIGURE 1.11: A summary example of several predicted and measured SM total cross sections in the ATLAS experiment. The theoretical expectations were calculated at NLO or higher [28].

[15] In the centre-of-mass inertial frame, the sum of the three momenta of all particles is equal to 0.
[16] Assuming the natural units system, where the fundamental constants $c = \hbar = 1$.

1.6 The Standard Model Effective Field Theory

As mentioned in section 1.1.5, the SM is most likely an incomplete theory. Unlike e.g. Supersymmetry, where a well-defined extension is proposed to extend the SM, a more model independent approach is to consider the SM as a low energy (IR) EFT of some fundamental theory valid at all energy scales (UV). In this case, the SM is expected to be a good approximation at relatively low energies (typically up to the TeV scale, which has been well affirmed so far), while it would break at some higher scale beyond the electroweak scale $\Lambda \gg \Lambda_{EW}$. Thus, an EFT approach [20] is based on the fact that a physical system depends on the energy scale at which it is considered, whereby it is not necessary to use the most fundamental laws of physics to achieve satisfying predictions, while it is sufficient to consider an approximate, simplified theory relevant at the corresponding scale, such as the SM at the electroweak scale. This approach is especially useful when physics at higher energies is unknown; one can parametrise the effects of missing higher energy content on observables of the known low energy theory.

As discussed in the previous sections, from the perturbative approach used in couplings such as α_s, calculations beyond the lowest order can lead to divergences, hence unphysical predictions such as infinite cross sections can occur, while in reality, measurable quantities are found finite. To match empirical measurements, counter terms are applied to cancel out divergences; the basic idea is to rewrite an expression that is initially a function of some large scale Λ, in terms of measurable, renormalised quantities in a given coupling strength at some scale Q^2, e.g. Λ_{EW}. In fact, EFT gives a firm ground to this *renormalisation concept*, and explains when renormalisable theories arise. As the SM is a good EFT up the TeV scale, it can be used as a basis to construct an EFT; if $\mathscr{L}_{UV}$ is the Lagrangian of a general UV theory including the SM field content ϕ_{SM} and some unknown fields ϕ_{BSM}, assuming the latter consist of heavy particle(s) that cannot be produced at energy scales where the SM is sufficient to describe physics, one can write an EFT of this UV theory as,

$$\mathscr{L}_{UV}(\phi_{SM}, \phi_{BSM}) \rightarrow \mathscr{L}_{EFT}(\phi_{SM}) = \mathscr{L}_{SM} + \sum_i g_i \mathscr{O}_i(\phi_{SM}), \tag{1.36}$$

with $\mathscr{O}_i$ a set of local effective operators, and g_i their corresponding effective couplings. There are a couple of benefits in the latter expression; the first is the fact that the SM Lagrangian is contained in the effective Lagrangian, and thus one can reproduce SM results. Secondly, the EFT Lagrangian depends only on SM fields such that BSM effects can be expressed model independently, i.e. no assumptions are made on the BSM content, as long as it is only relevant larger scales ($\Lambda \gg \Lambda_{EW}$). A theoretical framework that permits the description of effects of potential BSM theories is the Standard Model Effective Field Theory (SMEFT) framework [29], which relies on the assumption that new physics must be invariant under gauge symmetries while it

should be only relevant at high energy scales ($\Lambda \gg \Lambda_{EW}$). With these assumptions, one can write the effective Lagrangian eq. 1.36 as a parametrisation of every possible operator from the existing SM fields at each order in Λ characterising the energy scale at which the new physics is expected to be relevant. These higher dimensional operators $\mathcal{O}_i$, higher than the dimension four SM operators (d > 4), encode effects of BSM physics at scale Λ as,

$$\mathscr{L}_{EFT} = \mathscr{L}_{SM} + \sum_{d=5}^{\infty} \sum_{i} \frac{c_i^{(d)}}{\Lambda_i^{d-4}} \mathcal{O}_i^{(d)}, \tag{1.37}$$

where the higher order operators are suppressed by powers of $1/\Lambda$ of the new physics scale, and c_i are the operator associated coupling constants, the so-called *Wilson coefficients* containing information about UV physics above the Λ scale. In principle, any BSM theory can be matched to the EFT, upon the condition that new fields decouple for $\Lambda \to \infty$. The higher the order of the operator, the smaller its contribution at lower energy regimes as the suppression increases with powers of $1/\Lambda$. Consequently, the infinite sum can be truncated to obtain results with a given accuracy, as the aim is to compare experimental measurements which have finite precision. The procedure of determining the relevant and redundant operators is referred to as *power counting*. Having the adequate truncated sum, one can determine the Wilson coefficients to search for new physics; typically an observable has to be defined, with a process sensitive to new couplings that would modify the SM expected results. Any deviation from zero of these coefficients would indicate BSM physics. In this thesis, a preliminary study is presented where BSM contributions from anomalous quartic gauge-couplings to the $\gamma\gamma \to 4l^{\pm}$ process are investigated in the framework of the SMEFT.

Chapter 2

The Large Hadron Collider and the ATLAS experiment at CERN

2.1 European Council for Nuclear Research (CERN)

The European Council for Nuclear Research (or *Conseil Européen pour la Recherche Nucléaire* in French) is an international organisation with particle physics research as its main goal. The research physics programme is focussed on fundamental questions about the structure of our universe. This includes the SM of particle physics and beyond, as well as Dark Matter experiments, but also exotic isotope and cosmic ray experiments. It is located around the borders of France and Switzerland, near the worldwide centre for diplomacy, Geneva city. It currently has the world's largest laboratory in particle physics, with its main experiment, the Large Hadron Collider.

FIGURE 2.1: Bird's-eye view of the CERN (*Conseil Européen pour la Recherche Nucléaire*) Meyrin site between the French-Swiss border.

It has been a key centre for discoveries in particle physics, such as the discovery of the Z and W boson, and most recently the Higgs boson. Apart from physics, it was also the birthplace for many cutting edge technologies and inventions, such as the World Wide Web or touch screen technology. All this success has been the achievement of a large international collaboration, from different countries all over the world.

2.2 The Large Hadron Collider

Somewhere between France and Switzerland, one of the most incredible machines ever built by human beings can be found 175 meters underground. The Large Hadron Collider (LHC) [3] is the largest and most powerful particle accelerator in the world.[1] Initially, the main reason for building such a gigantic machine was to discover the last piece of the Standard Model, the Higgs boson, which was successfully achieved back in 2012. However, the physics programme of the LHC is not limited to this last discovery. As mentioned before, the SM is clearly not the end story. Many proposed theories supporting the extension of the SM predict new particles that could solve open questions about the universe around us.

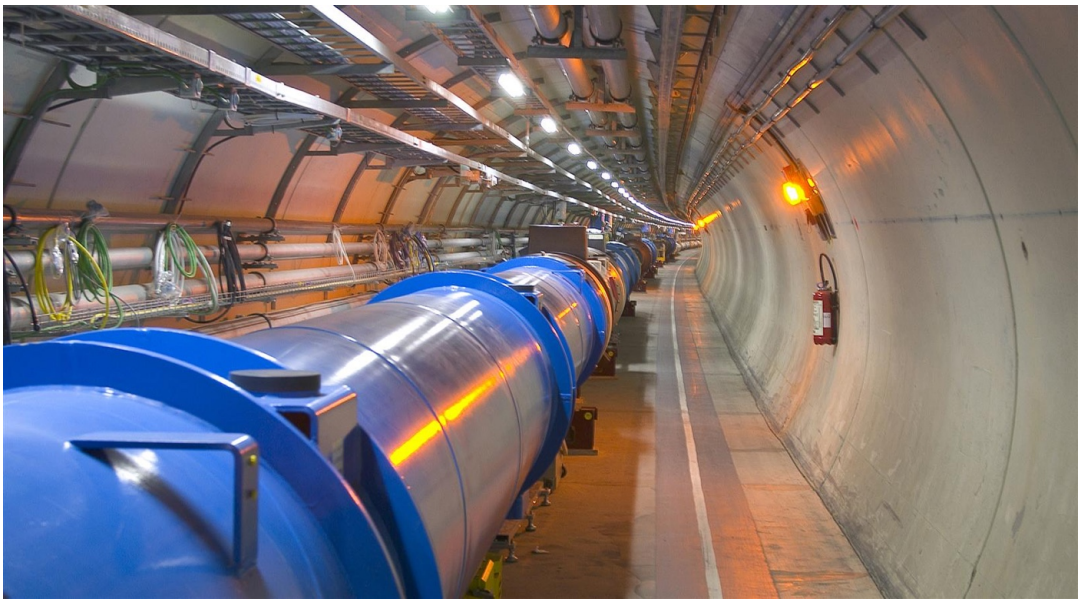

FIGURE 2.2: The Large Hadron Collider ring in the 175 meters underground tunnel between the French-Swiss border [33].

2.2.1 High energy particle accelerators

In general, the strategy for the hunt of new particles has been the same since the discovery of unstable particles from cosmic rays [86]. They could not be found in nature

[1] There are plans to build larger accelerators which would collide particles at a higher energies, e.g. the future circular collider [85].

due to their very short life time before decaying to stable particles, such as electrons. Some of these particles could be detected in *bubble chamber experiments* [34]; a sort of vessel filled with a hot transparent gas, where charged particles could leave tracks after ionising the gas molecules. Using a magnetic field, physicists could bend the particle trajectories and observe tracks with different properties than those coming from protons and electrons. For example, they could observe a negatively charged particle that would bend much less than the electron, suggesting its mass was heavier. These electron-like particles were the well-known muons, which are approximately 200 times heavier than electrons.

Since then, many other particles were discovered, including *mesons*[2]. Physicists quickly understood that the fundamental ingredient for producing particles was *energy*. Using cosmic rays to study properties of these unstable particles was not very efficient. The source of the interaction is unknown, collision events occur randomly, findings could not be reproduced; one had to find a way to produce these particles in a lab. This is how particle accelerators came to life; the basic idea was to accelerate charged particles in an electric field to gain momentum before colliding them into a target or another beam coming from the opposite direction. This would release energy that could possibly generate new particles. From the famous equation, $E = mc^2$, the higher the energy of the colliding particles, the more likely the production of heavier particles, including rare undiscovered particles.

Throughout the 20^{th} century, the search for new particles was driven by increases in collision energy. The reason for this ambition is the fact that, it is more likely that new particles are heavy, as particles within accessible energies should have been observed already. Moreover, the mass of the produced particle(s) has to be smaller than or equal to the centre-of-mass energy $\sqrt{s}$ of the colliding initial particles. Since then, many novel techniques and designs have resulted in different types of accelerators, with each upgrade producing a more efficient particle acceleration, permitting higher centre-of-mass energies. Figure 2.3 shows the evolution of the centre-of-mass energy of particle accelerators since the late 60s. The acceleration of particles in linear colliders is limited due to the difficulty of increasing and maintaining the electric field permitting the increase in energy of particles. At present, circular accelerators are the most successful, where energy is gained while the particles go through the same electric field in each loop. This necessitates the control of the beam in a circular trajectory using a magnetic field. However, this can also limit the acceleration of charged particles, which radiate when they are bent in a magnetic field, via so-called *synchrotron radiation* [36], and thus a limit is reached where the loss of energy due to radiation stagnates the gain. From *Larmor's formula* [37], the energy loss per

[2]bound states of quarks, with an equal number of quarks and anti-quarks.

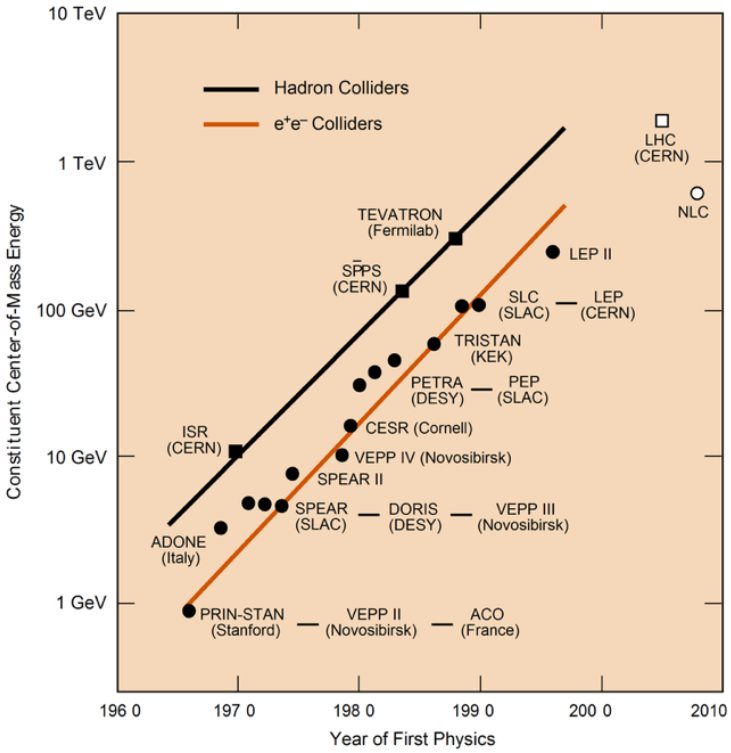

FIGURE 2.3: Progress in time of the collision centre-mass-energy of particle accelerators throughout the last century [35].

revolution in a circular accelerator is proportional to,

$$\delta E \sim \frac{1}{R}\left(\frac{E}{m}\right)^4, \tag{2.1}$$

where E is the energy of the charged particle, m its mass and R the radius of the accelerator. The higher the bending curvature, the more a charged particle radiates. Therefore larger circular accelerators (larger R) benefit from a smaller energy loss due to radiation. Also the lighter the particle, the more it radiates. This is the reason why *hadron* colliders perform better than electron colliders. Traditional particle accelerators were designed to fire charged particles to materials at rest, the so called fixed-target experiments. From conservation of momentum, the produced particles are created with a notable kinetic energy, which is wasted, i.e. does not contribute to the potential energy for particle creation. From equation 1.35, if a proton of 7 TeV[3] is collided into a proton at rest, the resulting centre-of-mass energy would be 115 GeV, which is not sufficient to produce an on-mass shell Higgs boson. On the other hand, one can achieve significantly higher centre-of-mass energies when colliding two beams of protons with the same energy, for which the collision happens in the centre-of-mass frame. In this case, the yield in centre-of-mass energy is 14 TeV, which is 2 orders of magnitude higher.

[3]In particle physics, energy is often given in Electronvolts (eV), which corresponds to the kinetic energy of an electron accelerated in a electric potential difference of 1 Volt.

2.2.2 The LHC as a proton collider

The design of the LHC was based, among other reasons, on the previously mentioned factors in order to maximise the centre-of-mass energy. It is a circular accelerator of 27 km in circumference, permitting the acceleration of two parallel proton[4] beams up to 7 TeV, travelling in opposite directions, before colliding them at specific collision points, where large detectors are built to record the high energy proton-proton interaction events. It is currently at the energy frontier, delivering a centre-of-mass energy of 13 TeV.

2.2.2.1 The LHC injection chain

Even though the LHC is praised for its performance, it is not the only accelerator used to reach the energy frontier. Figure 2.4 shows the series of accelerators that the protons have to go through before being injected in the LHC. It all starts from an ordinary bottle of hydrogen, where the molecules are dissociated to extract the negatively charged hydrogen atoms. The first acceleration happens in the linear particle accelerator, LINAC, where ions reach an energy of 160 MeV. The next boost occurs in the Proton Synchrotron Booster (PSB), where the electrons are kicked from the nucleus, leaving only protons in the loop, which get further accelerated to 1.4 GeV. Next, the protons are injected to the Proton Synchrotron (PS) where a gain of 26 GeV is achieved and the particles are grouped in bunches of 1.2 meters, separated by 7 meters from each other. Lastly, the protons reach an energy of 450 GeV in the Super Proton Synchrotron (SPS), before being injected into the LHC. Here protons are first injected into one ring, then in the opposite direction in the other ring, where they are finally accelerated to 7 TeV. In each beam, there are 2800 bunches, each containing approximately 100 billion protons. At this point, the protons are travelling at up to 99.999999% of the speed of light, with a revolution frequency of 11245 loops per second. This corresponds to 30 million crossings per second.

2.2.2.2 The LHC components

To achieve this high energy, the LHC is based on the same physics concepts as all circular accelerators. An electric field to accelerate the protons, and a magnetic field to control their trajectory. The components that make up the LHC are mainly cylindrical dipole magnets, which are essential to keep the beam trajectory inside the ring, and metallic chambers containing an electromagnetic field, known as radiofrequency cavities, where the protons are accelerated.

Figure 2.5 shows the cross section of an LHC dipole with the different components. There are 1232 of them. Each dipole is 15 m long, and weighs 35 tons. Inside these massive cylinders, two tubes with a diameter of a few centimetres are placed in

[4]It is sometimes used with ions, such as lead nuclei for different physics purposes, but most of the time with protons.

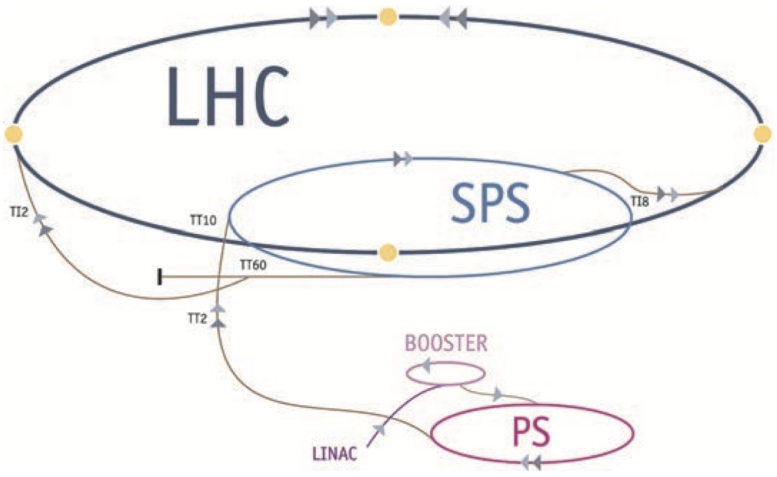

FIGURE 2.4: The injection chain of the accelerated protons before their way to the Large Hadron Collider [38].

parallel, where the two opposite direction proton beams circulate. To ensure the curvature of the beams, the tubes are placed in a high magnetic field generated by a current in cables around the beam pipes. This magnetic field is increased gradually while the protons are accelerated. The faster they travel, the higher the magnetic field is required to keep the beam inside the pipes. A maximum magnetic field of 8 Tesla's is reached when the protons reach the maximal acceleration energy of 7 TeV. To generate a magnetic field of this magnitude, a current of 12000 amperes is needed, which no ordinary cable can tolerate before melting. Therefore, superconducting[5] cables with almost no electric resistance are used, which are cooled to 2 degrees above the absolute zero. In order to prevent the accelerated protons interacting with molecules from the air, the tubes are placed under a vacuum, reaching a low pressure of 10^{-11} mbar, 10000 billion times lower than atmospheric pressure.

The maximum energy of 7 TeV is obtained after 10 million loops (approximately 20 minutes after their injection) through the superconducting radiofrequency cavities, where each cavity delivers 2 million Volts. There are 16 of them in total, 8 per beam. Inside these cavities, a longitudinal oscillating electric field at a frequency of 400 Megahertz ensures that when the protons arrive, the field is pointing in the same direction, hence they will be accelerated. Another important function of the cavities is to keep the bunches compact; after reaching the desired energy, a proton with the ideal arrival time in the bunch will not be accelerated, while those arriving earlier or later will be respectively decelerated and accelerated, resulting in a compact bunch. This is not the only attempt to keep the bunches confined, different configurations of magnets are used on top of the dipoles, such as quadruple magnets, to focus the beams and prevent the dispersion of the bunches. Finally, at the interaction points,

[5] made of a mixture of niobium and titanium

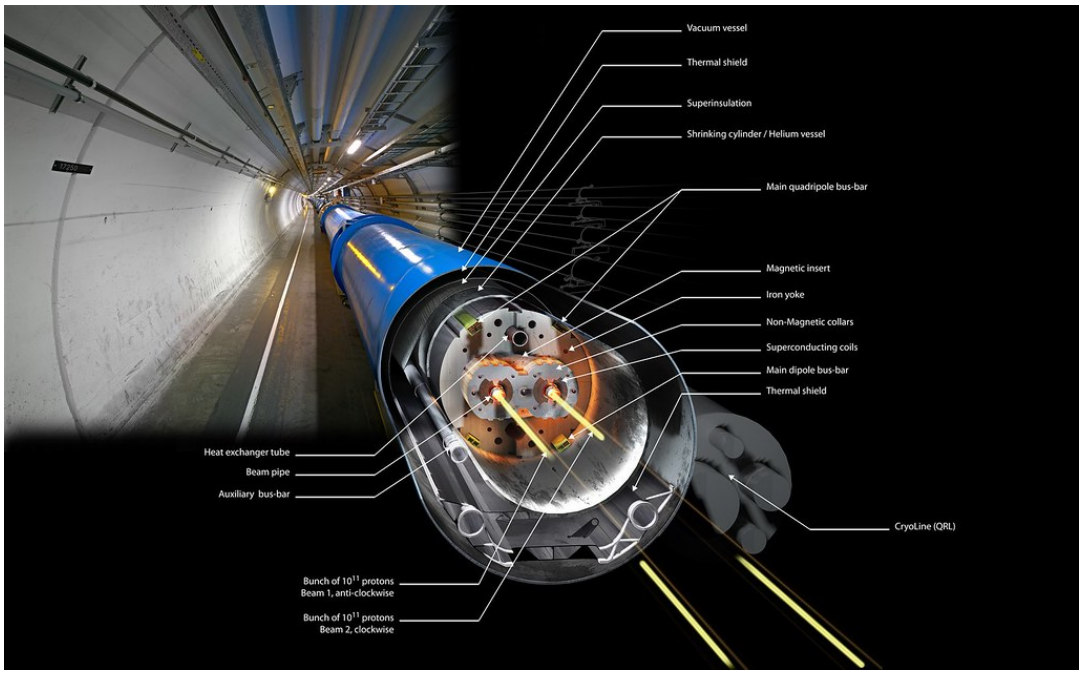

FIGURE 2.5: The LHC dipole magnet and its components. Inside the dipoles, a magnetic field is produced to bend and keep the protons inside the ring [39].

the diameter of bunches is reduced to 16 microns using specific focussing magnets.

2.2.2.3 The LHC parameters

Keeping the bunches tight and compact is very important to maximise the chances of collision events. On average, there are 20 collision events per bunch crossing with nominal beam currents at the LHC. This can be characterised with the *instantaneous luminosity*, L, which is a measure of the number of collision events per unit time per area. Using the beam parameters, L can be expressed by,

$$L = \frac{n_1 n_2 f_r}{4\pi\sigma_x\sigma_y}, \tag{2.2}$$

with f_r the revolution rate, n_1 and n_2 the number of protons per bunch in the first

and second beam, and σ_x and σ_y the transverse beam profile along the horizontal and vertical direction. To get an order of magnitude of L, one can approximate equation

2.2 with,

$$L \sim \frac{n^2}{tS_{eff}}, \tag{2.3}$$

where n is the number of protons per bunch (assuming equivalent beams), t the bunch-spacing in time and S_{eff} the effective transverse area of the bunch. For the LHC, the values of these parameters are

$$n \sim 1.15 \times 10^{11} \text{protons},$$
$$S_{eff} \sim 4\pi(16 \times 10^{-4})^2 \text{ cm}^2,$$
$$t \sim 25 \times 10^{-9} \text{s},$$

which results in,

$$L \sim 10^{34}\ s^{-1} cm^{-2},$$

i.e. the LHC can produce 10^{34} collision events per second and per cm^2. Table 2.1 shows some basic parameters of the LHC. Typically, collider experiments operate during well specified periods of time, referred to as *runs*, where the collision events are recorded by detectors around the interaction point. Figure 2.6 (a) shows the cumulative integrated luminosity delivered over time by the LHC, and the one recorded by the ATLAS detector (discussed in section 2.4) during the second run of $\sqrt{s}$ = 13 TeV proton-proton collision data-taking between 2015 and 2018, and Figure 2.6 (b) shows the latter as a function of the mean number of interactions per bunch crossing (μ) during this last run. The μ corresponds to the mean of the Poisson distribution of the number of interactions per crossing calculated for each proton bunch.

TABLE 2.1: The basic nominal parameters of the Large Hadron Collider [40].

			Injection	**Collision**	
	Energy	[GeV]	450	7000	
Luminosity	nominal	[cm^{-2}s^{-1}]		10^{34}	
	ultimate			2.5×10^{34}	
Number of bunches			2808		3564 bunch places
Bunch spacing		[ns]	24.95		
Intensity per bunch	nominal	[p/b]	1.15×10^{11}		
	ultimate	1.70×10^{11}			
Beam current	nominal	[A]	0.58		
	ultimate		0.86		
Transverse emittance (rms, normalized), nominal & ultimate		[μm]	3.5	3.75	Emittances equal in both planes, small blow-up allowed in LHC
Longitudinal emittance, total		[eVs]	1.0	2.5	Controlled blow-up during accel.
Bunch length, total (4σ)		[ns]	1.7	1.0	has to fit into 400 MHz buckets
Energy spread, total (4σ)		[10^{-3}]	1.9	0.45	

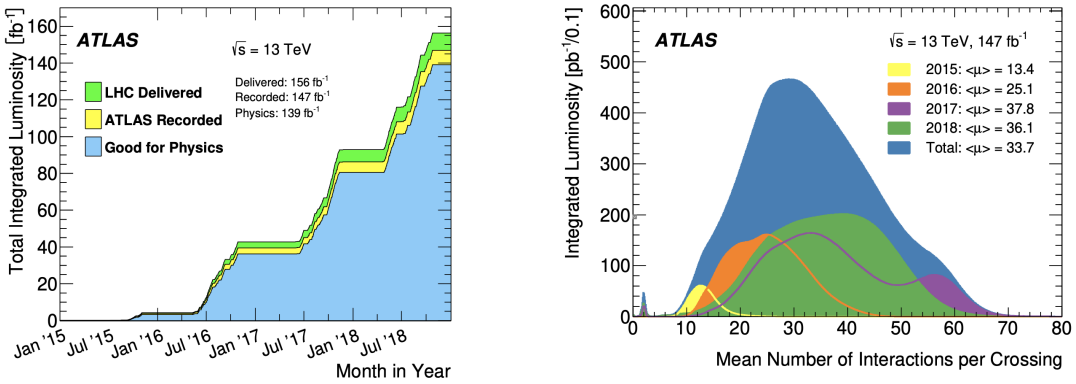

FIGURE 2.6: (a) The cumulative integrated luminosity delivered by the LHC, and the one recorded by the ATLAS detector (discussed in section 2.4) during the second run of $\sqrt{s} = 13$ TeV proton-proton collision data-taking between 2015 and 2018, while (b) shows the latter as a function of the mean number of interactions per bunch crossing (μ) during this last run [41]. . The μ corresponds to the mean of the Poisson distribution of the number of interactions per crossing calculated for each proton bunch.

2.3 High energy particle physics experiments

In general, most physical measurements are characterised by a fluctuating nature, which is impossible to predict with an absolute accuracy. Quantities with this property are said to be random variables that according to a probability distribution can take different values with different likelihoods. A consequence is the fact that repeated measurements, in the exact same experimental conditions, lead to different values. Results from these measurements are affected by this randomness, which is characterised by the so-called *statistical uncertainty*, that allows to make a probabilistic statement about where the true value of the desired quantity is likely to be found.

2.3.1 Measurements in high energy physics experiments

In fact, experimental particle physics is even strongly connected to *statistics* through quantum mechanics, where kinematic quantities are not uniquely defined such as in classical mechanics, but rather determined on the basis of their *probability distribution function* (PDF). The PDF $f(x)$ of a random variable x governs the distribution of a sample of N repeated measurements. These measurements are typically presented in a *histogram* divided into *bins* with a certain width, where each bin contains the frequency of measurements lying within the interval defined by the bin. In fact, a histogram can be interpreted as an approximation of the PDF, where increasing N while reducing the bin width improves the resemblance to $f(x)$, as $N \to \infty$.

In collider experiments such as the LHC, one is typically interested in the *cross section*[6] of a certain process, e.g. $p + p \rightarrow X$, which is a measure of the probability for this process to occur. It is defined as an effective area which is given by,

$$\sigma_{p+p\rightarrow X} = \frac{N_X}{\mathcal{L}} \qquad \text{, with } \mathcal{L} = \int L(t)dt, \tag{2.4}$$

where N_X is the number of events corresponding to the process $p + p \rightarrow X$ and $\mathcal{L}$ is the *integrated luminosity*, both of which can be measured. The latter quantity is an essential parameter; it quantifies the performance of the accelerator, but it is also important for predicting the number of expected events of a specific process.

Moreover, the centre-of-mass energy and the integrated luminosity are essential to make predictions for whether a certain process can be observed in an experiment. First of all, the cross section depends on the centre-of-mass energy of the collision events. Figure 2.7 shows as an example the SM Higgs boson production cross section, for the different production modes, as a function of the centre-of-mass energy, assuming a Higgs boson mass of 125 GeV. Clearly, in this case the cross section of producing a Higgs boson increases with the centre-of-mass energy. If the delivered centre-of-mass energy is known, one can predict the number of expected events given the corresponding cross section of the process and the integrated luminosity. In this case, the longer the data taking of an experiment, the larger the integrated luminosity and thus the larger the number of expected events, which yields in a more precise measurement.

Extending the data-taking runs (an expensive initiative) is unfortunately not the only challenge to get hands on rare events. Producing the events is half the job, the other challenge is to capture and successfully identify the rare particles, for which detectors are needed. As mentioned before, once the desired energy is achieved, the collision events take place at specific interaction points. There are four points on the LHC where the proton bunches are collided. In each of these interaction points, large detectors are built in order to record the collision events. These experiments were built and maintained by independent collaborations, and these are namely CMS [44], LHCb [45], ALICE [46] and the ATLAS collaboration [31]. Figure 2.8 shows the location of the different experiments on the interaction points of the LHC. They have different physics programs, with the exception of CMS and ATLAS, which have a lot of similarities in physics analyses. An example is the interest of both experiments in hunting for the Higgs boson, which they discovered independently back in 2012, putting more confidence in the discovery.

[6] Cross section in particle physics is used to quantify the area of hitting a target, unlike the meaning of the word as a slice.

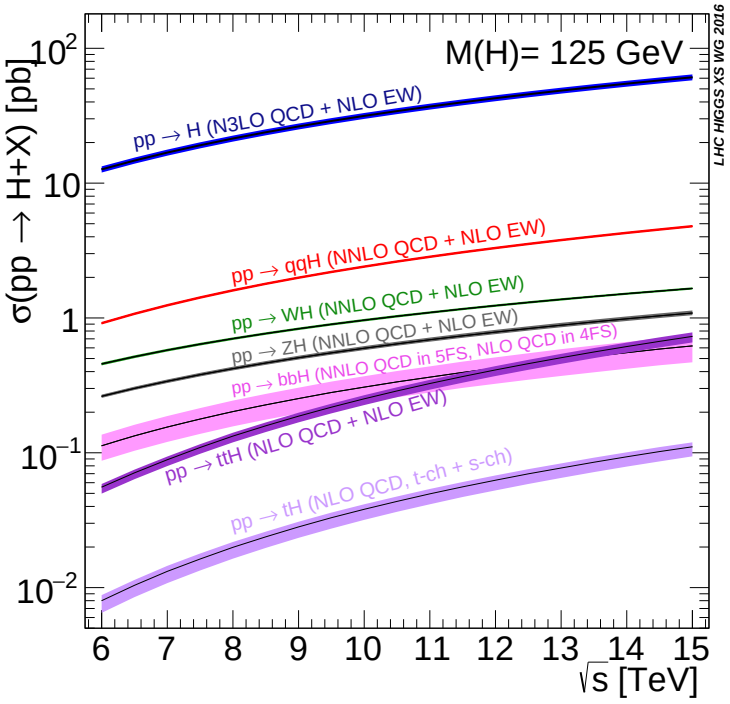

FIGURE 2.7: The Standard Model Higgs boson production cross sections as a function of the centre-of-mass energy in proton-proton collision events [25].

2.3.2 High energy particle physics data analysis

After running a collider experiment, a certain type of data about the collision events is collected. Typically, this information is stored as a sequence of numbers corresponding to the responses of the detector components. This data structure is then processed to be translated to familiar quantities, such as momentum, charge or angular variables. At this stage, each event is characterised by a set of reconstructed objects (to be identified as particles later on) with certain values of the measured quantities. As mentioned before, one is typically interested in studying a specific process. Therefore, out of the available data, one is interested in specific events with certain properties, such as the multiplicity of certain physics objects, that characterises the process in question. In this case, an *event selection* is defined to discriminate wanted from unwanted events. The resulting sample after the event selection is said to have *candidate events*.

Commonly, a theoretical prediction about the process is aimed to be tested, such as the cross section of a SM predicted process. It is therefore important to have an estimate of what the data would look like in case the theoretical hypothesis is true and in the opposite scenario. In particle physics, *Monte Carlo simulated events* [47] are at the heart of the data analysis, where simulation samples reflect the results one would obtain given the assumed theory. First of all, the current understanding of

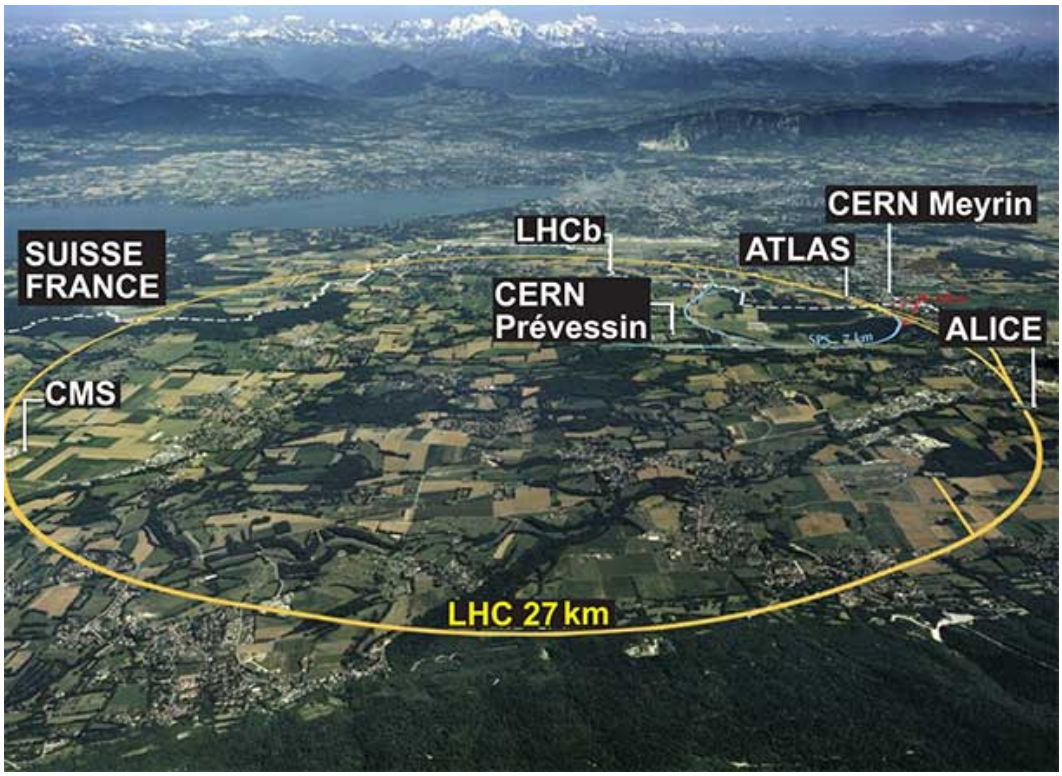

FIGURE 2.8: The Large Hadron Collider and the location of the different experiments on the interaction points [43].

the physics laws is simulated, e.g. the rate of the Higgs production in proton-proton interactions (Figure 1.7) given the experimental setup, but also the appearance of the process in detector language, i.e. the real detector response to the process. Moreover, two categories of quantities can be studied, the *true variables*, which are the exact simulated properties, and *reconstructed variables* reflecting the measured former quantities from simulated detector response, which can be directly compared to empirical data. In particular, different subatomic processes can yield events with the same final states. In the measured data, the event selection is often not sufficient to distinguish between the different types of events, i.e. there is no way to identify the origin of the individual events. Therefore, simulated events of different subatomic processes are very useful; one can predict the contribution of the different processes and compare it to the measured data.

In the case where a specific process is desired to be measured, two categories of simulated samples are needed; *signal event samples* of the wanted process and *background event samples* of processes with the same signal signature. Typically, background event samples contain the processes that have been measured and understood before. After comparing the predictions (signal + background) to the measured data, three scenarios can occur; the data is consistent with the background-only hypothesis, and therefore signal process can be rejected. In case the data is consistent with

the signal+background hypothesis, one can claim to have measured the signal process successfully. Finally, the data can be found to be in disagreement with both the signal+background hypothesis and the background only hypothesis, in which case the predictions are cast into doubt; either the background estimation has to be revised, or a new signal model is needed.

2.4 The ATLAS experiment

The ATLAS detector is as mentioned one of the large detectors at the LHC. It is build around one of the LHC's interaction points, where bunch-crossings take place. The proton-proton (and the heavy ion) collision events are recorded with the purpose of reconstructing and identifying inelastic subatomic processes[7]. It has been designed in order to meet the requirements in precision measurements at the level of the LHC high interaction rates, high radiation and large numbers of produced particles. The ATLAS experiment has a promising physics potential, mainly focussed on verifying the SM predictions and searching for physics beyond it. The ATLAS detector is cylinder-shaped, 44 m long and 25 m in diameter with a weight of no less than 7000 tons. Similar to an onion, the multi-purpose detector is made of different layers of sub-detectors. These are assembled such that the information from each part can be combined to reconstruct a full picture of the collision events. It has currently the largest superconducting magnet system in the world, consisting of a solenoid, a barrel toroid and two end-cap toroids, which is used to bend the trajectory of charged particles in order to determine their momenta. The ATLAS detection system can be divided into four main parts; the *Inner Detector*, the *Electromagnetic Calorimeter*, the *Hadronic Calorimeter* and the *Muon Spectrometer*. Figure 2.9 shows the scheme of the ATLAS detector and its different sub-detectors. Each part is discussed in the following sections after introducing the coordinate system used in ATLAS.

2.4.1 The ATLAS coordinate system

In order to describe the particles originating from the proton-proton interactions using the ATLAS detector, a right-handed coordinate system is used. The interaction point is taken as the origin, where in Cartesian coordinates (x, y, z), the z-axis lies along the beam direction, the x-axis points toward the centre of the LHC ring and the y-axis toward the sky. The xy-plane is then the transverse plane of the ATLAS detector, cutting it perpendicularly to the beam direction, in cylindrical coordinates (z, r, ϕ) it is spanned by ϕ the azimuthal angle and r the radius. The ATLAS detector includes almost the full azimuthal coverage in detection capacity, and a large portion in the polar angle. The latter is characterised by the *pseudorapidity*, which is a

[7] In contrast to soft interactions, where the initial protons are not broken-up, inelastic scatterings are at the heart of new particle creation.

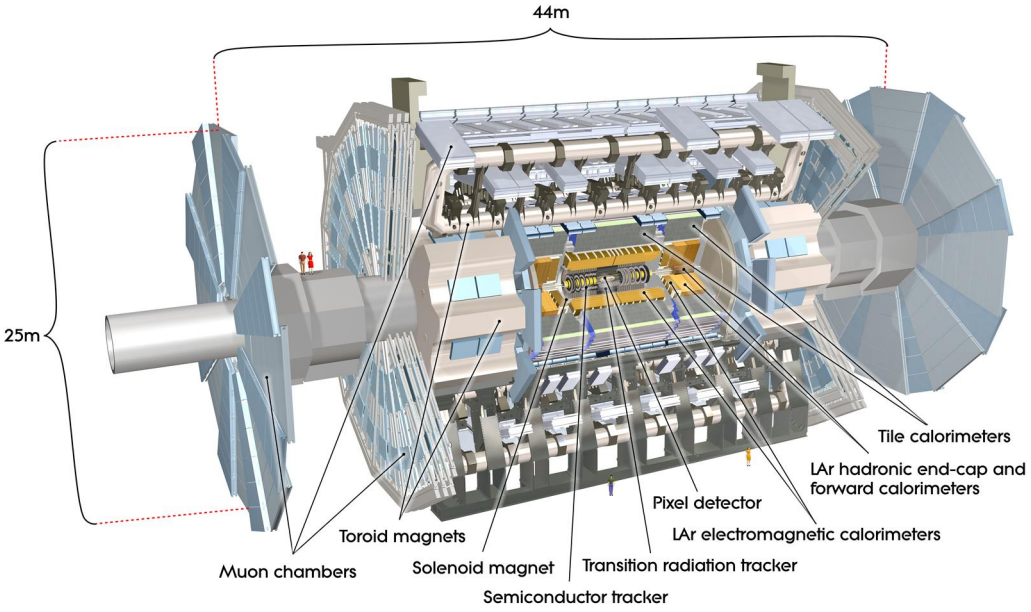

FIGURE 2.9: A schematic picture of the ATLAS detector showing its different layers of sub-detectors and components [31].

measure for describing the angle relative to the beam axis,

$$\eta = -\ln(\tan(\theta/2)), \tag{2.5}$$

with the polar angle θ defined as the angle from the positive z-axis. This quantity is particularly important to describe high energy particles from proton-proton interactions. Since the interactions happen between partons inside the protons, which carry an unknown fraction of the proton's momentum, collision events do not necessarily occur in the centre-of-mass frame of the lab frame. Therefore particles can be boosted along the z-axis. For this reason, the *rapidity* is used, which can be expressed as a function of the energy and the momentum component along the beam axis,

$$y = \frac{1}{2}\ln\left[\frac{E + p_z}{E - p_z}\right] \tag{2.6}$$

However, it is not Lorentz invariant, but differences of this quantity are. In the ultra-relativistic limit, the rapidity is equivalent to the pseudorapidity, which is easier to measure. Figure 2.10 shows different values of η for different polar angles. Along the transverse plane, $\eta = 0$, while it rapidly goes to infinity the closer to the beam axis. The same applies for the $90° < \theta < 180°$ region, but this time η picks up a minus sign. Furthermore, since proton-proton collisions are in fact parton-parton interactions, a significant unknown fraction of the beam energy is lost down the beam pipe. Therefore, an important quantity that is useful to characterise such hard inelastic processes

is the *transverse momentum*,

$$p_T = \sqrt{p_x^2 + p_y^2}, \qquad \text{with } |p| = p_T \cosh \eta. \tag{2.7}$$

Partons before the interaction move along the beam axis with a negligible momentum component in the transverse direction, and thus the net transverse momentum can be constrained to zero. When a hard collision takes place, the outgoing particles will have a significant momentum off the beam line, i.e. a significant transverse momentum, which are the events of interest. Similarly, the *transverse energy* can be defined as,

$$E_T = \sqrt{m^2 + p_T^2}, \tag{2.8}$$

with m the invariant mass. In the case where $m \ll p_T$, $E_T \approx p_T$.

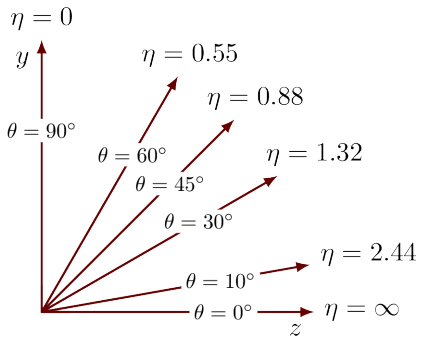

FIGURE 2.10: A schematic diagram showing different values of the pseudorapidity η with the corresponding polar angle θ values.

2.4.2 The ATLAS particle detection

From SM precision measurements to all kinds of BSM searches, it is important to stress that in general all one can measure from the different subatomic processes are the measurable decay products, such as electrons and muons. Collider experiments are often compared to crime scenes, where the suspects are often unknown, but based on traces they left, one can use these to reconstruct the scene in the hope of identifying the actors. Likewise, an exact picture of collision events is impossible to obtain; most of the SM particles decay (or get confined in the case of quarks) almost instantaneously after their creation, but also not all particles can interact with the detector in order to leave tracks of their passage. Consequently, events have to be reconstructed only based on the few particles that can interact with the different sub-detectors.

The ATLAS detector operates around the very intense environment close to the interaction point, where hundreds of billions of particles are scattered and created per second. In general, the particles detected in ATLAS are; electrons, photons, muons and hadrons, including baryons such as protons and neutrons, but also mesons such

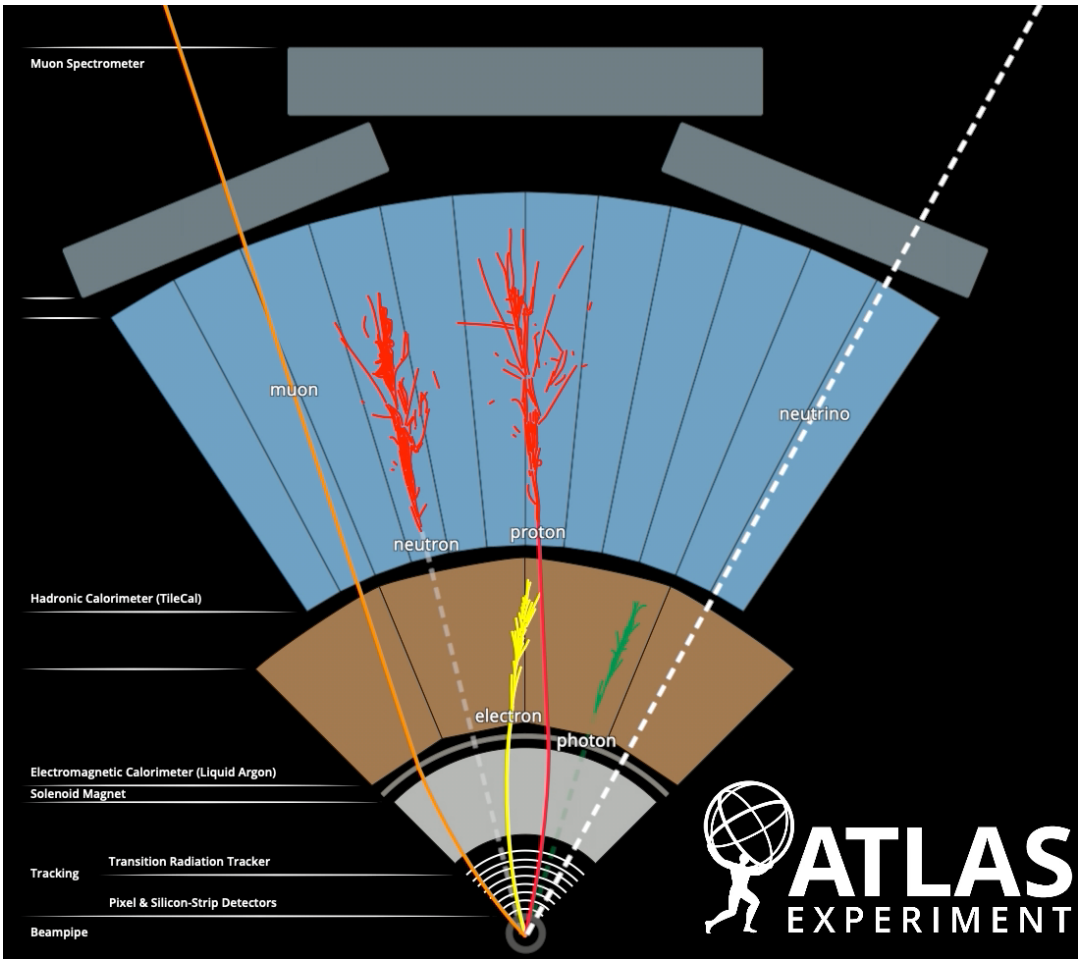

FIGURE 2.11: A visualisation of the different particle paths through the different layers of the ATLAS detector [31].

as pions and kaons. Figure 2.11 shows a visualisation of the interaction of the different particles with the several detector layers. The journey of emerging particles starts by passing through the Inner Detector, where only charged particles leave tracks, these are electrons, muons and charged hadrons. The next crossing is in the EM calorimeter, where this time also photons interact. Almost all electrons and photons are stopped by the EM calorimeter, while muons and some hadrons can make it to the next sub-detector. On top of charged hadrons, in the Hadronic calorimeter also neutral hadrons such as neutrons are detected. Finally, only muons survive the previous layers to reach the last sub-detector, the Muon Spectrometer, where they also leave tracks. In the next sections, the different detection mechanisms of the different sub-detectors are discussed.

2.4.3 The Inner Detector

The first part of the ATLAS detector that is the closest to the interaction point is the Inner Detector (ID). It has a cylindrical shape with a diameter of 2.1 m and a length of 6 m, covering the $|\eta| < 2.5$ region. It is itself composed of three sub-detectors, namely

a *pixel detector*, a *semiconductor tracker* and a *transition radiation tracker*. Figure 2.12 shows a schematic picture of the ID and its different parts. The *pixel detector* is made of four consecutive layers of semi-conducting pixel components, providing tracks of charged particles from which trajectories are reconstructed with high precision. It is very close to the interaction point, with a separation of only a few centimetres, enabling precise reconstruction of vertices. In ordinary words, it acts as a camera observing individual charged particles, with a minimal interaction avoiding interference with their initial trajectory. The *semiconductor tracker* has roughly the same

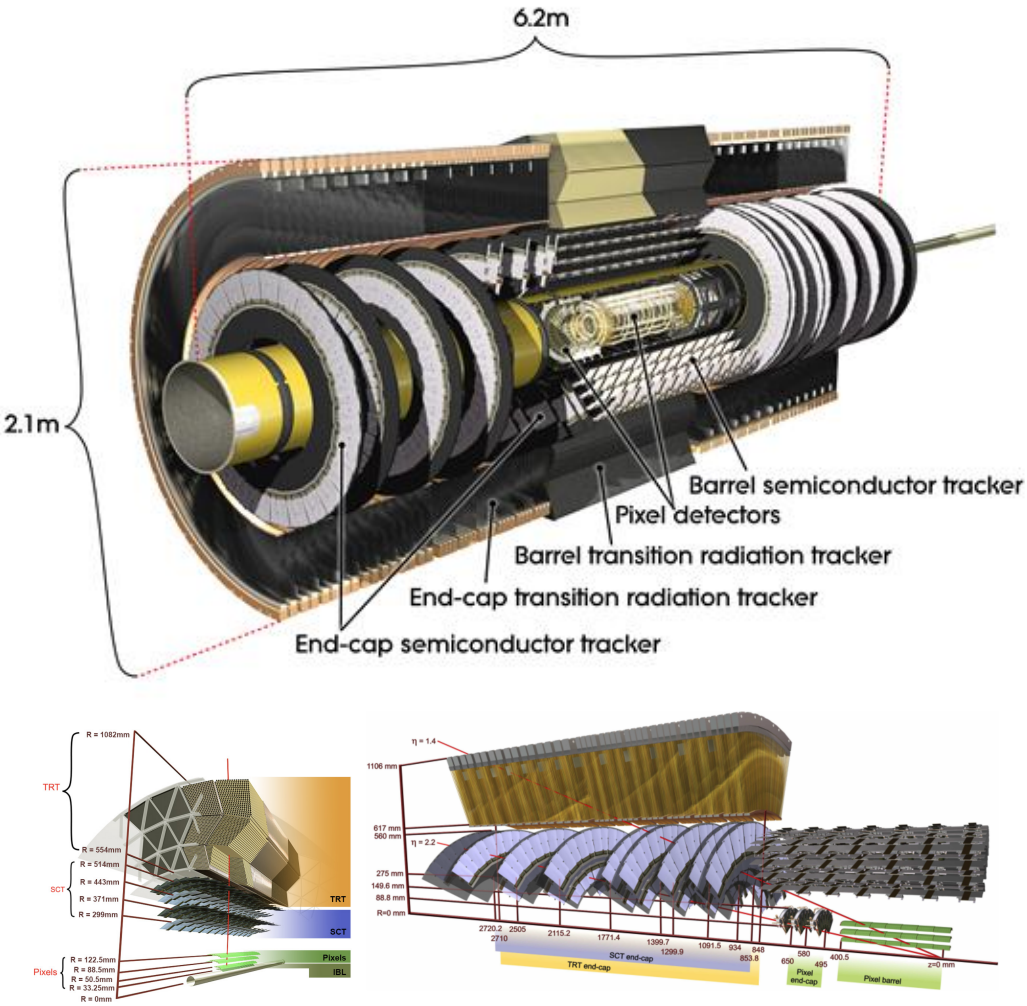

FIGURE 2.12: The innermost sub-detector of the ATLAS, the Inner Detector (ID), which is composed of three parts; a pixel detector, a semiconductor tracker and a transition radiation tracker [31].

function as the *pixel detector*. It has long, narrow silicon microstrips, which has the advantage of measuring charged particles over a large area. There are 4088 modules distributed over 4 cylindrical layers. The *transition radiation tracker* is the outermost part of the ID and is complementary to the silicon-based tracking devices, which enables radially extended track reconstruction up to $|\eta| = 2.0$. It is made of drift tubes of 4 mm in diameter and 144 cm in length. The straws are filled with a Xenon and

Argon gas mixture, which is ionised when charged particles traverse the medium between the straws. Wires in the straws conduct the electric charge produced during the ionisation as signal, which allows the determination of the particle's path. Table 2.2 shows the basic parameters of the ID and its components. Finally, the whole ID is contained within a superconducting solenoid, providing a magnetic field of 2 Teslas along the beam axis, which enables momentum measurements of charged particles bent along the transverse plane and their arrangement.

TABLE 2.2: The dimensions of the ID and its three components [31].

Item		**Radial extension (mm)**	**Length (mm)**
Overall ID envelope		$0 < R < 1150$	$0 < \|z\| < 3512$
Beam-pipe		$29 < R < 36$	
Pixel	Overall envelope	$45.5 < R < 242$	$0 < \|z\| < 3092$
4 cylindrical layers	Sensitive barrel	$33.3 < R < 122.5$	$0 < \|z\| < 400.5$
2×3 disks	Sensitive end-cap	$88.8 < R < 149.6$	$495 < \|z\| < 650$
SCT	Overall envelope	$255 < R < 549$ (barrel)	$0 < \|z\| < 805$
		$251 < R < 610$ (end-cap)	$810 < \|z\| < 2797$
4 cylindrical layers	Sensitive barrel	$299 < R < 514$	$0 < \|z\| < 749$
2×9 disks	Sensitive end-cap	$275 < R < 560$	$839 < \|z\| < 2735$
TRT	Overall envelope	$554 < R < 1082$ (barrel)	$0 < \|z\| < 780$
		$617 < R < 1106$ (end-cap)	$827 < \|z\| < 2744$
73 straw planes	Sensitive barrel	$563 < R < 1066$	$0 < \|z\| < 712$
160 straw planes	Sensitive end-cap	$644 < R < 1004$	$848 < \|z\| < 2710$

2.4.4 The Calorimeters

The basic principle of calorimeters is to measure the total energy of a particle by stopping it while absorbing its kinetic energy. They are made of materials with high density, such as lead (Pb), that act as absorbers. In the ATLAS detector, there are two kinds of calorimeters; the Electromagnetic (EM) Calorimeter and the Hadronic Calorimeter. Both detectors include the full azimuthal coverage. Figure 2.13 shows an overview of the different components of the calorimeters in the ATLAS detector.

2.4.4.1 The Electromagnetic Calorimeter

The EM Calorimeter is designed to measure the energy of electromagnetically interacting particles, such as electrons and photons. It is composed of a barrel component covering a pseudorapidity range of $|\eta| < 1.47$ and two end-cap components with $1.37 < |\eta| < 3.2$. It has an accordion shaped structure consisting of lead and steel particle absorbers. Figure 2.14 shows a scheme of a slice of the EM Calorimeter. Between the parallel accordion shaped layers, cooled liquid argon (LAr) surrounds three copper

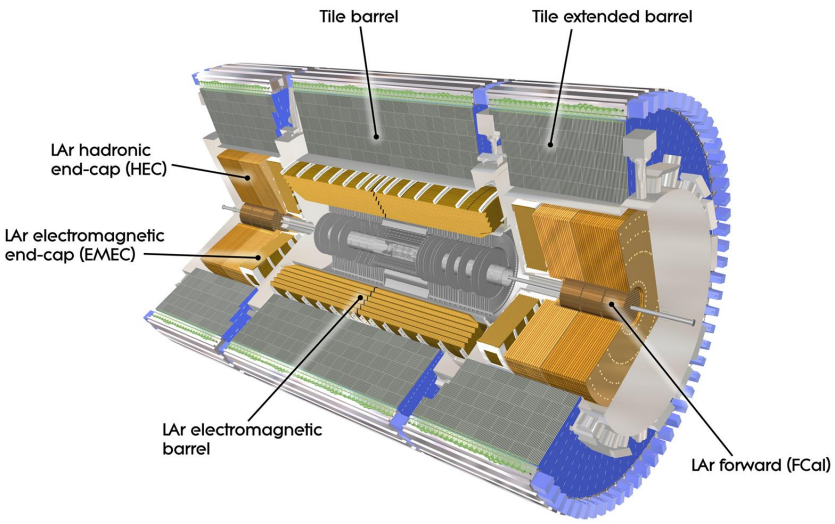

FIGURE 2.13: The Electromagnetic and Hadronic Calorimeters of the ATLAS detector designed to measure the energy of respectively electromagnetically interacting and hadronic particles [31].

layers. When a photon or an electron enters the EM Calorimeter, it interacts with the absorber, producing a shower of lower energy electrons and photons. A characteristic property of EM shower development is given by the so-called material's *radiation length* X_0, which is a measure for the length scale associated with the energy loss rate, described as the mean distance over which a charged particle looses $1/e$ of its initial energy due to radiation. Figure 2.15 shows X_0 as a function of $|\eta|$, the so-called material budget, characterising the amount of material a particle traverses through the various layers of the EM calorimeter. The secondary particles in the shower ionise the LAr, producing more negatively charged electrons. These electrons are attracted by an electric field to the copper layers, which act as electrodes used to conduct the signal. By collecting the charge produced by the shower, it is possible to deduce the total energy of the primary particle.

2.4.4.2 The Hadronic Calorimeter

The Hadronic Calorimeter on the other hand is designed to measure the energy of hadrons, such as protons, neutrons or pions. There are three parts, a barrel tile calorimeter covering $|\eta| < 1.7$, two end-cap components $1.5 < |\eta| < 3.2$ and two forward calorimeters $3.1 < |\eta| < 4.9$. The tile calorimeter is composed of arrays of steel and scintillator sheets, while the other parts are LAr based. Hadrons passing through the steel of the tile calorimeter interact with the iron nuclei, causing the production of showers of secondary particles, which results in a cascade. As opposed to the EM calorimeter, the shape of hadronic shower is due to strong interactions. The amount of material in the Hadronic Calorimeter is characterised by the *interaction length* λ, defined as the mean distance a hadron traverses whereby $1/e$ of its

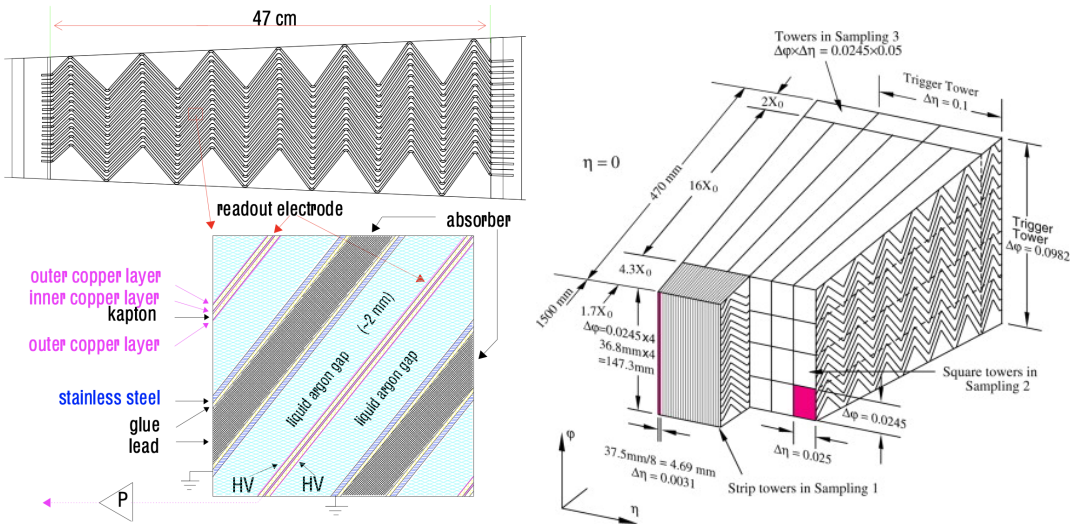

FIGURE 2.14: The Electromagnetic Calorimeter of the ATLAS detector designed to measure the energy of electromagnetically interacting particles [31].

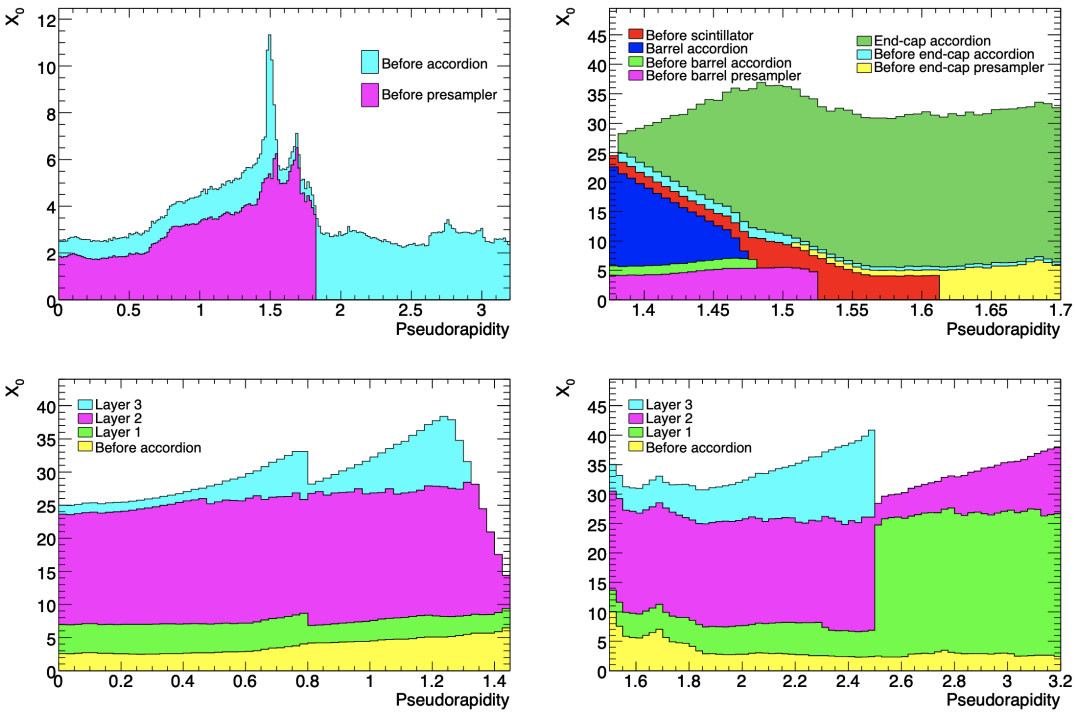

FIGURE 2.15: The radiation length X_0 as a function of $|\eta|$, the so-called material budget, characterising the amount of material a particle traverses through the various layers of the EM calorimeter [31].

initial energy is lost. Figure 2.16 shows the interaction length λ as a function of $|\eta|$, the so-called material budget, characterising the amount of material a hadron traverses through the Hadronic Calorimeter and Figure 2.17 shows a picture (A) and a diagram of a single module (B) of the Hadronic Tile Calorimeter. When these latter particles penetrate the scintillators, photons are radiated. The light intensity is then measured to determine the energy of the original particle. Finally, the main

parameters of the calorimeter system are summarised in Table 2.3.

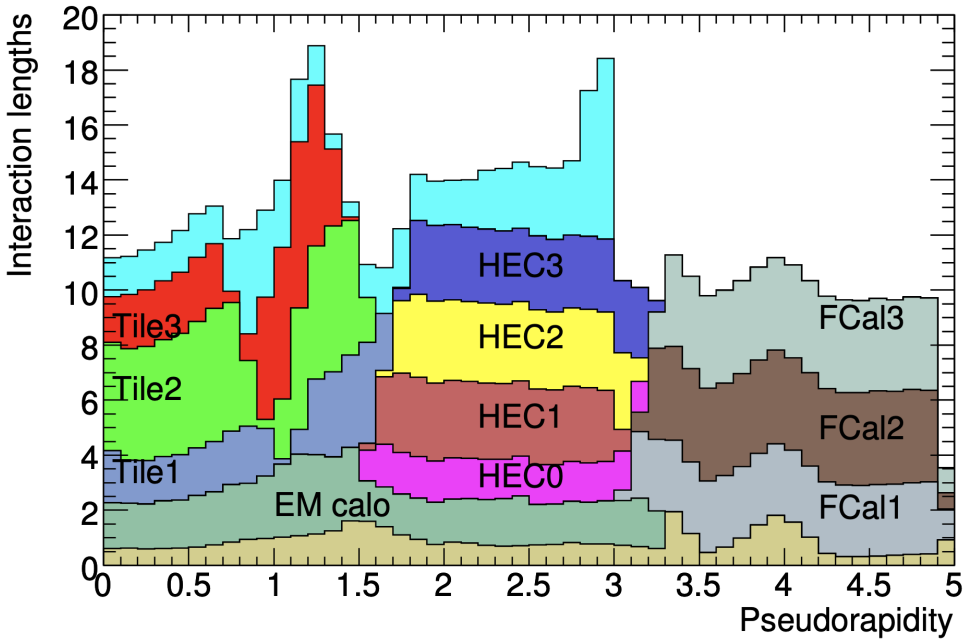

FIGURE 2.16: The interaction length λ as a function of $|\eta|$, the so-called material budget, characterising the amount of material a hadron traverses through the Hadronic Calorimeter [31].

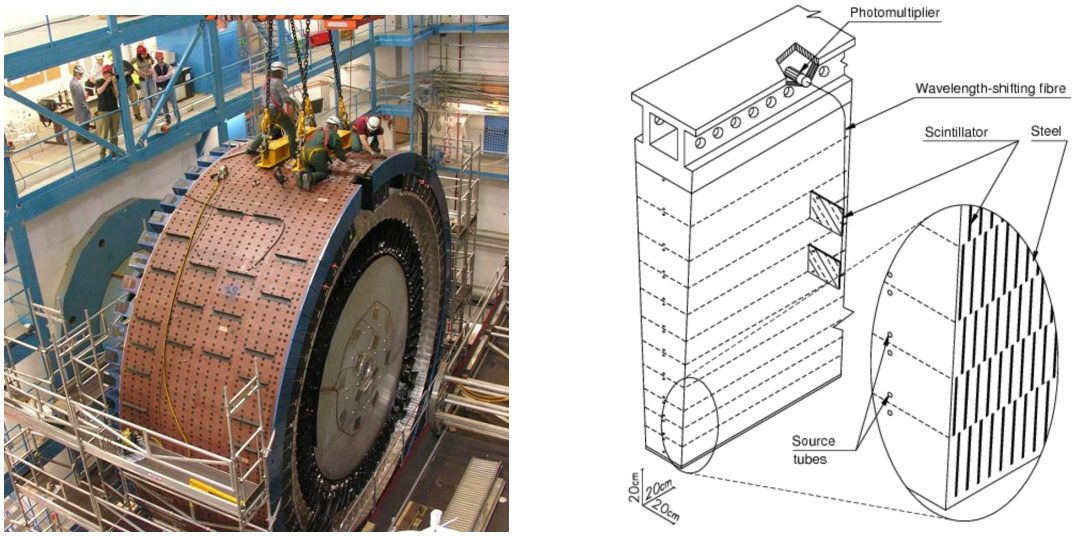

(A) (B)

FIGURE 2.17: A picture of Hadronic Tile Calorimeter with the full azimuthal coverage (A) and a diagram of one single module of this last calorimeter (B) [31].

TABLE 2.3: The basic parameters of the calorimeter system [31].

	Barrel		End-cap	
EM calorimeter				
Number of layers and $\|\eta\|$ coverage				
Presampler	1	$\|\eta\| < 1.52$	1	$1.5 < \|\eta\| < 1.8$
Calorimeter	3	$\|\eta\| < 1.35$	2	$1.375 < \|\eta\| < 1.5$
	2	$1.35 < \|\eta\| < 1.475$	3	$1.5 < \|\eta\| < 2.5$
			2	$2.5 < \|\eta\| < 3.2$
Granularity $\Delta\eta \times \Delta\phi$ versus $\|\eta\|$				
Presampler	0.025×0.1	$\|\eta\| < 1.52$	0.025×0.1	$1.5 < \|\eta\| < 1.8$
Calorimeter 1st layer	$0.025/8 \times 0.1$	$\|\eta\| < 1.40$	0.050×0.1	$1.375 < \|\eta\| < 1.425$
	0.025×0.025	$1.40 < \|\eta\| < 1.475$	0.025×0.1	$1.425 < \|\eta\| < 1.5$
			$0.025/8 \times 0.1$	$1.5 < \|\eta\| < 1.8$
			$0.025/6 \times 0.1$	$1.8 < \|\eta\| < 2.0$
			$0.025/4 \times 0.1$	$2.0 < \|\eta\| < 2.4$
			0.025×0.1	$2.4 < \|\eta\| < 2.5$
			0.1×0.1	$2.5 < \|\eta\| < 3.2$
Calorimeter 2nd layer	0.025×0.025	$\|\eta\| < 1.40$	0.050×0.025	$1.375 < \|\eta\| < 1.425$
	0.075×0.025	$1.40 < \|\eta\| < 1.475$	0.025×0.025	$1.425 < \|\eta\| < 2.5$
			0.1×0.1	$2.5 < \|\eta\| < 3.2$
Calorimeter 3rd layer	0.050×0.025	$\|\eta\| < 1.35$	0.050×0.025	$1.5 < \|\eta\| < 2.5$
Number of readout channels				
Presampler	7808		1536 (both sides)	
Calorimeter	101760		62208 (both sides)	
LAr hadronic end-cap				
$\|\eta\|$ coverage			$1.5 < \|\eta\| < 3.2$	
Number of layers			4	
Granularity $\Delta\eta \times \Delta\phi$			0.1×0.1	$1.5 < \|\eta\| < 2.5$
			0.2×0.2	$2.5 < \|\eta\| < 3.2$
Readout channels			5632 (both sides)	
LAr forward calorimeter				
$\|\eta\|$ coverage			$3.1 < \|\eta\| < 4.9$	
Number of layers			3	
Granularity $\Delta x \times \Delta y$ (cm)			FCal1: 3.0×2.6	$3.15 < \|\eta\| < 4.30$
			FCal1: $\sim$ four times finer	$3.10 < \|\eta\| < 3.15$,
				$4.30 < \|\eta\| < 4.83$
			FCal2: 3.3×4.2	$3.24 < \|\eta\| < 4.50$
			FCal2: $\sim$ four times finer	$3.20 < \|\eta\| < 3.24$,
				$4.50 < \|\eta\| < 4.81$
			FCal3: 5.4×4.7	$3.32 < \|\eta\| < 4.60$
			FCal3: $\sim$ four times finer	$3.29 < \|\eta\| < 3.32$,
				$4.60 < \|\eta\| < 4.75$
Readout channels			3524 (both sides)	
Scintillator tile calorimeter				
	Barrel		Extended barrel	
$\|\eta\|$ coverage	$\|\eta\| < 1.0$		$0.8 < \|\eta\| < 1.7$	
Number of layers	3		3	
Granularity $\Delta\eta \times \Delta\phi$	0.1×0.1		0.1×0.1	
Last layer	0.2×0.1		0.2×0.1	
Readout channels	5760		4092 (both sides)	

2.4.5 The Muon Spectrometer

Almost all SM particles produced in the proton-proton collision are stopped in the calorimeters, except muons and neutrinos. Neutrinos are simply not detected directly in ATLAS, while muons leave tracks in the ID and the calorimeters. Compared to electrons, muons are heavier which makes them less radiative as they interact electromagnetically, and they also lose less energy in interactions with the detectors. Therefore the muons can be detected in the outermost part of the ATLAS detector, called the *Muon Spectrometer*. It consists of three layers of chambers with tubes filled with a gas mixture of Argon and CO_2, covering a range of $|\eta| < 2.7$. The detection mechanism is similar to the TRT, where muons entering the straws ionise the gas and an electric current is measured through a wire inside the tubes. This enables the determination of the muon's path bent by the magnetic field, and hence its momentum. Figure 2.18 shows a schematic representation of the ATLAS Muon Spectrometer and its different components, along with the series of eight coils constituting the toroid magnet system, used to measure the momentum of muons. Figure 2.19 (A) shows a picture of the endcap chambers and (B) a simulation of how muons passing through the chambers leave tracks that are used to reconstruct the trajectory. Finally, Table 2.4 shows the basic parameters of the latter sub-detector.

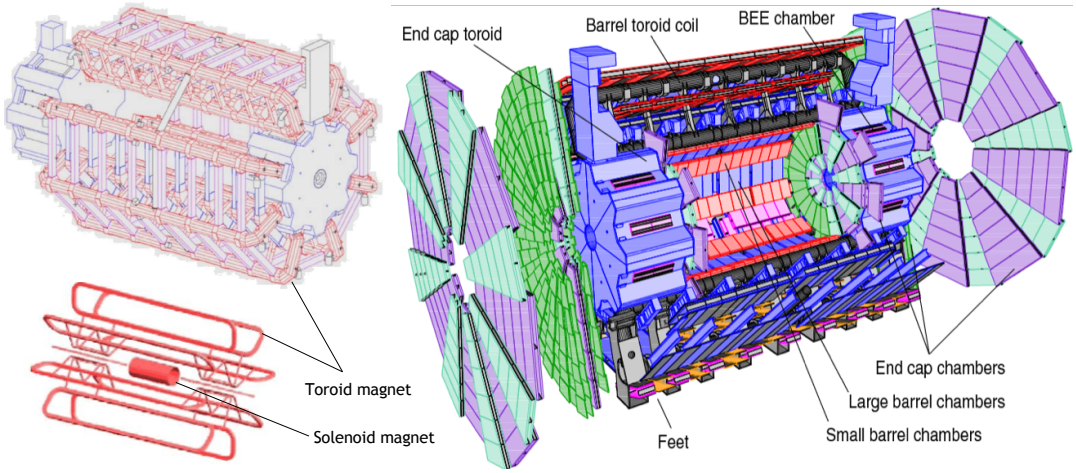

FIGURE 2.18: The Muon Spectrometer of the ATLAS detector designed to detect muons, along with the series of eight coils constituting the toroid magnet system, used to measure the momentum of muons. [48].

2.4.6 Primary vertex reconstruction in ATLAS

As opposed to fixed target experiments, where the interaction point of collision events is at the target, protons at the LHC can interact anywhere in the interaction region, where bunch crossings take place. Therefore, it is important to reconstruct the primary vertex of the individual collision events. In ATLAS, vertex reconstruction starts from collecting reconstructed charged particles paths using the ID, called *tracks*, which are using for finding and fitting the position of vertices. For the vertex

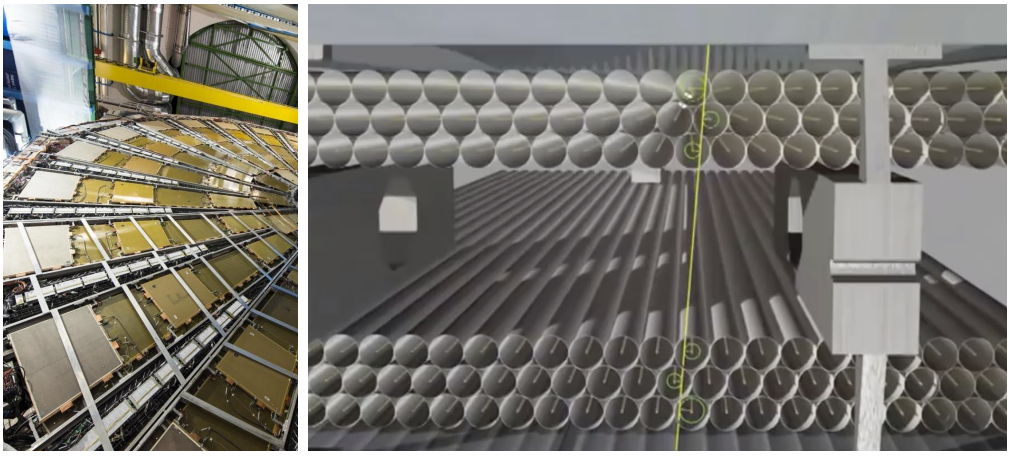

(A) (B)

FIGURE 2.19: A picture of the endcap chambers of the ATLAS Muon Spectrometer (A) and a simulation of muons passing through the chambers leave tracks that are used to reconstruct the trajectory (B) [48].

TABLE 2.4: The basic parameters of the Muon Spectrometer [31].

Monitored drift tubes	**MDT**
- Coverage	$\|\eta\| < 2.7$ (innermost layer: $\|\eta\| < 2.0$)
- Number of chambers	1088 (1150)
- Number of channels	339 000 (354 000)
- Function	Precision tracking
Cathode strip chambers	**CSC**
- Coverage	$2.0 < \|\eta\| < 2.7$
- Number of chambers	32
- Number of channels	31 000
- Function	Precision tracking
Resistive plate chambers	**RPC**
- Coverage	$\|\eta\| < 1.05$
- Number of chambers	544 (606)
- Number of channels	359 000 (373 000)
- Function	Triggering, second coordinate
Thin gap chambers	**TGC**
- Coverage	$1.05 < \|\eta\| < 2.7$ (2.4 for triggering)
- Number of chambers	3588
- Number of channels	318 000
- Function	Triggering, second coordinate

reconstruction, tracks are required to have $p_T > 0.4$ GeV and $|\eta| < 2.5$. Tracks with $|\eta| < 1.65$ must have at least 9 silicon hits, otherwise at least 11 hits are required. No pixel holes[8] are permitted, while at most one SCT hole is allowed. The procedure

[8] A hole is an expected hit based on the reconstructed trajectory that was not measured.

of reconstructing a vertex starts from selecting a seed position to fit the best vertex given the selected tracks. In this iterative process, tracks that are less compatible are down-weighed after each step to recompute the vertex position. Once the position of the vertex is determined, incompatible tracks are removed, which are used for other vertices. A minimum of two tracks per vertex are required. This process is repeated until no remaining tracks are found in the event. The vertices are then given as a set of three dimensional positions, with an associated covariance matrix containing the uncertainties.

2.4.7 The ATLAS Trigger system

As mentioned before, the LHC provides an instantaneous luminosity of $10^{34}\, s^{-1} cm^{-2}$, corresponding to a collision rate of 40 MHz. This represents an extraordinarily large amount of data if every event is recorded, which is not possible due to limitations in computing and data storage capacities. Also, not all events are equally interesting for the purpose of physics analyses, only a small fraction has characteristics that might lead to promising results. For this reason, the ATLAS Trigger and Data Acquisition system [42] is set in place for recording and managing an efficient and optimal data-taking, which ensures high quality information to be studied. In order to filter and reduce the data-taking rate, a *trigger system* is used to identify and select at high pace collision events that should be recorded for offline physics analyses.

The ATLAS trigger system can be decomposed in two-stages; a hardware-based system, the Level-1 (L1), and a software-based system, the High-Level Trigger (HLT). After every stage, the rate at which data is recorded is reduced, keeping only promising events in the loop. The L1 trigger is at the front line and relies on reduced-granularity information from the calorimeters and the MS to trigger. It reduces the rate of accepting collision events from an input rate of up to 40 MHz to a maximum of 100 kHZ. The L1 trigger is itself composed of two subsystems, namely the L1Calo and the L1Muon triggers, where the former processes inputs from the calorimeters, while the latter from the MS. Additionally, the L1 topological trigger (L1Topo) uses both sub-detectors to perform topology-based selections, typically on kinematic variables of particle candidates[9]. Events passing the L1 trigger are then stored temporarily along with their full detector response data. Finally, it is up to the HLT trigger to decide whether an event should be permanently stored for offline physics analyses. The software-based trigger reduces the event rate to an average of 1 kHz, where events are processes by reconstructing objects such as leptons and hadronic jets only to the extent required by the executed trigger algorithms. The ATLAS trigger system has been operating successfully, allowing the collection of balanced dataset for various offline physics analyses as well as for detector calibration and monitoring studies.

[9] At this stage, the particle identity is unknown, they are simply called objects to be identified.

2.4.8 The ATLAS collaboration

The ATLAS experiment has gathered more than 3000 physicists, from over 175 institutions (mainly universities) in 38 countries. It is not only a foundation for pure particle physics, but also for very challenging engineering and advanced computing research. This successful collaboration has played a key role in particle physics for many years, with the latest Higgs boson discovery in 2012, and is looking forward to more achievements and discoveries toward BSM physics.

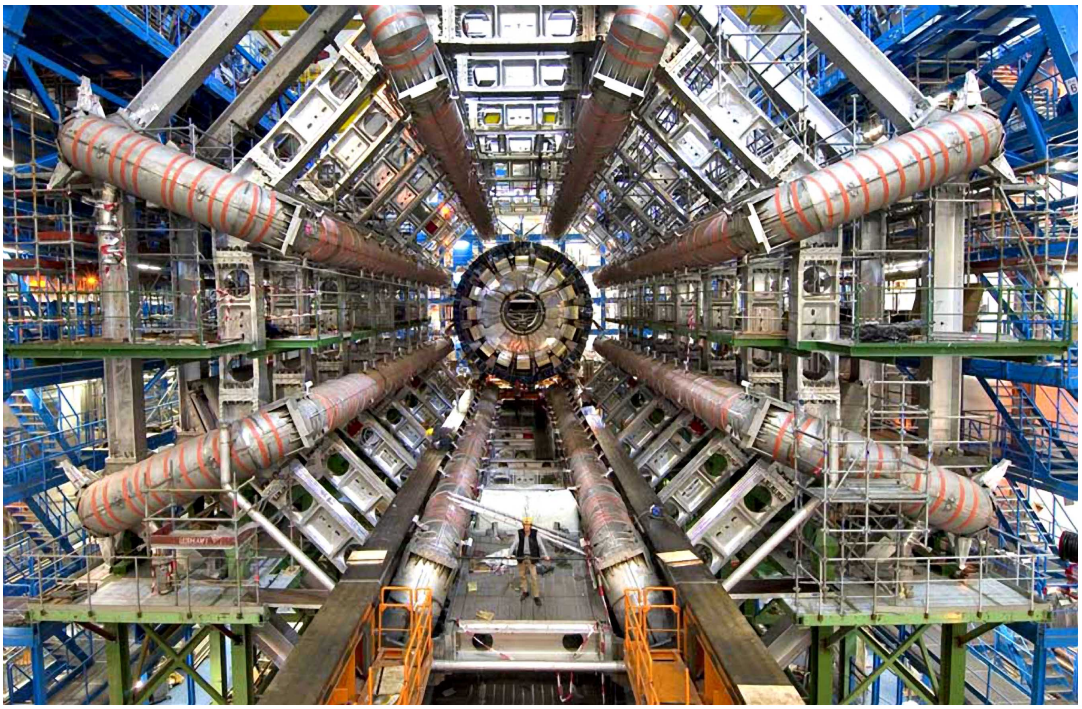

FIGURE 2.20: View of the ATLAS detector during its installation. The enormous size of the detector can be seen from the ATLAS member standing inside the toroid magnets [31].

Chapter 3

Background rejection study for electron reconstruction and identification using $\sqrt{s} = 13$ TeV proton-proton collision events recorded by the ATLAS detector

As mentioned before, all one can measure from the various subatomic processes are the decay products in the final state. For instance, the *golden decay channel*, one of the predicted and observed decay modes of the Higgs boson, $H \rightarrow ZZ^* \rightarrow 4l$ (with l either an electron or a muon), is completely determined from the four charged leptons in the final state. Therefore, it is crucial to identify the measurable decay products with high precision in order to reconstruct rare events accurately. Very often, cross sections of interesting processes such as the Higgs production are relatively low, hence operating at high energies and instantaneous luminosities is important to increase the probability of observing these events. However, there is a significant challenge that comes with this enhancement, which is the presence of all kinds of processes and interactions of less interest. These act as background for the desired signal signatures, and are inevitable and almost impossible to discard by means of an event selection. Therefore, identifying and understanding these backgrounds is crucial to make reliable predictions of interesting processes. In this chapter, a background rejection study for electron reconstruction and identification in the ATLAS experiment is presented. In the next section, electron reconstruction using the ATLAS detector is briefly introduced. Not all reconstructed electron candidates are genuine, prompt electrons, i.e. electrons from signal processes such as the Higgs boson decay. Therefore, identification techniques for electron candidates after reconstruction are required to discriminate fake from genuine electrons. These are discussed in the second section. Finally, in the last sections, a background rejection study is presented in the context of electron reconstruction. *This technical project was fulfilled in order to qualify for the ATLAS authorship, which is obtained by making a substantial contribution to the ATLAS performance tasks.*

3.1 Electron reconstruction

As mentioned before, electrons are very important for a wide range of analyses as decay products. Therefore measuring them with high precision is crucial. However, it is not an easy task in a dense environment near the high energy interactions at the LHC. For the reconstruction of electrons in ATLAS, measurements from the ID and the EM calorimeter are used. Having tracks from the former sub-detector and energy deposits in the latter, one can check if at least one track in the ID is matched to a cluster in the EM calorimeter, subject to electron reconstruction requirements. In summary, the reconstruction of electrons is based on three characteristic signatures; the shape of energy clusters in the EM calorimeter, identified tracks in the ID and tracks closely matched to energy clusters. Reconstructed objects passing the electron reconstruction criteria are referred to as electron candidates. Figure 3.1 illustrates the path of a genuine electron going through the different parts of the ID and the EM calorimeter. A detailed description of the electron reconstruction in ATLAS can be found in [50].

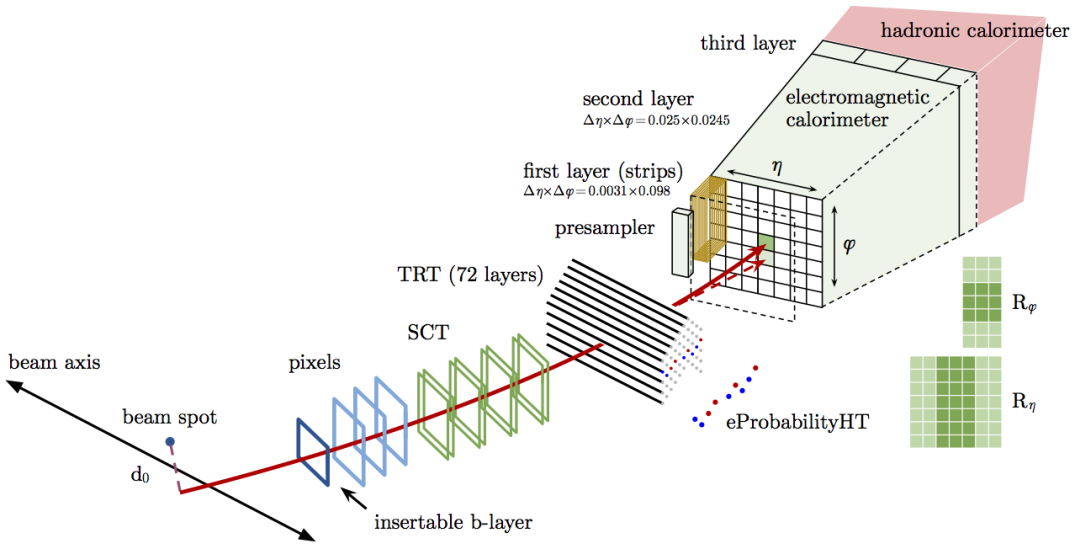

FIGURE 3.1: An illustration showing the path of a prompt electron going through the different parts of the ID and the EM Calorimeter in the ATLAS detector [49].

3.1.1 Electron topological clusters reconstruction

For the electron reconstruction, the first step is to reconstruct the energy deposits in the EM calorimeter, where so-called *topological clusters* are formed. These are obtained from a seed, which is a calorimeter cell with a significance $|\zeta^{EM}_{cell}| \geqslant 4$, defined as,

$$\zeta^{EM}_{cell} = \frac{E^{EM}_{cell}}{\sigma^{EM}_{noise}}, \tag{3.1}$$

with E_{cell}^{EM} the cell energy at EM scale and σ_{noise}^{EM} the expected noise. Neighbouring cells with significance $|\zeta_{cell}^{EM}| \geq 2$ are collected and added to the primary seed. Each added cell is then considered as a seed cell in the next iteration, where the neighbours are collected cluster. In the case where two clusters share a cell, these are merged. After all cells with $|\zeta_{cell}^{EM}| \geq 2$ have been collected, the remaining neighbouring cells with $|\zeta_{cell}^{EM}| > 0$ are also added to the cluster. Finally, the topological clusters are subjected to selection criteria, reducing signal interference from background interactions, referred to as *pile-up*[1]. For the electron reconstruction performance studies, a Monte Carlo simulation sample of single-electron events are used. Figure 3.2 shows the cluster reconstruction efficiency as a function the generator E_T of the simulated electron. Only electron candidates in the central calorimeters, covering the pseudorapidity range $|\eta| < 2.5$, are considered. The efficiency is calculated from the ratio of the number of reconstructed clusters and the number of produced electrons. Clearly, the higher the electron E_T, the higher the reconstruction efficiency, which has a turn-on effect around 5 GeV.

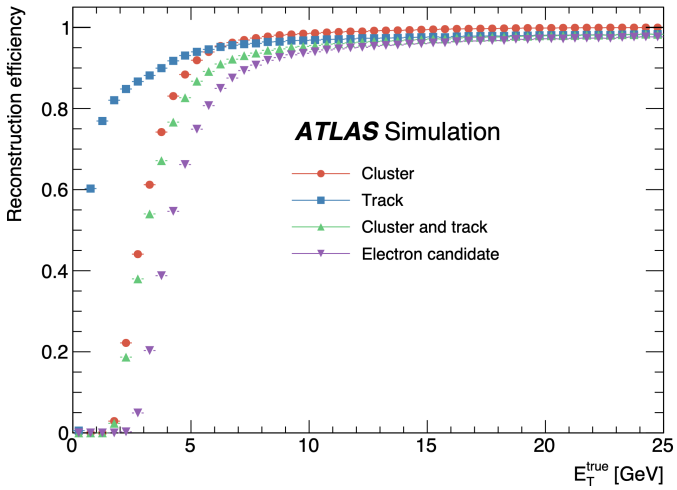

FIGURE 3.2: The reconstruction efficiency of cluster, track, both cluster-track combined and the final reconstructed electron candidate, as a function of the generator E_T of the simulated electron (obtained from a simulated single-electron sample) [50]. Only electron candidates in the central calorimeters, covering the pseudorapidity range $|\eta| < 2.5$, are considered.

3.1.2 Track reconstruction

The following step is the reconstruction of potential electron tracks. Tracks from charged particles are reconstructed from hits in the ID. There are three steps in the procedure of track reconstruction; pattern recognition, ambiguity resolution and TRT extension. A pattern recognition algorithm [109] is used to identify track candidates, while taking into account the energy loss due to bremsstrahlung from the

[1]The high LHC luminosity comes with a considerable amount of background to interesting physics events known as pile-up.

particle interaction with the ID materials. Only identified tracks with $p_T > 0.4$ GeV are considered, and these are fitted using the ATLAS Global χ^2 Track Fitter [110]. The next step is the ambiguity resolution, where tracks sharing hits are resolved to minimise the ambiguity. Each track is attributed a score based on the quality of the fit. A selection criteria based on kinematic cuts, the total number of hits and the shared hits of the tracks is applied. Finally, tracks passing the latter selection are then used as input in order to find sets of compatible TRT measurements for the track extension. Figure 3.2 shows the track reconstruction efficiency as a function the generator E_T of the simulated electrons. Similarly to the cluster reconstruction, a turn-on reconstruction efficiency is measured, with this time a lower threshold of around 1 GeV.

3.1.3 Track-cluster matching

As mentioned before, an electron candidate is reconstructed from an EM cluster matched to an ID track. This is done by extrapolating the track using the measured track momentum to match the energy cluster. To improve the matching quality, a rescaling of the momentum can be performed to account for significant energy losses due to bremsstrahlung. The requirement for a track to be matched to a cluster should satisfy,

$$|\eta_{cluster} - \eta_{track}| < 0.05,$$
$$-0.10 < q \times (\phi_{cluster} - \phi_{track}) < 0.05,$$

with q the track measured charge. In case several tracks point to the same cluster, the one with the highest ranking score is chosen, where the latter is based on criteria including the number and origin of the track hits and the angular separation between the track and cluster, defined as,

$$\Delta R = \sqrt{\Delta\eta^2 + \Delta\phi^2}. \tag{3.2}$$

Figure 3.2 shows the electron reconstruction efficiency, including the track-to-cluster matching, as a function the generator E_T of the simulated electron. Also the reconstruction efficiency of tracks matched to clusters using a Gaussian-sum-filter fitting algorithm [111] is shown, which is used for tracks with silicon hits loosely matched to clusters. The electron reconstruction efficiency is optimal above approximately 5 GeV.

3.2 Electron identification

As many kinds of particles are created in collision events at the LHC, and not only electrons interact with the detector. Other particles, such as hadrons produced in

hadronic jets[2], from all kinds of processes can leave tracks in the ID and energy deposits in the EM calorimeter. These background processes can lead to the reconstruction of objects that mimic an electron signature in the detector. Therefore robust electron identification techniques are required to discriminate fakes from signal prompt electrons. Reconstructed electron candidates passing the electron identification criteria are referred to as identified electrons. A detailed description of the electron identification in ATLAS can be found in [50].

3.2.1 Main background sources for prompt electrons

Electron identification techniques are typically developed in MC simulation studies where background processes generating fake electrons are investigated. Using MC events, background objects passing the electron reconstruction can be identified using generator level information. In this study, simulation samples are used corresponding to all generic 2→2 processes in proton-proton collisions at $\sqrt{s} = 13$ TeV [50], with pile-up conditions corresponding to those in the 2017 data taking period. These were generated using PYTHIA8 [74] with the A14 set of tuned parameters. Analysing the samples, three main background categories contributing to fake electrons are distinguished, namely:

- Non-isolated[3] electrons from heavy-flavour decays (i.e. decays from hadrons containing heavy quarks, namely charm or bottom quarks)
- Background electrons from photon conversions, which result in electron pair production after interaction with detector components
- Misidentified hadrons (jets) from light-flavour quarks

After removing signal electrons from the abundant production of Z boson, W boson or J/ψ decays, the fraction of the three background sources is plotted as a function of the reconstructed electron p_T and η in Figure 3.3. Only electron candidates with $p_T > 17$ GeV and within the central region of the ATLAS detector ($|\eta| \leq 2.47$) are considered. The distinction between the different sources of background is obtained from generator-level information. Clearly, light-flavour hadrons are the most dominant source of background. Electrons from photon conversions represent the second largest source, while heavy-flavour decays account for less than 1% of the total background. The composition of the different sources is relatively constant across the p_T spectrum, while photon conversions increase with higher $|\eta|$ values. This last effect is due to the increasing travel length in the detector as $|\eta|$ increases. The more material a photon can interact with, the higher the probability for an electron pair production. Figure 3.4 shows the amount of ID material in the yz-plane. A particle

[2]Jets are collimated streams of particles from the hadronisation of high energy quarks and gluons (consequence of QCD confinement), which are reconstructed in the EM and the Hadronic calorimeters.

[3]The isolation requirement is based on the sum of the energy deposits around an object within a ΔR cone. Prompt leptons are in general isolated.

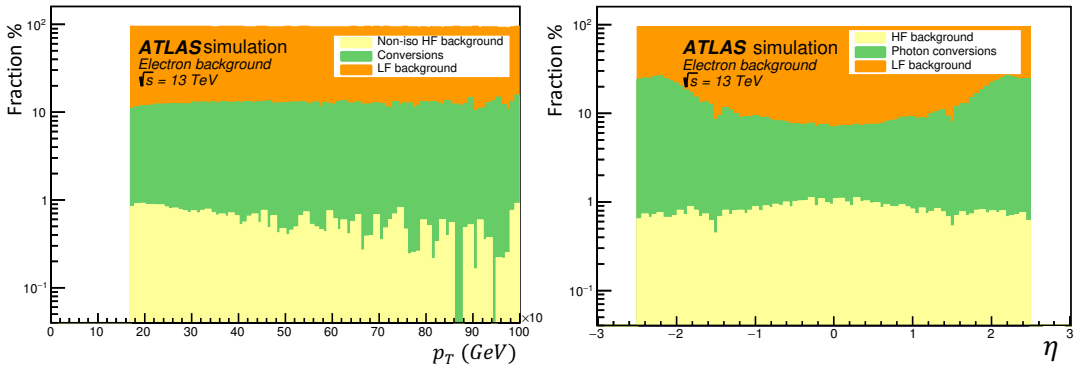

FIGURE 3.3: The fraction of the three background sources w.r.t. the total background as a function of p_T and η in MC simulation samples of all generic $2 \rightarrow 2$ processes in proton-proton collisions at $\sqrt{s} = 13$ TeV [50].

with $\eta = 1.5$ clearly travels through more material in the sub-detector than one with $\eta = 1.0$.

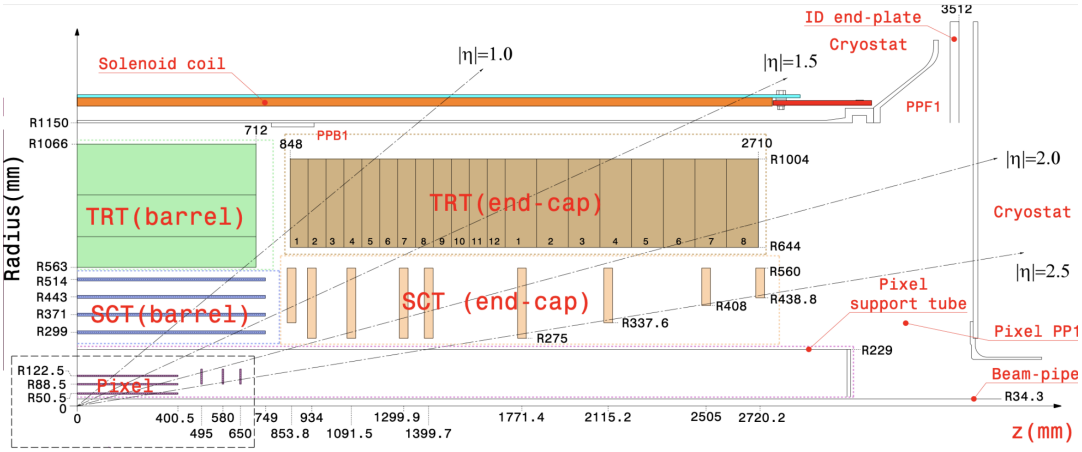

FIGURE 3.4: The travel length of particles through the different parts of the detector as a function of η [31]. Clearly, particles with higher values of η travel through more material in the detector.

3.2.2 Electron identification discriminating variables

In order to discriminate between prompt electrons and the three previously mentioned backgrounds, a set of discriminating variables are defined. These quantities are classified depending on the sub-detector in which they are measured. Table 3.1 shows the electron identification discriminating variables used in ATLAS; the first column indicates the associated sub-detector, while the second and third column the definition of the quantities. In MC simulation studies, the different variables are typically designed to maximise the discrimination between prompt electrons and the three types of backgrounds. As a consequence, the rejection power of each variable on the three background types is different. In the fourth column of Table 3.1, the targeted background type is given per variable.

TABLE 3.1: List of discriminating variables used in the electron identification. The first three columns indicate the type and definition of the quantities, while the fourth column shows the type of targeted background, with *LF*, γ and *HF* standing, respectively, for light-flavour hadrons, background electrons from photon conversions and non-isolated electrons from heavy-flavour decays. The usage of variables in the identification menus is indicated in the last column, where 'LH' indicates the likelihood method and 'C' a direct cut [50].

Type	Description	Name	Rejects			Usage
			LF	γ	HF	
Hadronic leakage	Ratio of E_T in the first layer of the hadronic calorimeter to E_T of the EM cluster (used over the range $\lvert\eta\rvert < 0.8$ or $\lvert\eta\rvert > 1.37$)	R_{had1}	x	x		LH
	Ratio of E_T in the hadronic calorimeter to E_T of the EM cluster (used over the range $0.8 < \lvert\eta\rvert < 1.37$)	R_{had}	x	x		LH
Third layer of EM calorimeter	Ratio of the energy in the third layer to the total energy in the EM calorimeter. This variable is only used for $E_T < 80$ GeV, due to inefficiencies at high E_T, and is also removed from the LH for $\lvert\eta\rvert > 2.37$, where it is poorly modelled by the simulation.	f_3	x			LH
Second layer of EM calorimeter	Lateral shower width, $\sqrt{(\Sigma E_i \eta_i^2)/(\Sigma E_i) - ((\Sigma E_i \eta_i)/(\Sigma E_i))^2}$, where E_i is the energy and η_i is the pseudorapidity of cell i and the sum is calculated within a window of 3×5 cells	$w_{\eta 2}$	x	x		LH
	Ratio of the energy in 3×3 cells over the energy in 3×7 cells centred at the electron cluster position	R_ϕ	x	x		LH
	Ratio of the energy in 3×7 cells over the energy in 7×7 cells centred at the electron cluster position	R_η	x	x	x	LH
First layer of EM calorimeter	Shower width, $\sqrt{(\Sigma E_i (i - i_{max})^2)/(\Sigma E_i)}$, where i runs over all strips in a window of $\Delta\eta \times \Delta\phi \approx 0.0625 \times 0.2$, corresponding typically to 20 strips in η, and i_{max} is the index of the highest-energy strip, used for $E_T > 150$ GeV only	w_{stot}	x	x	x	C
	Ratio of the energy difference between the maximum energy deposit and the energy deposit in a secondary maximum in the cluster to the sum of these energies	E_{ratio}	x	x		LH
	Ratio of the energy in the first layer to the total energy in the EM calorimeter	f_1	x			LH
Track conditions	Number of hits in the innermost pixel layer	n_{Blayer}		x		C
	Number of hits in the pixel detector	n_{Pixel}		x		C
	Total number of hits in the pixel and SCT detectors	n_{Si}		x		C
	Transverse impact parameter relative to the beam-line	d_0		x	x	LH
	Significance of transverse impact parameter defined as the ratio of d_0 to its uncertainty	$\lvert d_0/\sigma(d_0)\rvert$		x	x	LH
	Momentum lost by the track between the perigee and the last measurement point divided by the momentum at perigee	$\Delta p/p$	x			LH
TRT	Likelihood probability based on transition radiation in the TRT	eProbabilityHT	x			LH
Track–cluster matching	$\Delta\eta$ between the cluster position in the first layer and the extrapolated track	$\Delta\eta_1$	x	x		LH
	$\Delta\phi$ between the cluster position in the second layer of the EM calorimeter and the momentum-rescaled track, extrapolated from the perigee, times the charge q	$\Delta\phi_{res}$	x	x		LH
	Ratio of the cluster energy to the track momentum, used for $E_T > 150$ GeV only	E/p	x	x		C

3.2.3 Electron identification efficiency and rejection power

In order to maximise the rejection of fake electrons, while identifying prompt electrons with high efficiency, an optimal identification selection is required. Before applying any discrimination, the collection of reconstructed electron candidates contains a number of prompt electrons, S_0 and a number of fake electrons, B_0. After application of the identification requirements, the collection is reduced to S_{id} ($\leq S_0$) and B_{id} ($\leq B_0$). The efficiency for identifying prompt electrons and the rejection of fake electrons can be defined respectively as,

$$\epsilon_{id} = \frac{S_{id}}{S_0}, \tag{3.3}$$

$$R_{id} = \frac{B_0}{B_{id}}. \tag{3.4}$$

An ideal identification selection would yield $\epsilon_{id} = 1$ and $1/R_{id} = 0$. In reality, the two quantities are anti-correlated; the higher the identification efficiency, the lower the rejection power and vice versa. It is therefore necessary to compromise, in some cases a high identification efficiency is required, while in others the rejection power is more important. For this reason, three identification working points are defined in ATLAS, namely the *loose*, *medium* and *tight* menus. The identification criteria are designed such that electrons passing the *tight* requirements are a subset of those passing the *medium* one, and *medium* electrons a subset of *loose* electrons. The tighter the working point, the lower ϵ_{id} and the higher R_{id}. Figure 3.5 shows the electron identification efficiency as a function of the electron E_T and η in data collected in 2015-2017 corresponding to an integrated luminosity of 81 inverse femtobarns[4] (fb^{-1}). For this measurement, $Z \rightarrow e^-e^+$ events were selected in data and MC for electrons with $E_T > 15$ GeV, and J/ψ[5]$\rightarrow e^-e^+$ for $E_T < 15$ GeV electrons. The former process is generated using the generator POWHEG [65], while the latter is obtained from PYTHIA8 [74] with the A14 set of tuned parameters. These latter processes are measured with high precision, and are often considered as standard reference candles for calibration measurements. For prompt signal electrons, the efficiencies are typically optimised to be 93%, 88% and 80% respectively for the *loose*, *medium* and *tight* menus, for an electron at E_T = 40 GeV. As expected, the tighter the identification menu, the lower the signal efficiency of selecting prompt electrons. In the E_T spectrum, the efficiency tends to increase with higher E_T values. This is due to a large amount of background in the low E_T range, which results in a less efficient electron identification. Finally, the η spectrum is relatively constant, with a small decrease in efficiency toward higher $|\eta|$ values, especially around $|\eta| = 1.5$. The latter effect is due to the transition gap between the barrel and endcap of the EM

[4] The inverse femtobarn is a measure for the number of events per femtobarn, which is a unit of area equivalent to $10^{-28}m^2$. Barns are convenient to use for the small cross sections in particle physics.

[5] J/ψ is meson composed of a charm quark and anti-quark with a significant leptonic branching ratio.

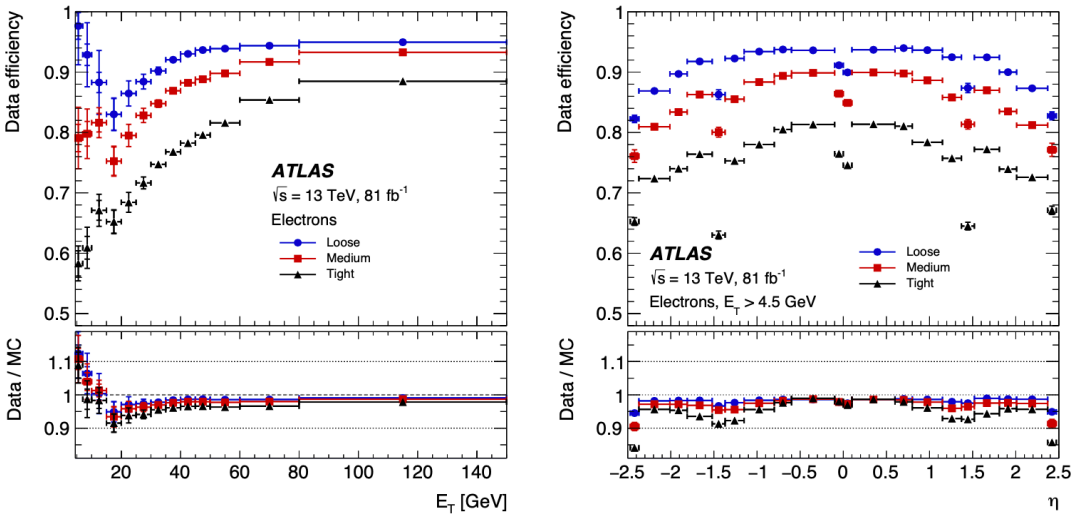

FIGURE 3.5: The electron identification efficiency as a function of the electron E_T and η in data collected in 2015-2017 corresponding to an integrated luminosity of 81 fb^{-1} compared to MC. For this measurement, $Z \to e^-e^+$ events were selected in data and MC for electrons with $E_T > 15$ GeV, and $J/\psi \to ee$ for $E_T < 15$ GeV electrons [50].

calorimeter ($|\eta| \in [1.37, 1.52]$), which is known as the crack region.

3.2.4 The likelihood discriminant identification method

For the discrimination between signal and background electrons, typically a set of discriminating variables are used, where differences in the signal and background PDFs are exploited. For the electron identification, these studies are first conducted in MC samples, using signal samples including prompt electrons and background samples enriched in fake electrons. From differences in the PDFs, cut values on the latter variables are defined to discriminate between fake and prompt electrons.

Figure 3.6 (A) shows an example, where the background and signal MC distribution is plotted for some identification variable X. Clearly, the two distributions are well separated. In this case, applying an optimal cut-based selection results in a high ϵ_{id} and R_{id}. A reconstructed electron having an X value smaller than the cut value is rejected, while one with an equal or higher value passes the selection. However, this approach is not always the most efficient method, for example in the case where the two distributions have a significant overlap. Figure 3.6 (B) shows an example where background and signal have a large overlapping region. In this case, applying a cut-based selection would result in either a large signal efficiency loss if the cut is tight, or a small background rejection if the cut is loose.

A more advanced method of discriminating is the likelihood (LH) discriminant approach, which is currently the method used for the identification of electrons in ATLAS. It consists of building a likelihood calculated from the product of various PDF's

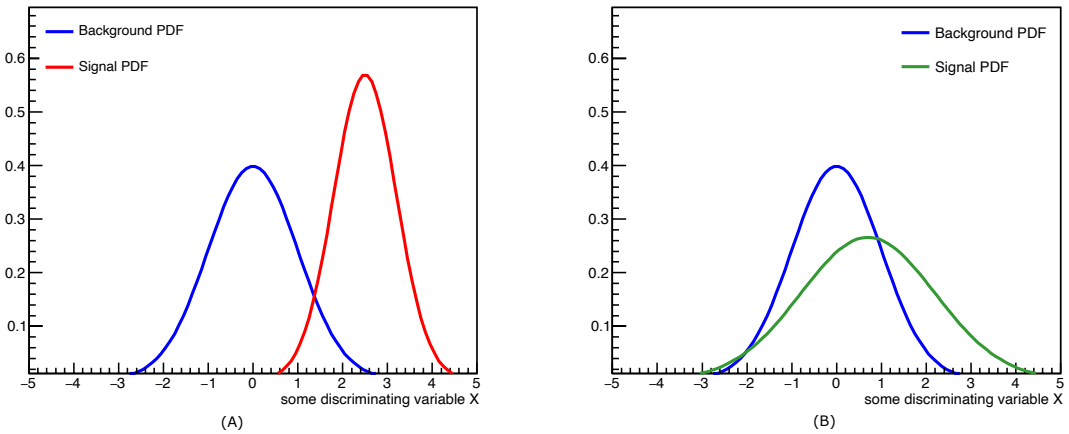

FIGURE 3.6: Example of a signal and background distribution with well seperated PDFs (A) and overlapping PDFs (B).

from the discriminating variables listed in Table 3.1. A separate likelihood is formed for signal and background as follows,

$$L_{S(B)}(\vec{x}) = \prod_{i=1}^{n} P_{S(B),i}(x_i), \tag{3.5}$$

where L_S and L_B are, respectively, the signal and background likelihood, $\vec{x}$ represents the set of discriminating variable, and $P_{S,i}(x_i)$ and $P_{B,i}(x_i)$ the value of the signal and background PDF at value x_i. These PDFs are typically extracted from data measurements, where the so-called *Tag and Probe method* [49] is used to select signal electrons from $Z \rightarrow e^- e^+$ decays, while reconstructed electron candidates failing to pass the selection criteria are used for the background likelihood construction. The likelihood approach consists of defining a discriminant variable for each reconstructed electron. Given the signal and background likelihood value of the reconstructed electron, the discriminant is constructed as follows,

$$d_L = \frac{L_S}{L_S + L_B}. \tag{3.6}$$

This last is defined such that its value peaks at unity for genuine electrons and at zero for fake electrons. The value of this quantity for a corresponding reconstructed electron determines whether it passes the electron identification or not. The last column of Table 3.1 shows which identification variable is used in the likelihood, "LH" indicates that the PDF of the quantity is used in the likelihood while "C" means a direct cut on the variable is used.

3.3 Rejection power of the electron identification menus

As mentioned before, there are three main background sources for prompt signal electrons, namely light-flavour hadrons, background electrons from photon conversions and non-isolated electrons from heavy-flavour decays. In this section, an MC study is presented, where the rejection of the three background sources is investigated using the different identification menus.

3.3.1 Identification efficiency for background categories

As shown in Figure 3.3, it is possible to classify the different types of background sources, i.e. for every reconstructed electron, one can consult the identity and the origin of interaction of the particle. Using equation 3.3, the efficiency of the three previously mentioned background sources passing the electron identification menus can be calculated. After excluding signal electrons from Z, W and J/ψ decays, the identification is applied on the enriched background sample used in Figure 3.3. Figure 3.7 shows the inclusive background (i.e. combining the three background categories) identification efficiency as a function of η and p_T for the three identification menus. From equation 3.4, the inverse of this background identification efficiency

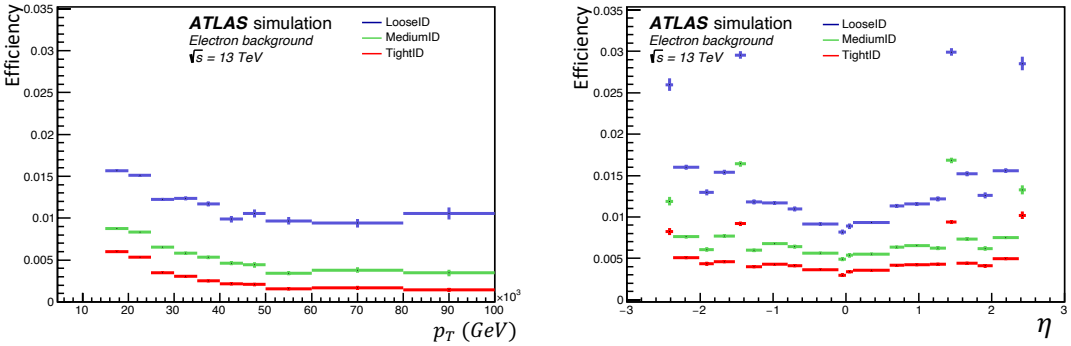

FIGURE 3.7: The inclusive background identification efficiency as a function of η and p_T for the different identification menus.

can be interpreted as the rejection. However, it is more convenient to compare efficiency curves rather than rejections. Therefore, the former is always used for comparisons in this study, while both terms are used interchangeably in the discussion. The lower the efficiency, the higher the rejection. As expected, the tighter the identification menu, the larger the rejection (i.e. lower the identification efficiency). From the p_T spectrum, one can conclude that the rejection power of the identification is higher toward higher p_T values. This was expected from the low identification efficiency of low p_T signal electrons, where the abundance in background complicates the discrimination between prompt and fake electrons. The rejection in terms of η is relatively constant for the medium and tight menus, while the loose menu shows a slight decrease in rejection toward higher η values. The crack region is as expected low in rejection, similarly to the low signal efficiency in Figure 3.5.

Figure 3.8 shows a comparison of the rejection of the three different background sources for the *medium* menu. Clearly, light-flavour hadrons are rejected the best. This is due to the fact that the identification menus were initially designed to reject mostly hadrons by exploiting the large discriminating power of shower shape variables between electrons and hadrons, namely EM calorimeter related quantities. This can be seen in the fourth column of Table 3.1, where almost all variables impact the light-flavour background. Furthermore, non-isolated electrons from heavy-flavour decays are better rejected at higher p_T values, while the rejection for photon conversions and light-flavour hadrons is relatively constant. In the η spectrum, the rejection is overall relatively constant, with a slightly better rejection of light-flavour hadrons in the central detector region (around $\eta = 0$)

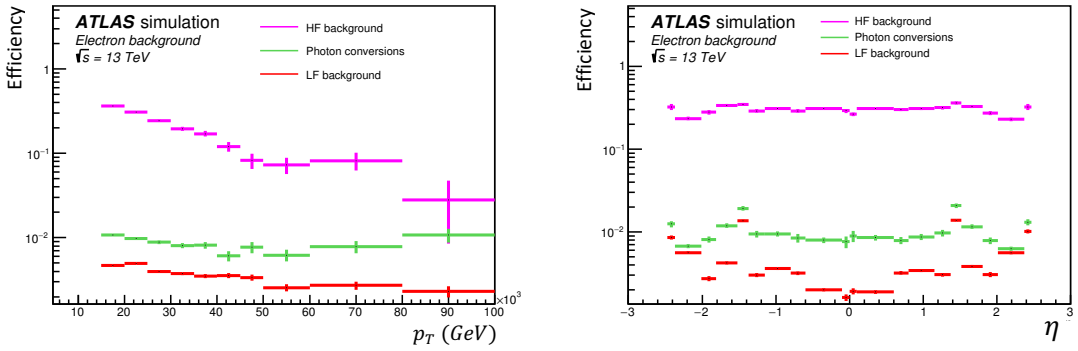

FIGURE 3.8: The background identification efficiency for the *medium* identification-menu of the various background sources as a function of η and p_T.

Results are summarised in Table 3.2, where the inclusive efficiency for all cases is calculated with equation 3.3. Also the background composition relative to the total background after identification is shown.

TABLE 3.2: Summary table of background identification efficiency for the different identification menus per background source. Also the fraction of the background sources after identification is shown.

Selection	MC efficiency [%] Background	Background composition [%]			MC efficiency [%] for background categories		
		non-iso e	bkg e	hadrons	non-iso e	bkg e	hadrons
Track quality	100 %	0.9 %	12.1 %	87.1 %	100 %	100 %	100 %
LooseLLH	1.401+/-0.008 %	22.1 %	29.6 %	48.3 %	35.7+/-0.5 %	3.43+/-0.04 %	0.776+/-0.007 %
MediumLLH	0.748+/-0.006 %	32.3 %	15.0 %	52.6 %	27.8+/-0.4 %	0.928+/-0.020 %	0.450+/-0.005 %
TightLLH	0.455+/-0.005 %	39.1 %	16.2 %	44.7 %	20.5+/-0.4 %	0.607+/-0.016 %	0.232+/-0.004 %

The second column shows the efficiency of the total background after each identification menu, which as expected decreases with more stringent identification menus. The third column shows the variation in background composition after each menu. Finally, the identification efficiency for the individual background sources is given.

The rejection of light-flavour hadrons is as expected the highest compared to the other background processes.

3.3.2 Background rejection in $Z \to e^-e^+$ events

As mentioned before, the $Z \to e^-e^+$ process is one of the standard reference candles when it comes to calibration and performance studies. In this section, the same previous rejection measurements are reproduced using this time a $Z \to e^-e^+$ MC signal sample (the same sample used for the signal efficiency Figure 3.5). The fractions of the three background sources relative to the total background are compared in Figure 3.9, where the top plots correspond to the enriched background MC sample, and the bottom plots to $Z \to e^-e^+$ MC. The background composition as a function of η and p_T is relatively similar, with light-flavour hadrons in high abundance in both samples.

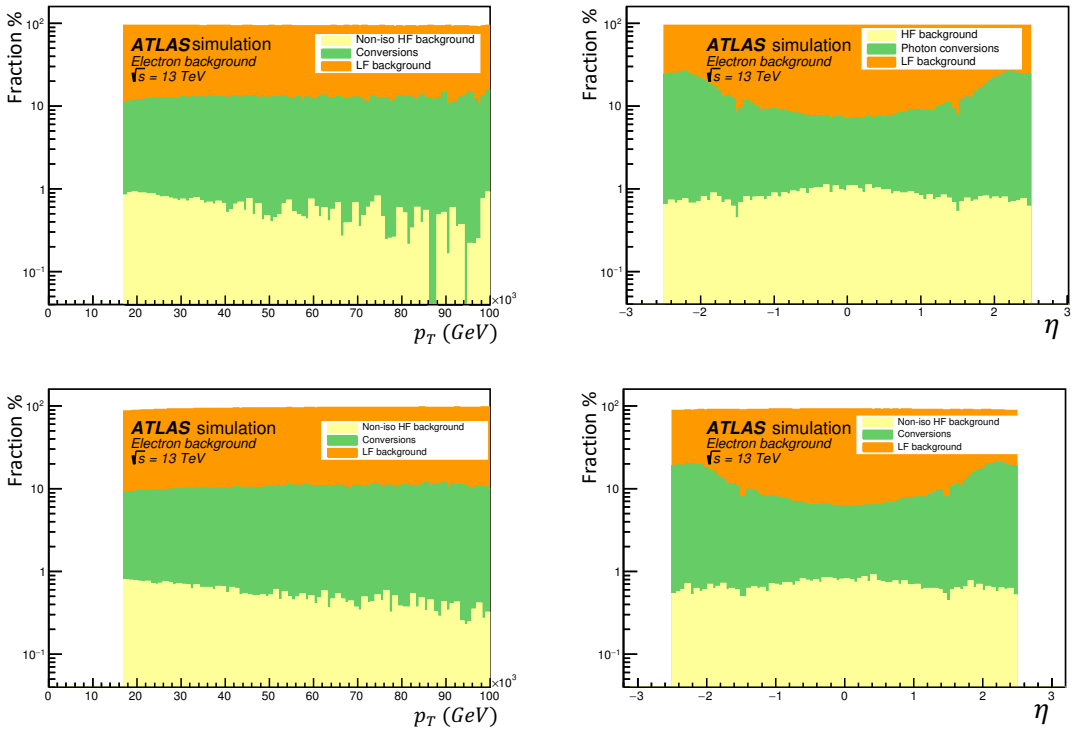

FIGURE 3.9: The fraction of the three background sources relative to the total background as function of p_T and η. The two top plots correspond to the background enriched sample, while the other two plots on the bottom correspond to the $Z \to e^-e^+$ sample.

Comparing the inclusive background identification efficiency in the two samples (Figure 3.10), it is clear that the rejection is overall higher in the $Z \to e^-e^+$ sample. The η distributions are relatively similar in shape, however the efficiency curves are more stable over the p_T spectrum for $Z \to e^-e^+$, especially for the *loose* identification menu. Finally, the total identification efficiency for all background categories is shown on Table 3.3. Also the identification efficiency of signal electrons from prompt decays of J/ψ, the Z and W boson are included. The results can be compared to those

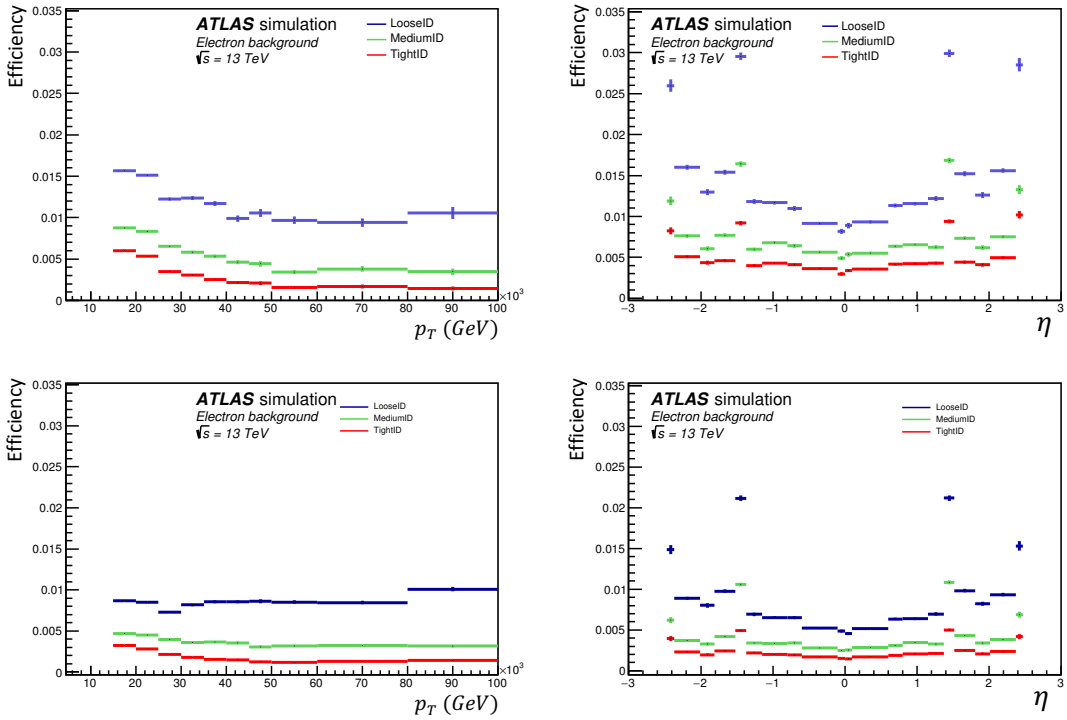

FIGURE 3.10: The inclusive background identification efficiency as a function of η and p_T for the three different identification menus. The top plots correspond to the background enriched sample, while the bottom plots correspond to the $Z \to e^-e^+$ sample.

on Table 3.2. In general, the overall rejection in $Z \to e^-e^+$ is slightly higher in all backgrounds. Also the fractions of the three background sources with respect to the total background after each identification menu are presented in Table 3.4. There are no significant differences in the background composition between the two samples after each identification menu.

TABLE 3.3: Summary table for the background identification efficiency for the different identification menus per background source. Also the signal identification efficiency is shown in the second column.

	Efficiency of signal and the various background categories in Zee sample			
Tightness level	Signal (Z, W or Jpsi)	Non-Iso Background	Conversions	Hadrons
Reconstructed probes	100 %	100 %	100 %	100 %
LooseLLH	93.027 ± 0.011 %	26.17 ± 0.33 %	2.502 ± 0.025 %	0.4327 ± 0.0035 %
MediumLLH	87.411 ± 0.011 %	19.56 ± 0.28 %	0.649 ± 0.013 %	0.2190 ± 0.0025 %
TightLLH	78.587 ± 0.010 %	14.20 ± 0.23 %	0.406 ± 0.010 %	0.0950 ± 0.0016 %

3.3.3 Rejection comparison with 2012 published results

Similar rejection measurements have been performed using 2012 data, collected during the first run of the LHC at $\sqrt{s} = 8$ TeV. Results were published in the following

TABLE 3.4: The composition of the background sources after each identification menu.

Background enriched MC			
Selection	Total fraction of background categories		
	non-iso e	bkg e	hadrons
Reconstructed probes	0.865 %	12.07 %	87.07 %
LooseLLH	22.09 %	29.61 %	48.30 %
MediumLLH	32.3 %	15.04 %	52.6 %
TightLLH	39.1 %	16.2 %	44.7 %

Zee			
Selection	Total fraction for background categories		
	non-iso e	bkg e	hadrons
Reconstructed probes	0.763 %	9.95 %	89.28 %
LooseLLH	23.68 %	29.43 %	46.89 %
MediumLLH	35.6 %	15.48 %	48.9 %
TightLLH	45.3 %	17.2 %	37.5 %

paper [51]. Having results of the identification rejection of the three main background sources from the previous section, numbers are compared to the published ones (top Table 3.5). It should be noted that only reconstructed electrons within $E_T \in [20, 50]$ GeV were used for the 2012 results, the numbers from this study were also recalculated for this E_T range to enable the comparison (bottom Table 3.5).

TABLE 3.5: Comparison of background rejection results between 2012 published results (top table) [51] and numbers calculated in this study (bottom table). The first column of numbers represents the identification efficiency of the inclusive background after each ID menu, the second column the composition of each background sources with respect to the total background, and the last column shows the efficiency numbers per background source.

20 GeV< E_T < 50 GeV							
Selection	MC efficiency [%] Background (prompt e excluded)	Background composition [%]			MC efficiency [%] for background categories		
		non-iso e	bkg e	hadron	non-iso e	bkg e	hadron
Track quality	100	1.1	16.1	82.8	100	100	100
LooseLH	0.94 ± 0.02	40.2	42.0	17.9	34.8±0.8	2.44±0.07	0.20±0.01
MediumLH	0.51 ± 0.01	48.8	40.6	10.7	23.1±0.7	1.29±0.05	0.066±0.005
VeryTightLH	0.29 ± 0.01	63.7	28.9	7.4	16.9±0.7	0.51±0.03	0.026±0.003

20 GeV< E_T < 50 GeV							
Selection	MC efficiency [%] Background	Background composition [%]			MC efficiency [%] for background categories		
		non-iso e	bkg e	hadrons	non-iso e	bkg e	hadrons
Track quality	100 %	0.9 %	12.1 %	87.1 %	100 %	100 %	100 %
LooseLLH	1.401+/-0.008 %	22.1 %	29.6 %	48.3 %	35.7+/-0.5 %	3.43+/-0.04 %	0.776+/-0.007 %
MediumLLH	0.748+/-0.006 %	32.3 %	15.0 %	52.6 %	27.8+/-0.4 %	0.928+/-0.020 %	0.450+/-0.005 %
TightLLH	0.455+/-0.005 %	39.1 %	16.2 %	44.7 %	20.5+/-0.4 %	0.607+/-0.016 %	0.232+/-0.004 %

Comparing both results, the identification efficiency of background is in general higher in this study, i.e. the rejection is lower. The efficiency for the inclusive background is approximately a factor of 1.5 lower in the 2012 results. Also, the relative background composition of the three background sources is different after each ID menu. For example, the light-flavour background is more rejected compared to results from this study, but has a lower fraction in the background composition. In fact, it is difficult to judge the background rejection in both cases since the latter is calculated relative to the electron reconstruction, while the electron reconstruction rejection of background (or the efficiency of reconstructing fake electrons) is unknown in the latter cases. In fact, the electron reconstruction was updated in Run-2 (2015-2018) compared to Run-1 (2010-2013), which resulted in a different background rejection

of the electron reconstruction. As a consequence, it is not possible to make a quantitative comparison without the latter rejection in both cases. One would need to calculate these numbers relative to the electron reconstruction rejection in order to make a meaningful comparison. Although the latter numbers do not exist for the 2012 results, in the next part of this study, the background rejection in the context of the electron reconstruction is calculated and discussed.

3.4 Electron reconstruction efficiency for background fake electrons

As previously stated, not only genuine electrons from prompt decays are reconstructed as electrons. Therefore, the electron identification is designed to discriminate between signal and fake electrons after reconstruction. The three previously mentioned identification operating points (*loose*, *medium* and *tight*) are in reality optimised to reach specific benchmark efficiencies, which are difficult to obtain due to the mismodelling of calorimeter shower shape quantities in MC. It is in fact a complex task to target specific background signatures. Therefore, a preferable way of optimising these identification menus can be achieved based on the rejection of background processes. In this study, a background rejection study for the electron reconstruction is presented. In this study, only statistical uncertainties are considered.

3.4.1 Background rejection for the electron reconstruction

As mentioned in section 3.1, the reconstruction of electron candidates relies on the ID for the identification of charged-particle tracks, and the EM calorimeter for the localised clusters of energy deposits. Electrons undergo bremsstrahlung radiation, whereby they lose energy while traversing the different parts of the detector. Photons from this radiation cause electron-positron pair production, which are usually emitted in a collimated fashion along with the primary electron. This characteristic signature is exploited in the electron reconstruction algorithm [50], which takes into account the shape of the energy clusters in the EM calorimeter and their close matching with tracks from the ID.

For the rejection of background sources in the context of the electron reconstruction, hadronic jets are considered as the main background, as they can leave tracks in the ID and energy deposits in the EM calorimeter. Hadronic jets are extensively produced at the LHC, and are by far the most dominant source of fake electrons, as shown in the previous section. Therefore, the electron reconstruction rejection measurement is calculated in multi-jet events, where the fraction of jets reconstructed as electrons is studied. Moreover, the efficiency of reconstructing jets as electrons will be calculated, in MC as well as in data of proton-proton collision events at $\sqrt{s} = 13$

TeV, corresponding to the data taking year of 2017.

For the electron identification rejection measurement, MC generator information was used to distinguish between the different background sources. In order to perform the measurements in data, one can only rely on reconstructed quantities. Therefore, it is important to use a process that is easy to trigger, high in abundance and is measured with high precision. A process that satisfies these requirements is the standard reference candle $Z \rightarrow e^{-}e^{+}$. The latter process has the advantage of having a characteristic signature with a low background, and is in high abundance given its high cross section at $\sqrt{s}$ = 13 TeV. Also, the fact that Z boson production at the LHC is associated with hadronic jets, referred to as Z+jets, multi-jet events are reconstructed which are crucial for this study.

3.4.1.1 Jet reconstruction

Hadronic jets originate from the hadronisation process of partons resulting in collimated streams of particles that interact with the ID and the calorimeters. Jets in this study are reconstructed from topological clusters using an algorithm known as the anti-k_T [113], which proceeds sequentially by reconstructing jets in a regular, cone-like geometry based on the QCD splitting of partons. The anti-k_T reconstruction is performed for a specific value of the anti-k_T distance parameter, R, that specifies the nominal radius of the reconstructed jets. A jet radius of 0.4 is used for all jets mentioned in this thesis. Moreover, four-momentum measurements of jets include corrections for the non-compensating response of calorimeters, energy losses in crack regions, pile-up contributions and signal losses due to noise effects. Jets originating from pile-up are rejected using an algorithm discriminating based on the fraction of tracks from jets originating from the primary vertex. In the case of pile-up jets in the forward region, having a p_T < 50 GeV and corresponding to $|\eta|$ > 2.5 where there is no ID coverage, the rejection is performed using an algorithm that discriminates based on missing transverse momentum. More details on jet reconstruction can be found in [84].

3.4.1.2 Jet and fake electron selection for the rejection measurement

In the context of the electron reconstruction background rejection, one is interested in the number of rejected jets per fake reconstructed electron. The inverse of this number, R_{jets}, is equivalent to the efficiency of reconstructing a fake electron from a jet,

$$\epsilon_{jets \rightarrow fakes} = \frac{1}{R_{jets}}. \tag{3.7}$$

For this rejection measurement, only fake electrons that overlap with reconstructed jets are considered. This overlap is quantified by measuring the spacial angular separation between the fake reconstructed electron and the jet, which is given by ΔR

defined in eq. 3.2. The efficiency of jets being reconstructed as fake electrons can then be calculated as,

$$\epsilon_{jets \to fakes} = \frac{N_{jets \to fakes}}{N_{jets}}, \tag{3.8}$$

where $N_{jets \to fakes}$ represents the number of jets that are close to a fake reconstructed electron, within $\Delta R(fake, jet) < 0.4$, and N_{jets} the number of jets in the event. In the case where two fake electrons are within $\Delta R(fake, jet) < 0.4$ of the same jet, the closest is always selected. Double counting of fake electrons that are close to two different jets is also avoided.

3.4.1.3 Z+jets event selection for the rejection measurement

As mentioned before, the rejection measurement for the electron reconstruction is performed in Z+jets events, a so-called *Drell-Yan process*, where a quark and an anti-quark annihilate to create a Z boson. The latter decays to a pair of electrons with a branching ratio of approximately 3.4% [112]. At the LHC, this process is associated with partons from the hard scatter which become hadronic jets. Figure 3.11 shows an example of the $Z \to e^- e^+$ Drell-Yan process in this latter case.

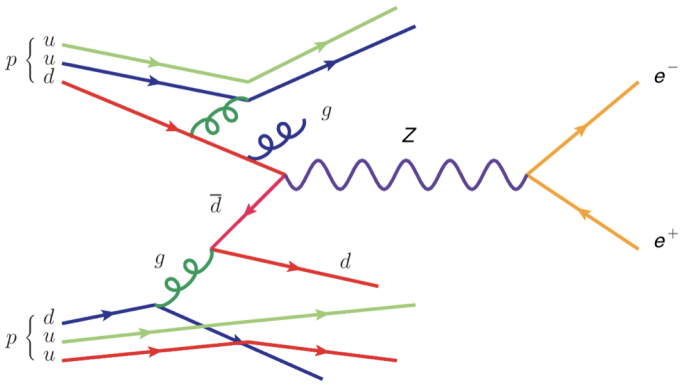

FIGURE 3.11: An example of the $Z \to e^- e^+$ Drell-Yan process in association with the parton remnants of the protons which become hadronic jets.

The best way of selecting these events is by exploiting the characteristic signature of the electronic Z boson decay, where two opposite charged electrons are produced. Prompt genuine electrons from the Z decays can be identified by requiring per event the following requirements (the so-called Z boson mass window):

- at least two reconstructed electrons per event,
- the pair is required to be opposite-charged,
- both reconstructed electrons are required to pass the medium identification menu,

- both reconstructed electrons are required to pass the track isolation requirement,
- the invariant mass of the electron pair is required to be within $m_{ee} \in [81.18, 101.18]$ GeV (Z boson resonance).

For the track isolation requirement, a track based isolation variable is defined as,

$$\Delta_{iso}^{track} = \frac{\sum p_{T,i}}{p_{T,el}}, \tag{3.9}$$

with the numerator representing the scalar p_T sum of tracks around the electron within a cone of $\Delta R = 0.2$, and the denominator the p_T of the electron. The track isolation requirement for prompt electrons is $\Delta_{iso}^{track} < 0.15$. Per event, the pair of electrons satisfying the Z mass window requirements that is the closest to $m_Z = 91.18$ GeV, is tagged as the Z electron pair. Although events are selected by requiring the pair of Z electrons, these are removed for the rejection measurement. Since one is only interested in jets being reconstructed as fake electrons, all jets are included in the selection, except those close to the Z prompt electrons ($\Delta R(e, jet) < 0.4$). All other reconstructed electrons in the corresponding events are considered as fake electrons. This relies on the assumption that background processes to Z+jets have a negligible contribution around the Z boson resonance in data. For example, ZW di-boson production can lead to a signal contamination, where a third prompt electron coming from the W boson ($W \rightarrow e\nu$) would be considered as a fake electron. Finally, only reconstructed electrons in the central detector region with $|\eta| < 2.47$ and $p_T > 30$ GeV are selected for the rejection measurement.

Figure 3.12 shows the invariant mass distribution of the two selected Z electrons in Z+jets MC and in 2017 data, where the bottom ratio plot reflects the data/MC agreement[6]. The modelling around the Z mass peak is relatively good, with some discrepancy toward the tails of the distribution. There are two reasons for the latter effect. The first is the fact that the MC does not include all calibration scale factors, which are for the purpose of this study irrelevant (i.e. the goal is not to measure the Z peak with high precision). The second reason is the contribution of background processes in data, mainly from top-quark pair and di-boson production, which include at least two prompt electrons in the final state. These are expected to be more prominent toward the tails, as the Z boson contribution falls off away from the resonance. Nevertheless, for the selected invariant mass window the contamination is negligible. Finally, the importance of selecting the Z electrons is only to ensure prompt electrons are selected and removed equivalently in data and MC to perform the rejection measurement on jets.

[6]The ratio of the number of events gives the percentage difference between data and MC, the further from unity the worse the agreement.

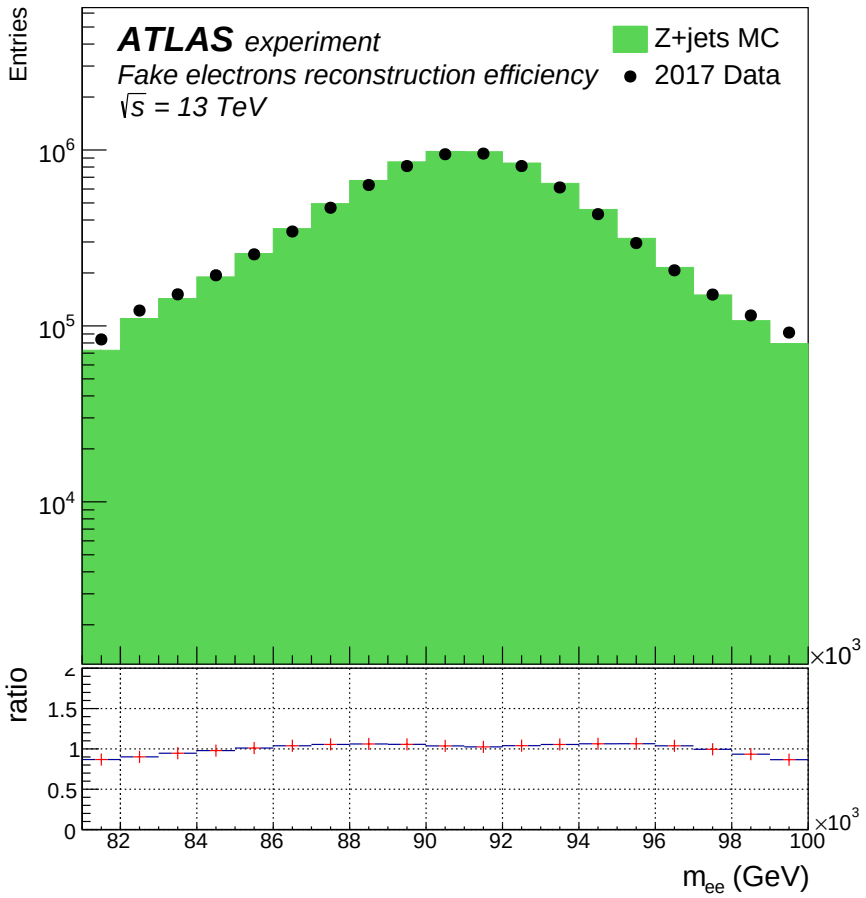

FIGURE 3.12: The invariant mass distribution of the pair of electrons selected with the Z mass window method. The green histogram represents the Z+jets MC distribution, while the black dots the 2017 data. The MC distribution is normalised to the luminosity and corrected for pile-up.

3.4.1.4 Jet and fake electron kinematic distributions

Figure 3.13 shows respectively the p_T (A) and η distribution (B) of all jets in the selected $Z \rightarrow e^- e^+$ events (except those within $\Delta R(e, jet) < 0.4$, which are removed), and jets associated with fake reconstructed electrons. Also the fake electron p_T and η distributions are shown for comparison. On the η spectrum, the all-jets distribution has two peaks around $|\eta| = 1.3$, corresponding to the crack region of the EM calorimeter. For the fake electrons and their associated jets, the η distributions are very close. This is a consequence of the ΔR matching, which ensures the proximity of jets and the associated fake electrons. Also, the peaks in the crack region do not show up in these last two distributions, which is related to the low efficiency of reconstructing electrons around the crack region.

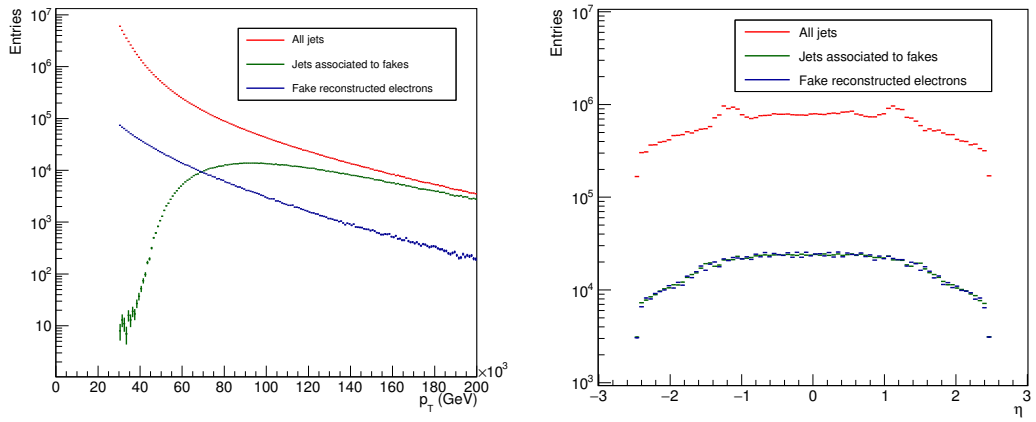

(A) (B)

FIGURE 3.13: The p_T (A) and η (B) distribution of jets and fake electrons in Z+jets MC events. The red plots represent the jet p_T and η distributions of all jets in the events (except those within $\Delta R(e, jet)$ < 0.4), while the green distributions shows the same quantities for jets close to fake reconstructed electrons, and the blue curves for fake electrons .

On the other hand, the p_T distributions of fake electrons and their associated jets do not look similar at all. First of all, the electron p_T and jet p_T are not reconstructed in the same way, and therefore their calibration is different, but most importantly, the energy of an electron is reconstructed using the EM calorimeter, while a jet is reconstructed from the EM and Hadronic calorimeter. Therefore, if a jet is reconstructed as an electron, only the EM calorimeter part of the jet is taken into account. As a consequence, the reconstructed energy of a fake electron is lower than the energy of the associated jet. Furthermore, the jet p_T distribution on Figure 3.13 (A) is shifted toward higher p_T values compared to the electron p_T distribution, which follows the expectation. Also, after applying a p_T cut at 30 GeV for both fake electrons and jets, the fact that jets matched to fakes are in low abundance close to the cut suggests that there are no fake electrons to be associated with, since they would have a lower p_T than 30 GeV, whereas the distribution of all jets clearly peaks at low p_T values.

The correlation between fake electrons and the associated jets can be further investigated with the two-dimensional scatter plot Figure 3.14, where the jet p_T versus electron p_T are plotted. The electron p_T shows a strong dependence on the jet p_T, where the electron p_T is always lower than its associated jet p_T. It is also important to note that the correspondence between the jet p_T and the electron p_T; for a given jet p_T, there is a range of associated electron p_T values. This would suggest that jets are reconstructed with different possible fractions of their energy deposits. Investigating further the relationship between the jet and the fake electron p_T, Figure 3.15 shows the distribution of the relative difference between jet and electron p_T,

calculated as,

$$\Delta_{p_T}^{rel.} = \frac{p_T^{jet} - p_T^{fake}}{p_T^{jet}}. \tag{3.10}$$

The resulting distribution resembles approximately a Gaussian, with a mean of 0.5875 $\pm$ 0.0002, representing the most likely fraction, and a standard deviation of 0.1304 $\pm$ 0.0003. In summary, observations from Figures 3.13 - 3.15 are consistent with the expectations that the selected jets are indeed reconstructed as fake electrons, which are essential for the rejection measurement.

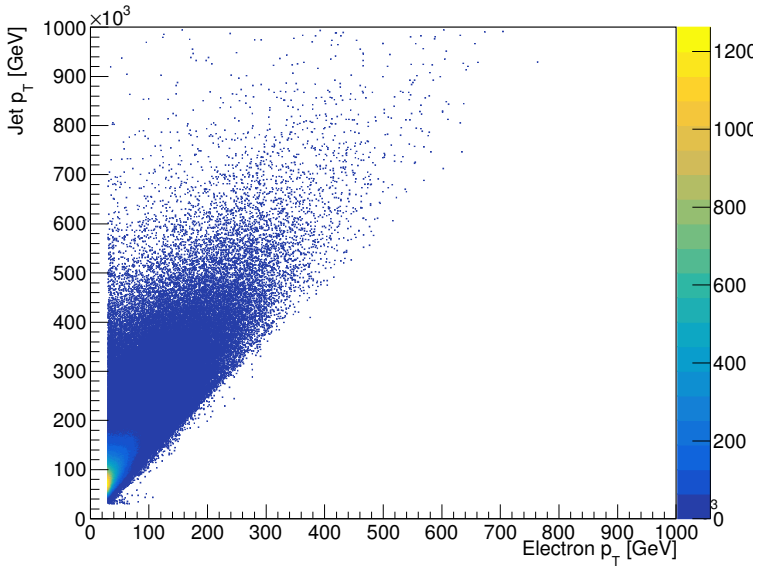

FIGURE 3.14: The two-dimensional scatter plot of the jet p_T versus the associated fake electron p_T in Z+jets MC events.

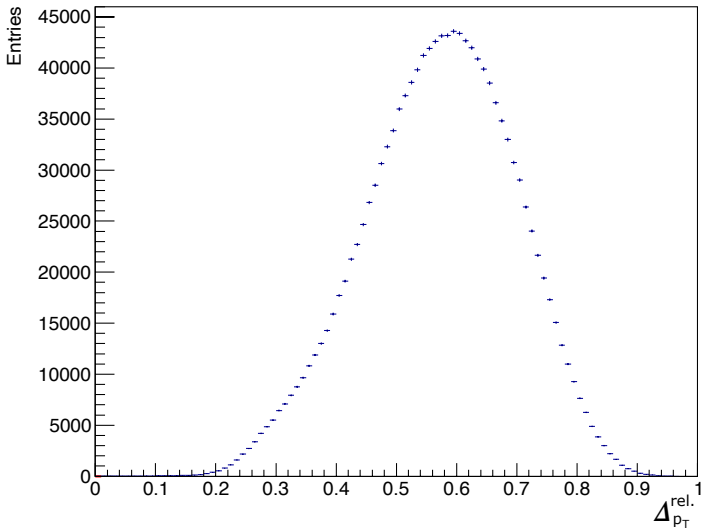

FIGURE 3.15: The distribution of the relative jet vs. electron p_T difference (according to eq. 3.10).

3.4.2 Reconstruction efficiency of jets as electrons in Z+jets MC

Finally, having the η and p_T distributions of all jets, reconstructed fake electrons and their associated jets (Figure 3.13 (A) and (B)), the reconstruction efficiency of jets as electrons in terms of jet p_T (electron p_T) can be calculated by dividing the green (blue) distribution by the red one. Figure 3.16 (A) and (B) show the efficiency, respectively, in terms of η and p_T bins. In the η spectrum, the efficiency is relatively constant at around 2-3%. On the other hand, the p_T spectrum has a turn-on efficiency curve, where the higher the jet p_T, the higher the efficiency of being reconstructed as a fake electron. This was expected from Figure 3.13 (A), where low p_T jets matched to fakes were in low abundance around the 30 GeV cut. Equivalently, this implies that the electron reconstruction rejection is higher in the low p_T region.

Analogously, the reconstruction efficiency in terms of the electron p_T is also calculated. Figure 3.17 (A) and (B) represent, respectively, the efficiency in terms of electron p_T and η. The η curve is very similar to the jet η efficiency as expected from the similarity in Figure 3.13 (B), which is constant at around 2-3%. The electron p_T spectrum is different, the turn-on effect is less distinct. However, the efficiency (rejection) is similarly higher (lower) for higher p_T values. Finally, the total efficiency in Z+jets MC (with pile-up conditions corresponding to those in the 2017 data taking period) is found to be, $\epsilon_{jets \to fakes} = 2.797 \pm 0.002$ %, which corresponds to a rejection of $R_{jets} = 35.76 \pm 0.03$ (statistical uncertainty only).

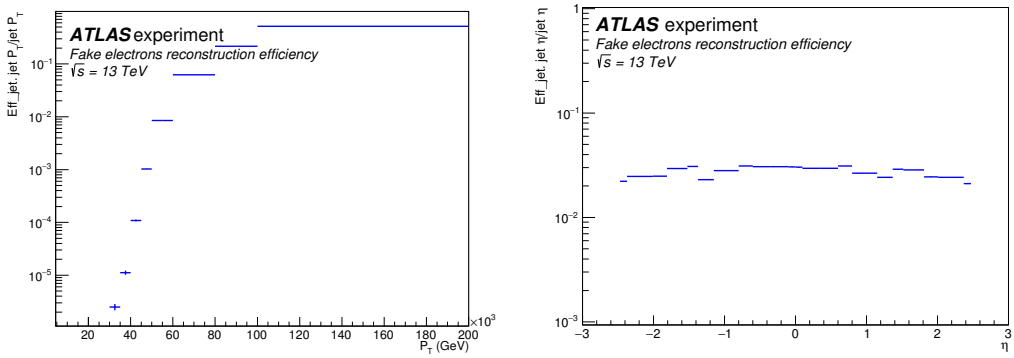

(A) (B)

FIGURE 3.16: The efficiency of jets reconstructed as fake electrons in terms of jet p_T (A) and jet η (B). Only the statistical uncertainties are presented which are negligible.

3.4.3 Reconstruction efficiency of jets as electrons in 2017 data

After estimating the efficiency/rejection in Z+jets MC events, the next step is to perform the same measurements in data. As mentioned before, data corresponding to the 2017 data-taking year is used in this study. Similarly, the same event selection

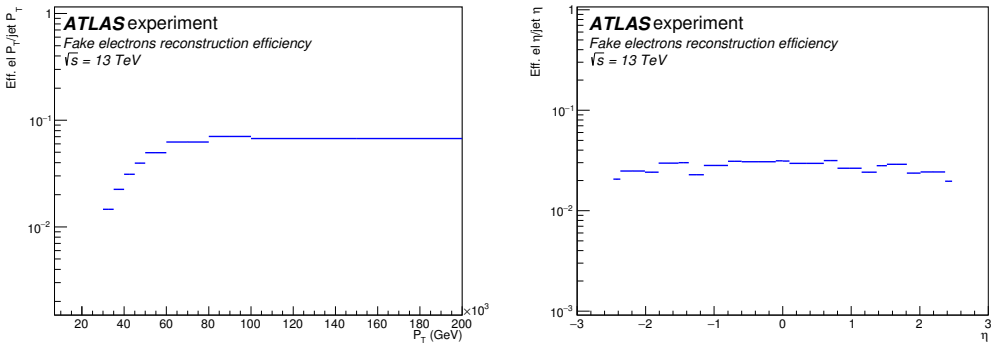

(A) (B)

FIGURE 3.17: The efficiency of jets reconstructed as fake electrons in terms of electron p_T (A) and η (B). Only the statistical uncertainties are presented which are negligible.

and efficiency calculation are performed as described in section 3.4.1.2 and 3.4.1.3. The overall efficiency and rejection in 2017 data are respectively $\epsilon_{jets \to fakes} = 5.461 \pm 0.007$ % and $R_{jets} = 18.31 \pm 0.02$. This result is almost a factor of two higher (lower) than expected in MC. Comparing the results in jet p_T and η bins (Figure 3.20 and 3.21), data and MC are in disagreement on both spectra, with data having a higher (lower) efficiency (rejection) than in MC.

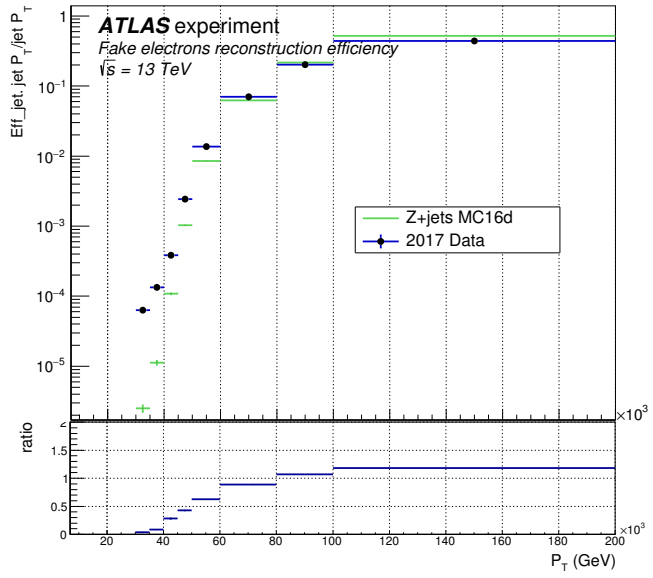

FIGURE 3.18: MC/data comparison of the efficiency of reconstructing jets as fake electrons in jet p_T bins.

In the jet η spectrum, the discrepancy between data and MC is constant, with the exception of the crack regions, where peaks appear in the ratio plot. In the p_T spectrum, the ratio plot is not constant. The disagreement is larger in the lower p_T region.

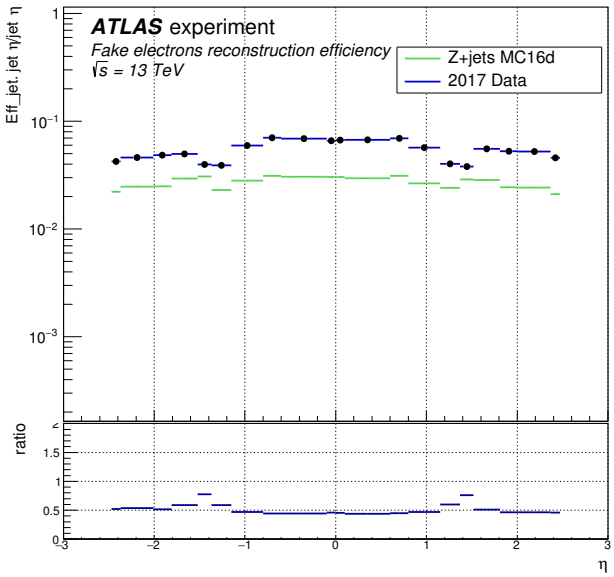

FIGURE 3.19: MC/data comparison of the efficiency of reconstructing jets as fake electrons in jet η bins.

This large discrepancy is not yet understood, but it can raise the question about differences in efficiency of selecting prompt electrons in data and MC. Appendix A.2 contains a study where the rejection in the $Z \to e^-e^+$ event selection based on reconstruction quantities (section 3.4.1.3) is compared to the rejection in a generator-level based (exact) event selection. The measurements are found to be compatible, therefore the event selection is probably not at the origin of the discrepancy. As mentioned in section 3.4.1.3, prompt electron contamination from di-boson events could be suspected, with ZW production being the most prominent, where three prompt electrons can be produced ($Z \to e^-e^+$ and $W^\pm \to e^\pm\nu$). The two Z electrons are removed for the efficiency calculation, but the third prompt electron from the W is then tagged as a fake electron. This case was investigated using a ZW di-boson MC (generated with POWHEG [65]). The signal contamination yield of prompt electrons tagged as fakes is determined using generator information. After normalising the yield of events to the data luminosity, the number of prompt electrons expected from ZW di-boson process in data was found to be 2231.4 ± 3.8 events. This is less than 0.3% of the total number of fake tagged electrons in data. Subtracting this number from data and recalculating the efficiency and rejection, no significant difference is observed. Therefore, one can conclude that the ZW di-boson process is negligible and cannot be at the origin of the data-MC disagreement.

Similarly, the measurements are also performed in terms of electron η and p_T. For the η spectrum, similar conclusions to the jet η case can be made. The electron p_T efficiency comparison is slightly better than in jet p_T. The ratio plot is in general flatter, with a better agreement in the low p_T region. Furthermore, the two-dimensional

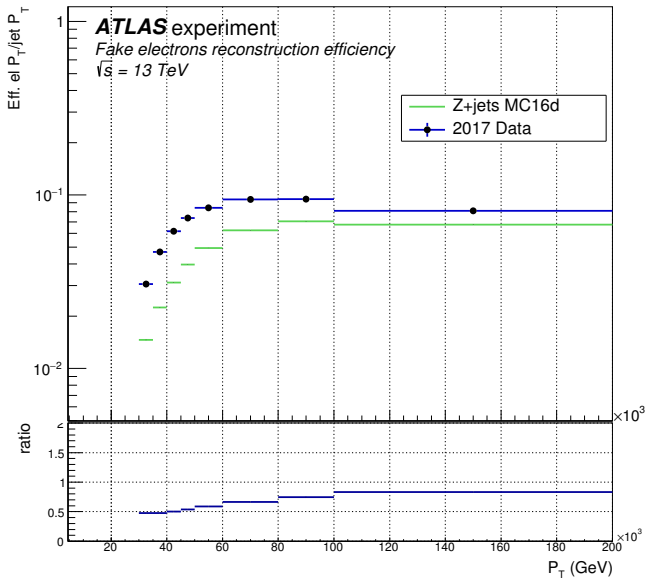

FIGURE 3.20: Data/MC comparison of the efficiency of reconstructing jets as fake electrons in electron p_T bins.

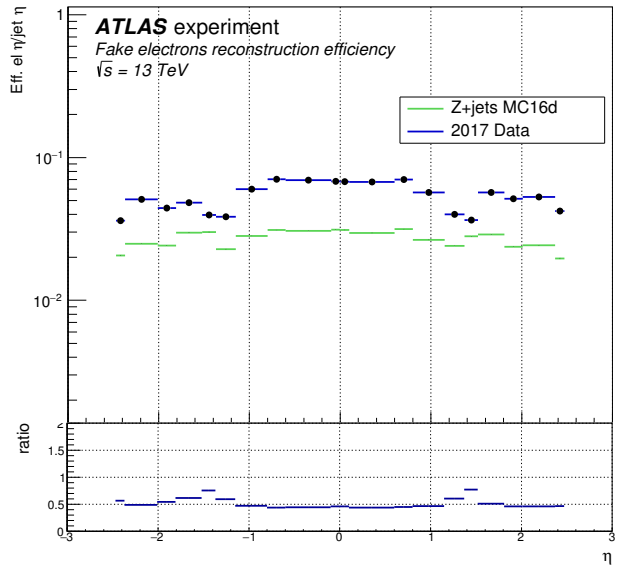

FIGURE 3.21: Data/MC comparison of the efficiency of reconstructing jets as fake electrons in electron η bins.

plot with jet p_T versus electron p_T in data is shown (Figure 3.22). Comparing it to Figure 3.14 for Z+jets MC, the assumption on the jet p_T always higher than the associated electron p_T is not observed in data. The low p_T region shows significantly more events with jet p_T smaller than the associated fake electron p_T, which could be at the origin of the discrepancy in the low p_T region between data and MC. An attempt to improve the agreement by adding a veto on jets with a p_T smaller than the associated fake electron p_T was applied, but only a slight improvement in the low p_T region was observed.

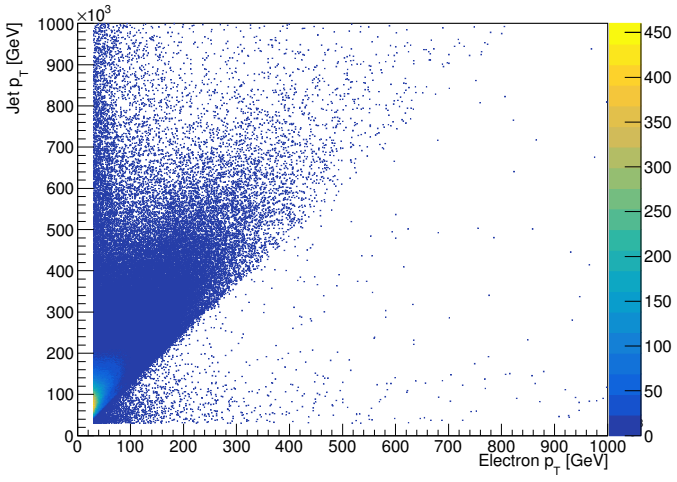

FIGURE 3.22: The two-dimensional scatter plot of jet versus the associated fake electron p_T in data events.

3.5 Summary & conclusion of the analysis

As mentioned in section 3.1, electrons are reconstructed from matching tracks in the ID with energy deposits in the EM calorimeter. As many other charged particles can interact with the latter sub-detectors, not all reconstructed electrons are genuine electrons from prompt decays. In the first part of this study, the background for signal electrons was investigated in background enriched MC samples. Background electrons were classified into three categories using MC generator information, namely light-flavour hadrons, photon conversions and non-isolated electrons from heavy-flavour decays. The efficiency of identifying these background sources as genuine electrons was calculated and compared in the background enriched MC and Z+jets MC. Efficiencies were also calculated in η and p_T bins. Results were compared for each identification working point (*loose*, *medium* and *tight*), which were found to be different in the background enriched MC and Z+jets MC, with an overall higher rejection in Z+jets MC. In general, the light-flavour background was found to be the most rejected background. Photon conversions were the second, while the heavy-flavour background was the least rejected. Finally, Run-1 efficiency numbers published in 2012 [51] were reproduced for comparison. The background efficiency was overall higher in this study, with a factor 1.5 difference in the inclusive background measurement. However, conclusions on the latter comparison were difficult to make since the efficiencies were calculated relative to the electron reconstruction, which is different in Run-1 and Run-2. Therefore, the electron reconstruction background rejection in both cases is necessary for a meaningful comparison.

In the second part of the study, the electron reconstruction background rejection was investigated. In the context of the electron reconstruction, jets were considered as the main background, as they leave tracks in the ID and energy deposits in the EM calorimeter. The reconstruction efficiency (inverse of the rejection) was defined as the ratio of jets overlapping with fake electrons over the total number of jets in the events. The background rejection was calculated in Z+jets MC as well as in 2017 data. The overall rejection is found to be 35.76 ± 0.03 for Z+jets MC and 18.31 ± 0.02 in data, which is almost a factor of two in difference. Results were also presented and compared in η and p_T bins, where the disagreement is found larger in the low p_T region. This mismodelling has been further investigated. Prompt electron contamination from other processes in data was suspected to be at the origin of the discrepancy. As the ZW di-boson process was expected to have the largest contribution, a MC estimation was performed to investigate signal contamination from the latter process. The yield was found to be negligible, suggesting the observed difference is not related to the signal electrons. Furthermore, modelling of multi-jet processes in event generators is a difficult task [92], and is therefore expected to be the reason behind the mismodelling. Finally, in this study only statistical uncertainties were considered, whereas systematics are necessary for a final conclusion.

Chapter 4

Measurement of the Higgs boson mass in the $H \to ZZ \to 4\ell$ decay channel using $\sqrt{s} = 13$ TeV proton-proton collision events recorded by the ATLAS detector

4.1 Overview of the Higgs boson mass measurements

As mentioned in section 1.4, the Higgs boson mass is a free parameter in the SM which has to be empirically measured. Its value is crucial in order to determine the Higgs boson production cross section and the branching ratios of its decay modes. As shown in Figure 1.7, once the mass m_H is known, the SM takes it as an input in order to predict the latter quantities, which is a direct verification of the theory. The Higgs boson was successfully observed by the ATLAS and CMS collaborations in 2012. The discovery was achieved using a part of Run-1 LHC proton-proton collision events at $\sqrt{s}$ = 7 TeV for the 2011 dataset and $\sqrt{s}$ = 8 TeV for the 2012 dataset. In the case of the ATLAS experiment, these datasets corresponded to an integrated luminosity of respectively 4.8 fb^{-1} and 5.8 fb^{-1}, while CMS collected 5.1 fb^{-1} and 5.3 fb^{-1}. As the Higgs boson was measured for the first time, the ATLAS collaboration reported a mass measurement of 126.0 $\pm$ 0.6 GeV [52] (statistical and systematic uncertainties included), while the CMS collaboration reported 125.3 $\pm$ 0.6 GeV [53]. Initially, the search for the Higgs boson was performed using five of its decay modes, namely $H \to WW \to l^{\pm}\nu l^{\pm}\nu$, $H \to b\bar{b}$, $H \to \tau\tau$, $H \to ZZ \to 4l^{\pm}$ and $H \to \gamma\gamma$, where the most significant excesses were found in the last two decay modes. Using these $H \to ZZ \to 4l^{\pm}$ and $H \to \gamma\gamma$ decay modes, a combined analysis conducted by both ATLAS and CMS (using the full Run-1 data, approximately 5 fb^{-1} at 7 TeV and 20 fb^{-1} at 8 TeV) yielded a mass measurement of 125.09 $\pm$ 0.24 GeV [54]. Figure 4.1 shows a summary of the Run-1 Higgs boson mass measurements from CMS and ATLAS in the $H \to ZZ \to 4l^{\pm}$ and $H \to \gamma\gamma$ decay modes including the combined

analysis measurements.

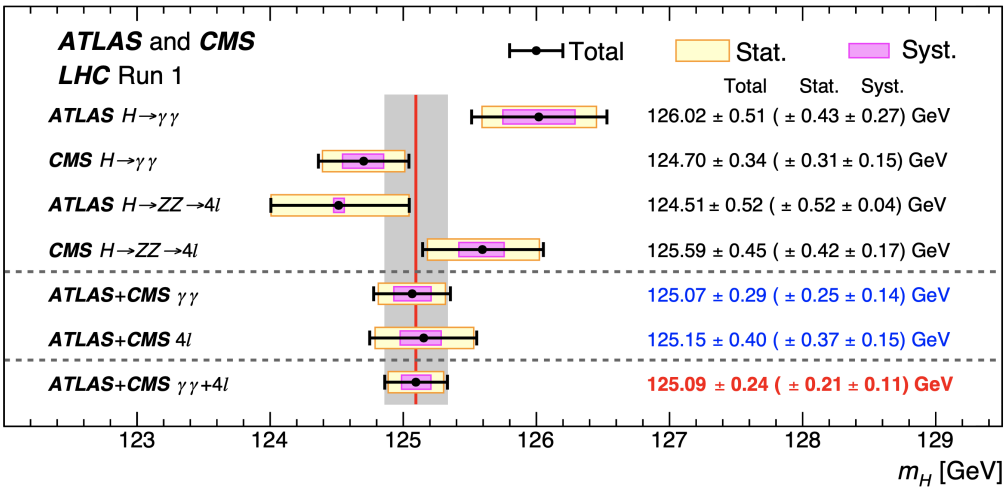

FIGURE 4.1: Summary of the Run-1 Higgs boson mass measurements from CMS and ATLAS in the $H \to ZZ \to 4l^{\pm}$ $H \to \gamma\gamma$ decay modes including the combined analysis measurements [54].

As mentioned before, during the second run of the LHC (2015-2018), the operating centre-of-mass energy corresponded to 13 TeV. Using a fraction of the Run-2 dataset corresponding to the 2015-2016 period of data-taking, the ATLAS collaboration released a mass measurement of 124.86 $\pm$ 0.27 GeV [56], combining the $H \to ZZ \to 4l^{\pm}$ and $H \to \gamma\gamma$ decay modes. As a result of a larger Higgs boson production cross section at 13 TeV and a larger dataset with 36.1 fb^{-1}, this measurement is more precise than the combined Run-1 measured value, with a reduction of 140 MeV in the total uncertainty. Combining Run-1 and Run-2, the resulting mass corresponds to 124.97 $\pm$ 0.24 GeV [56], gaining an extra 30 MeV relative to the 36.1 fb^{-1} measurement. Figure 4.2 shows a summary of all the Higgs boson mass measurements in ATLAS with the $H \to ZZ \to 4l^{\pm}$ and $H \to \gamma\gamma$ decay modes including results using a fraction of the Run-2 datasets and the combined analysis measurements.

In this thesis, a measurement of the Higgs boson mass in the $H \to ZZ \to 4l^{\pm}$ decay mode is performed, using the Run-2 data (2015-2018) of proton-proton collision events corresponding to 139 fb^{-1} of recorded data by the ATLAS detector. Also the combined measurement using the Run-1 and Run-2 datasets is presented. These results are published and can be found in [1].

4.2 The $H \to ZZ^* \to 4\ell$ golden decay channel

Many factors can affect the ability of measuring the Higgs boson mass with precision, including the branching ratio of the decay channels, the reconstructed final state objects resolution, the selection efficiency of signal events or the background

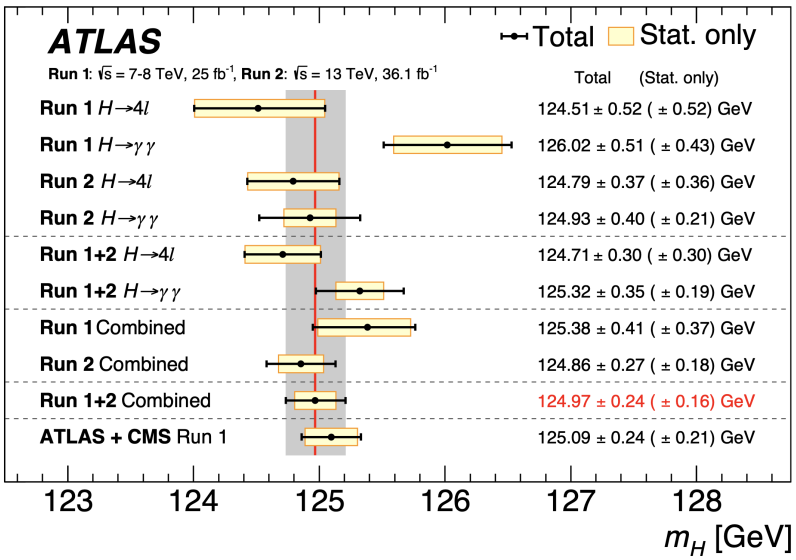

FIGURE 4.2: Summary of the Higgs boson mass measurements from ATLAS in the $H \to ZZ \to 4l^{\pm}$ and $H \to \gamma\gamma$ decay modes including results using a fraction of the Run-2 datasets and the combined analysis measurements [55].

estimation. As mentioned in section 1.4, the Higgs boson can decay in many ways. Figure 1.7 (B) shows the branching ratios of the different decay modes. The $H \to b\bar{b}$ decay is by far the most prominent, with a branching ratio of 57.8% for m_H = 125 GeV. However, it is not an easy task to identify its events in the overwhelming QCD production of multi-jets at the LHC; the search requires a high identification efficiency of bottom quark jets, and a high rejection of light-flavour jets, which is difficult to obtain. This fact makes the $H \to b\bar{b}$ decay channel not ideal for the mass measurement. The second largest branching ratio is from $H \to WW$, where each W boson decays to a charged lepton and its associated neutrino. In general, electrons and muons are reconstructed and identified with high efficiency using the ATLAS detector. This is not the case with τ leptons, where their very short lifetime prevents them from traversing the detector (i.e. they decay inside the beam pipe). Also, their overwhelming branching ratio to hadronic final states (65%) causes a high probability of misidentification. Therefore, τ leptons are used in dedicated analysis and are not considered[1] in a leptonic final state searches of e.g. $H \to WW$ and $H \to ZZ$ decays. Although the $H \to WW \to l^{\pm}\nu l^{\pm}\nu$ decay mode benefits from a significant branching ratio (BR($H \to WW$) = 21.6% and BR($H \to WW \to l^{\pm}\nu l^{\pm}\nu$) = 5.4% for m_H = 125 GeV), involving well reconstructed electrons and muons, the remaining neutrinos are undetected. These are indirectly measured, as mentioned in section 2.4.1, since partons inside the protons have a negligible transverse momentum as they travel in the beam pipe, and so the total momentum in the transverse direction can be constrained to be zero before collision. From the conservation of momentum

[1] However, their decay to electrons and muons is taken into account.

law, any imbalance in the total transverse momentum after collision can be associated to missing undetected particle(s), such as neutrinos. This indirect measurement of neutrinos in the $H \to WW \to l^{\pm}\nu l^{\pm}\nu$ decay search, using the so-called *missing transverse energy*, results in a poor mass resolution. The next leading decay modes in decreasing order of branching ratio are $H \to gg$, $H \to \tau\tau$ and $H \to c\bar{c}$, which are also for the same previously stated reasons not ideal for the mass measurement.

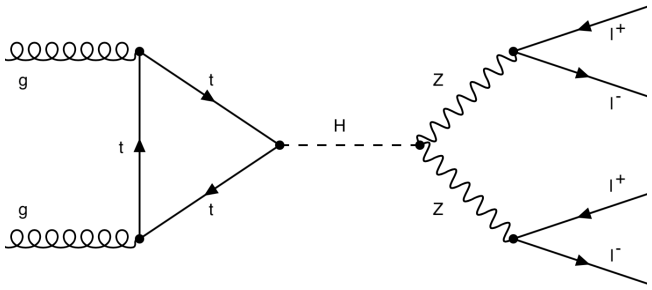

FIGURE 4.3: Feynman diagram of the $H \to ZZ \to 4l^{\pm}$ golden decay channel through a gluon-gluon fusion Higgs production as an example.

One of the best ways to measure the mass of the Higgs boson with high precision is through the $H \to ZZ \to 4l^{\pm}$ decay channel, a.k.a *the golden decay channel*. It is fully reconstructed from the four charged leptons originating from the intermediate two Z boson decays. Figure 4.3 shows the Feynman diagram of the the golden channels through a gluon-fusion Higgs boson production. Given the high efficiency in reconstruction and identification of the decay products, these decay channels provide a clean final state signature. The Higgs boson mass, m_H, is measured from the invariant mass of these four leptons, m_{4l}, which is reconstructed with an excellent resolution, typically 1-2%. Even though its branching ratio is relatively small, BR($H \to ZZ$) = 2.7% and BR($H \to ZZ \to 4l^{\pm}$) = 0.0124% for m_H = 125 GeV, it benefits from a high signal over background ratio. In this decay mode, there are three golden final states from the intermediate Z boson decay channels; the two bosons can both decay to a pair of opposite charged muons resulting in a four muon final state ($H \to ZZ \to 4\mu$), or both can decay to a pair of opposite charged electrons and this would yield a four electron final state ($H \to ZZ \to 4e$). Finally, one Z boson can decay to a pair of electrons, while the second boson to a pair of muons ($H \to ZZ \to 2e2\mu$).

4.3 Signal and background MC simulation events

As mentioned in section 2.3.2, it is impossible to identify the type and origin of individual events in data. Therefore, it is important to study all sources leading to

the desired signal signature. In the case of the search for the $H \to ZZ \to 4l^{\pm}$ decay channels, many processes can lead to four charged leptons production in the final state. The signal processes are those including the $H \to ZZ \to 4l^{\pm}$ decays, while other processes producing four reconstructed charged leptons are considered as background.

4.3.1 MC simulation of $H \to ZZ \to 4l^{\pm}$ events

Starting with the signal events, Figure 1.8 shows the leading processes for the Higgs boson production which contribute to the four lepton final state. Each of these processes is simulated using MC generators, providing samples of the generator and reconstruction properties of the events. As mentioned in section 1.3, apart from the leading order diagram contribution, there is an infinite number of higher order processes including more vertices that result in the same final state. The leading order process represents the most important contribution, contributions of the higher order diagrams provide successive corrections to the total contribution. In this analysis, MC samples are provided with different levels of accuracy.

A complete description of MC generated simulation events can be found in [57, 58]. The SM Higgs Boson samples for the gluon-gluon fusion (ggH) process are produced at NLO accuracy in the strong coupling constant α_s using the POWHEG NNLOPS generator [59–69], with the PDF4LHC (NNLO) set of parton distribution functions (PDFs) [61]. Higgs boson production via vector-boson fusion (VBF), in association with a vector boson (VH) or in association with a top-quark pair ($\bar{t}tH$) is given at NLO precision with the POWHEG NNLOPS MC generator [59–69], with the PDF4LHC NLO set. The $gg \to ZH$ process is also simulated with the POWHEG MC generator, but only at LO accuracy. The production in association with a top quark (tH) and a bottom-quark pair ($\bar{b}bH$) is simulated at NLO accuracy using the MADGRAPH5_AMC@NLO generator [70,71] with the NNPDF30 PDF set [72]. The PYTHIA8 generator [74] is used for the $H \to ZZ \to 4l^{\pm}$ decay as well as for parton showering, hadronisation, and simulation of the underlying event. The Higgs boson production via the ggH, VBF and VH processes is simulated with different mass points, ranging between m_H = 123 and 127 GeV. The generation of different mass points is essential for modelling the signal m_{4l} distribution as a function of m_H in a model independent way, i.e. without assuming the exact Higgs mass. The least contributing processes tH and $\bar{t}tH$, or $\bar{b}bH$, are simulated assuming m_H = 125 GeV. These samples are normalised to cross-sections obtained from the most recent predictions provided by the LHC Higgs Working Group [75].

4.3.2 Background processes to $H \to ZZ \to 4l^{\pm}$ decay channels

There are a few other processes which can lead to the same final state as the signal events. The most prominent background for the $H \to ZZ \to 4l^{\pm}$ decay is the QCD-induced ZZ di-boson production. This process has the exact same topology and decay channels as the signal process, and is therefore often referred to as the *irreducible background*, i.e. it can not be distinguished and discriminated from signal events by means of a trivial event selection. Figure 4.4 shows the Feynman diagrams of leading ZZ di-boson production through $q\bar{q}$ annihilation and gg fusion, with $q\bar{q} \to ZZ$ the most dominant process. These processes are estimated using an MC simulation generated from SHERPA v2.2.2 [76–79] at NLO precision, with $q\bar{q} \to ZZ$ including electroweak corrections at NLO precision. Furthermore, very rare productions of triple vector bosons, namely ZZZ, WWZ and WZZ (or in short VVV), can also lead to four or more prompt leptons from these vector boson decays. Figure 4.5 shows the Feynman diagrams of such triple vector boson production. Their contribution is also estimated from MC simulation samples, also generated using SHERPA [76–79] at NLO accuracy. Similarly, top quark pair production associated with a Z boson in an all leptonic final state can lead to the same signal signature. Figure 4.6 shows the Feynman diagrams of $t\bar{t} + Z$ production through $q\bar{q}$ and gg interactions. This last process is simulated using MADGRAPH5_AMC@NLO [70,71] and PYTHIA8 [74].

The second category of background is composed of processes that do not necessarily contain only prompt leptons. As discussed in section 3.2 in the case electrons (which is also true for muons), the reconstruction and identification of leptons is not infallible against the various background sources for non-prompt and misidentified leptons. In section 3.4, it was shown that on top of Z boson prompt electrons,

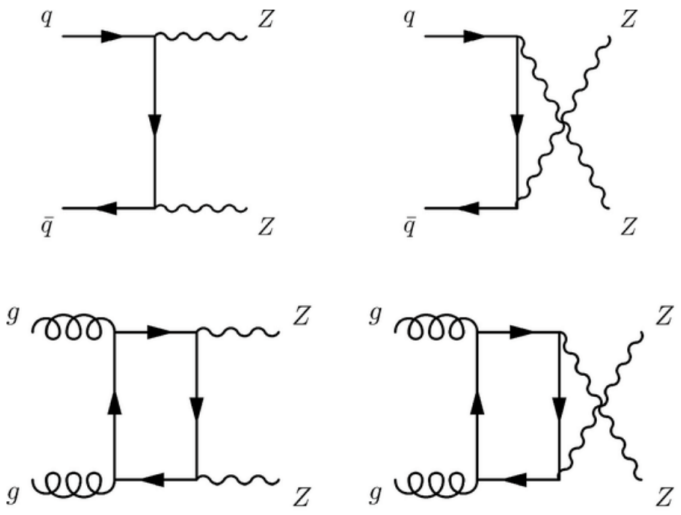

FIGURE 4.4: Feynman diagrams of ZZ di-boson production through $q\bar{q}$ annihilation and gg fusion. The u-channels are included since particles in the final state are identical.

hadronic jets from the Z+jets production could also be misidentified as electrons. In combination with the prompt Z electrons, these events can also appear as four lepton final states. Similarly, $t\bar{t}$ and WZ di-boson production can lead to the same effect. This category is referred to as the *reducible background*. Z+jets MC samples are simulated with SHERPA [76–79] at NLO for a number of jets $n_{jets} \in [0, 2]$ and at LO for $n_{jets} \in [3, 4]$ per event. $t\bar{t}$ and WZ di-boson production are simulated using POWHEG-BOX_V2 [63–65].

Finally, the ATLAS detector response is simulated by the GEANT4 framework [80] and reconstructed in the same way as collision data. Additional proton-proton interactions in the same and nearby bunch crossings are included in the simulation to take into account the pile-up contribution. These events are generated using the PYTHIA8 generator [74] and the NNPDF2.3LO PDF set [81].

4.4 Selection and categorisation of Higgs boson candidate events

As explained in section 2.3.2, among all recorded events, one has to select those having the characteristics corresponding to the topology of the desired signal process to be measured. For the selection of $H \to ZZ \to 4l^{\pm}$ events, requirements on

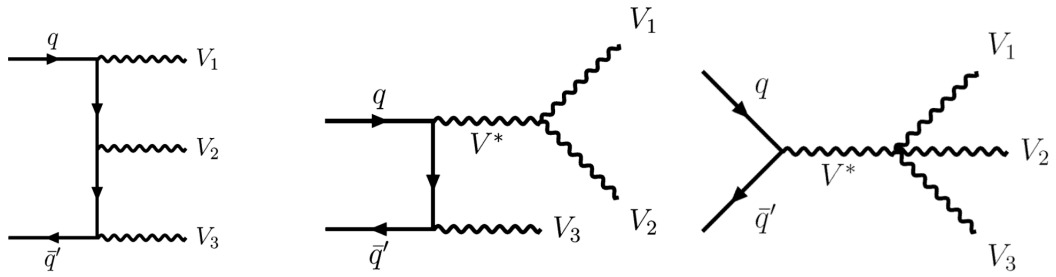

FIGURE 4.5: Feynman diagrams of triple vector boson production through $q\bar{q}$ interactions, including diagrams with triple and quartic vertices.

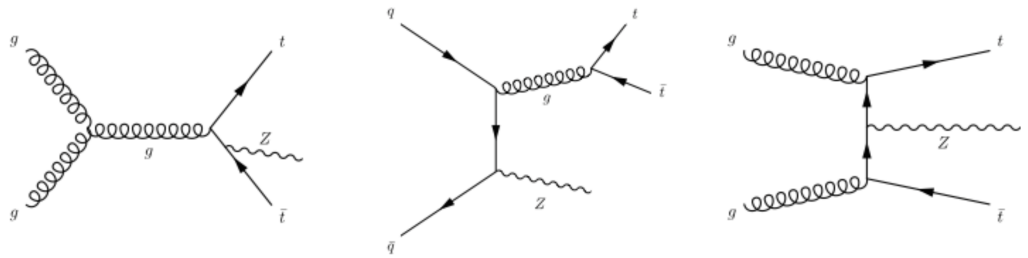

FIGURE 4.6: Feynman diagrams of $t\bar{t} + Z$ production through $q\bar{q}$ and gg interactions.

the reconstructed physics objects (electrons, muons and hadronic jets) and the event properties are discussed in next sub-sections.

4.4.1 Vertex requirements

The first requirement on event-level concerns the reconstruction of vertices; only those reconstructed from ID tracks with $p_T > 0.4$ GeV are considered. Events must have at least one vertex with at least three associated tracks. The vertex with the highest sum of the track p_T squared ($\sum p_T^2$) is chosen as the primary vertex. In the $H \to ZZ \to 4l^{\pm}$ decay, the four leptons are required to appear from the primary vertex as they are expected to emerge from the interaction point (The Higgs and Z boson decay almost instantaneously after creation, $\tau_H \sim 10^{-22}$ s and $\tau_Z \sim 10^{-25}$ s [83]). Therefore, their tracks are required to be within a distance of $|z_0 \cdot \sin(\theta)| < 0.5$ mm from the primary vertex, with z_0 the longitudinal impact parameter. In the case of tracks from muons, an additional cut on the transverse impact parameter is applied ($d_0 < 1$ mm) to maximise the rejection of cosmic backgrounds. Figure 4.7 shows a scheme visualising the definitions of the impact parameters.

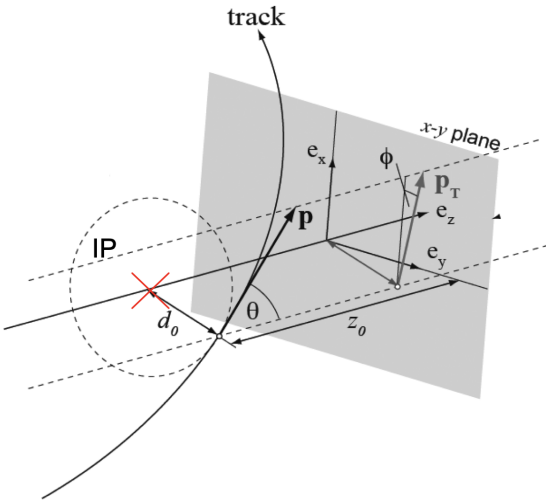

FIGURE 4.7: Scheme showing the definition of the longitudinal and transverse impact parameters, z_0 and d_0 of a reconstructed track [115].

4.4.2 Electron requirements

The electron reconstruction and identification requirements are analogous to those described in sections 3.1 and 3.2. For this specific analysis, the loose identification menu is used, which in combination with the track hit requirements results in a total efficiency of reconstruction and identification of approximately 95%. On top of the conditions already discussed, electrons are required to have $E_T > 7$ GeV, $|\eta| < 2.47$ and an impact parameter significance $|d_0/\sigma_{d_0}| < 5$.

4.4.3 Muon requirements

Muon reconstruction in ATLAS is performed using the Muon Spectrometer (MS) and the ID. Measurements from these sub-detectors are then combined in order to find muon tracks suitable to be used as physics objects. The reconstruction of muons within the ID scope ($|\eta| < 2.7$) are mainly reconstructed from a global fit of tracks from both sub-detectors. These are referred to as *combined muons*. The MS in the central region ($|\eta| < 0.1$) lacks in coverage due to cabling and services for the ID and the calorimeters. In this region, muons are identified by matching an ID track to segments of tracks in the MS or energy deposits in the calorimeters corresponding to a minimal ionisation, as muons have a small energy loss in calorimeters. The former muons are referred to as *segment-tagged muons*, and the latter *calorimeter-tagged muons*. Consequently, kinematics of these muons are fully determined from ID tracks. Finally, beyond the ID coverage ($2.5 < |\eta| < 2.7$), muons can be reconstructed from MS tracks having hits in all MS layers (*stand-alone muons*), and if any, combined with tracklets[2] in the ID (*silicon-associated forward muons*). A fully detailed description of the muon reconstruction and identification can be found in [82]. For the $H \to ZZ \to 4l^{\pm}$ analysis, combined muons are favoured while allowing at most one muon from the other types per event. Every muon is required to pass the loose identification and have a $p_T > 5$ GeV, except for calorimeter-tagged muons which are required to have a $p_T > 15$ GeV and $|\eta| < 0.1$. Also, an impact parameter significance $|d_0/\sigma_{d_0}| < 3$ is required to reject heavy-flavour decays.

4.4.4 Hadronic jet requirements

Although jets are not part of the selected physics objects for the mass measurement, they represent a significant background for electrons as discussed in section 3.4. Therefore, the overlap of these objects with electrons and muons are considered (see next section). Following the definition from section 3.4.1.1, jets are required to pass the pile-up rejection and must have a $p_T > 30$ GeV and $|\eta| < 4.5$.

4.4.5 Overlap removal requirements

Jets reconstructed according to section 3.4.1.1, electrons and muons can be reconstructed from same tracks and/or energy deposits. It is therefore necessary to make a decision to solve the ambiguity. In the case where muons and electrons are reconstructed from the same ID tracks, the electron is always rejected, except in the case of calorimeter-tagged muons, where these are rejected instead. Jets overlapping within $\Delta R < 0.2$ of an electron or $\Delta R < 0.1$ of a muon are removed.

[2] A shorter form of a track.

4.4.6 Trigger requirements

As mentioned in section 2.4.7, not all events are worth analysing. Therefore a set of triggers are configured to select events with potential interesting physics features. In this analysis, a set of lepton triggers are defined in order to preselect $H \to ZZ \to 4l^{\pm}$ event candidates, namely single-lepton, di-lepton and tri-lepton triggers. These triggers have a p_T threshold which is variable through the different periods of data-taking; the threshold increases with the years and peak luminosity. Table B.1-B.4 in Appendix B summarises the used triggers and their corresponding thresholds given the lepton type and the year of data-taking. In the case where more than one trigger is listed, the *or-statement* is intended. The higher threshold triggers complement the lower ones while having a looser lepton selection criteria. In MC studies using signal samples at m_H = 125 GeV, a combined efficiency of these triggers is found to be approximately 98%, 99%, 97%, and 99% for respectively the 4μ, $2\mu 2e$, $2e2\mu$, and $4e$ final states.

4.4.7 Quadruplet selection

Having the physics objects passing the previous requirements, the next step is to form a so-called *lepton quadruplet*. First of all, leptons are required to originate from one common vertex; the ID tracks are used in a vertex fit [57], where the value of the goodness of fit χ^2/N_{dof} is required to be smaller than 5 for the 4μ channel, and 9 for channels including electrons to take into account the inferior resolution of electron tracks. Per event, two pairs of the same lepton flavour are required, with each pair having a positive and a negatively charged lepton. As mentioned in section 1.4, if the produced Higgs boson is on-mass shell (assuming m_H = 125 GeV), typically one of the Z bosons from the $H \to ZZ$ decay is off-mass shell to satisfy $m_H \geqslant 2m_i$, with m_i the mass of the identical particles it decays to. This fact implies that leptons from the two Z bosons (the on-shell and off-shell) have different properties; those produced from the on-shell Z boson decay are expected to have a higher momentum than those from the off-shell decay. For this reason, the four leptons are classified according to their p_T. The three consecutive leading leptons in p_T are required respectively to have $p_{T,1} > 20$ GeV, $p_{T,2} > 15$ GeV and $p_{T,3} > 10$ GeV. The same lepton flavour opposite charge sign (SFOS) pair with the closest invariant mass to that of the Z boson, m_Z = 91.1876 GeV, is tagged as the *leading lepton pair* from the on-shell Z boson. Its invariant mass is required to lie within $m_{12} \in [50, 106]$ GeV to ensure the leptons originate from the Z boson decay. The second pair is referred to as the *sub-leading lepton pair*, which is more likely to originate from the off-shell Z^* boson[3]. Its invariant mass m_{34} is required to be within $m_{min} < m_{34} < 115$ GeV, where $m_{min} = 12GeV$ for $m_{4l} < 140$ GeV, raising linearly to 50 GeV for $m_{4l} = 190$ GeV and remaining $m_{min} = 50GeV$ for $m_{4l} > 190$ GeV. This discrimination based on the invariant mass of the lepton pair distinguishes between the $2e2\mu$ and $2\mu 2e$ final states, where the

[3]The star "*" is used to indicate a virtual off-mass shell particle.

first mentioned pair represents the leading one. In the case of the $4e$ and 4μ, an additional cut is defined on the alternative pairs (i.e. SFOS pairs formed otherwise than previously described) of 5 GeV on their invariant mass, to reject leptonic decays from J/ψ ($m_{J/\psi}$ = 3.0969 GeV). Furthermore, the angular separation ΔR between two lepton pairs should be higher than 0.1 if the two pairs are of the same lepton flavour, and 0.2 in the other case. As mentioned in section 3.2.1, leptons from prompt decays are characterised with a high isolation. A track based isolation variable was defined for electrons in eq. 3.9, which is also valid for muons but with a different cone size $\Delta R = 0.3$. Similarly, a calorimeter based isolation quantity can be defined as,

$$\Delta_{iso}^{calo} = \frac{\sum E_{T,i}}{E_{T,lep}}, \tag{4.1}$$

with the numerator representing the scalar E_T sum of calorimeter deposits around the lepton within a cone of $\Delta R = 0.2$ for electrons and 0.3 for muons, and the denominator the E_T of the lepton. For electrons, $\Delta_{iso}^{track} < 0.15$ and $\Delta_{iso}^{calo} < 0.20$ are required, while for muons $\Delta_{iso}^{track} < 0.15$ and $\Delta_{iso}^{calo} < 0.30$.

4.4.8 Quadruplets ambiguity solving

Events can contain more than one quadruplet satisfying the above requirements. For instance, in the VH production mode, the vector boson (Z or W) can decay to prompt electron(s) on top of those coming from the $H \to ZZ \to 4l^{\pm}$ decay. This can also be the case for the $t\bar{t}H$ production mode. Therefore, it is likely that a lepton not associated to the Higgs boson decay can be selected in the quadruplet. In the case where these are found within a channel, the quadruplets with the closest invariant mass of the leading and sub-leading pair to m_Z are favoured. From MC studies, the efficiency of selecting signal events is not equivalent among the four decay channels. For $4e$, 4μ, $2e2\mu$ and $2\mu2e$, the signal efficiency calculated similarly to eq. 3.3 is found to be respectively 31%, 21%, 17% and 16%. If multiple decay channels are found with quadruplets passing the criteria in the same event, the quadruplet with the highest efficiency is chosen. In this last case, if an additional lepton, satisfying the above object selection, is found, all quadruplet combinations are reconsidered. Following a method based on the matrix-element, where a generator is used to calculated this value for all combinations, the quadruplet with the highest matrix-element value is selected. MADGRAPH5_AMC@NLO [70,71] is used for the computation, where the value is calculated with LO accuracy. This method was studied and was found to increase the probability of selecting the correct quadruplet. Finally, the full $H \to ZZ \to 4l^{\pm}$ event selection is summarised in Table 4.1.

TABLE 4.1: Summary of the event selection requirements discussed in section 4.4. The leading and sub-leading lepton pairs are denoted as m_{12} and m_{34} respectively.

Physics Objects	
ELECTRONS	
Loose Likelihood quality electrons with hit in innermost layer, $E_T > 7$ GeV and $\|\eta\| < 2.47$	
Interaction point constraint: $\|z_0 \cdot \sin\theta\| < 0.5$ mm (if ID track is available)	
MUONS	
Loose identification with $p_T > 5$ GeV and $\|\eta\| < 2.7$	
Calo-tagged muons with $p_T > 15$ GeV and $\|\eta\| < 0.1$, segment-tagged muons with $\|\eta\| < 0.1$	
Stand-alone and silicon-associated forward restricted to the $2.5 < \|\eta\| < 2.7$ region	
Combined, stand-alone (with ID hits if available) and segment-tagged muons with $p_T > 5$ GeV	
Interaction point constraint: $\|d_0\| < 1$ mm and $\|z_0 \cdot \sin\theta\| < 0.5$ mm (if ID track is available)	
JETS	
anti-k_T jets with *bad-loose* identification, $p_T > 30$ GeV and $\|\eta\| < 4.5$	
OVERLAP REMOVAL	
Jets within $\Delta R < 0.2$ of an electron or $\Delta R < 0.1$ of a muon are removed	
VERTEX	
At least one collision vertex with at least two associated track	
PRIMARY VERTEX	
Vertex with the largest p_T sum	
Event Selection	
QUADRUPLET SELECTION	- Require at least one quadruplet of leptons consisting of two pairs of same-flavour opposite-charge leptons fulfilling the following requirements: - p_T thresholds for three leading leptons in the quadruplet: 20, 15 and 10 GeV - Maximum one calo-tagged or stand-alone muon or silicon-associated forward per quadruplet - Leading di-lepton mass requirement: $50 < m_{12} < 106$ GeV - Sub-leading di-lepton mass requirement: $m_{\text{threshold}} < m_{34} < 115$ GeV - $\Delta R(\ell, \ell') > 0.10$ for all leptons in the quadruplet - Remove quadruplet if alternative same-flavour opposite-charge di-lepton gives $m_{\ell\ell} < 5$ GeV - Keep all quadruplets passing the above selection
ISOLATION	- Contribution from the other leptons of the quadruplet is subtracted - Loose isolation working point for all leptons
IMPACT PARAMETER SIGNIFICANCE	- Apply impact parameter significance cut to all leptons of the quadruplet - For electrons: $d_0/\sigma_{d_0} < 5$ - For muons: $d_0/\sigma_{d_0} < 3$
BEST QUADRUPLET	- If more than one quadruplet has been selected, choose the quadruplet with the highest Higgs decay ME according to channel: 4μ, $2e2\mu$, $2\mu2e$ and $4e$
VERTEX SELECTION	- Require a common vertex for the leptons: - $\chi^2/\text{ndof} < 5$ for 4μ and < 9 for others decay channels

4.5 Background estimation for $H \to ZZ \to 4l^{\pm}$ events

From eq. 2.4, the number of expected events from a specific process, given the associated integrated luminosity of the dataset, can be estimated using the predicted (or previously measured) cross section of this process. Typically, MC simulated events are generated with a larger number of events compared to data, which has the advantage of reducing the statistical uncertainty. Consequently, a normalisation factor is calculated to be applied to the MC number of simulated events to scale it to the data luminosity, i.e. to obtain the number of expected events of this process in the corresponding dataset. This normalisation factor is given by,

$$\omega_{lumi} = \frac{\mathcal{L} \cdot \sigma_i \cdot \epsilon_s \cdot A}{N_i} \tag{4.2}$$

with N_i and σ_i the number of simulated events and the cross section of the process, A the expected kinematic acceptance of the signal, and ϵ_s the signal efficiency accounting for the rate of signal events passing the final selection. In general, searches consisting of a prediction which is compared to measured data are performed as a *blinded analyses*, i.e. the data is not revealed before the estimation is finalised. This is to avoid experimentalist bias, whereby the estimation is biased with prejudice following from prior knowledge on the data measurement. However, it is not necessary to blind all the data, for instance, one can unblind parts of the data where no measurements are performed, e.g. in kinematic regions where the data has been already analysed in previous measurements. These regions are often characterised by the absence of the signal process and are referred to as *control regions* (CRs). They are obtained by altering the signal event selection and/or object requirements, making them orthogonal to the *signal region* (SR) where the signal is expected to be measured. CRs can be very useful for extracting normalisation and extrapolation factors to be used in the SR, but also to perform closure tests and checks to validate assumptions.

4.5.1 Irreducible background estimation

As discussed in section 4.3.2, the irreducible background contains at least four prompt electrons from vector boson decays, which can be well estimated using MC. All irreducible background sources are fully estimated and normalised according to eq. 4.2, except the dominant ZZ background, where the normalisation is obtained from scaling MC to data in mass ranges where no signal is expected, namely for events with quadruplets having $m_{4l} < 115$ GeV and $m_{4l} > 130$ GeV. These mass regions are referred to as the side-band CRs which are dominated by the ZZ *continuum background*. This approach has the benefit of being independent of theoretical uncertainties of the ZZ background cross section and systematic uncertainties on the luminosity.

4.5.2 Reducible background estimation

For the reducible background, MC predictions are less reliable due to the presence of fake and non-isolated reconstructed leptons, which are in fact difficult to simulate with accuracy. Consequently, the agreement between the measured data and MC is relatively poor, as was the case for the background rejection study in section 3.4. Therefore, data-driven methods are exploited in order to extract the contribution of these backgrounds. In the case of the reducible background, CRs are defined in order to estimate the contribution of the various background sources to electrons and muons, which is then extrapolated to the SR using transfer factors. The estimation of non-pompt and fake reconstructed electrons and muons is treated separately in dedicated CRs.

4.5.2.1 Muon background estimation

In the case of muons, heavy-flavour decays including non-prompt muons are the main source of background, in contrast with electrons. There are four CRs defined by modifying the signal selection 4.4, with each CR enriched in a specific background source. A heavy-flavour background enhanced CR is obtained by inverting the d_0-significance requirement on at least one of the sub-leading leptons without the isolation cut, and by removing the vertex requirement on the quadruplet. This CR is dominated by leptons from heavy-flavour decays that are displaced and non-isolated. The second CR is enriched in $t\bar{t}$, which is obtained by altering the SFOS requirement to opposite charged different flavour leading lepton pair ($e\mu + ll$), as each top quark can decay to any lepton flavour independently from the other. Consequently, the CR is free from leading Z boson SFOS pairs, and is dominated by $t\bar{t}$ leptons. Analogously to the previous CR, the vertex requirement is dropped, and the d_0-significance and isolation cuts are not applied on the sub-leading pair. The third CR is constructed to enhance the light-flavour background, where the standard selection is applied, except the isolation requirement on the sub-leading pair is altered. Finally a last CR is defined where all backgrounds have a significant contribution. In this CR, the sub-leading pair is required to have same charged leptons, with no isolation or d_0-significance requirements. The CRs are respectively referred to as *inverted-d_0 CR*, *$e\mu + ll$ CR*, *inverted-isolation CR and the same-sign CR*.

The estimation of background muons is obtained from a global fit method used across the CRs to fit data with MC templates, where the estimated contribution of the various backgrounds is fitted using analytic functions in the invariant mass spectrum of the leading lepton pair, m_{12}. From this method the normalisation of each background component is obtained from data, which can be extrapolated to the SR. In the following paper [57], a detailed study on the background estimation for the $H \to ZZ \to 4l^{\pm}$ analysis is presented. This thesis is based on the same event selection and background estimation. Figure 4.8 shows the m_{12} distributions for data and

MC simulated events for different processes for the CRs used in the fit; (a) shows the inverted-d_0 CR, (b) inverted-isolation CR, (c) $e\mu + ll$ CR, and (d) the same-sign CR. The different CRs show clearly the enhancement in the various background components and the necessity for a data-driven procedure to correct for the observed mismodelling.

4.5.2.2 Electron background estimation

The same electron backgrounds discussed in section 3.1 and 3.2 are relevant for the electron background estimation in the $H \to ZZ \to 4l^{\pm}$ analysis. These are mainly misidentified light-flavour jets, which is the most dominant background for prompt electrons, followed by photon conversions and non-prompt electrons from heavy-flavour decays. The latter background is small enough to be estimated from MC. Using the number of hits in the innermost layers of the pixel detector in the ID, n_{pixel}, the light-flavour background can be discriminated from conversions background, as

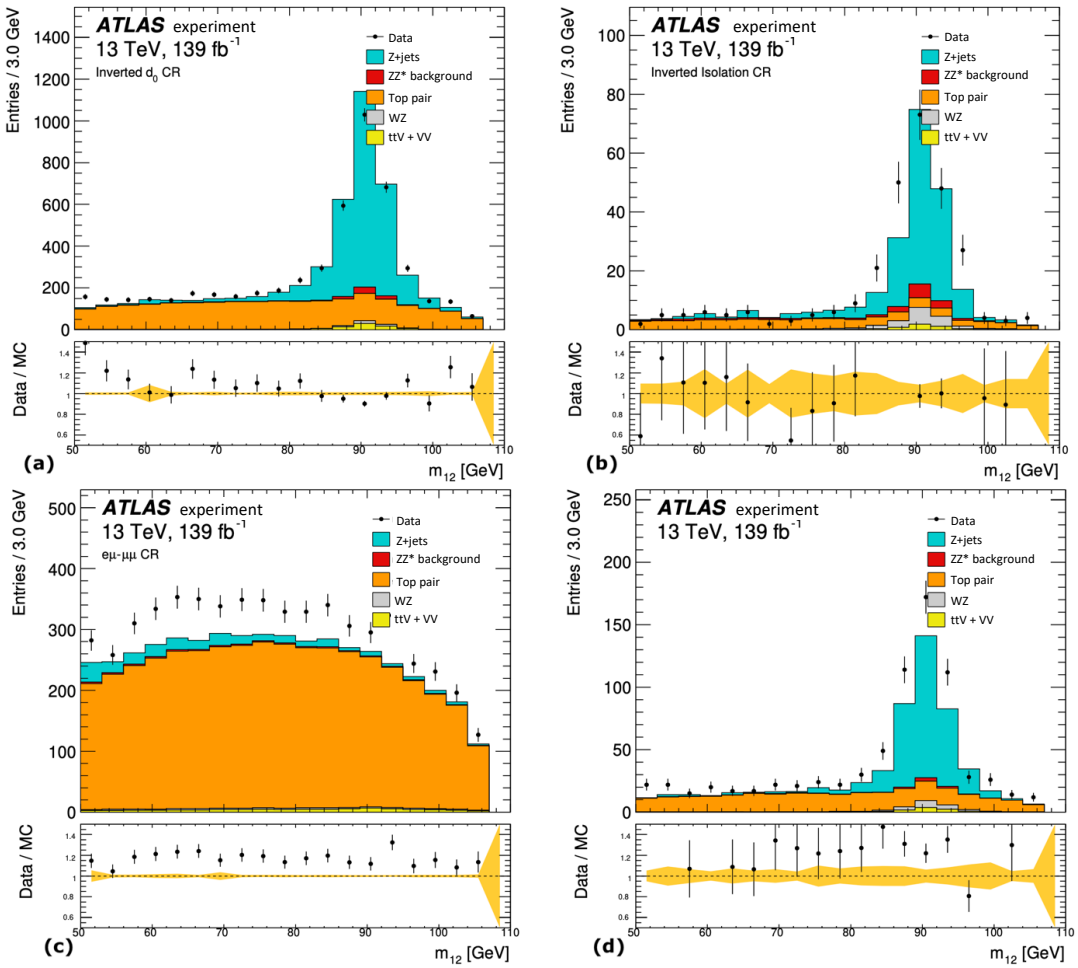

FIGURE 4.8: The data/MC m_{12} distributions for different processes in the four control regions (defined in section 4.5.2.1) used in the simultaneous fit.

photons often traverse the pixel detector before decaying to produce a pair of electrons, which are not detected by the innermost layers of the ID ($n_{pixel} = 0$). Similarly to the muon background case, the electron background estimation is extracted from a background enriched CR, referred to as the $3l + X$ CR. This CR is constructed by relaxing the selection and identification requirements on the sub-leading pair lepton with the lowest p_T value (X). Only those requirements related to the track and d_0-significance are kept. Also, by requiring that this lepton has the same charge sign as its associated lepton, the veto of signal events is guaranteed. More than one quadruplet is accepted in this CR, even those sharing the same leading pair. Although this last requirement suppresses the ZZ background, about 10% remains in the $3l + X$ CR, which is due to the fact that prompt electrons from ZZ can be missed in the quadruplet selection and end up replaced by a fake electron.

A second CR is defined to complement the $3l + X$ CR, which is relatively limited in number of events. The $Z + X$ CR is obtained by selecting per event a pair of SFOS leptons satisfying the same requirements imposed on the leading pair of the quadruplets (excluding tri-lepton and e-μ trigger requirements). In addition, a third reconstructed electron X is selected having the same properties of the X electron from the $3l + X$ CR. Moreover, this X electron is required to be separated from the Z-pair with $\Delta R > 0.1$. This three lepton CR has the advantage of having an abundant sample of events. The distribution of n_{pixel} for events falling in the $3l + X$ CR is fitted to templates which characterise the light-flavour and photon conversions background in order to extract the yield of each component. As the $3l + X$ CR is reduced in statistics, the $Z + X$ CR is used to extract the these templates from MC, which are

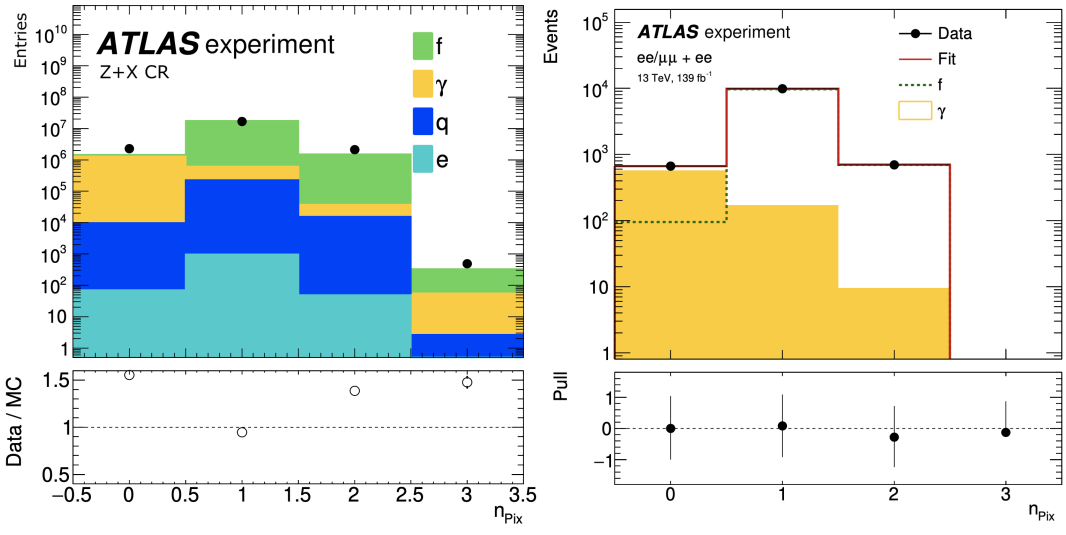

(A) (B)

FIGURE 4.9: Distribution of n_{pixel} in the $Z + X$ CR for data and MC before correction (A) and the fit results in the n_{pixel} distribution for the $3l + X$ CR (B). f represents the light-flavour, γ photons and q heavy-flavour background, while e stands for signal Z electrons.

corrected to match data. Using an unfolding tool, referred to as the *sPlot method* [57], the contribution of the light-flavour and photon conversions background in the fit to n_{pixel} to the data distribution is determined in terms of X electron p_T and the number of associated reconstructed jets. Furthermore, the efficiency of a background object to pass the signal electron selections is needed to extrapolate the fitted background yields in the $3l + X$ CR to the SR. These efficiencies are also extracted from the $Z + X$ CR, which are estimated as a function of the X p_T and the jet multiplicity in the corresponding event. Figure 4.9 (A) shows the distribution of n_{pixel} in the $Z + X$ CR for data and MC before correction. The contribution of the different background sources is shown in log-scale, with the light-flavour and photon conversions being the dominant backgrounds. Figure 4.9 (B) shows the fit results in the n_{pixel} distribution for the $3l + X$ CR. The final estimation of each background in the SR is obtained separately for the two components with the simple function,

$$N_{SR} = \sum_i s_i \sum_j \epsilon_{ij} \cdot N_{ij}, \tag{4.3}$$

where the index i runs over p_T bins and j over jet multiplicity bins, ϵ_{ij} the efficiency for a given background component in the latter bins, s the corresponding p_T scale factor from the MC templates and N_{ij} the weighted sum of number of events for each background component in the $3l + X$ CR derived from the *sPlot method*. More details on the methodology can be found in [57]. A short comparison study on the estimated reducible background electrons using two different MC generators is presented in Appendix B.2, with the purpose of testing the dependency on MC generators using different methods of simulating physics processes.

4.6 Techniques to improve the precision of the Higgs mass measurement

As previously mentioned, the observable used to determine the Higgs boson mass is the reconstructed four lepton invariant mass. It is therefore important to measure this quantity with high precision in order to increase the accuracy of the Higgs boson mass measurement. To improve the resolution of the reconstructed leptons, a few techniques are considered, which directly affect the uncertainty on the Higgs boson mass.

4.6.1 Final state radiation inclusion

Within the four lepton production from the intermediate Z boson pair of the Higgs boson decay, photons can be radiated by the charged leptons. This effect is referred to as *final-state radiation* (FSR). This photon would then carry a fraction of the lepton's momentum. Consequently, if the photon has a significant fraction, the invariant mass calculated from only the final state leptons would be underestimated, which

would degrade the resolution and cause the m_{4l} distribution to be shifted with respect to the true m_H distribution. Therefore, including these photons can improve the lepton resolution, hence the precision of the mass measurement. In ATLAS, photons are reconstructed in a very similar way to electrons, where their EM calorimeter energy cluster is either matched to a conversion vertex (*converted photons*) or not in the absence of any associated track or vertex (*unconverted photons*). More details about the photon reconstruction and identification can be found in [50].

In $H \to ZZ \to 4l^{\pm}$ analysis, a recovery algorithm [57] is used to include the FSR photons with the quadruplet leptons. There are two types; *collinear* and *distant FSR photons*. The former photons are found close to the lepton within $\Delta R < 0.15$, while the latter photons are found outside this angular separation. Per event, collinear FSR photons are only considered for muons from the leading lepton pair, since the electron reconstruction includes already such photons in the electron energy clusters. In the case of distant FSR photons, candidates are considered in all cases; for electrons and muons from leading and sub-leading lepton pairs. At most one FSR photon is included per quadruplet, where collinear photons are favoured. If two collinear FSR photons are measured, the one with the highest E_T is selected. If only distant FSR photons are reconstructed, one is included only if the leading lepton pair has an invariant mass $m_{12} < 81$ GeV and $m_{4l} > 190$ GeV. Also, tighter photon identification requirements are imposed in this case. Similar to collinear photons, the highest in E_T is always preferred. Furthermore, the threshold at which an FSR photon is considered is $E_T > 1.5$ GeV for collinear photons, and $E_T > 10$ GeV for distant ones. In both cases, if the associated invariant mass pair is larger than 100 GeV, the FSR photon is not included.

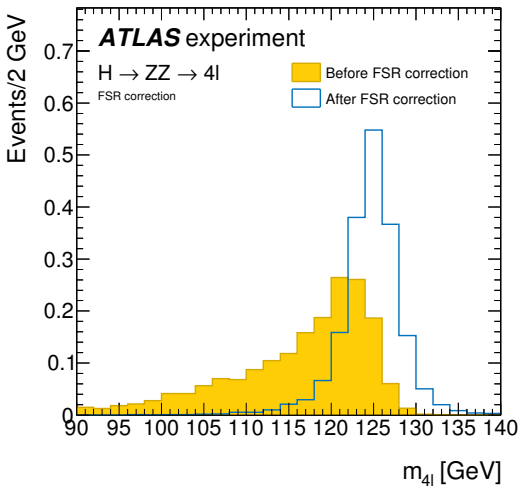

FIGURE 4.10: The m_{4l} signal MC distribtion before and after FSR correction. The comparison includes only events with identified FSR photons.

Figure 4.10 shows the distributions of Higgs signal MC before and after including the FSR photons. Only events including FSR leptons were selected for this comparison. From MC studies, about 4% of the total expected events in the signal region are affected by FSR. From the comparison, as expected before the FSR inclusion the m_{4l} distribution is smeared and shifted toward lower mass values from underestimating m_{4l}, while after FSR inclusion, the distribution is sharper and centred around the nominal mass value (m_H = 125 GeV). The FSR inclusion contributes up to 2% to the improvement on the Higgs mass measurement uncertainty.

4.6.2 Machine-learning based signal-background discrimination

As mentioned in section 4.2, the golden decay channels are characterised by a large signal over background ratio. This advantage can be accentuated using machine-learning techniques to further discriminate signal from the irreducible ZZ^* background, which is initially difficult to distinguish from signal events using a trivial event selection. Similarly to the likelihood discriminant for the electron identification (section 3.2.4), a signal-background discriminant D_{4l} is calculated by training a *deep feed-forward neural network* to classify signal- and background-like events based on kinematic variables associated to the quadruplet, in addition to a discriminant built from the ratio of the matrix elements of the Higgs decay $\mathscr{M}_{HZZ}$ and the irreducible ZZ background $\mathscr{M}_{ZZ^*}$ defined as,

$$K_{ZZ^*} = \ln\left(\frac{|\mathscr{M}_{HZZ}|^2}{|\mathscr{M}_{ZZ^*}|^2}\right), \tag{4.4}$$

with the matrix element values calculated using the MADGRAPH5_AMC@NLO [70, 71] at LO accuracy. This discriminant increases the signal-background separation. TENSORFLOW [94] and KERAS [93] are used for the deep learning. Lepton-based kinematic variables used in the training include the FSR recovery described in the previous section. Moreover, the training is performed separately for the same ($4e$ and 4μ) and opposite flavour pairs ($2\mu 2e$ and $2e2\mu$) decay channels. Figure 4.11 shows the signal and background distributions of variables used in the training for the same and different flavour pairs. The transverse momentum and the pseudorapidity of the four-lepton system, p_T^{4l} and η^{4l}, are compared for signal and ZZ background events, along with the K_{ZZ^*} discriminant. The ggH, VBF and VH signal samples and the $qqZZ$, $ggZZ$ and electroweak ZZ background samples are used for this comparison. To reduce dependency on m_H, signal events are taken from samples with different simulated mass points, as described in section 4.3.1. Figure 4.12 shows the distribution of the D_{4l} discriminant which provides a score on how likely a quadruplet originates from a Higgs or a background decay process. Also, the associated *receiver operating characteristic* (ROC) curve is shown in Figure 4.13, demonstrating background rejection versus signal efficiency. Based on MC studies,

using the neural network score as an additional discrimination between signal and background improves the precision of the m_H measurement with up to 2%.

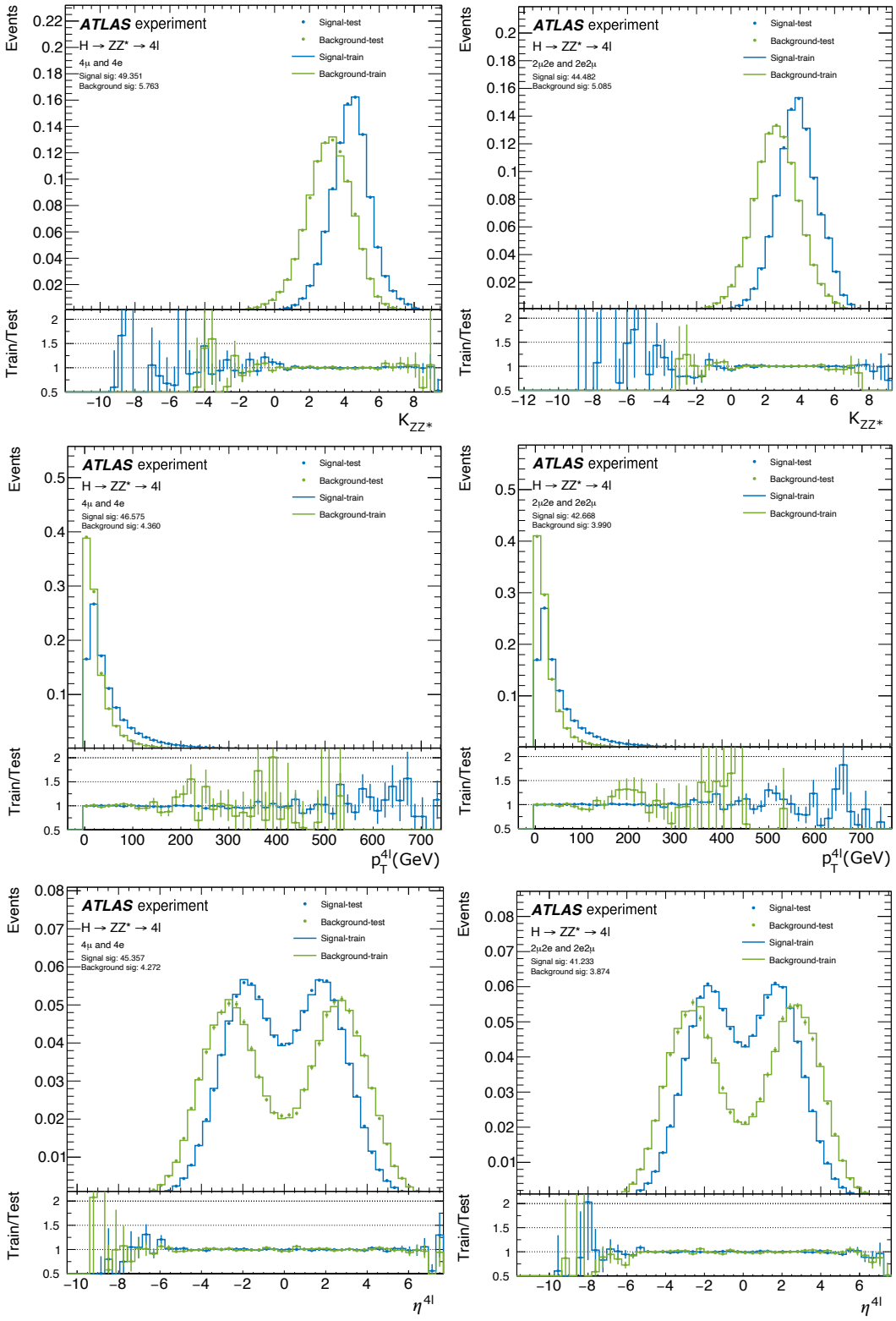

FIGURE 4.11: The input training variables for the same-flavour (4μ and $4e$) and different-flavour ($2\mu 2e$ and $2e2\mu$) D_{4l} training. The distribution of the corresponding variables in the training and testing samples are shown.

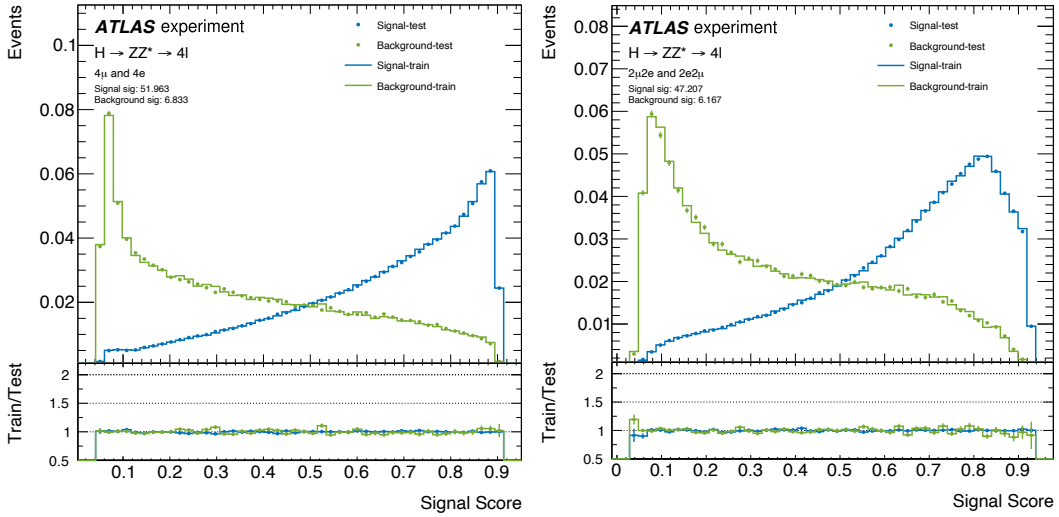

FIGURE 4.12: The neural network score shown for signal and background in the same-flavour (4μ and $4e$) and different-flavour ($2\mu 2e$ and $2e2\mu$) final states. The distributions in training and testing samples are shown.

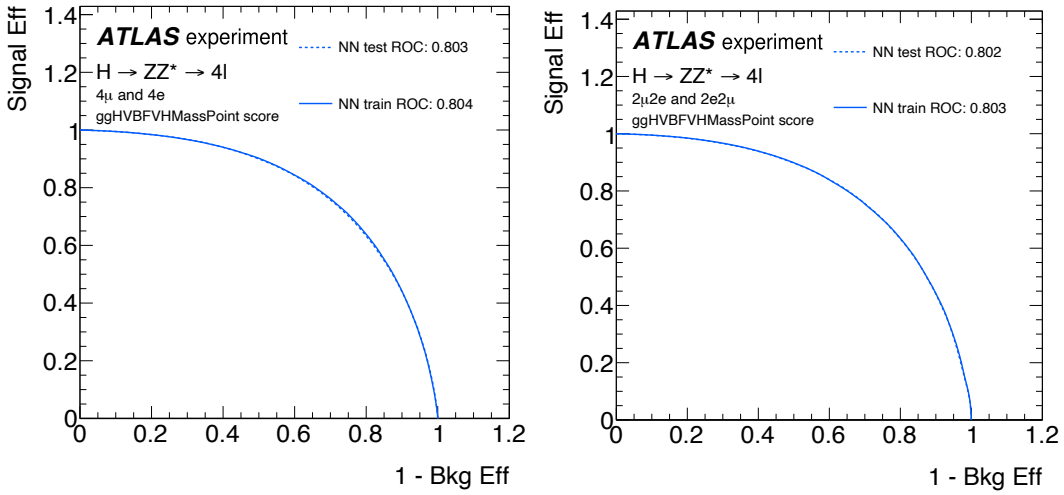

FIGURE 4.13: The ROC for the same-flavour (4μ and $4e$) and different-flavour ($2\mu 2e$ and $2e2\mu$) final states.

4.6.3 The leading lepton pair invariant mass constraint fit

As stated before, in the $H \to ZZ^*$ decay, typically one of the Z bosons is on-mass shell while the other is off-mass shell. Consequently, the pair of leptons produced from this on-shell Z boson are more likely to have higher momenta compared to the off-shell pair, and their invariant mass is expected to be closer to m_Z. In fact, knowledge about the characteristics of the Z boson can be used to improve the resolution of the measured leptons, which has a direct impact on the uncertainty of the m_{4l} measurement.

The Z boson was very well measured by Large Electron-Positron Collider (LEP) [101] before the LHC was build, which was also known as the *Z boson factory*. As mentioned in section 1.4, unlike the Higgs boson, the Z boson has a significant natural width. Consequently, m_{4l} is limited by the Z boson's intrinsic parameters. Its mass and width were measured in the di-lepton decay channels at LEP to be $m_Z = 91.1876$ GeV and $\Gamma_Z = 2.4952$ GeV, with uncertainties of the order 10^{-3} GeV [102]. These measurements determine the mass distribution of the Z boson, which follows a *Relativistic Breit-Wigner* (BW) [103] centred at m_Z with width Γ_Z, also known as the *Z lineshape*. Invariant mass values around the peak are associated to an on-mass shell Z boson production, while toward the tails to an off-mass shell production. From this PDF, one can obtain a prediction of the masses at which Z bosons are produced in di-lepton events, which can be used to constrain the resolution of these leptons. For the $H \to ZZ \to 4l^{\pm}$ mass measurement, this constraint is performed in a kinematic fit on the leading lepton pair, which is expected to originate from an on-shell production.

The exact mass of a generated Z boson decaying to a pair of leptons can be written as,

$$(m^{gen}_{l_1 l_2})^2 = (p^{gen}_{l_1} + p^{gen}_{l_2})^2, \tag{4.5}$$

with $p^{gen}_{l_1}$ and $p^{gen}_{l_1}$ the four-momenta of the associated leptons. $m^{gen}_{l_1 l_2}$ can be interpreted as a random variable distributed as,

$$m^{gen}_{l_1 l_2} \sim BW(m_Z, \Gamma_Z). \tag{4.6}$$

Considering the reconstructed quantities, the lepton momenta resolution has to be taken in account, and thus the reconstructed invariant mass $m^{reco}_{l_1 l_2}$ is not simply distributed as the Z lineshape. Figure 4.14 shows the $m^{gen}_{l_1 l_2}$ versus $m^{reco}_{l_1 l_2}$ distribution of the leading lepton pair from a ggH MC simulation of a Higgs boson $H \to ZZ \to 4l^{\pm}$ decay. It is clear that the $m^{reco}_{l_1 l_2}$ distribution is smeared compared to $m^{gen}_{l_1 l_2}$, which is expected from reconstruction resolution effects. Using the Z lineshape governing $m^{gen}_{l_1 l_2}$, one can reduce these resolution effects by maximising the following likelihood,

$$P(m^{gen}_{l_1 l_2} | m^{reco}_{l_1 l_2}, \sigma_{m^{reco}_{l_1 l_2}}). \tag{4.7}$$

In other words, given the reconstructed invariant mass and its resolution, the aim is to find the most likely true mass $m_{l_1l_2}^{constrained}$ which maximises the likelihood eq. 4.7. Thus, $m_{l_1l_2}^{constrained}$ is the best estimate of $m_{l_1l_2}^{gen}$. Using *Bayes theorem* of conditional probabilities, it can be shown that the likelihood eq. 4.7 is proportional to,

$$P(m_{l_1l_2}^{gen}|m_{l_1l_2}^{reco},\sigma_{m_{l_1l_2}^{reco}}) \sim P(m_{l_1l_2}^{reco}|m_{l_1l_2}^{gen},\sigma_{m_{l_1l_2}^{reco}}) \cdot P(m_{l_1l_2}^{gen}), \tag{4.8}$$

where,

$$P(m_{l_1l_2}^{gen}) = BW(m_{l_1l_2}^{gen}|m_Z,\Gamma_Z). \tag{4.9}$$

Although the fit is intended to improve the resolution of the invariant mass of the leading lepton pair, a kinematic constraint is applied on the momenta of the leptons, which is equivalent given eq. 4.5. Constraining the momenta instead of the invariant mass has the advantage of indirectly constraining $m_{l_1l_2}^{reco}$ as well as m_{4l}^{reco}, with the latter quantity being the objective for improving the Higgs boson mass measurement. Per leading lepton pair, the algorithm takes as input the momenta and the associated uncertainties, performs a kinematic fit assuming a Gaussian distributed resolution for the momenta uncertainties, then returns the corrected momenta which correspond to the most likely true Z mass $m_{l_1l_2}^{constrained}$. This procedure is referred to as the *Z mass constraint* (ZMC). Figure 4.14 shows a comparison between the constrained invariant mass of the leading lepton pair $m_{l_1l_2}^{constrained}$ and the unconstrained invariant mass $m_{l_1l_2}^{unconstrained}(=m_{l_1l_2}^{reco})$ in the di-muon channel as an example. The former distribution is significantly narrower than the latter, a consequence of the ZMC which moves $m_{l_1l_2}^{reco}$ closer to the Z peak. It should be noted that $m_{l_1l_2}^{constrained}$ is not distributed as a BW, since it is significantly dependent on the reconstructed kinematics and their uncertainties. This is in fact not an issue, since the aim is not to measure the Z boson

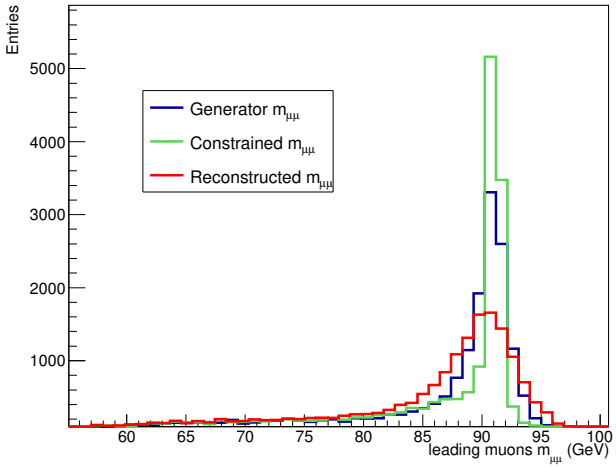

FIGURE 4.14: The exact generator-level versus the reconstructed invariant mass distribution of the leading lepton pair from a Higgs boson decay. Also the constrained invariant mass is compared to the former distributions.

mass distribution, the ZMC is only used as a tool to improve the momentum resolution of leptons and consequently the mass resolution of the Higgs boson while using known properties of the intermediate Z boson resonance.

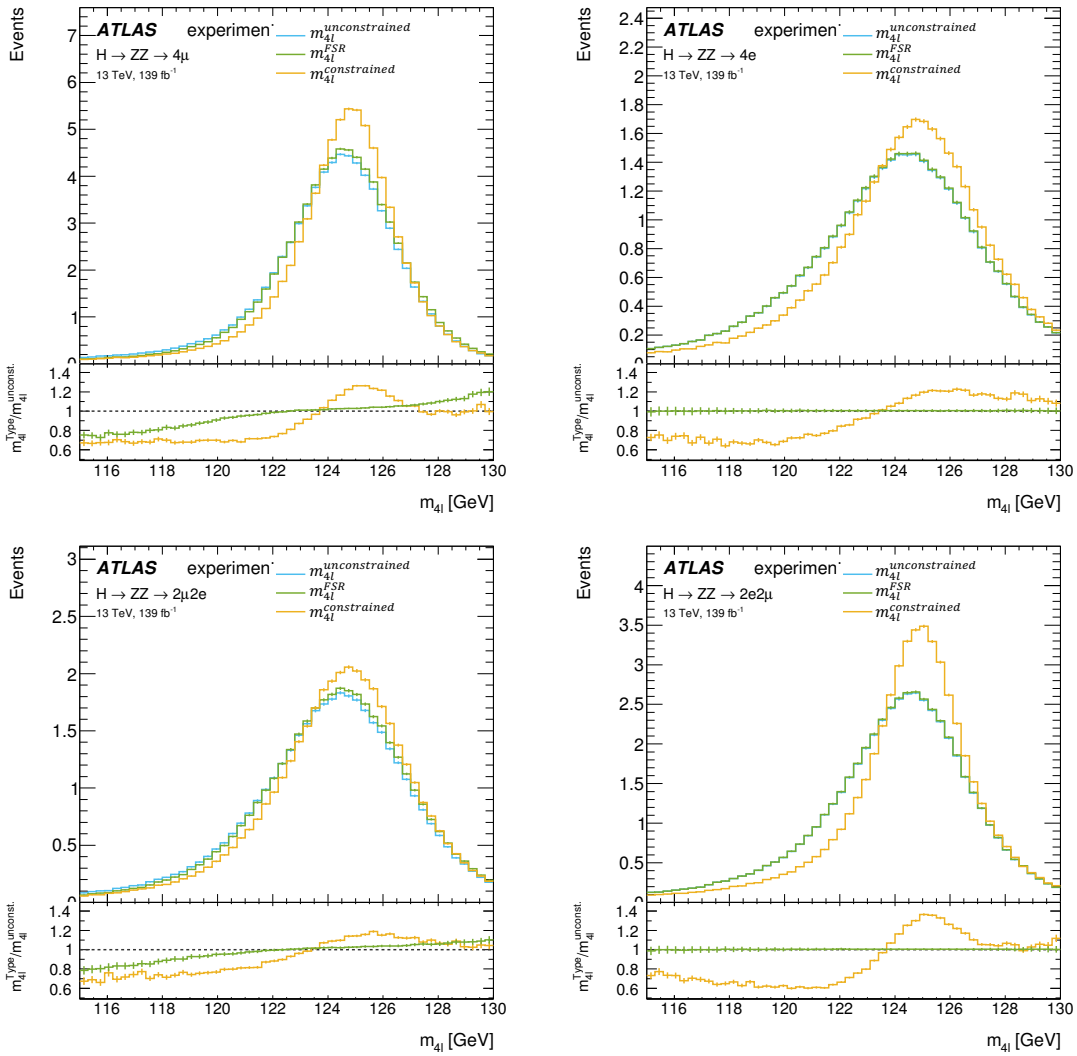

FIGURE 4.15: The impact of recovering additional FSR and applying the ZMC in addition to FSR recovery is shown for the 4μ (top left), $4e$ (top right), $2\mu 2e$ (bottom left), and $2e2\mu$ (bottom right) final states.

Figure 4.15 shows the impact of the ZMC on m_{4l} across the four decay channels. The ZMC is always applied after including FSR correction, if any. Therefore, three versions of m_{4l} are compared, showing the improvement in the resolution after each correction which is translated as a reduction in the distribution width. In the following sections, unless otherwise stated, m_{4l} refers to $m_{4l}^{constrained}$ including the FSR and ZMC correction.

4.7 Data/MC disagreement after ZMC

Among all attempts to improve the Higgs boson mass resolution, the ZMC method has the most significant impact, with up to 19% reduction on the m_{4l} uncertainty. However, using the Run-2 data (139 fb^{-1}) for preliminary results, a significant disagreement was observed between the data and MC distributions of the leading lepton pair invariant mass after applying the ZMC. Moreover, this mismodelling was only found in decay channels involving muons in the leading pair, i.e. 4μ and 2μ2e. Using the $Z + X$ CR (defined in section 4.5.2.2), which is initially used to estimate the fake electrons background using the X electron, the kinematics of the leading lepton pair are investigated. As mentioned before, the $Z + X$ CR has the advantage of having an abundant sample of events, with over 2×10^7 events.

4.7.1 Origin of the data/MC disagreement after ZMC

Figure 4.16 and 4.17 show the invariant mass of the leading lepton pair in data and MC before (A) and after (B) the constraint, for respectively di-electron and di-muon events. Only statistical uncertainties are considered, which are negligible given the large number of events. In the case of leading electron pairs, a good agreement is observed, before and after the constraint. This is clearly not the case for the leading muons, where after the constraint the agreement between data and MC shows a significant discrepancy. In other words, the ZMC is not operating equivalently in data and MC for di-muon events.

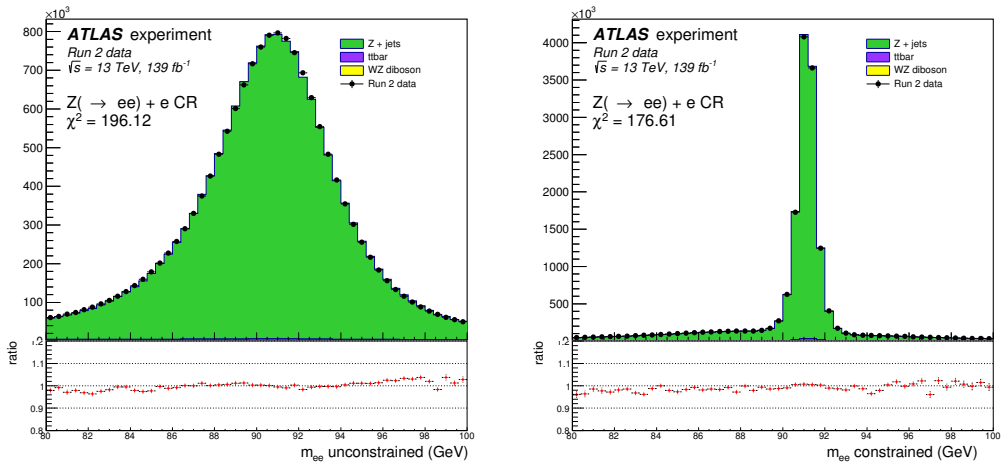

(A) (B)

FIGURE 4.16: The invariant mass spectrum of the leading electron pair before (left) and after (right) the Z-mass constraint

A first attempt to understand the reason behind this disagreement is done by comparing distributions of input variables to the ZMC in data and MC. Before the ZMC,

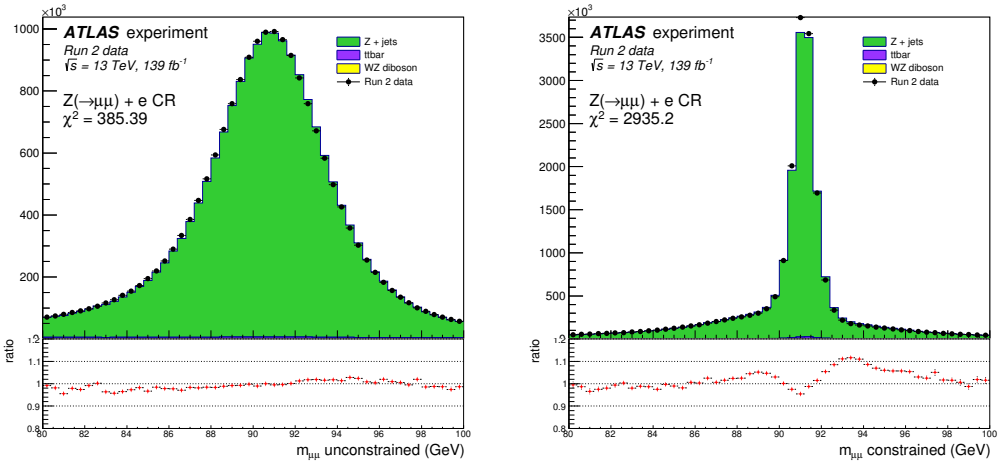

(A) (B)

FIGURE 4.17: The invariant mass spectrum of the leading muon pair before (left) and after (right) the Z-mass constraint

the invariant mass depends only on the kinematics of the leading muons,

$$m_{\mu_1\mu_2}^{unconstrained} = \sqrt{2p_{T,1}p_{T,2}(\cosh(\eta_1 - \eta_2) - \cos(\phi_1 - \phi_2))}, \tag{4.10}$$

while $m_{\mu_1\mu_2}^{constr.}$ is obtained from the ZMC kinematic fit, where the lepton uncertainties are also inputs. As mentioned in section 4.4.3, muons are reconstructed by fitting tracks from hits in the MS and/or the ID. Figure 4.7 can be visualised as a reconstructed muon track. Also, the different reconstructed parameters are indicated. The output parameters from the track fit are namely d_0, z_0, ϕ, θ, q/p and their associated uncertainties, with the last parameter being the charge over momentum ratio (definition of the other parameters can be found in the sections 2.4.1 and 4.4.1). The uncertainties of these parameters are given by the following covariance matrix,

$$Cov(d_0, z_0, \phi, \theta, q/p) = \begin{pmatrix} \sigma_{d_0}^2 & \sigma_{d_0}\sigma_{z_0} & \sigma_{d_0}\sigma_{\phi} & \sigma_{d_0}\sigma_{\theta} & \sigma_{d_0}\sigma_{q/p} \\ \sigma_{z_0}\sigma_{d_0} & \sigma_{z_0}^2 & \sigma_{z_0}\sigma_{\phi} & \sigma_{z_0}\sigma_{\theta} & \sigma_{z_0}\sigma_{q/p} \\ \sigma_{\phi}\sigma_{d_0} & \sigma_{\phi}\sigma_{z_0} & \sigma_{\phi}^2 & \sigma_{\phi}\sigma_{\theta} & \sigma_{\phi}\sigma_{q/p} \\ \sigma_{\theta}\sigma_{d_0} & \sigma_{\theta}\sigma_{z_0} & \sigma_{\theta}\sigma_{\phi} & \sigma_{\theta}^2 & \sigma_{\theta}\sigma_{q/p} \\ \sigma_{q/p}\sigma_{d_0} & \sigma_{q/p}\sigma_{z_0} & \sigma_{q/p}\sigma_{\phi} & \sigma_{q/p}\sigma_{\theta} & \sigma_{q/p}^2 \end{pmatrix} \tag{4.11}$$

Since before applying the ZMC, the $m_{\mu_1\mu_2}^{unconstr.}$ distributions in data and MC, which are calculated from only the kinematic variables (eq. 4.10), were in good agreement, this suggests that the disagreement in $m_{\mu_1\mu_2}^{constr.}$ after the ZMC application must come from the additional parameters used in the fit, i.e. the covariance matrix elements. In the ZMC, since the kinematic fit is applied on the lepton momenta, $\sigma_{q/p}$ represents the most important parameter for the constraint. Figure 4.18 shows the data/MC comparison of this latter parameter of the covariance matrix for each lepton of the

leading muon pair, where the two distributions are clearly incompatible. In Appendix B.3, Figures B.1 - B.2 show the same comparison of the other covariance matrix elements, where the same conclusion is valid.

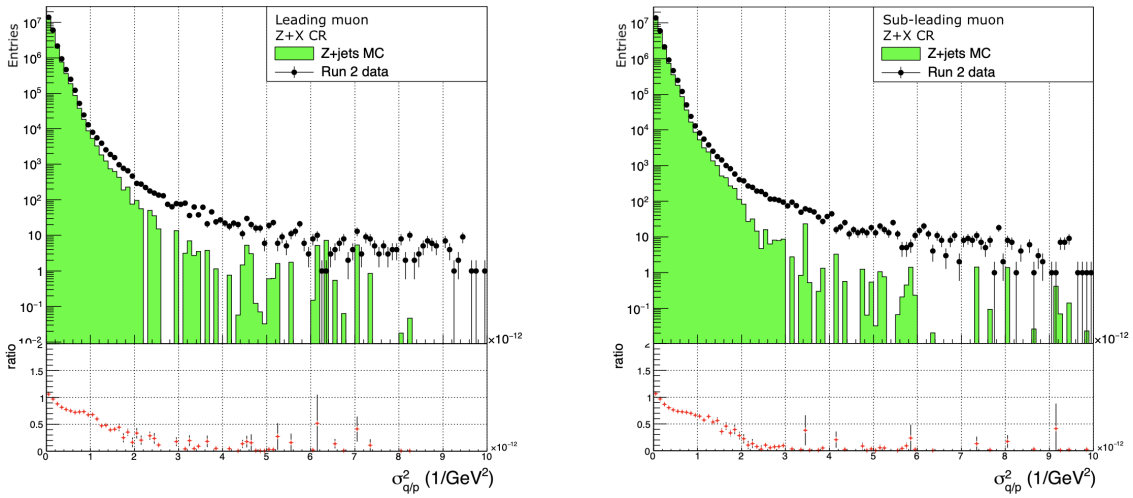

FIGURE 4.18: The $\sigma^2_{q/p}$ distributions of the leading (left) and sub-leading (right) muon in data and MC.

4.7.2 Track momentum uncertainty correction strategy

Similarly to track parameters, modelling track uncertainties in simulation is a difficult task. Therefore, it has to be corrected using data PDFs. As previously described in the case of electrons, muons in ATLAS are used in many physics analyses. For this reason, dedicated performance studies are performed for the reconstruction, calibration and identification of these physics objects. Muons included in this analysis have been calibrated in these muon performance studies to match data in events of the standard candles $Z \rightarrow \mu^-\mu^+$ for muons with $p_T > 10$ GeV and $J/\psi \rightarrow \mu^-\mu^+$ for muons with $5 < p_T < 20$ GeV. However, this calibration is not propagated to the covariance matrix including the muon uncertainties, which are clearly mismodelled as shown in Figures B.1-B.2. In the case of electrons, since the energy is measured in the EM calorimeter, the electron covariance matrix is not derived from the electron-track. Therefore, the energy resolution is used as the equivalent of $\sigma_{q/p}$ in muons to perform the ZMC. As opposed to $\sigma_{q/p}$, the electron energy resolution is well corrected to match data along with the energy scale [50]. This can be seen in Figure 4.19, were the data and MC distribution are in good agreement, and so there is no mismodelling after performing the ZMC (Figure 4.16 (B)). It is therefore necessary to derive corrections in the case of the muon $\sigma_{q/p}$, which is crucial for the data/MC agreement of the $m^{constr.}_{\mu_1\mu_2}$ spectrum calculated from the ZMC.

Typically, different parts of the ATLAS detector have different responses due to many factors, e.g. differences in the alignment and/or the quality of components.

Therefore, a correction of $\sigma_{q/p}$ in simulation to match data has to be performed per detector region, to avoid averaging the response of the different parts of the sub-detectors. For this reason, bins in η and ϕ are defined such that the bin edges are in line with the muon chamber boundaries of the MS, which are typically divided into sectors. Figure 4.20 shows a scheme of the ATLAS MS detector in the $x-y$ and $z-y$ plane. In the transverse plane, the different muon chambers defining the MS azimuthal sectors are shown (A). In the $z-y$ plane, the muon chambers are shown for the barrel ($|\eta| < 1.05$) and the endcap ($1.05 < |\eta| < 2.7$) regions, with the former shown in green, and the latter shown in blue. In these MS sectors, the $\sigma_{q/p}$ distribution is investigated in order to perform the correction per sector.

Furthermore, the track momentum uncertainty of muons with different momenta can vary significantly. Therefore, to minimise this dependency the correction is performed on the relative $\sigma_{q/p}$, i.e. $\sigma_{q/p}$ divided by q/p ($= \sigma^{rel.}_{q/p}$). This is necessary to avoid momentum biases; e.g. a muon with p_T = 30 GeV in MC should not be corrected as a muon with p_T = 90 GeV in data. However, $\sigma_{q/p}$ is not linearly dependent on q/p. Consequently, $\sigma^{rel.}_{q/p}$ retains a small dependency on the momentum. Therefore, additional p_T bins are defined where the momentum dependence is relatively constant over the $\sigma^{rel.}_{q/p}$ spectrum. Finally the correction is performed using only combined muons (muons obtained from a global refit of the ID and MS tracks), which outnumber other types of muons by far in this analysis, since combined muons are always favoured and at most only one from the other types is accepted in the quadruplet selection (section 4.4). In summary, the correction of the track momentum uncertainty is performed separately in bins of p_T, η and ϕ. The bin boundaries

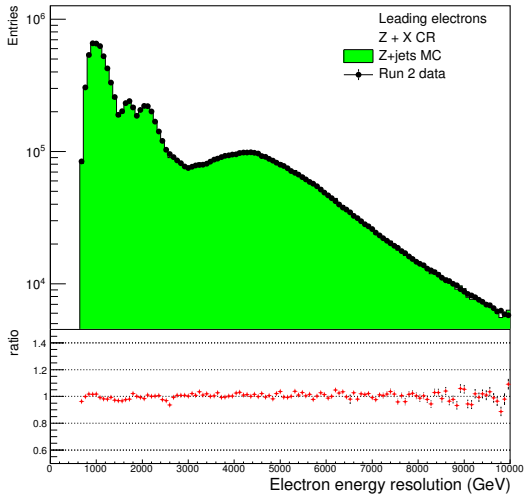

FIGURE 4.19: The leading electrons resolution distribution in data and MC.

are defined as follows:

$$p_T = \{10, 25, 35, 40, 45, 50, 60, 100, 300\} \text{ GeV}, \tag{4.12}$$

$$|\eta| = \{0, 0.4, 0.8, 1.05, 1.15, 1.25, 1.5, 1.7, 2.0, 2.1, 2.3, 2.5, 2.6\}. \tag{4.13}$$

In the barrel region, $|\eta| < 1.05$, the large sector boundaries are:

$$(-0.180 + k \times 0.785 < \phi < 0.180 + k \times 0.785) \vee (\phi > 2.960 \wedge \phi < -2.960), \tag{4.14}$$

for k an integer within [-3, 3][4], and the small sector boundaries are:

$$0.180 + k \times 0.785 < \phi < 0.605 + k \times 0.785, \tag{4.15}$$

for $k \in$ [-4, 3]. In the endcap region, $1.05 < |\eta| < 2.7$, the large sector boundaries are:

$$(-0.131 + k \times 0.784 < \phi < 0.131 + k \times 0.784) \vee (\phi > 3.011 \wedge \phi < -3.011), \tag{4.16}$$

for $k \in$ [-3, 3], and the small sector boundaries are:

$$0.131 + k \times 0.784 < \phi < 0.655 + k \times 0.784, \tag{4.17}$$

for $k \in$ [-4, 3]. In total, 3024 $p_T \times \eta \times \phi$ bins are defined for the $\sigma^{rel.}_{q/p}$ correction.

Figure 4.21 and 4.22 show the data/MC comparison of the $\sigma^{rel.}_{q/p}$ distributions of the

[4]The symbols $\wedge$ and $\vee$ denote respectively the logic operators AND and OR.

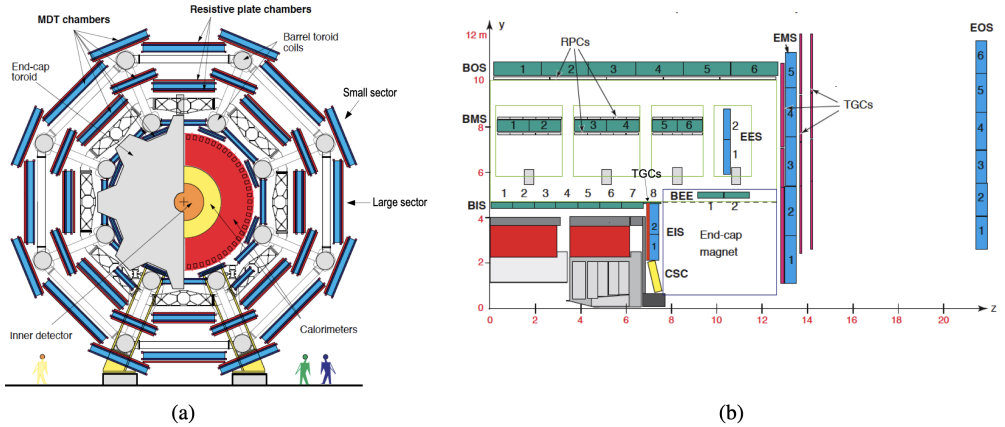

FIGURE 4.20: The ATLAS MS detector in the $x - y$ and $z - y$ plane. In the transverse plane, the different muon chambers defining the MS azimuthal sectors are shown (A). In the longitudinal plane, the chambers are shown for the barrel ($|\eta| < 1.05$) and the endcap ($1.05 < |\eta| < 2.7$) regions, with the former shown in green, and the latter shown in blue.

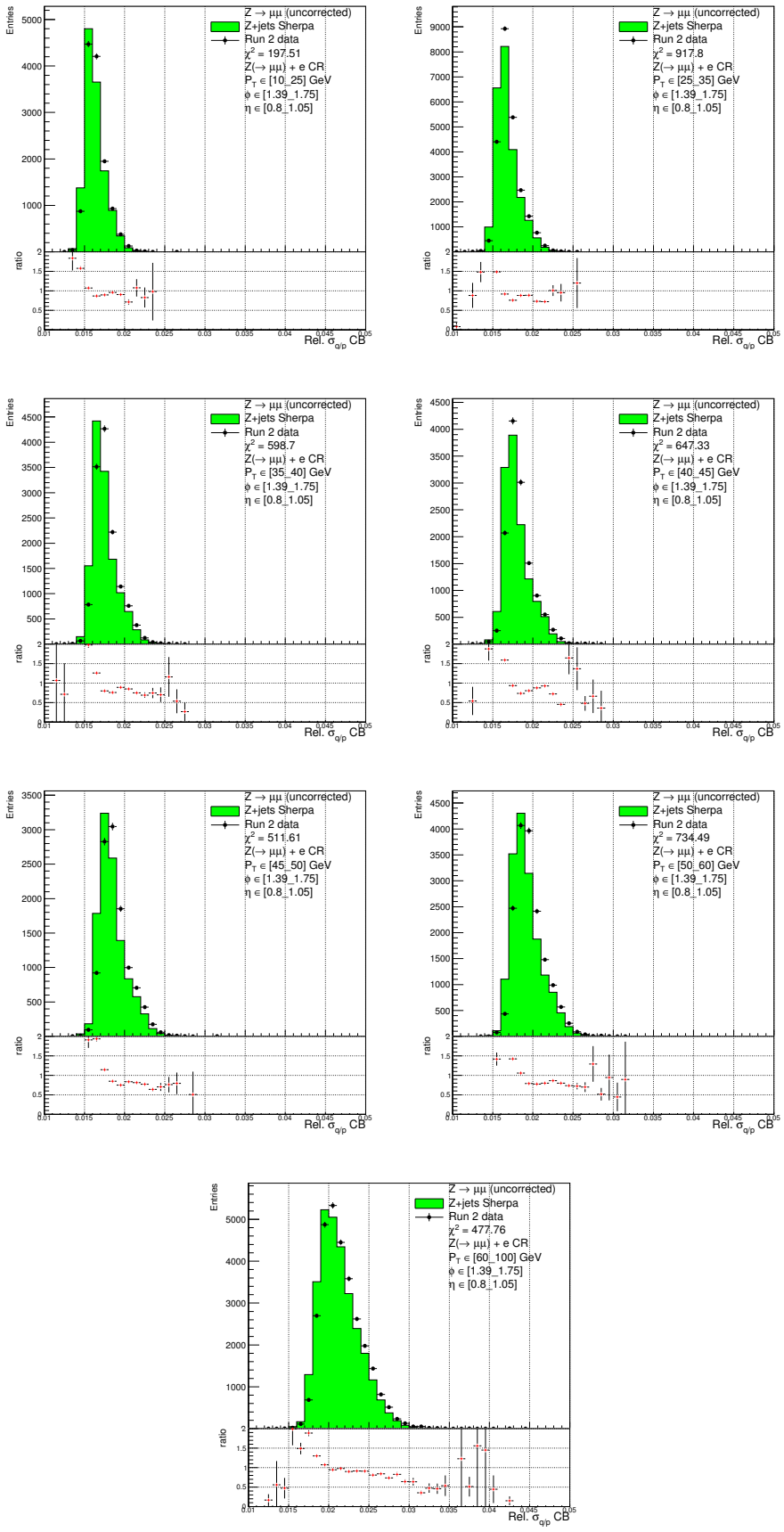

FIGURE 4.21: Data/MC relative $\sigma_{q/p}$ distributions of the leading muon pair in the $Z + X$ CR for specific η, ϕ, p_T bins in the barrel region.

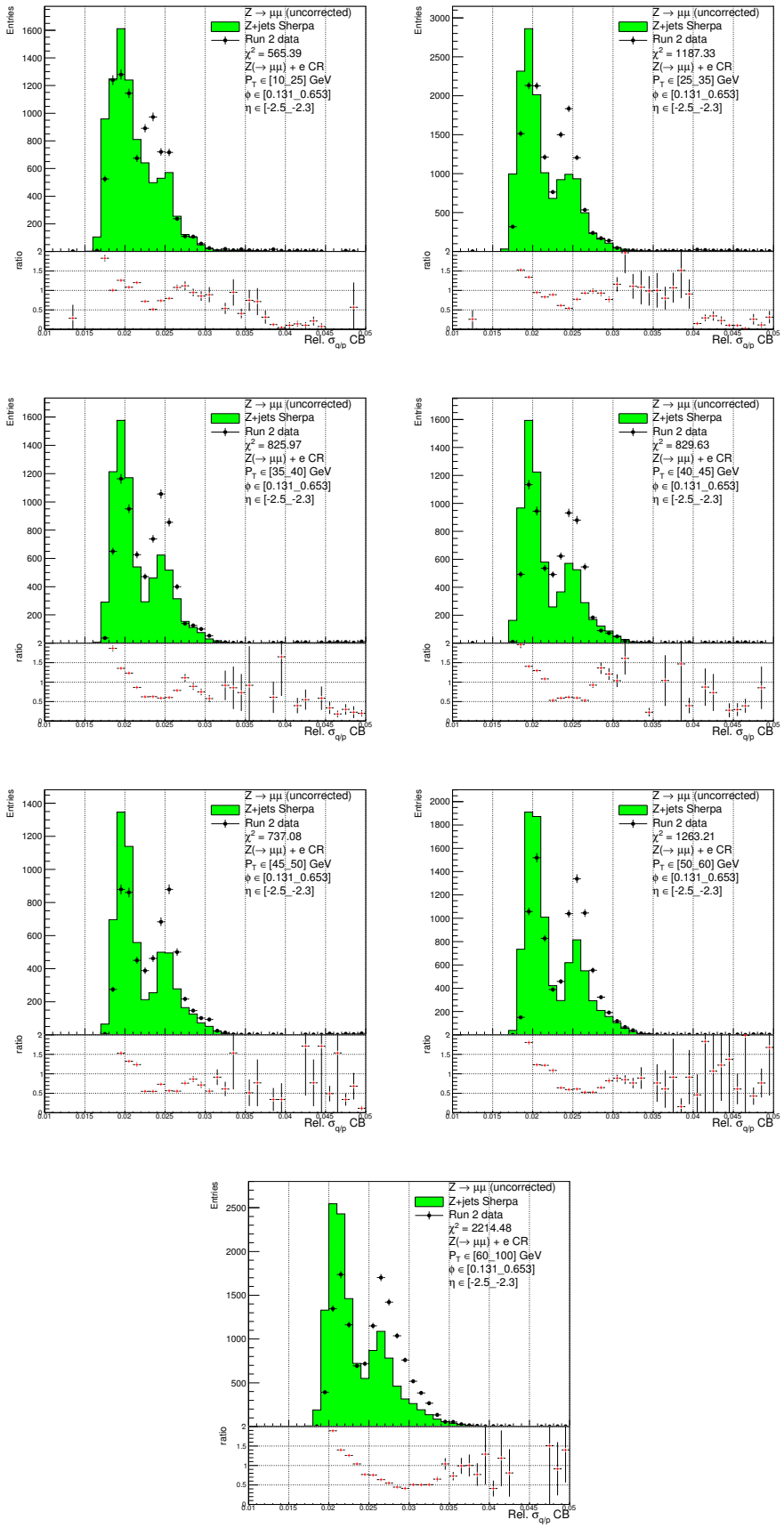

FIGURE 4.22: Data/MC relative $\sigma_{q/p}$ distributions of the leading muon pair in the $Z + X$ CR for specific η, ϕ, p_T bins in the endcap region.

leading muons in different η, ϕ and p_T bins. Figure 4.21 shows an example of a specific bin in η and ϕ in the barrel region for different p_T bins, while Figure 4.22 shows an example in the endcap region. The MC distributions are clearly mismodelled in all bins compared to data. Moreover, the $\sigma^{rel.}_{q/p}$ appears to be underestimated in simulation, which can be seen from the shift compared to data. Comparing the $\sigma^{rel.}_{q/p}$ distribution in the barrel and endcap region, the former is characterised with a single-peak distribution, while the latter has a multi-peak structure. This has been checked for all $p_T \times \eta \times \phi$ bins, where the same characteristics are observed for the barrel and endcap region bins. This difference in distribution shape has been investigated in muon performance studies, where the geometry of the MS in the endcap region is found to be at the origin of the multi-peak structure. However, this effect is not related to the MC mismodelling, which appears to be constant in all bins of the barrel and the endcap regions.

Figures 4.23 and 4.24 show the $\sigma^{rel.}_{q/p}$ distribution of the leading muons as a function of p_T for examples in bins of the barrel and the endcap regions. Per definition, the p_T bins were optimised such that the $\sigma^{rel.}_{q/p}$ is constant over these bins, while taking into account the number of events in data to avoid large statistical uncertainties on the distributions. Furthermore, additional checks on the origin of the mismodelling are performed. One of the generic suspects is often the effect of pile-up events. Typically, the average number of interactions per bunch crossing, $<\mu>$, is indicates

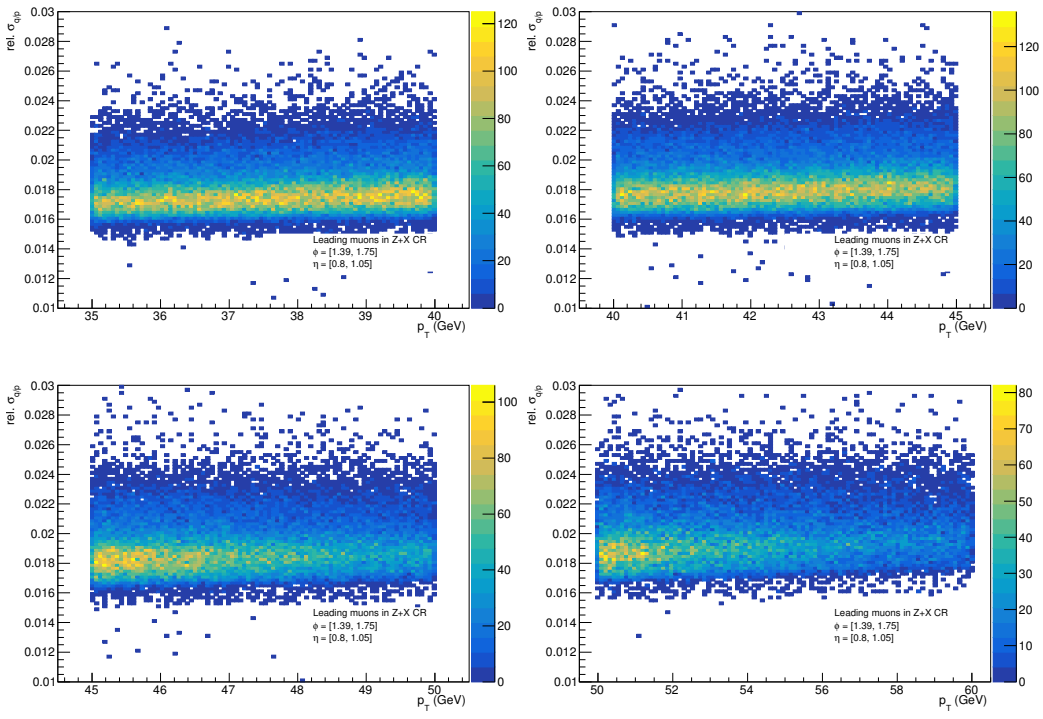

FIGURE 4.23: The $\sigma^{rel.}_{q/p}$ distribution of the leading muons as a function of p_T in an example bin of the barrel.

the number of pile-up events. Figure 4.25 and 4.26 show the $\sigma^{rel.}_{q/p}$ distribution of the leading muons as a function of <μ> in data and MC, for the same $\eta \times \phi$ bins shown in Figures 4.23 and 4.24 respectively. The distribution is relatively constant, showing no correlation. Figure 4.28 shows a comparison of the data/MC $\sigma^{rel.}_{q/p}$ agreement for different bins of <μ>, for the same regions shown in Figures 4.23 and 4.24. The bottom ratio plots show the data/MC disagreement of the $\sigma^{rel.}_{q/p}$ in bins of <μ>, where the mismodelling appears to be constant in the different <μ> bins, from which one can conclude that it is not pile-up related.

Finally, for the same $p_T \times \eta \times \phi$ bins shown in Figure 4.21 and 4.22, the $\sigma^{rel.}_{q/p}$ is investigated in data and MC samples for muon performance studies. These samples have been used to derive the final Run-2 precision calibration and the selection criteria are designed to cover a large range in phase space that includes most of the probed ATLAS analyses (i.e. not specific to the $H \to ZZ \to 4l^{\pm}$ analysis). Since the Z+jets process has the largest number of simulated muons and is by far the most dominant process in the analysis region of interest, di-muon events are used for data and Z+jets MC. Figures 4.29 and 4.30 show the data/MC $\sigma^{rel.}_{q/p}$ distributions of the leading muon pair in Z+jets di-muon events for the same barrel and endcap regions as shown in Figure 4.21 and 4.22. The same mismodelling in $\sigma^{rel.}_{q/p}$ is observed in the samples, confirming claims that the $\sigma^{rel.}_{q/p}$ disagreement is not limited to the samples

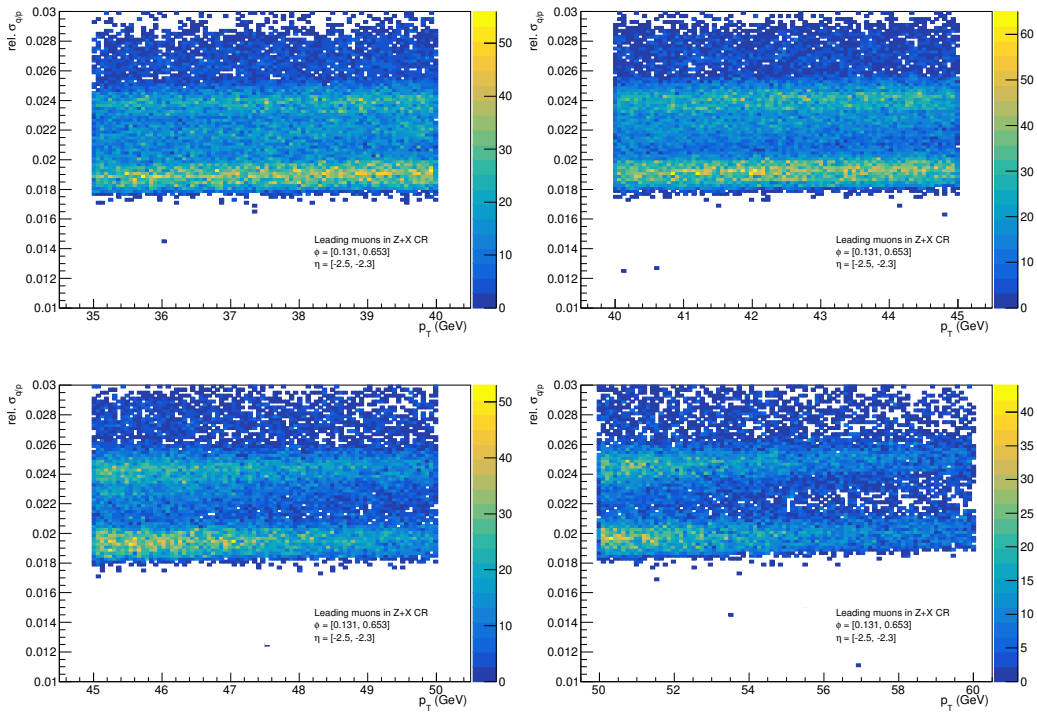

FIGURE 4.24: The $\sigma^{rel.}_{q/p}$ distribution of the leading muons as a function of p_T in an example bin of the endcap.

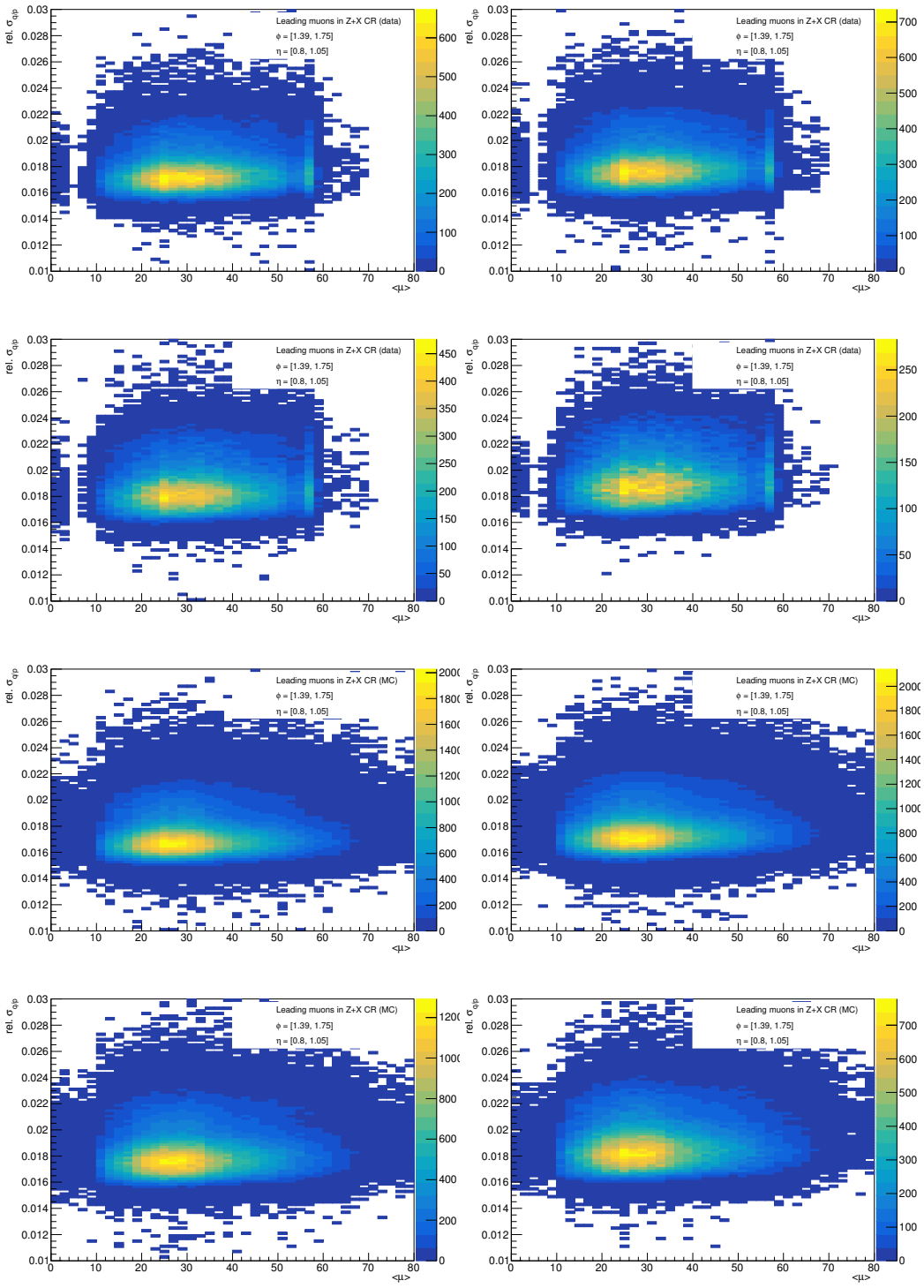

FIGURE 4.25: The $\sigma^{rel.}_{q/p}$ distribution of the leading muons as a function of <μ> in data (top four) and MC (bottom four), for the same regions in Figure 4.23.

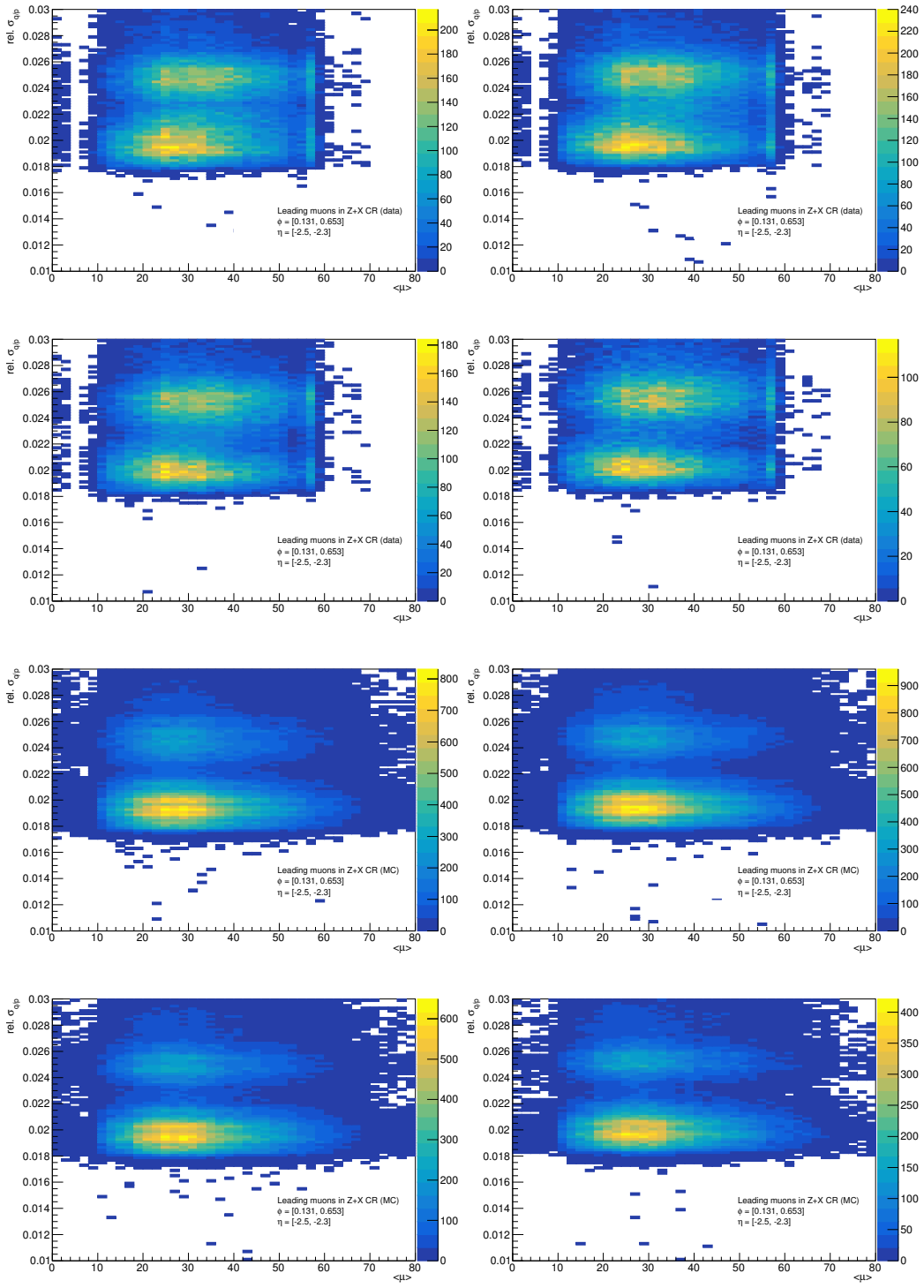

FIGURE 4.26: The $\sigma^{rel.}_{q/p}$ distribution of the leading muons as a function of <μ> in data (top four) and MC (bottom four), for the same regions in Figure 4.24.

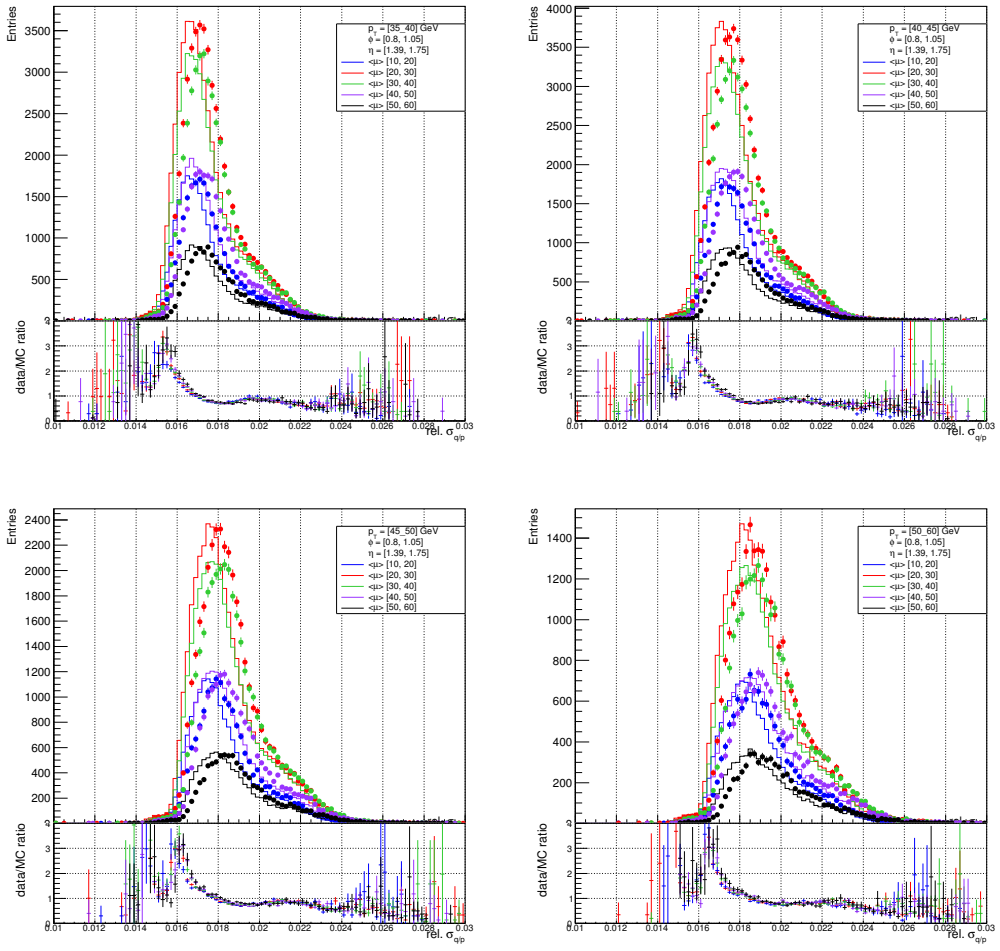

FIGURE 4.27: Comparison of the $\sigma^{rel.}_{q/p}$ agreement of the leading muons for different bins of $<\mu>$, for the same regions in Figure 4.23.

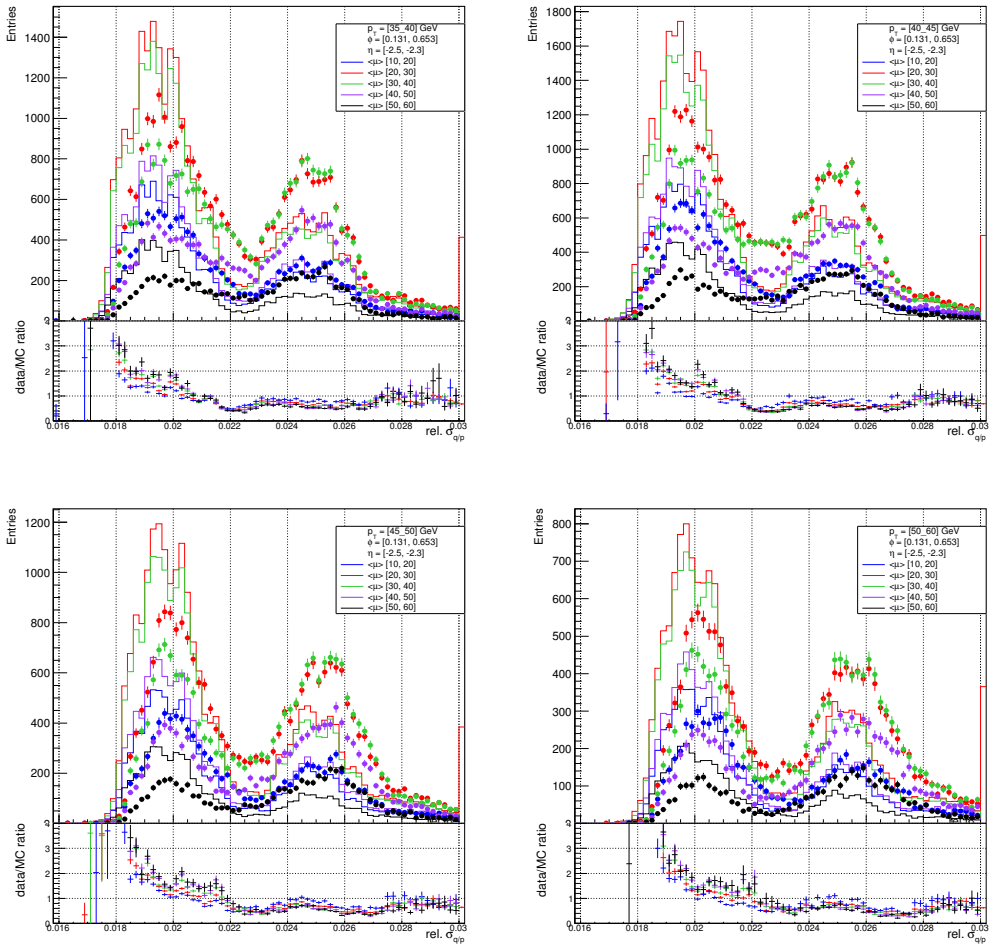

FIGURE 4.28: Comparison of the $\sigma^{rel.}_{q/p}$ agreement of the leading muons for different bins of <μ>, for the same regions in Figure 4.24.

and the selection criteria of this analysis. To make this correction analysis independent (i.e. not only dedicated to the $H \to ZZ \to 4l^{\pm}$ analysis), the described data and MC samples of $Z \to \mu^-\mu^+$ events are used for the correction of the $\sigma^{rel.}_{q/p}$. It should be noted that the di-muon event selection in these samples is different from the leading lepton pair selection in the $H \to ZZ \to 4l^{\pm}$ event selection. Since no third lepton is required, the latter samples are more inclusive containing a larger number of events. The full di-muon event selection can be found in [82].

4.7.3 Correction for the muon track momentum uncertainty

As mentioned in the previous section, to solve the data/MC disagreement in the invariant mass of the leading muon pair after ZMC application, the aim is to derive corrections to the $\sigma^{rel.}_{q/p}$ in the previously defined $p_T \times \eta \times \phi$ bins to model the data as closely as possible. In general, corrections to simulation can be divided into two types, *event-level* and *bias-corrections*. In the former, typically event weights (often referred to as scale factors) are derived to be applied on the MC number of events to scale it to data. In the case of bias-corrections, the quantity used (or the estimator) is targeted for the correction. Typically, the bias is estimated first to correct the quantity by subtracting the bias from the initial estimate.

In the case of $\sigma^{rel.}_{q/p}$, the mismodelling in Figures 4.21 and 4.22 suggests a bias in the MC estimator on lepton-level. As mentioned in section 4.6.3, the ZMC is an event based kinematic constraint, where the reconstructed invariant mass of the leading muons $m^{reco}_{l_1 l_2}$ is replaced by an estimate of the most likely true mass $m^{constrained}_{l_1 l_2}$, according to BW($m_Z$, Γ_Z). The fact that before the ZMC the invariant mass of the leading muons is in agreement, suggests that the muon momenta are not constrained equivalently in data and MC due to the difference in uncertainties; a muon in MC with $p_T = 30$ GeV has on average a smaller uncertainty than a muon in data with the same p_T, and consequently the constraint fit output in both cases will be different. In order to obtain equivalent results, the $\sigma_{q/p}$ bias has to be estimated to correct MC to match data. In the next section, the bias correction methods are investigated.

4.7.3.1 Parametric bias correction methods

Bias-correction techniques can vary depending on the application and the form of the distortion between data and MC. In the case of the $\sigma^{rel.}_{q/p}$ comparison, Figures 4.21 and 4.22 show MC distributions shifted toward lower values compared to the data distributions. Therefore, in the first instance one could consider a *linear scaling*, where $\sigma^{rel.}_{q/p\ MC}$ is corrected for the mean bias of the distributions, i.e. by shifting every initial $\sigma^{rel.}_{q/p\ MC}$ value by,

$$\sigma^{rel.}_{q/p} \longrightarrow \sigma^{rel.\ corr.}_{q/p\ MC} = \sigma^{rel.}_{q/p} + \hat{\mu}_{data} - \hat{\mu}_{MC}, \tag{4.18}$$

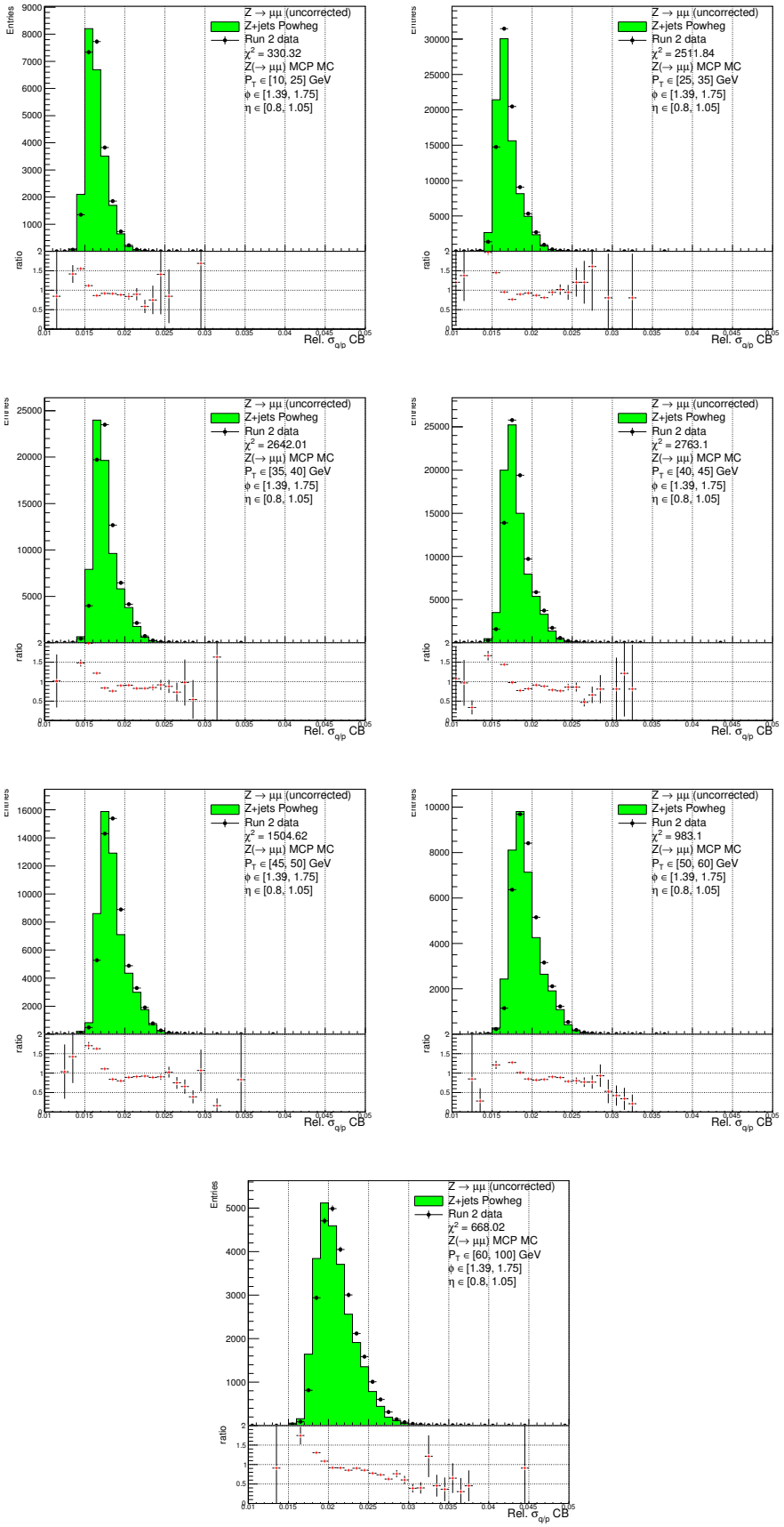

FIGURE 4.29: Data/MC $\sigma^{rel.}_{q/p}$ distributions of the muon pair in Z+jets di-muon events for the same barrel region shown in Figure 4.21.

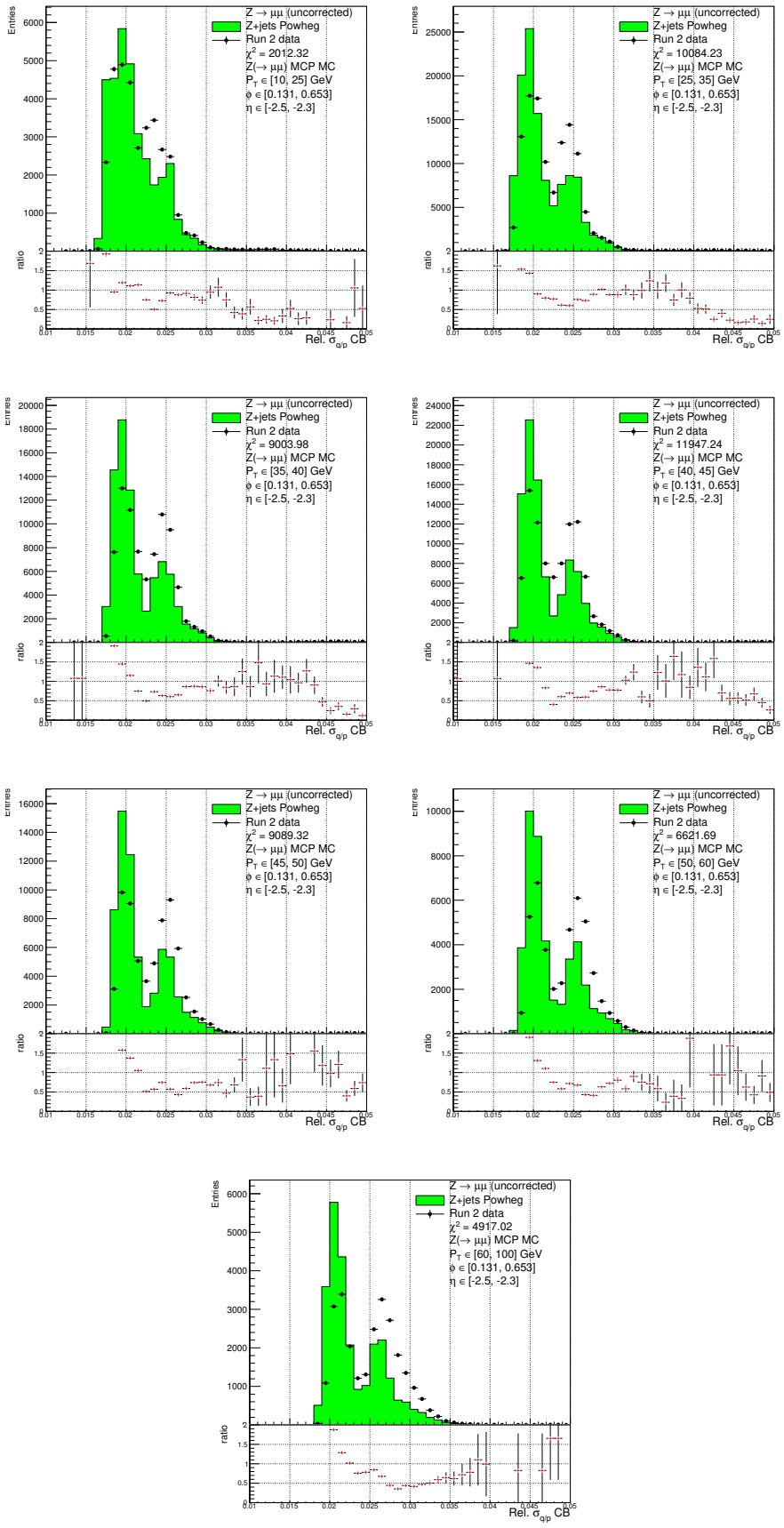

FIGURE 4.30: Data/MC $\sigma^{rel.}_{q/p}$ distributions of the muon pair in Z+jets di-muon events for the same endcap region shown in Figure 4.22.

with $\hat{\mu}_{data}$ and $\hat{\mu}_{MC}$ the mean values of the data and MC distributions. Linear scaling is a simple correction method that is effective if the bias is only on the mean. An example is shown in Figure 4.31, where two histograms (normalised to the same area) of some random, normally distributed variable $X \sim \mathcal{N}(\mu, \sigma)$ are plotted. Initially, the red and black distributions have different mean values. After applying a linear scaling correction on the red histogram, the resulting green distribution fits the black PDF well. This method works well as long as the shape parameters of both distributions are similar.

In the case where both parameters, mean and variance, are different, a linear scaling correction is no longer enough to obtain an agreement in both distributions. Figure 4.32 shows a case where on top of a shift in the mean value, the red histogram has a smaller variance compared to the black distribution. For symmetric histograms close to normal distributions, as in Figure 4.32, the *variance scaling* correction method can be applied, where the variance of the distribution can be adjusted in order to fit the target shape. Following the same notation from eq. 4.18, variance scaling can be achieved by,

$$\sigma^{rel.}_{q/p} \longrightarrow \sigma^{rel.\ corr.}_{q/p\ MC} = \frac{\sigma_{data}}{\sigma_{MC}} \cdot (\sigma^{rel.}_{q/p} - \hat{\mu}_{MC}) + \hat{\mu}_{MC}, \tag{4.19}$$

with σ^2_{data} and σ^2_{MC} the variance in data and MC. Figure 4.32 shows the resulting green distribution after correcting the red histogram with a linear followed by a variance scaling method.

So far, the PDFs were assumed to be more or less similarly distributed, which in

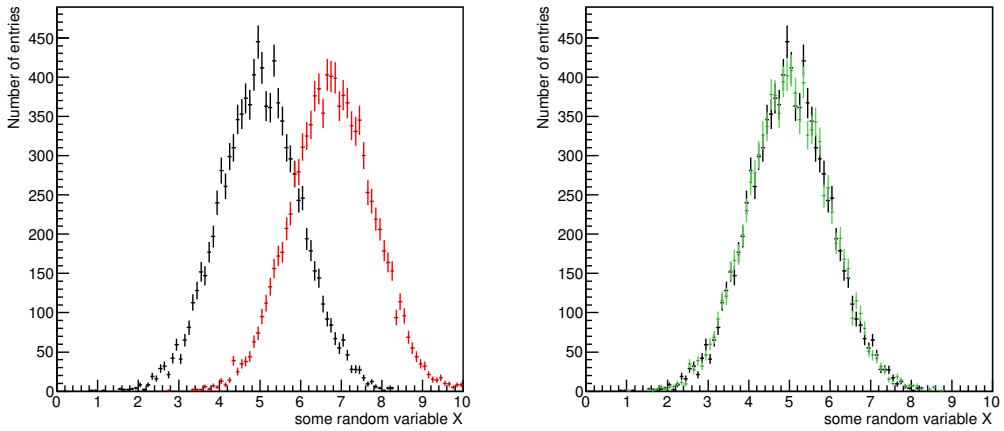

FIGURE 4.31: Two distributions of a random, normally distributed variable $X \sim \mathcal{N}(\mu, \sigma)$ with different mean parameters (left). Using linear scaling, the red distribution is corrected to match the black histogram, which is given by the green distribution (right).

reality is often not the case. Another method that is less dependent on the shape parameters is the *smearing correction method*, where the MC is convolved with a normal distribution,

$$f(\sigma^{rel.}_{q/p}) \longrightarrow f(\sigma^{rel.\ corr.}_{q/p\ MC}) = f(\sigma^{rel.}_{q/p}) * G(\mu, \sigma). \tag{4.20}$$

The idea behind this method is to add noise to the initial MC value to obtain the corrected histogram. Using a random generator, a randomly generated value from a normal distribution centred around the initial MC value is used as the corrected MC value. The mean and width of the associated normal distribution are fitted to obtain the optimal parameters that maximise the data/MC agreement. This is typically achieved by optimising for the χ^2 value of the fit, which provides a measure for the compatibility of both distributions. As a result, the corrected MC will be smeared with the Gaussian noise, and if necessary shifted to match the data distribution. Figure 4.33 shows an example, where two slightly different non-symmetric PDFs are compared. The red distribution is shifted and smeared (and smoothed using a *Kernel Density Estimation* method for removing fluctuations) to fit the black histogram. As long as the PDFs are not significantly different, this technique is efficient. However, it is limited to the case where the MC is narrowly distributed compared to data, which is typically the case when the latter does not include the same resolution effects.

4.7.3.2 Quantile mapping correction for $\sigma^{rel.}_{q/p}$

For the $\sigma^{rel.}_{q/p}$ correction, the previously mentioned bias-correction methods have been considered. However, it turned out that none of the above methods were sufficient

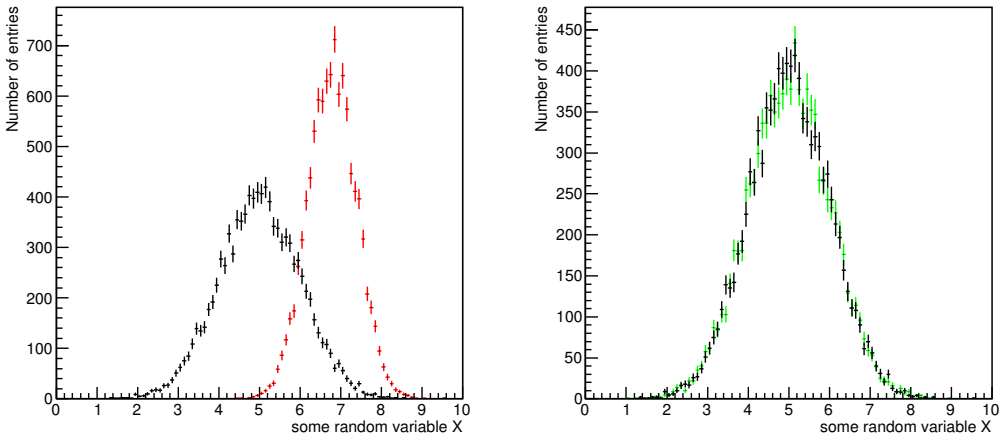

FIGURE 4.32: Two distributions of a random, normally distributed variable $X \sim \mathcal{N}(\mu, \sigma)$ with different mean and variance parameters (left). Using linear scaling in combination with variance scaling, the red distribution is corrected to match the black histogram, which is given by the green distribution (right).

to tackle the disagreement in all $p_T \times \eta \times \phi$ bins. As shown in Figures 4.21 and 4.22, MC appears to be shifted compared to data. As a first attempt, the linear scaling method would be a reasonable choice. Figure 4.34 shows the initial $\sigma^{rel.}_{q/p}$ MC distribution before (left) and after (right) the linear scaling correction compared to data in a barrel region $p_T \times \eta \times \phi$ bin. As mentioned before, bins from the latter region have single-peak distributions, often compared to a *single-sided Crystal Ball* distribution. In this case, the linear scaling method is sufficient to achieve a decent agreement. This can be judged quantitatively from the reduction of the χ^2 value before and after the correction. The remaining mismodelling can be removed using the smearing method; in fact, the PDFs shown in Figure 4.33 are taken from the $\sigma^{rel.}_{q/p}$ distributions in data and MC from a barrel region bin, where the agreement after smearing is relatively good. However, this is no longer enough when it comes to the multi-peak distributions in the endcap region. Figure 4.35 shows an example before (left) and after (right) the linear scaling correction, this time in an endcap region $p_T \times \eta \times \phi$ bin. Clearly, after the linear scaling correction, the agreement remains relatively poor. Analogously, the variance scaling and the smearing method fail in most of the endcap region bins due to the complex shaped of the distributions.

Moreover, there are 3024 $p_T \times \eta \times \phi$ bins to correct, which is challenging to control, especially when the disagreement is not uniform over all bins. In the previously discussed correction methods, requirements on the shape parameters of the PDFs had to be satisfied in order for the correction to be effective. Such methods are referred to as *parametric correction methods*, where the bias is determined from the shape parameters of the PDFs. Considering the particularity of the $\sigma^{rel.}_{q/p}$ correction task, the

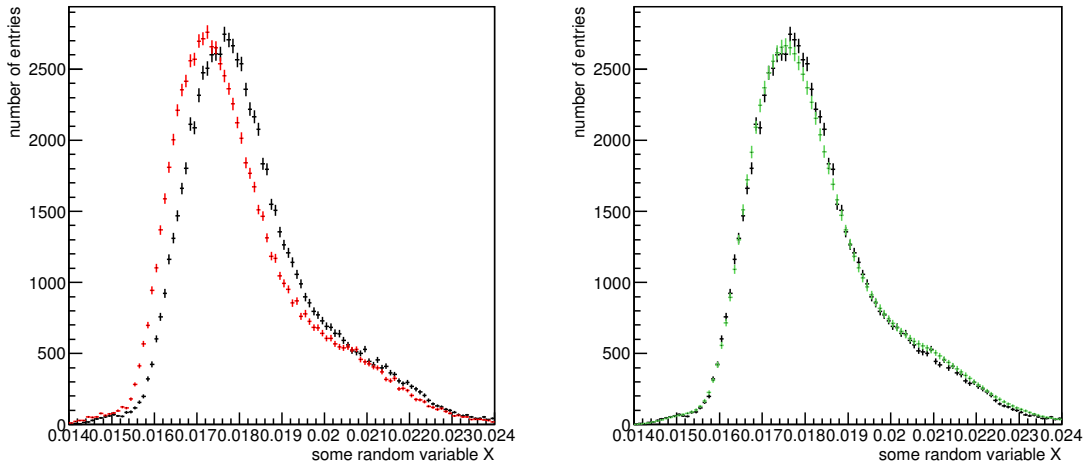

FIGURE 4.33: Two distributions of a random distributed variable X with slightly different mean and shape parameters (left). The red distribution is first smeared with a fitted smearing factor to match the black histogram, which is given by the green distribution (right).

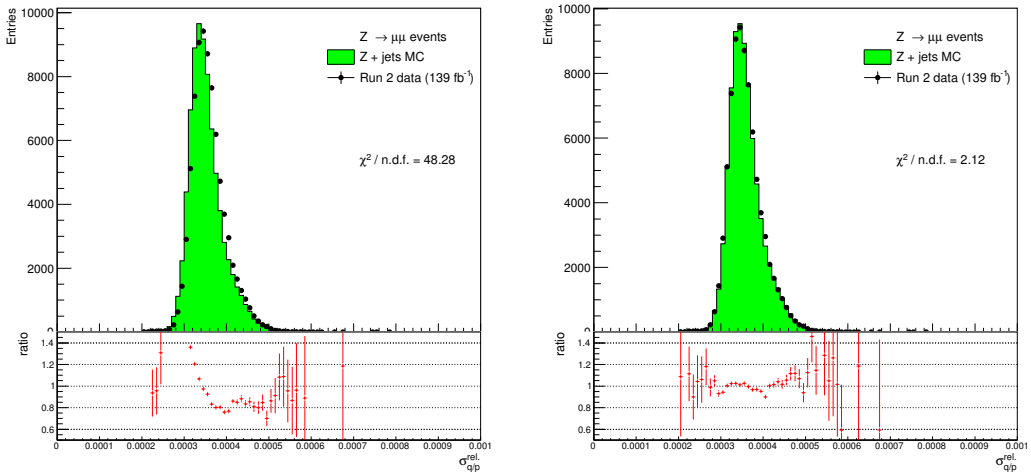

FIGURE 4.34: The initial $\sigma^{rel.}_{q/p}$ MC distribution before (left) and after (right) the linear scaling correction compared to data in a barrel region bin.

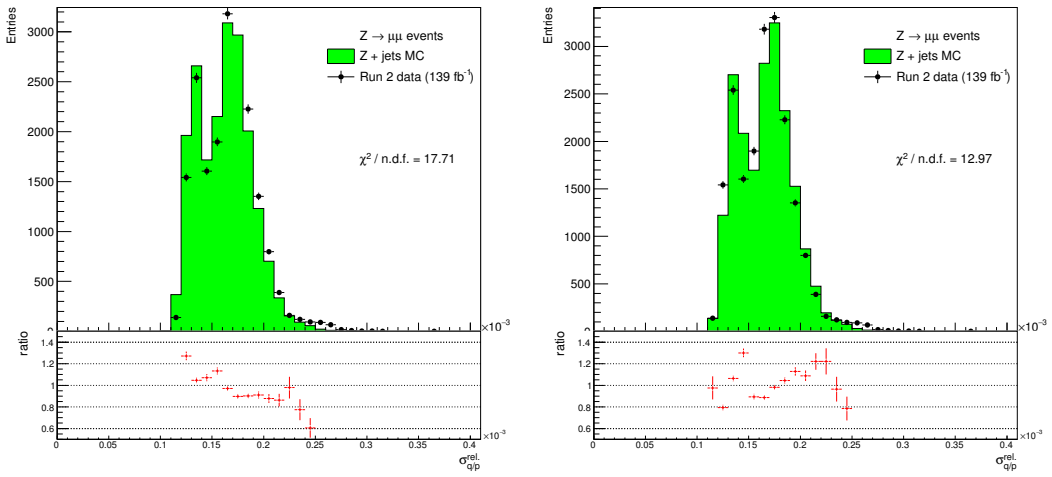

FIGURE 4.35: The initial $\sigma^{rel.}_{q/p}$ MC distribution before (left) and after (right) linear scaling correction compared to data in endcap region bin.

solution is found in a *non-parametric correction method*, namely in a bias correction method referred to as *quantile mapping* (QM). This method has the advantage of being completely independent of the shape parameters of the PDFs. Therefore, it can be used to correct any MC distribution to any data PDF, regardless of the compatibility of both PDFs. The basic idea behind this method is to match the *empirical cumulative distribution function* (ECDF) of MC to the one in data at every point of the $\sigma^{rel.}_{q/p}$ spectrum,

$$F_{MC}(\sigma^{rel.}_{q/p\ MC}) = F_{data}(\sigma^{rel.}_{q/p\ data}), \tag{4.21}$$

with F_{MC} and F_{data} the ECDFs of MC and data given by,

$$F_{MC}(\sigma^{rel.\ max}_{q/p\ MC}) = \int_0^{\sigma^{rel.\ max}_{q/p\ MC}} f_{MC}(\sigma^{rel.}_{q/p}) \cdot d\sigma^{rel.}_{q/p}, \tag{4.22}$$

$$F_{data}(\sigma^{rel.\ max}_{q/p\ data}) = \int_0^{\sigma^{rel.\ max}_{q/p\ data}} f_{data}(\sigma^{rel.}_{q/p}) \cdot d\sigma^{rel.}_{q/p}. \tag{4.23}$$

If the ECDFs are equivalent, so will be the PDFs. In this case, the initial $\sigma^{rel.}_{q/p}$ MC value is replaced by,

$$\sigma^{rel.}_{q/p\ MC} \longrightarrow \sigma^{rel.\ corr.}_{q/p\ MC} = F^{-1}_{data}(F_{MC}(\sigma^{rel.}_{q/p\ MC})), \tag{4.24}$$

where this is achieved by projecting the initial $\sigma^{rel.}_{q/p\ MC}$ to its corresponding corrected value via quantile correspondence. Figure 4.36 shows the connection between a PDF and its corresponding CDF and quantile distribution. The aim of the QM method is to determine for each $\sigma^{rel.}_{q/p}$ in MC, the data $\sigma^{rel.}_{q/p}$ value having the same quantile, which is assigned as the corrected $\sigma^{rel.}_{q/p}$ value. In other words, for a given $\sigma^{rel.}_{q/p}$ in MC defining a probability $F_{MC}(\sigma^{rel.}_{q/p})$, one is after the $\sigma^{rel.}_{q/p}$ value in data that returns the same probability area. In fact, this is exactly what is desired for the ZMC fit; for each MC muon with certain kinematic parameters, one is interested in the most likely $\sigma_{q/p}$ uncertainty of a muon in data with the same kinematic parameters. As a consequence, muons from MC and data will have their momenta constrained equivalently, resulting in a similar invariant mass spectrum of the leading muon pair post ZMC.

In practice, a projection correction map is constructed using a set of pre-defined quantiles. Per $p_T \times \eta \times \phi$ bin, a map is derived, which can be used to extract the corrected $\sigma^{rel.}_{q/p}$ value, given the initial $\sigma^{rel.}_{q/p}$ value. Figure 4.37 show the different steps of the QM correction. The first plot shows the initial $\sigma^{rel.}_{q/p}$ distribution in data and MC Figure 4.37 (a). From these PDFs, the corresponding ECDFs are calculated and are plotted in Figure 4.37 (b). Similar to the disagreement between the PDFs, the ECDFs are also different in data and MC. This difference is exploited to construct the correction map; for a given MC $\sigma^{rel.}_{q/p}$ value, the $F_{MC}(\sigma^{rel.}_{q/p})$ value is read from the y-axis. Drawing a horizontal line on this ECDF value, the corresponding data $\sigma^{rel.}_{q/p}$ value (= $F^{-1}_{data}(F_{MC}(\sigma^{rel.}_{q/p\ MC}))$) is extracted. Repeating this procedure for the set of

pre-defined quantiles, one can construct a $\sigma^{rel.}_{q/p\ MC}$ vs. $\sigma^{rel.\ corr.}_{q/p\ MC}$ map (Figure 4.37 (c)). After performance studies taking in account the computational efficiency (keeping the size of the pre-defined quantiles manageable for 3024 bins), while maximising the correction efficiency and reducing the uncertainties on the corrected $\sigma^{rel.}_{q/p}$ output, the optimal choice was found to be a set of quantiles from 0 to 1 with a resolution of 0.0025 (i.e. 400 uniformly distributed quantiles). Between values from the pre-defined quantiles, a linear interpolation is used to determine the corrected $\sigma^{rel.}_{q/p}$. Smoother interpolation methods have been tested, but no additional gain was observed compared to the linear interpolation.

Furthermore, the correction map in Figure 4.37 (c) obtained from the non-parametric QM method encodes the form of the mismodelling. If the $\sigma^{rel.}_{q/p}$ PDFs in data and MC were equivalent, this curve would be a straight line with a slope equal to one with an intercept at the origin, i.e. the linear function $\sigma^{rel.}_{q/p} = \sigma^{rel.\ corr.}_{q/p}$. If the mismodelling was only a shift, this would correspond to a straight line with a non-zero intercept, in which case the linear scaling method would be sufficient as a correction. In general, one could fit this curve encoding the mismodelling with any compatible function ζ to determine its parameters, such that the correction on $\sigma^{rel.}_{q/p}$ can be performed analytically,

$$\sigma^{rel.}_{q/p} \longrightarrow \sigma^{rel.\ corr.}_{q/p\ MC} = \zeta(\sigma^{rel.}_{q/p}). \tag{4.25}$$

This has the advantage of reducing the correction to a few parameters, rather than the 400 pre-defined quantiles. This has been tested through the different $p_T \times \eta \times \phi$ bins using high order polynomials to fit curves of correction maps derived from the QM method. Successful results were observed in some bins (mainly in the barrel region), however, this was not the case in bins where the mismodelling is too complex to be fitted (typically in the endcap region). Figure 4.38 shows an example where the correction using polynomials is successful (A) and another where the modelling is not optimal (B). To avoid compromising correction performance, maps with 400 pre-defined quantiles are kept as the nominal choice.

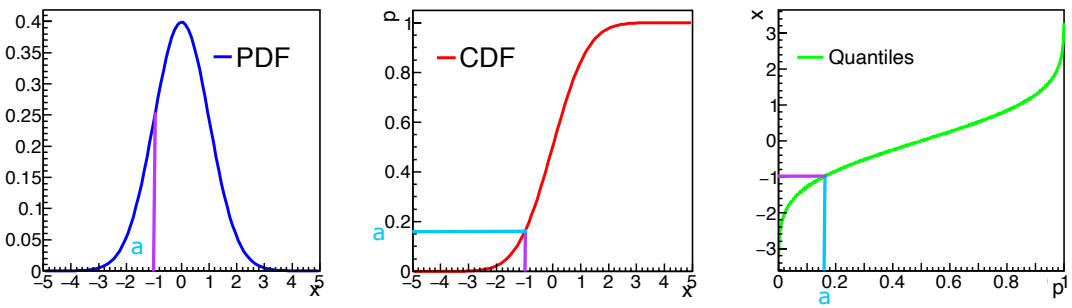

FIGURE 4.36: An example showing the connection between a CDF and its corresponding PDF through a quantile corresponding to the value a of some random variable X.

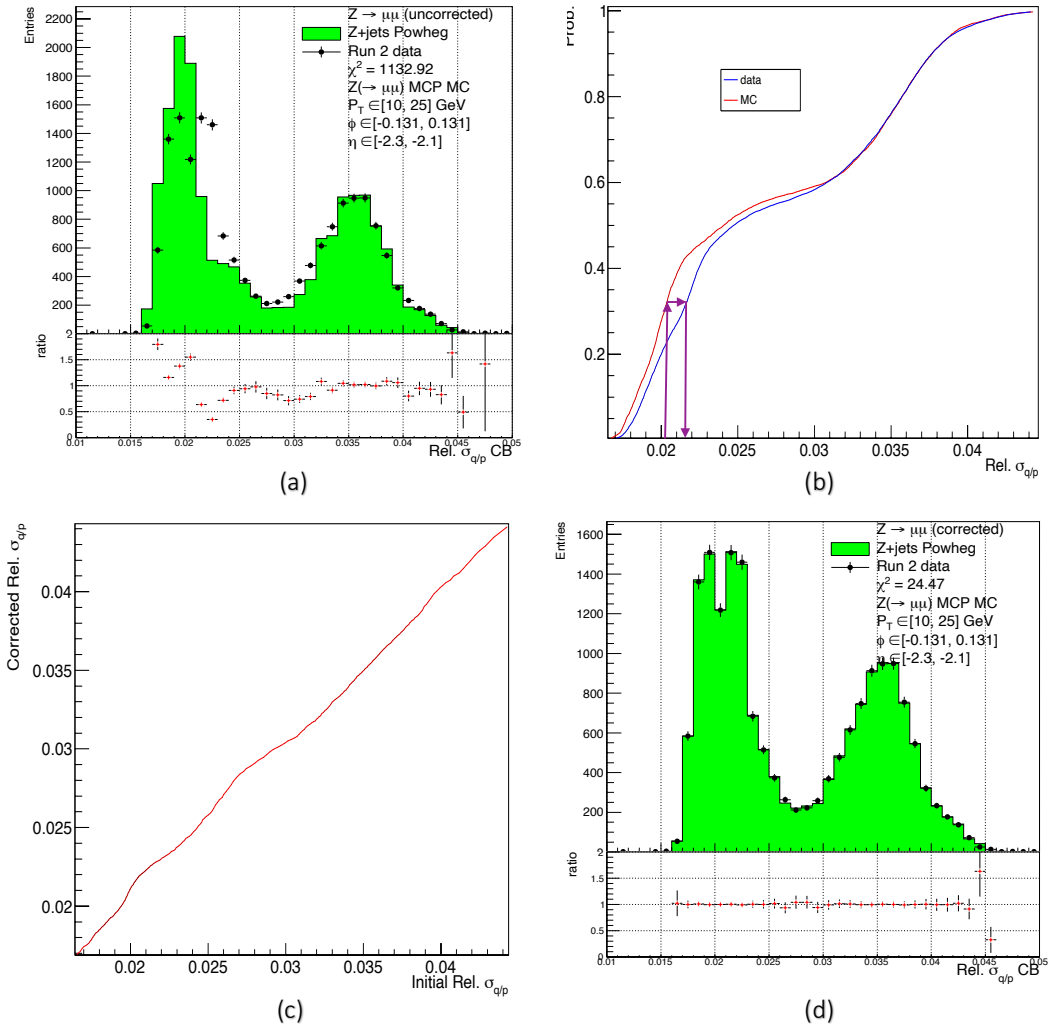

FIGURE 4.37: The $\sigma^{rel.}_{q/p}$ distribution in data and MC before (top left) and after (bottom right) the QM correction. Also the ECDFs of data and uncorrected MC are shown (top right), along with the constructed map (bottom left) from their difference.

Finally, the latter map can be then used to correct the MC distribution, which is shown on Figure 4.37 (d). Clearly, the agreement is spot on after the QM correction, even with a complex shaped distribution, which was purposely chosen to illustrate the performance of the QM method. The agreement is similar across all 3024 bins, a consequence of the non-parametric correction method, where no prior assumptions on the shape parameters of the distributions are necessary to perform the correction.

As mentioned in section 4.7.2, the correction maps are derived in the inclusive calibration samples containing $Z \to \mu^-\mu^+$ events, which are then applied on muons selected in this analysis. Figures 4.39 and 4.40 show the $\sigma^{rel.}_{q/p}$ distribution in $Z \to \mu^-\mu^+$ data and MC events after QM correction for the same barrel and endcap regions shown in Figures 4.21 and 4.22. Similarly to Figure 4.37 (d), the agreement is recovered in all bins, for the barrel region as well as the endcap region.

Having the correction maps derived from the inclusive calibration samples containing $Z \to \mu^-\mu^+$ events, these can be applied to the leading muons in the $Z + X$ CR. Figure 4.41 and 4.42 show the $\sigma^{rel.}_{q/p}$ distribution in di-muon $Z + X$ data and MC events after using the previously derived correction maps for the same barrel and endcap regions shown in Figures 4.21 and 4.22. In general, the agreement is recovered, which can be seen from the reduction in the χ^2 value compared to Figures 4.21 and 4.22. The agreement from Figures 4.39 and 4.40 is better due to the fact that the correction maps were derived from the same samples. Other reasons behind the

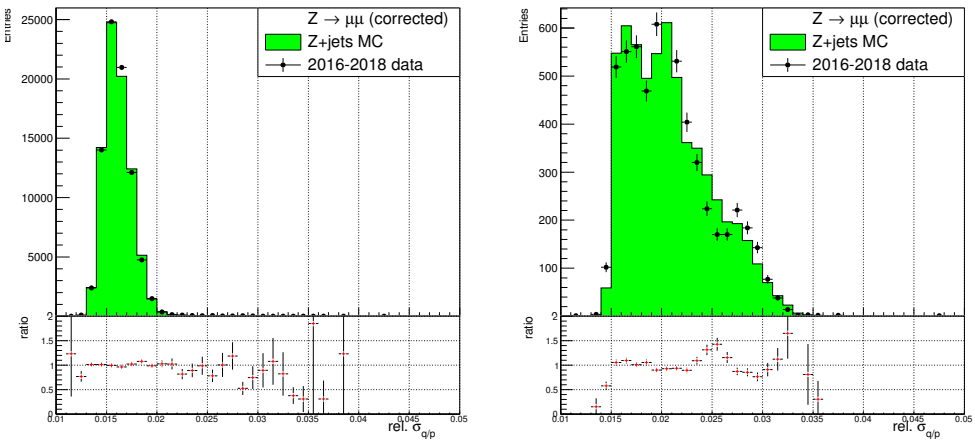

(A) (B)

FIGURE 4.38: The $\sigma^{rel.}_{q/p}$ data/MC distributions after correction using polynomials, fitted to the corresponding correction maps derived from the QM correction. (A) shows an example in the barrel region while (B) in the endcap region.

differences in agreement lie in the different di-muon event selection in the calibration and the $Z + X$ CR samples. As mentioned before, the calibration samples are more inclusive and have tighter selection criteria on Z muons, while the $Z + X$ CR is not constructed for the purpose of measuring the Z peak with precision. Another reason is the difference in generator used to simulate the di-muon events, where the $Z \rightarrow \mu^-\mu^+$ calibration samples are simulated from POWHEG [63] and the $Z + X$ samples from SHERPA [76]. A study has been performed, where the correction maps were derived from the $Z + X$ CR. In Appendix B.4, these are compared to the previously derived correction maps from the calibration samples, and are found compatible within the uncertainties. In fact, both sets of correction maps were used for the ZMC kinematic fit, and no significant difference was observed in the resulting MC distributions of the leading muon invariant mass.

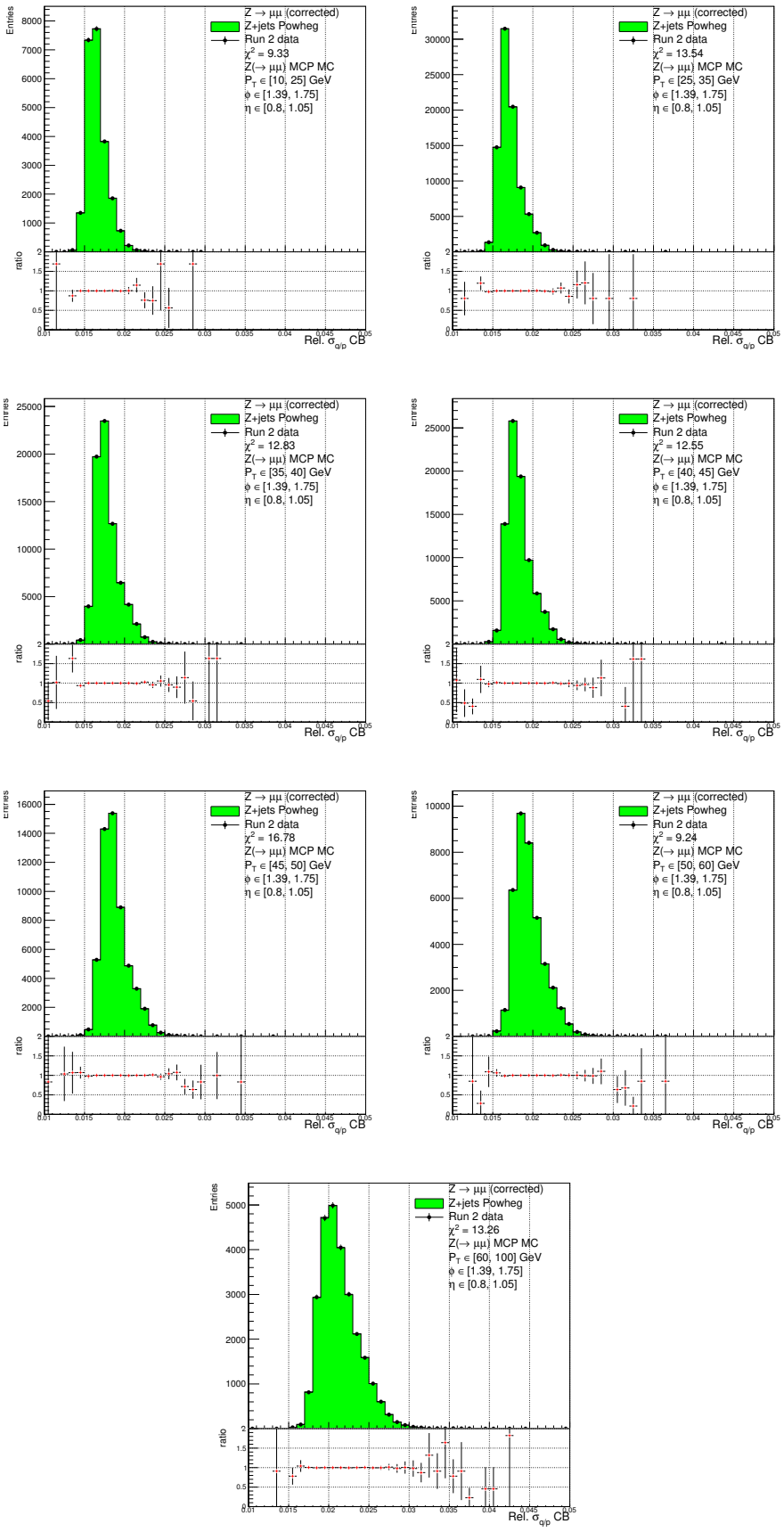

FIGURE 4.39: Data/MC $\sigma^{rel.}_{q/p}$ distributions of the muon pair in Z+jets di-muon events after QM correction for the same barrel region shown in Figure 4.21.

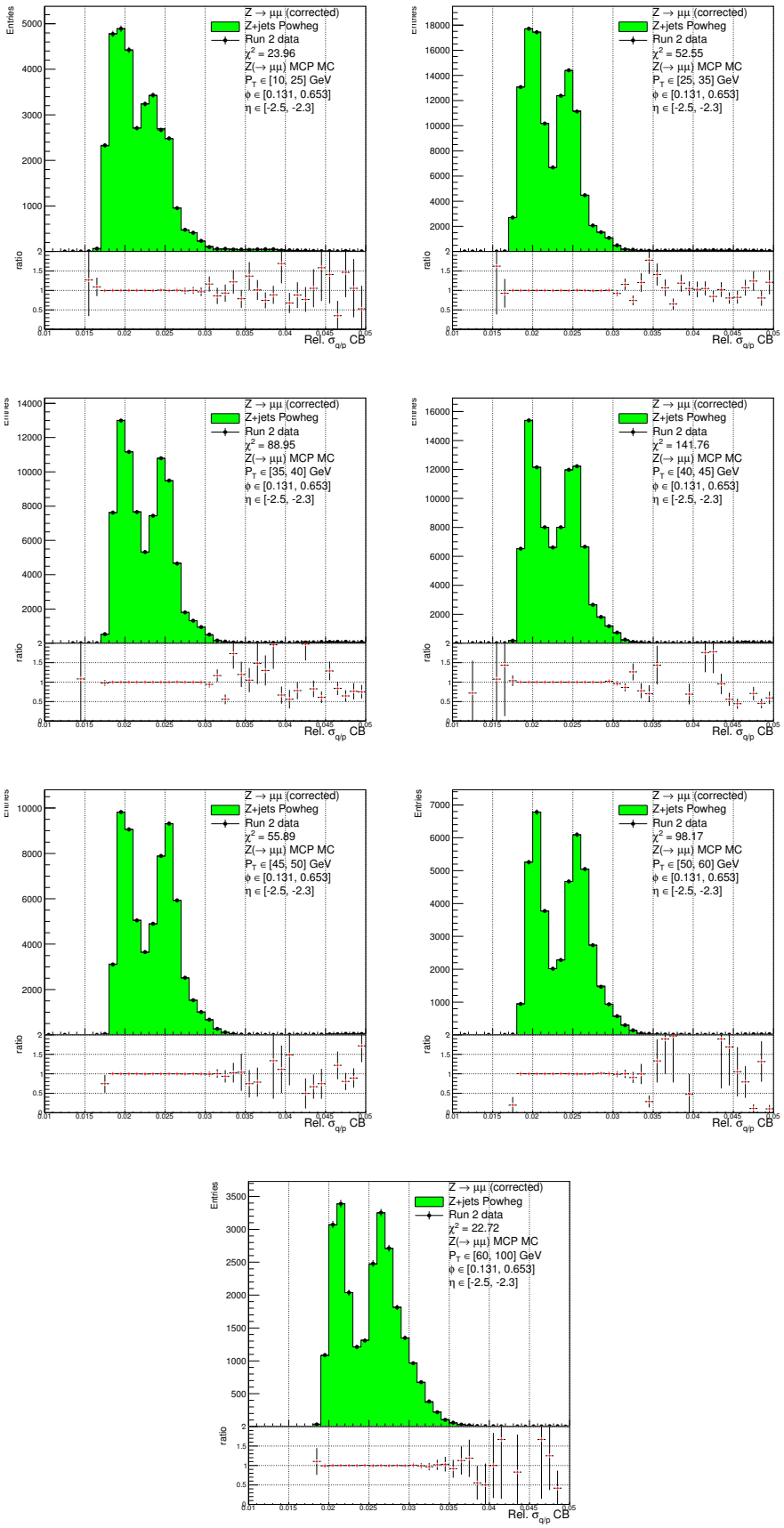

FIGURE 4.40: Data/MC $\sigma^{rel.}_{q/p}$ distributions of the muon pair in Z+jets di-muon events after QM correction for the same endcap region shown in Figure 4.22.

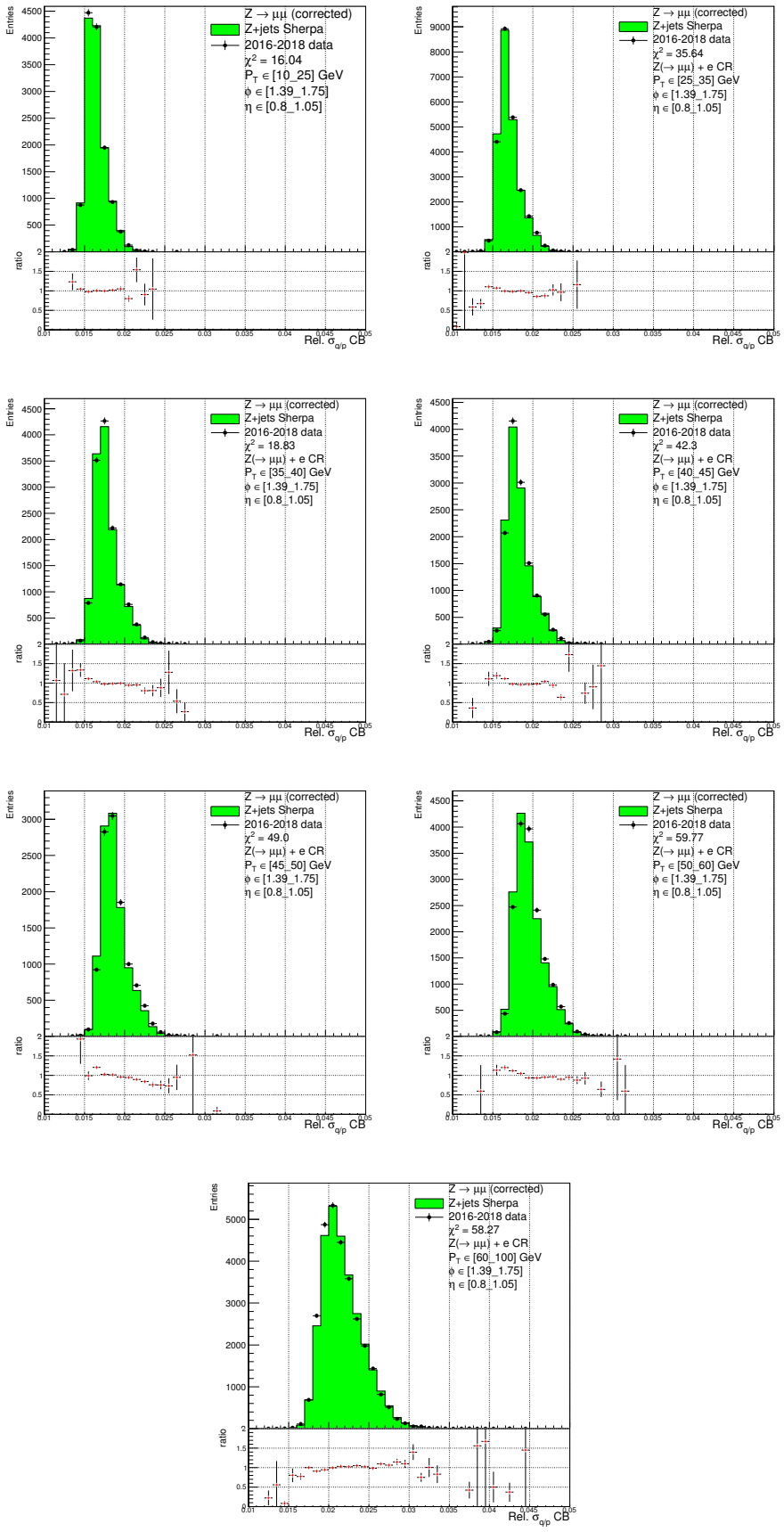

FIGURE 4.41: Data/MC $\sigma^{rel.}_{q/p}$ distributions of the leading muon pair in the $Z + X$ CR after the quantile mapping corrections for same barrel region in Figure 4.21

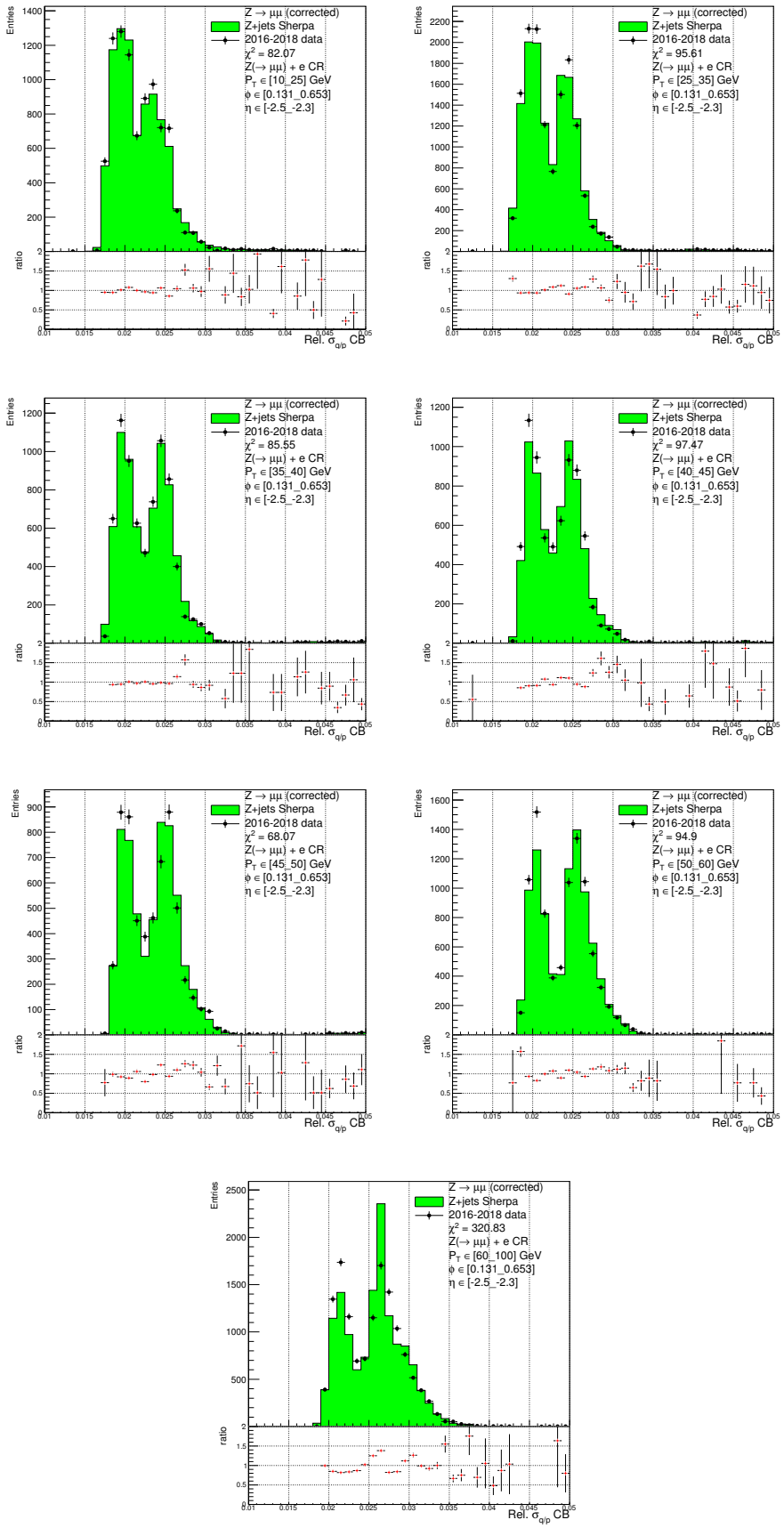

FIGURE 4.42: Data/MC $\sigma^{rel.}_{q/p}$ distributions of the leading muon pair in the $Z + X$ CR after the quantile mapping corrections for same endcap region in Figure 4.22

4.7.3.3 Impact of the track momentum uncertainty after the ZMC

As mentioned in section 4.7.3, the aim is to solve the disagreement in the leading muon invariant mass after the ZMC, which was suspected to originate from a mismodelling of the muon $\sigma_{q/p}$ in MC. The strategy to solve this issue was to correct the muon $\sigma_{q/p}$ in MC to match data, such that the ZMC constrains muons in MC and in data equivalently. In the previous section, corrections for the muon $\sigma^{rel.}_{q/p}$ in bins of p_T, η and ϕ were derived using a QM correction method. The correction is given in a format such that the initial MC $\sigma^{rel.}_{q/p}$ value is taken as input and the corrected value is output from the correction maps. As mentioned before, the ZMC takes as input the kinematic variables of the lepton pair and their corresponding uncertainties. For muons, the latter quantities are given by the covariance matrix of the reconstructed muon track. Using the correction maps, all elements of the covariance matrix (eq. 4.11) containing $\sigma_{q/p}$ have to be corrected.

Per muon, before the ZMC fit is applied, the following procedure is performed:

- The initial $\sigma_{q/p}$ value of the muon is retrieved from the covariance matrix in addition to the q/p value in order to calculate $\sigma^{rel.}_{q/p}$ from their ratio.
- From the kinematic values of the muon, the corresponding $p_T \times \eta \times \phi$ bin is determined to retrieve the adequate correction map.
- Using the correction map, the calculated initial $\sigma^{rel.}_{q/p}$ value is input to extract the corresponding corrected $\sigma^{rel.}_{q/p}$ value.
- Finally, the corrected $\sigma_{q/p}$ value is calculated by multiplying the corrected $\sigma^{rel.}_{q/p}$ value by the initial q/p value of the corresponding muon, which is then used to replace the initial $\sigma_{q/p}$ in the covariance matrix.

With the updated covariance matrices of the MC muons, $m^{constr.}_{\mu_1\mu_2}$ is recalculated. Figure 4.43 show the data and MC $m^{constr.}_{\mu_1\mu_2}$ distributions before (A) and after (B) the $\sigma_{q/p}$ correction. The agreement is significantly improved after the correction as expected, which can be seen from the reduction in the χ^2 value before and after correction. However, there is a small remaining mismodelling around $m^{constr.}_{\mu_1\mu_2} \in [92, 96]$ GeV, which has been investigated by performing a few checks.

As mentioned in the previous section, correction maps derived from the $Z + X$ CR were applied to investigate differences with the calibration samples, but also to test if this small disagreement was $\sigma_{q/p}$ related. Deriving these maps from $Z + X$ CR results in a spot on correction with not the slightest disagreement in the $\sigma_{q/p}$ spectra, exactly as in Figures 4.39 and 4.40. After recalculating $m^{constr.}_{\mu_1\mu_2}$ with these correction maps, the difference in agreement in the $m^{constr.}_{\mu_1\mu_2} \in [92, 96]$ GeV region was less than 1%, suggesting that the disagreement is not due to the $\sigma_{q/p}$. Although the other elements in the muon covariance matrix were expected to have no significant impact on the ZMC, these were also corrected and used to recalculate $m^{constr.}_{\mu_1\mu_2}$. Not the

slightest difference was observed as expected. Since the issue was not related to the muon covariance matrices, the remaining suspects are the kinematic variables of the muons. Although using these latter quantities resulted in a decent unconstrained invariant mass $m_{\mu_1\mu_2}^{unconstr.}$ agreement (Figure 4.17 (A)), there is an effect to be considered.

As previously mentioned, the unconstrained invariant mass $m_{\mu_1\mu_2}^{unconstr.}$ depends only on the lepton η, ϕ and p_T as shown in eq. 4.10. From Figure 4.17 (A), the agreement is relatively good, slightly worse toward the tails, but remains relatively small. Compared to the unconstrained invariant mass $m_{\mu_1\mu_2}^{unconstr.}$, the $m_{\mu_1\mu_2}^{constr.}$ distribution is narrower around m_Z, a consequence of the ZMC which, as discussed in section 4.6.3, aims to pull the invariant mass of the on-mass shell Z leptons closer to m_Z. In fact, a scatter plot can be constructed to map the $m_{\mu_1\mu_2}^{unconstr.}$ of each lepton pair to its corresponding $m_{\mu_1\mu_2}^{constr.}$ after the ZMC. Figure 4.44 shows the two-dimensional $m_{\mu_1\mu_2}^{unconstr.}$ versus $m_{\mu_1\mu_2}^{constr.}$ distribution. As expected, the ZMC moves events from the left and right side of the peak around toward m_Z. By compressing events from the smeared $m_{\mu_1\mu_2}^{unconstr.}$ to the narrow $m_{\mu_1\mu_2}^{constr.}$ distribution, the small discrepancies in the former build up around the Z peak of the latter distribution, and as a result are less negligible. To verify this effect, one can derive scale factors from the $m_{\mu_1\mu_2}^{unconstr.}$ data/MC ratio plot on Figure 4.17 that make the data/MC $m_{\mu_1\mu_2}^{unconstr.}$ agreement perfect, then apply these scale factors to the $m_{\mu_1\mu_2}^{constr.}$ spectrum, which removes the propagated discrepancies from $m_{\mu_1\mu_2}^{unconstr.}$ to the $m_{\mu_1\mu_2}^{constr.}$ distribution. Figure 4.45 shows the $m_{\mu_1\mu_2}^{constr.}$ of the leading muons including the $\sigma_{q/p}$ correction on the left plot, and on the right plot including the $\sigma_{q/p}$ correction as well as the scale factors derived from the $m_{\mu_1\mu_2}^{unconstr.}$ spectrum. Clearly, the agreement is significantly improved after the application of

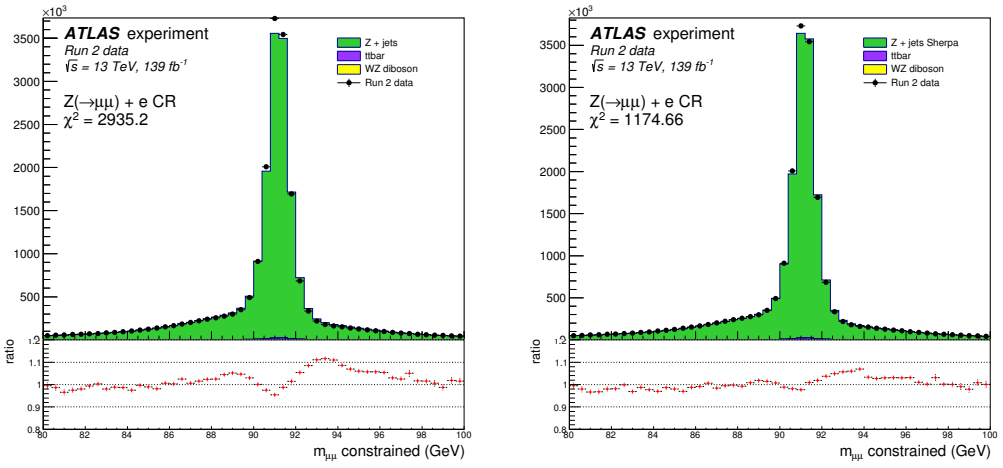

(A) (B)

FIGURE 4.43: The invariant mass spectrum of the leading muon pair after the ZMC, before (A) and after (B) correcting the MC $\sigma_{q/p}$ to match data.

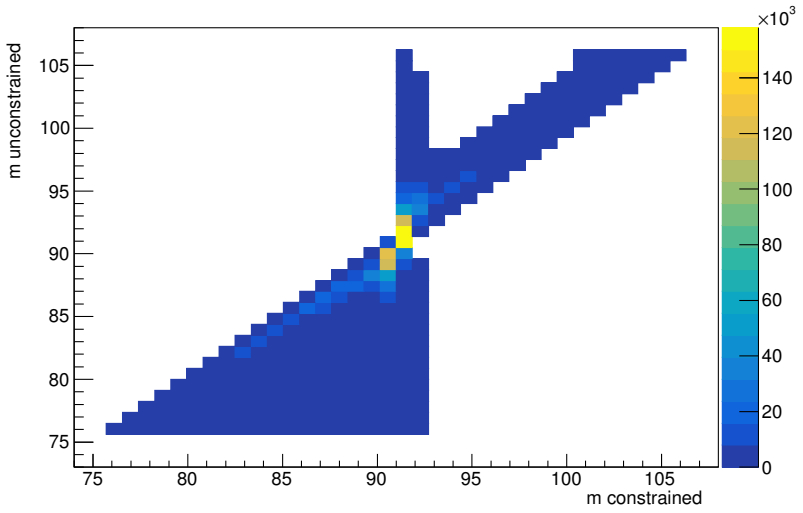

FIGURE 4.44: Two-dimensional scatter plot of the unconstrained invariant mass $m_{\mu_1\mu_2}^{unconstr.}$ versus the constrained invariant mass $m_{\mu_1\mu_2}^{constr.}$ of the leading muon pair in data.

the scale factors, reducing the χ^2 value by more than a factor of 2.

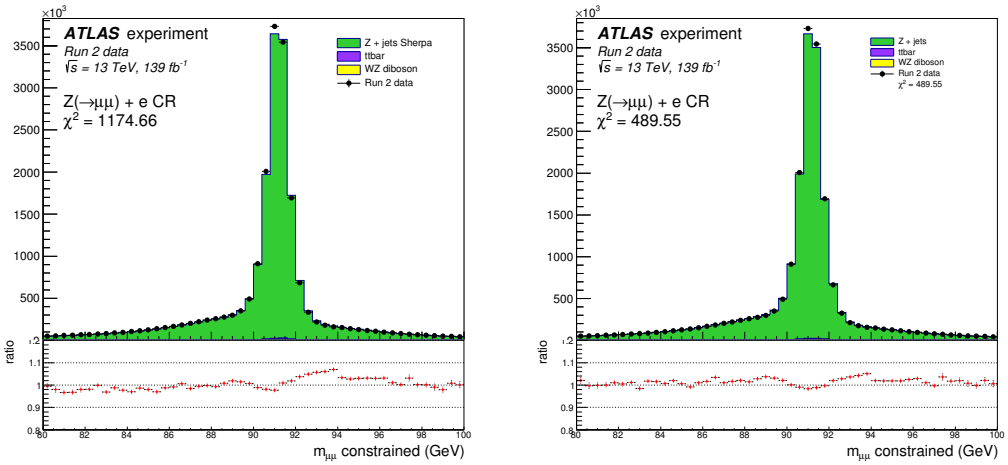

FIGURE 4.45: The left plot shows the constrained invariant mass of the leading muons including the $\sigma_{q/p}$ correction and the right plot including the $\sigma_{q/p}$ correction as well as the scale factors derived from the unconstrained spectrum discussed in section 4.7.3.3.

The previously derived scale factors are in fact only used to investigate the origin of the remaining small discrepancy in the agreement between data and MC after the $\sigma_{q/p}$ correction. After identification of the mismodelling source, the calibration of the muons is updated, which improves the correction on their kinematic variables. Figure 4.46 shows the resulting $m_{\mu_1\mu_2}^{constr.}$ agreement after the latest calibration. Similarly to Figure 4.45, the agreement is recovered, which is 15% better than even the

result from the scale factors.

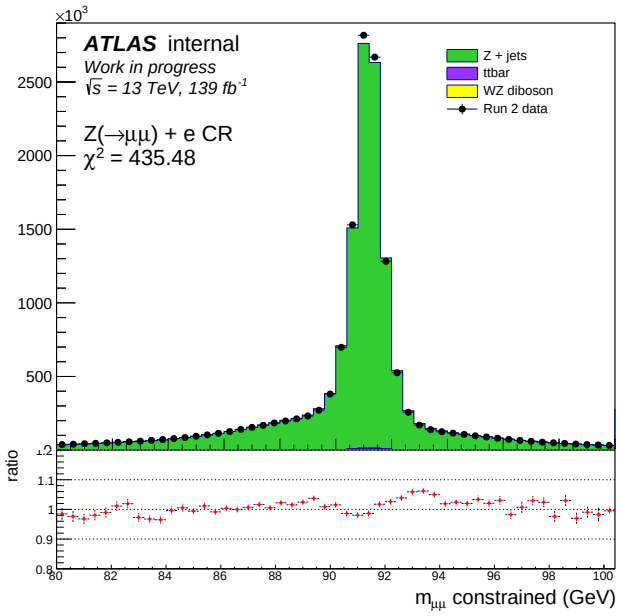

FIGURE 4.46: The constrained invariant mass of the leading muon pair after $\sigma_{q/p}$ correction using an updated calibration of the muons with an improved correction on their kinematic variables.

Finally, in order to make a conclusion on the data/MC agreement, systematic uncertainties are required. As mentioned before, only statistical uncertainties have been presented so far, which are negligible in the invariant mass spectra. Systematic uncertainties on the invariant mass are obtained from propagation of the systematic uncertainties on the lepton kinematic quantities. For the purpose of this study, where the $Z + X$ CR is used only to address the ZMC issue observed in the leading muon events, the systematic uncertainties can be approximated. From the (unconstrained[5]) invariant mass measurement of the Z muons in the $Z \to \mu^-\mu^+$ calibration samples, a systematic uncertainty of 0.2% is measured for the mean of the distribution, and 3% on the width [82]. Using these values and the two-dimensional MC map between the $m^{unconstr.}_{\mu_1\mu_2}$ and $m^{constr.}_{\mu_1\mu_2}$ (similar to Figure 4.44), one can calculate an estimate of the systematic uncertainties in the $m^{constr.}_{\mu_1\mu_2}$ distribution by projecting those from the $m^{unconstr.}_{\mu_1\mu_2}$ spectrum through the two-dimensional map. In practice, five $m^{unconstr.}_{\mu_1\mu_2}$ distributions are constructed,

$$m^{unconstrained}_{\mu_1\mu_2}(\mu, \sigma), \tag{4.26}$$

$$m^{unconstrained}_{\mu_1\mu_2}(\mu + 0.2\%, \sigma), \tag{4.27}$$

[5]The ZMC is only used in $H \to ZZ \to 4l^{\pm}$ analysis and never on the calibration samples.

$$m_{\mu_1\mu_2}^{unconstrained}(\mu - 0.2\%, \sigma). \tag{4.28}$$

$$m_{\mu_1\mu_2}^{unconstrained}(\mu, \sigma + 3\%), \tag{4.29}$$

$$m_{\mu_1\mu_2}^{unconstrained}(\mu, \sigma - 3\%). \tag{4.30}$$

The first distribution is the nominal one from Figure 4.17. The second and third distributions are obtained by shifting the nominal distribution respectively with +0.2% and -0.2% of the mean value. The fourth distribution is constructed by smearing the nominal PDF (as described in 4.7.3.1) to reach a width larger by 3%. For the fifth distribution, since it is impossible to narrow a histogram using a random generator (i.e. as opposed to smearing[6]), uncertainties on the width are assumed to be symmetric, such that,

$$\Delta_{width,up} = |N_{nominal} - N_{smeared}|, \tag{4.31}$$

$$\Delta_{width,down} = -|N_{nominal} - N_{smeared}|, \tag{4.32}$$

with N the number of events per bin and thus in each bin of the fifth distribution,

$$N_{width,up} = N_{nominal} + (N_{nominal} - N_{smeared}). \tag{4.33}$$

Figure 4.47 shows the nominal $m_{\mu_1\mu_2}^{unconstr.}$ distribution and its derived variations from the systematic uncertainties on the mean (A) and the width (B). The last four histograms can be combined to determine the total variations on the number of events per bin i of the $m_{\mu_1\mu_2}^{unconstr.}$ distribution compared to the nominal case, defining the total systematic uncertainties,

$$\Delta_i^{total,up} = |N_i^{max} - N_i^{nominal}|, \tag{4.34}$$

$$\Delta_i^{total,down} = -|N_i^{nominal} - N_i^{min}|, \tag{4.35}$$

with N_i^{max} and N_i^{min} the number of events from the variation that yields in, respectively, the highest and lowest event count in a given bin. In the same way, five two-dimensional $m_{\mu_1\mu_2}^{unconstr.}$ versus $m_{\mu_1\mu_2}^{constr.}$ distributions are constructed. The number of events in two-dimensional bin (i, j), with i the $m_{\mu_1\mu_2}^{unconstr.}$ bin and j the $m_{\mu_1\mu_2}^{constr.}$ bin, is given by N_{ij}. In this case, the uncertainties are given by,

$$\Delta_{ij}^{total,up} = |N_{ij}^{max} - N_{ij}^{nominal}|, \tag{4.36}$$

$$\Delta_{ij}^{total,down} = -|N_{ij}^{nominal} - N_{ij}^{min}|, \tag{4.37}$$

Summing over j yields back $\Delta_i^{total,up}$ and $\Delta_i^{total,down}$ of the one-dimensional i-th bin of $m_{\mu_1\mu_2}^{unconstr.}$ distribution. Similarly, summing over i yields the uncertainties on the one-dimensional $m_{\mu_1\mu_2}^{constr.}$ distribution. As a result, the desired systematic uncertainties in the data/MC ratio of the $m_{\mu_1\mu_2}^{constr.}$ distribution can be determined, which is

[6] If the PDF was approximately Gaussian, variance scaling could be used to narrow the width

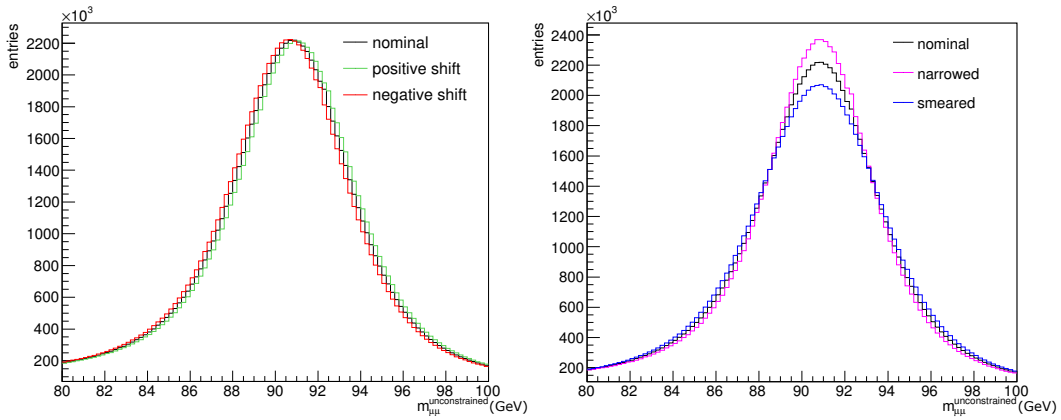

(A) (B)

FIGURE 4.47: The five $m_{\mu_1\mu_2}^{unconstr.}$ distributions obtained from variations according to the systematic uncertainties on the mean (A) and width (B) of the $m_{\mu_1\mu_2}^{unconstr.}$ distribution.

shown in Figure 4.48. The uncertainties are smoothed using a smoothing algorithm [104] through the bins, which is represented by the envelope around the ratio plot. Considering these propagated systematic uncertainties, the agreement is clearly restored. The lower mass region appears to have larger uncertainties. This can be understood from Figure 4.44, showing the number of events moving from $m_{\mu_1\mu_2}^{unconstr.}$ to $m_{\mu_1\mu_2}^{constr.}$; one can observe a clear asymmetry between the < 91 and > 91 GeV region in the distribution. In fact, the $m_{\mu_1\mu_2}^{unconstr.}$ distribution itself is asymmetric, having a larger width in the < 91 GeV region compared to the opposite side. Consequently, after smearing for the width uncertainty, both regions have different variations, leading to larger ones on the left side of the peak.

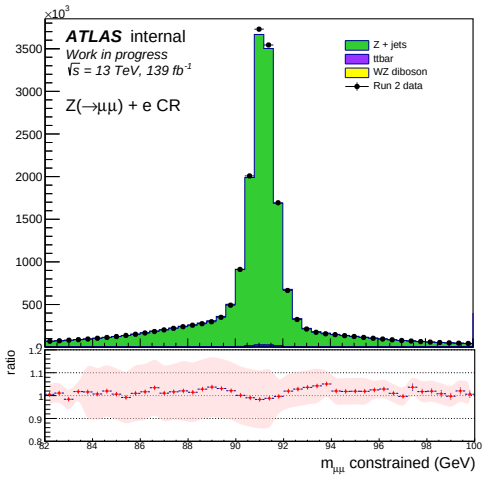

FIGURE 4.48: The constrained invariant mass $m_{\mu_1\mu_2}^{constr.}$ of the leading muons after $\sigma_{q/p}$ correction including the approximated systematic uncertainties.

4.7.3.4 Impact of the track momentum uncertainty in the signal region

As mentioned before, the purpose of ZMC is to improve the resolution of the measured leptons, which has a direct impact on the width of the m_{4l} distribution, hence the precision of the Higgs boson mass measurement. In the previous sections, the $Z + X$ CR was used to understand and rectify the mismodelling in the di-muon invariant mass spectrum after applying the ZMC, which was mainly caused by a mismodelling in the muon track momentum uncertainties. After solving the disagreement by deriving corrections on the latter quantity, the following step consists of studying the impact of the $\sigma_{q/p}$ corrections in the SR, where the Higgs boson mass is measured. In fact, the uncertainty on the main observable of this analysis, $\sigma_{m_{4l}}$ is calculated from the propagation of the four lepton uncertainties. Therefore, the $\sigma_{q/p}$ correction is not only a solution to the ZMC matter, but also an indirect correction of the estimated $\sigma_{m_{4l}}$.

In the following, a comparison is presented where the MC distribution of kinematic variables related to the quadruplets (selected according to section 4.4) is shown before and after the $\sigma_{q/p}$ correction. This comparison is performed using MC samples of the Higgs boson signal and the irreducible ZZ background, while each decay channel is analysed individually. The $4e$ channel is left out, since no muons are involved, hence no changes are expected. Figures 4.49 - 4.54 show the comparison in the four lepton invariant mass $m_{4l}^{constrained}$ (A), the $m_{4l}^{constrained}$ uncertainty $\sigma_{m_{4l}}$ (B), the leading lepton invariant mass $m_{12}^{constrained}$ (C) and the sub-leading lepton invariant mass m_{34} (D).

From the ratio agreement plot between the distributions before and after $\sigma_{q/p}$ correction, it is clear that the most prominent changes are in the σ_{m4l} distributions, as $\sigma_{q/p}$ is directly propagated to the m_{4l} uncertainty. As expected, changes are more significant in the 4μ channel compared to the $2\mu 2e$ and $2e2\mu$ cases, since in the former channel all leptons are affected by the $\sigma_{q/p}$ correction. Moreover, after the $\sigma_{q/p}$ correction, the means of the $\sigma_{m_{4l}}$ distributions appear to have a positive shift compared to the initial distributions, suggesting that the uncertainties were underestimated before the correction. This is indeed expected, since the mismodelled MC $\sigma_{q/p}$ distributions were shifted toward lower values compared to data in all $p_T \times \eta \times \phi$ bins. Another difference lies in the leading lepton invariant mass, where the distributions after the $\sigma_{q/p}$ correction of the 4μ and $2\mu 2e$ channels have a narrower peak compared to the initial distributions. This is also expected from the disagreement in leading muon pair invariant mass after the ZMC (Figure 4.17), where the data peak was narrower than the initial MC distribution before $\sigma_{q/p}$ correction. It should be noted that for the $2e2\mu$ channel, no changes are observed since the leading lepton pair consists of electrons, and the ZMC is only applied to the leading pair. This is confirmed in the sub-leading lepton invariant mass m_{34} spectra. In all decay channels, before and after $\sigma_{q/p}$ correction, the m_{34} distributions remain unchanged. Finally, the $m_{4l}^{constrained}$

spectra show small changes which originate from the constrained momenta of the leading pair after ZMC, namely an overall small positive shift of a few MeV and a slightly narrower width with a difference < 1 MeV in the Higgs boson signal MC.

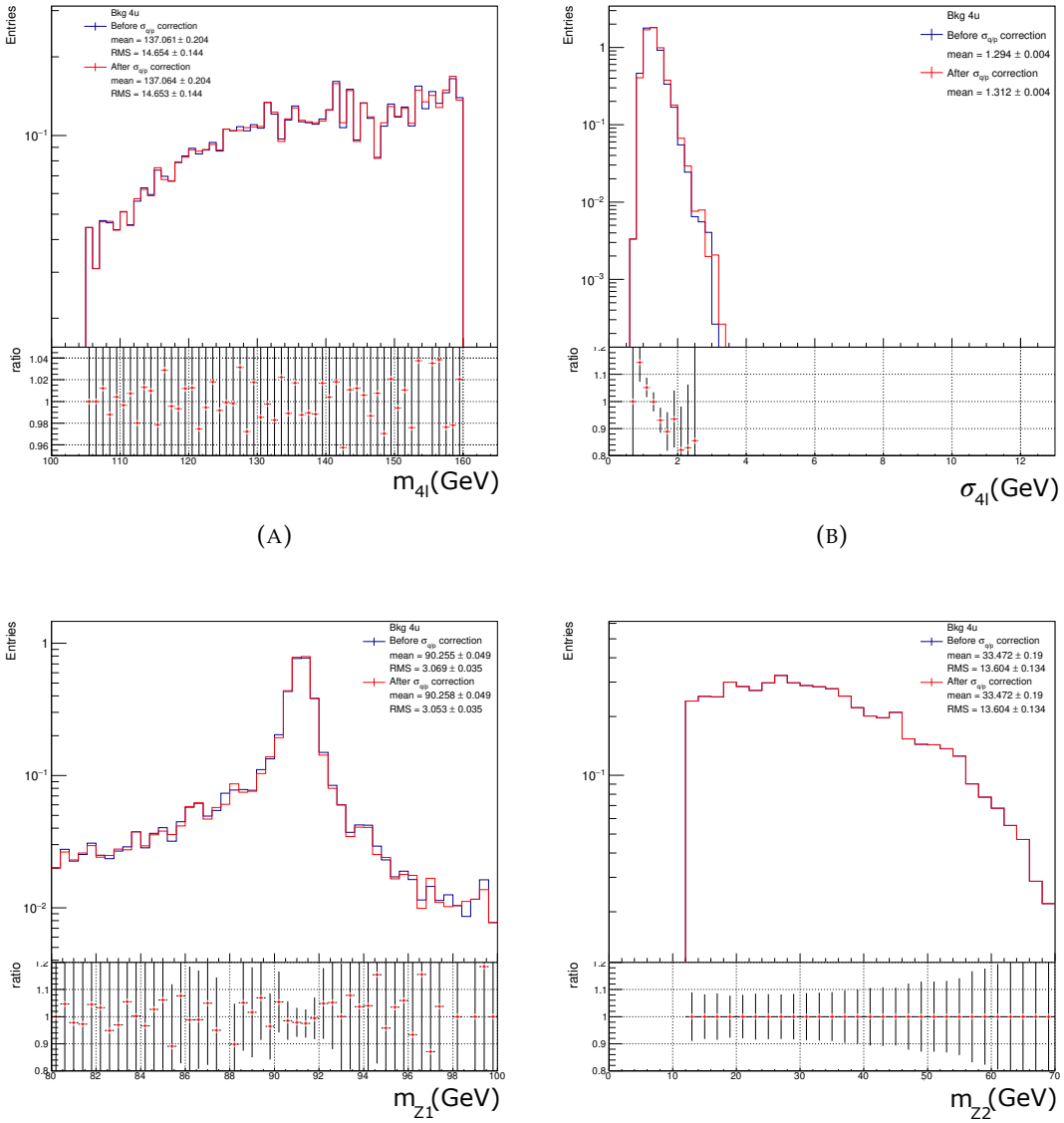

(A) (B)

(C) (D)

FIGURE 4.49: ZZ background MC kinematic distributions in the 4μ signal region before and after applying the $\sigma_{q/p}$ correction.

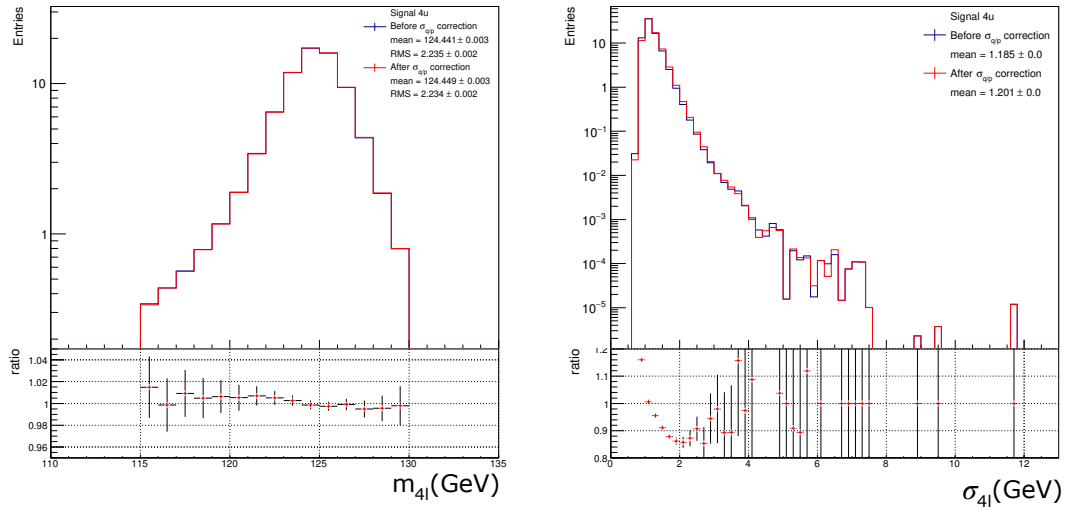

(A) (B)

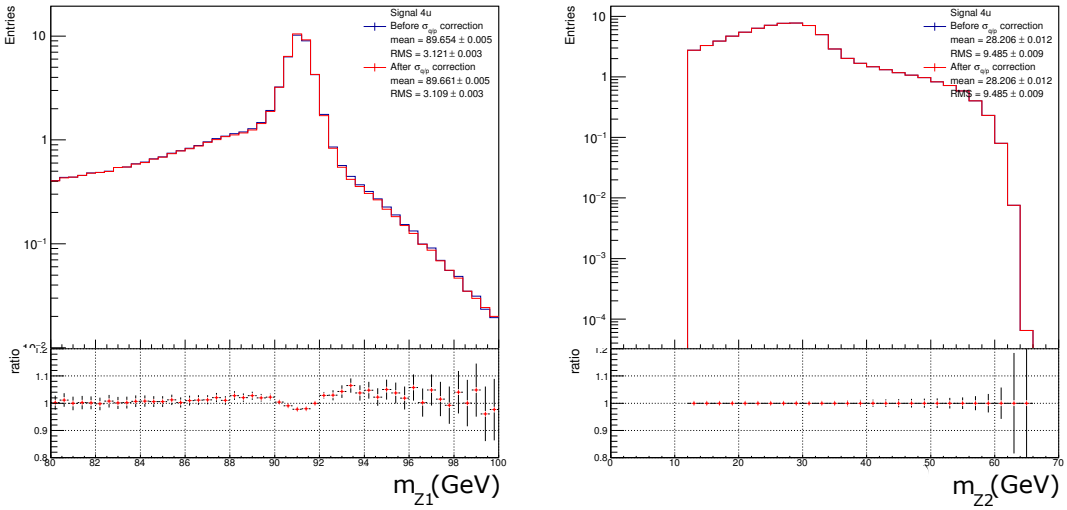

(C) (D)

FIGURE 4.50: Higgs MC kinematic distributions in the 4μ signal region before and after applying the $\sigma_{q/p}$ correction.

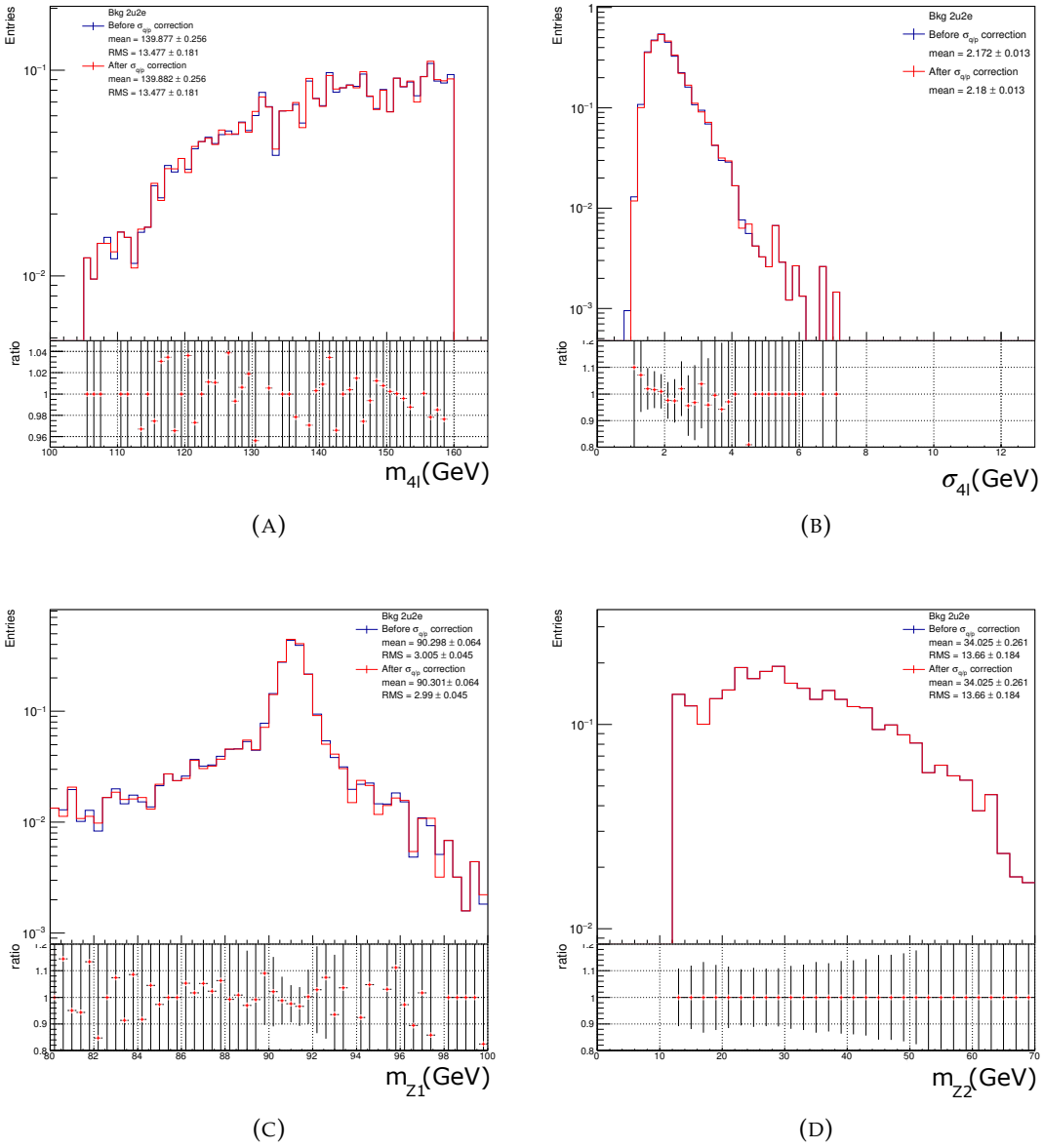

(A) (B)

(C) (D)

FIGURE 4.51: ZZ background MC kinematic distributions in the $2\mu 2e$ signal region before and after applying the $\sigma_{q/p}$ correction.

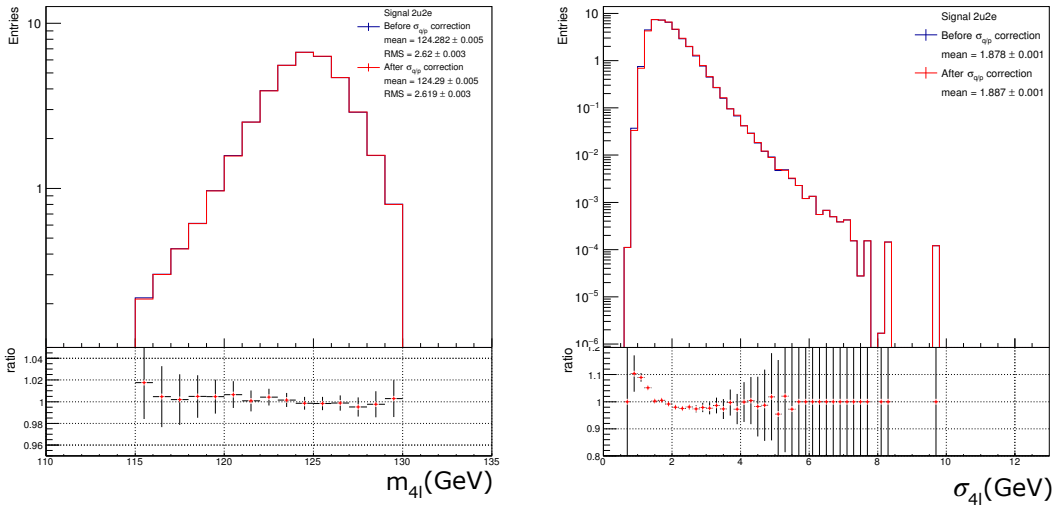

(A) (B)

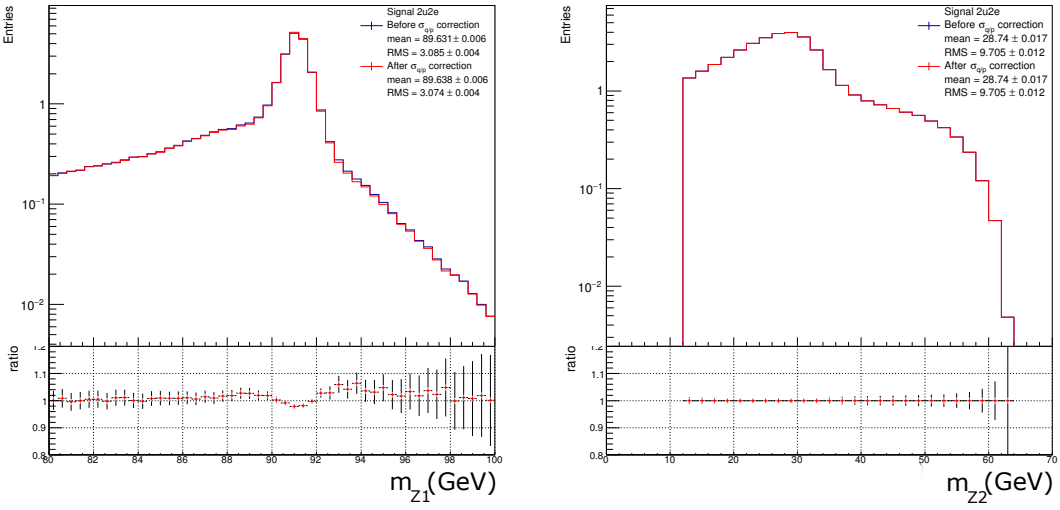

(C) (D)

FIGURE 4.52: Higgs MC kinematic distributions in the $2\mu 2e$ signal region before and after applying the $\sigma_{q/p}$ correction.

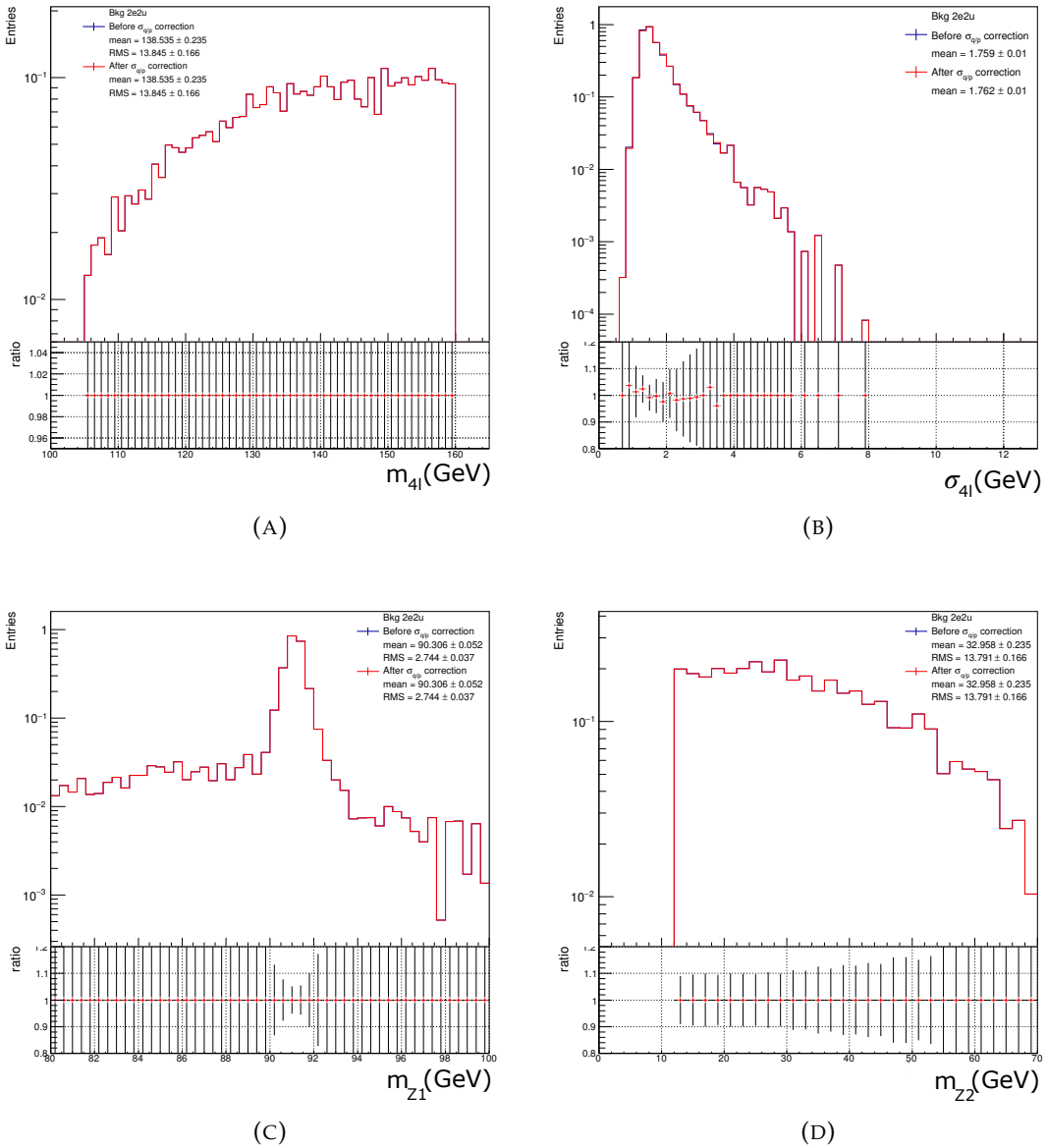

(A) (B)

(C) (D)

FIGURE 4.53: ZZ background MC kinematic distributions in the 2e2μ signal region before and after applying the $\sigma_{q/p}$ correction.

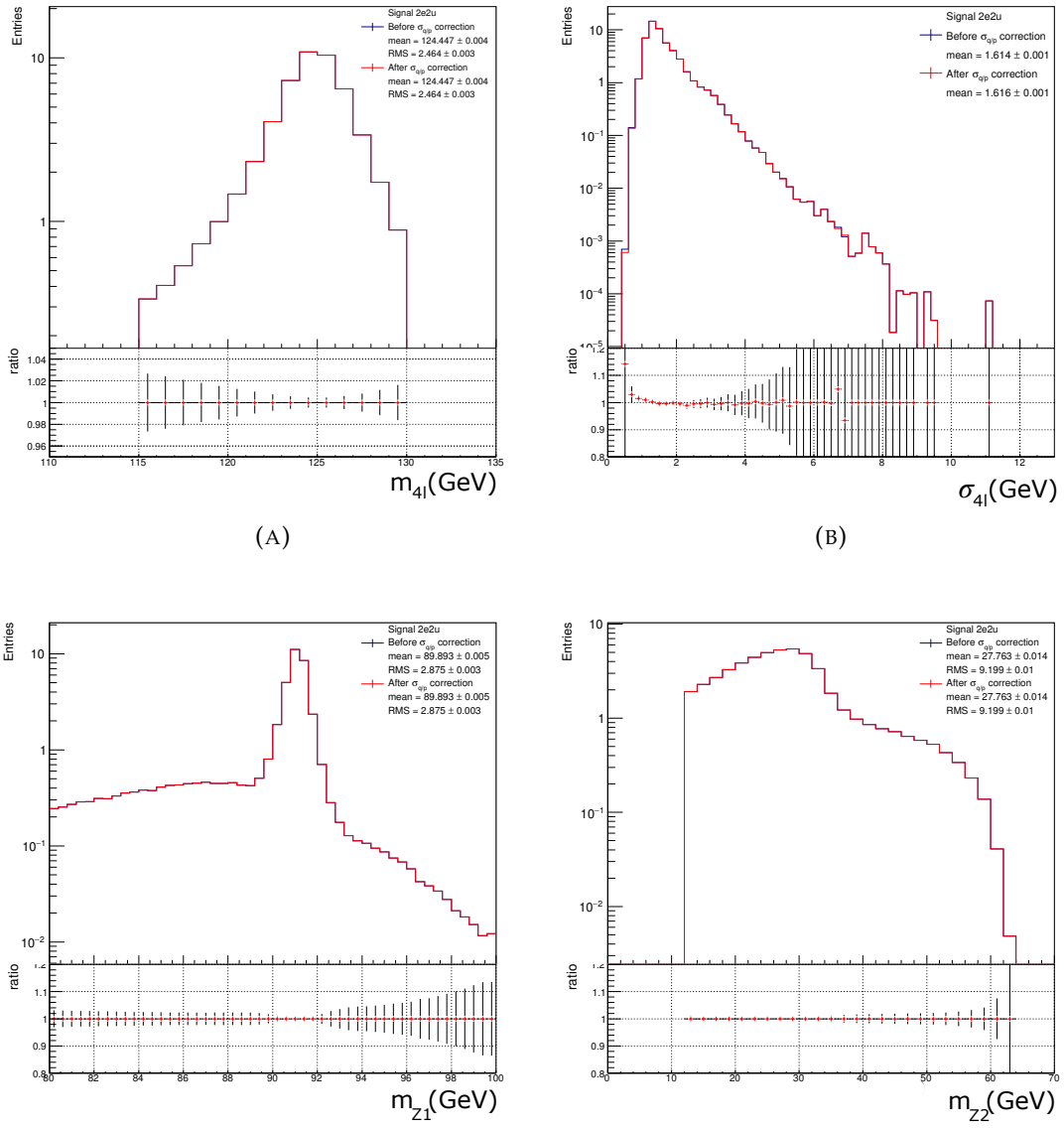

(A) (B)

(C) (D)

FIGURE 4.54: Higgs MC kinematic distributions in the 2e2μ signal region before and after applying the $\sigma_{q/p}$ correction.

4.8 Signal and background model

As mentioned in section 1.4, the real mass distribution of the Higgs boson is expected to follow a narrow relativistic BW lineshape with a width of 4 MeV. On the other hand, the signal observable m_{4l} is distributed as the convolution of the theoretical lineshape with the detector response from the associated reconstructed leptons. In fact, this signal lineshape is entirely governed by the detector response, since this is more than 2 orders of magnitude larger compared to the natural Higgs boson width.

In order to describe the m_{4l} lineshape, an analytic model is fitted to the signal and background MC using an unbinned maximum likelihood fit. For this fit, the following likelihood is constructed,

$$L(m_H|m_{4l}, D_{4l}, \sigma_{4l}) = \prod_i P_i(m_{4l}, D_{4l}, \sigma_{4l}|m_H), \tag{4.38}$$

with i running over the data events. Such a fit will determine the optimal m_H value that maximises the likelihood, given the measured m_{4l}, D_{4l} and σ_{4l} parameters. In practice, this three-dimensional PDF can be simplified with a set of assumptions, while writing it as the product of conditional[7] PDFs, which clarifies the assumptions made. Moreover, a likelihood is written for signal and background separately to take into account their differences. Both likelihoods are then combined with a Poisson likelihood to build the extended likelihood [105], to take into account the Poisson distributed number of observed events used in the m_H measurement.

4.8.1 The signal and background likelihood

In the case of the signal likelihood, the three-dimensional PDF in eq. 4.38 can be factorised as follows,

$$P_s(m_{4l}, D_{4l}, \sigma_{4l}|m_H) = P_s(m_{4l}|D_{4l}, \sigma_{4l}, m_H) \cdot P_s(D_{4l}|\sigma_{4l}, m_H) \cdot P_s(\sigma_{4l}|m_H). \tag{4.39}$$

As mentioned in section 4.6.2, the discriminant D_{4l} is obtained by training a neural network with signal and background kinematic variables and the K_{ZZ^*} discriminant. Since the training does not directly depend on the m_{4l} uncertainty, $P_s(D_{4l}|\sigma_{4l}, m_H)$ can be reduced to $P_s(D_{4l}|m_H)$. Also, the σ_{4l} dependence on m_H is found to be negligible across the different mass points, thus $P_s(\sigma_{4l}|m_H) \approx P_s(\sigma_{4l})$.

The same PDF can be written in the case of the background model, with the same assumptions,

$$P_b(m_{4l}, D_{4l}, \sigma_{4l}) = P_b(m_{4l}|D_{4l}, \sigma_{4l}) \cdot P_b(D_{4l}) \cdot P_b(\sigma_{4l}), \tag{4.40}$$

[7] P(A,B) = P(A | B)·P(B)

where this time the dependence on m_H is not included. In fact, from MC studies $P_s(\sigma_{4l})$ and $P_b(\sigma_{4l})$ are found to be relatively equivalent. For this reason, both PDFs can be excluded from the signal and background terms of the likelihood. Finally, for background, m_{4l} and D_{4l} are assumed to have a negligible dependence on σ_{4l}, such that $P_b(m_{4l}, D_{4l}, \sigma_{4l}) \approx P_b(m_{4l}, D_{4l})$.

4.8.2 The signal and background m_{4l} models

4.8.2.1 Background model

The $P_b(m_{4l}, D_{4l})$ PDF for background is obtained from smoothing the individual background distributions in MC using the RooNKeysPDF algorithm [104]. The smoothed PDFs are derived in each decay channel separately. As mentioned in section 4.3.2, the main background source in the SR comes from the irreducible ZZ continuum. Its shape distribution is extracted from MC, while its normalisation is obtained from data in the unblinded side band CR. For the very rare VVV and ttZ processes with a tiny contributions, shape and normalisation are taken from MC. In the case of the reducible background, each background is first weighted to its data-driven estimate (described in section 4.3.2) before the smoothing. Figures 4.55 and 4.56 show, for the dominant $qq \to ZZ$ process in each final state channel, the PDF projected to the D_{4l} dimension ($P_b(m_{4l}, D_{4l}) \to P_b(D_{4l})$), and the m_{4l} dimension ($P_b(m_{4l}, D_{4l}) \to P_b(m_{4l})$), respectively.

4.8.2.2 Signal model

For the signal model, an analytic function is used to describe $P_s(m_{4l}|D_{4l}, \sigma_{4l}, m_H)$, namely a *double-sided Crystal Ball* (DCB) function [106], whose parameters are derived by simultaneously fitting the m_{4l} distribution in MC for the different simulated mass points. A DCB function has a normally distributed core while the tails follow a power-law,

$$P_s(m_{4l}|D_{4l}, \sigma_{4l}, m_H) = P_{\mathrm{DCB}}(m_{4l}|\mu_{DCB}, \sigma_{DCB}, \alpha_{high}, \alpha_{low}, n_{high}, n_{low}) \tag{4.41}$$

$$= N \times \left\{ \begin{array}{ll} exp\left(-\frac{(x-\mu_{DCB})^2}{2\sigma_{DCB}^2} \right), & \text{for } \alpha_{low} \leq \frac{(x-\mu_{DCB})}{\sigma_{DCB}} \leq \alpha_{high} \\ A_{low} \times (B_{low} - \frac{(x-\mu_{DCB})}{\sigma_{DCB}})^{-n_{low}}, & \text{for } \frac{(x-\mu_{DCB})}{\sigma_{DCB}} < \alpha_{low} \\ A_{hi} \times (B_{hi} - \frac{(x-\mu_{DCB})}{\sigma_{DCB}})^{-n_{high}}, & \text{for } \frac{(x-\mu_{DCB})}{\sigma_{DCB}} > \alpha_{high} \end{array} \right\},$$

where N is a normalisation constant and,

$$A_{low} = \frac{n_{low}}{|\alpha_{low}|} \times exp\left(-\frac{|\alpha_{low}|^2}{2} \right),$$

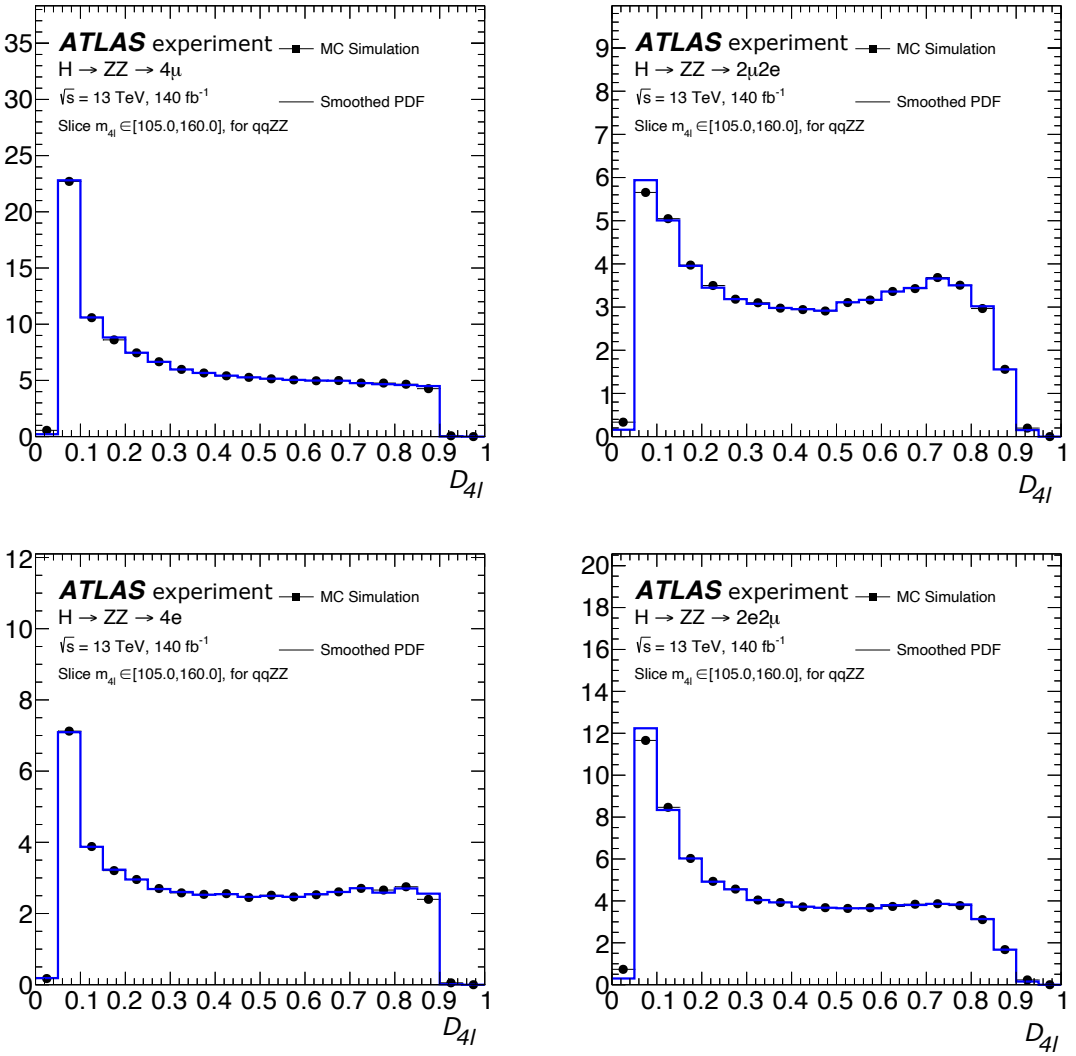

FIGURE 4.55: MC and the smoothed PDF distributions of the dominant $qq \to ZZ$ process projected to the D_{4l} dimension, in the 4μ, $2\mu 2e$, $4e$, and $2e2\mu$ final states.

$$A_{hi} = \frac{n_{high}}{|\alpha_{high}|} \times exp\left(- \frac{|\alpha_{high}|^2}{2} \right),$$

$$B_{low} = \frac{n_{low}}{|\alpha_{low}|} - |\alpha_{low}|,$$

$$B_{hi} = \frac{n_{high}}{|\alpha_{high}|} - |\alpha_{high}|.$$

The mean of the DCB μ is parametrised as a linear function of m_H, which consequently is replaced by the linear coefficients in the DCB function. This choice is motivated from MC studies. Figure 4.57 shows μ as a function of m_H from fitting a DCB function to MC distributions with different mass points. Clearly, a linear dependence is observed across the four decay channels. Moreover, the intercept of this linear function is also found to be linearly dependent on D_{4l}, such that $\mu_{DCB} = f(m_H, D_{4l})$.

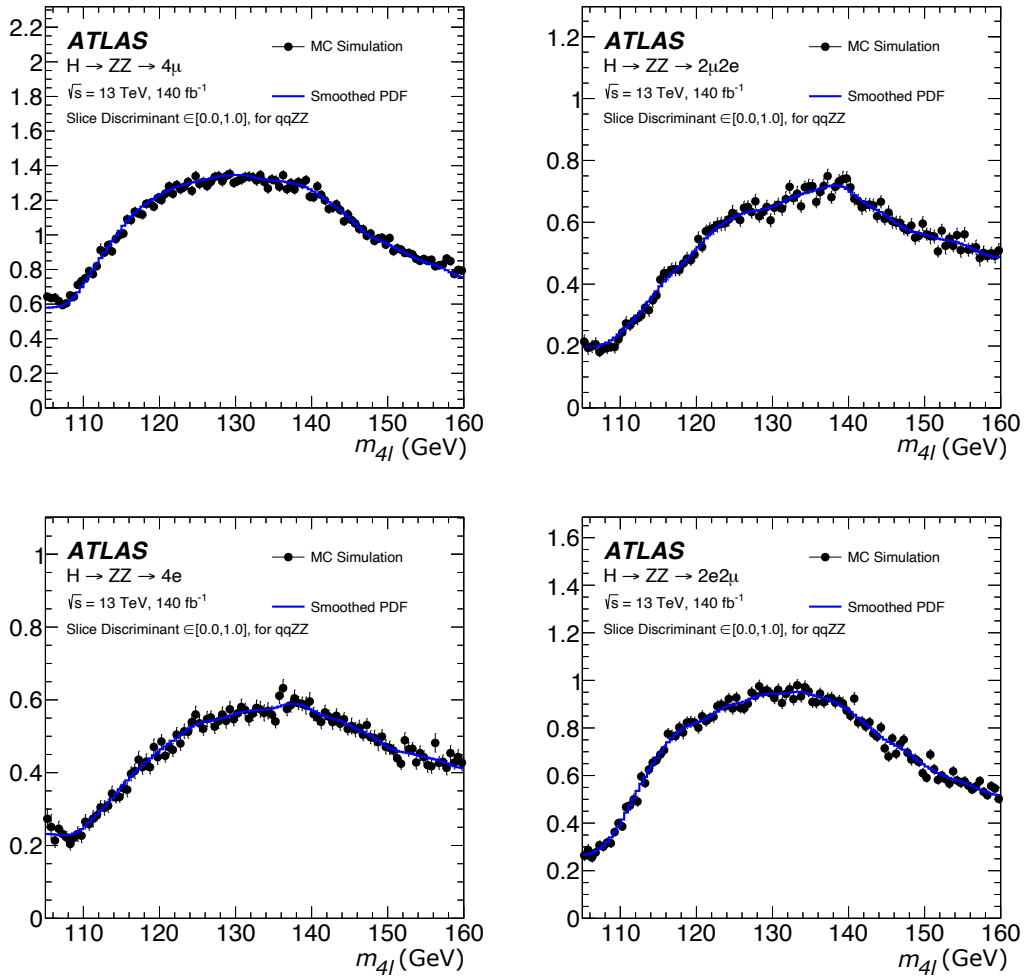

FIGURE 4.56: MC and the smoothed PDF distributions of the dominant $qq \to ZZ$ process projected to the m_{4l} dimension, in the 4μ, $2\mu 2e$, $4e$, and $2e2\mu$ final states.

Also, the width of the DCB, σ_{DCB}, is parametrised as a function of σ_{4l}, which reflects the per-event resolution. As the detector response varies per event, e.g. from the different channels, since electrons and muons are not reconstructed with the same precision, not all quadruplets are measured with the same resolution. In fact, $\sigma_{DCB}(\sigma_{4l})$ is analytically difficult to estimate, therefore, a *quantile regression neural network* (QRNN) is used to predict the per-event resolution. The same tools described for the D_{4l} discriminant are used for the training, namely KERAS [93] and TENSORFLOW [94]. The input variables are the individual lepton kinematics as well as the constrained $p_{T,4l}$ and its uncertainties. The QRNN is trained such that the resolution on m_{4l} in MC, $|m_{4l}^{constr.} - m_{4l}^{gen}|$, is targeted. Figure 4.58 shows the observed σ_{DCB} distribution and that predicted by the QRNN using the side-band CRs. These are defined within $105 < m_{4l} < 115$ GeV and $130 < m_{4l} < 160$ GeV, which as mentioned before are enriched in the irreducible ZZ background events and have a negligible signal contribution. Clearly, the data/MC comparison shows a good agreement.
Figure 4.59 shows for each final state, the first PDF of the signal likelihood eq. 4.39,

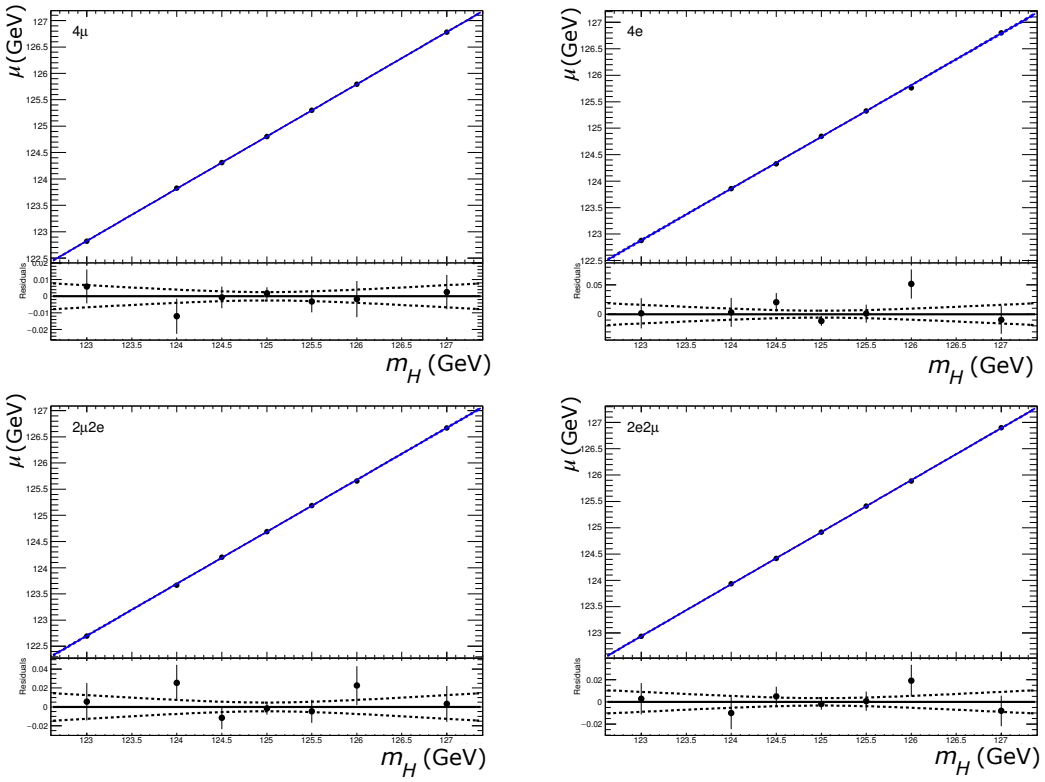

FIGURE 4.57: Fitted μ vs m_H from fitting a DCB model to MC mass points for the 4μ (top left), $4e$ (top right), $2\mu 2e$ (bottom left), and $2e2\mu$ (bottom right) final states. There is a strong linear relationship, however, the slope is not exactly 1 in each case.

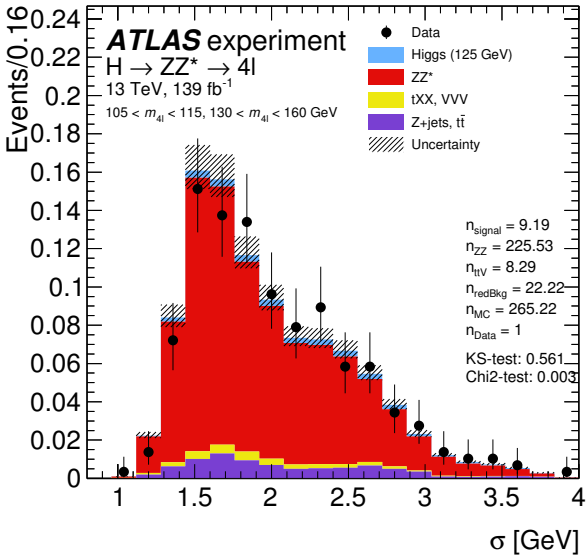

FIGURE 4.58: The observed σ_{DCB} distribution and that predicted by the QRNN using the side-band CRs, corresponding to $105 < m_{4l} < 115$ GeV and $130 < m_{4l} < 160$ GeV.

$P_s(m_{4l}|D_{4l}, \sigma_{4l}, m_H)$, described by a DCB eq. 4.41, with its mean μ_{DCB} and width σ_{DCB} parametrised as a function of D_{4l}, σ_{4l} and m_H. Both distributions are normalised to unity for the comparison. Across all channels, the fitted DCB appears to match the signal MC closely. The second PDF, $P_s(D_{4l}|m_H)$, is obtained by morphing signal templates through interpolation from the ggH, VBF and VH MC at different mass points. Figure 4.60 shows in each final state the original and interpolated $P_s(D_{4l}|m_H)$ PDFs for the different mass points. Furthermore, the normalisation for the signal model is obtained from the likelihood fit, where it is taken as freely floating parameter in each decay channel.

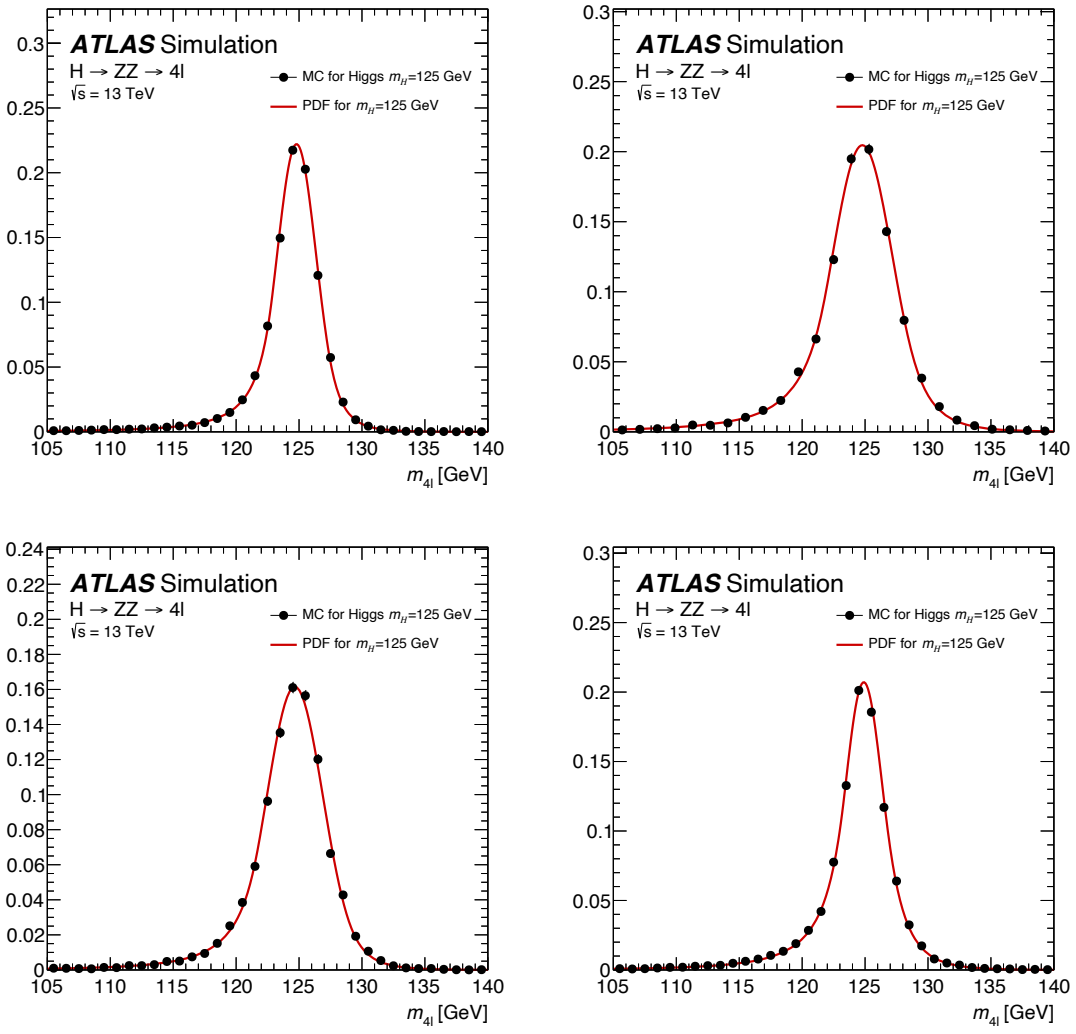

FIGURE 4.59: The $P_s(m_{4l}|D_{4l}, \sigma, m_H)$ signal model described by a DCB, with its mean and width parametrised as a function of D_{4l}, σ_{4l} and m_H, 4μ (top left), $4e$ (top right), $2\mu 2e$ (bottom left), and $2e2\mu$ (bottom right) final states. Both distributions are normalised to unity.

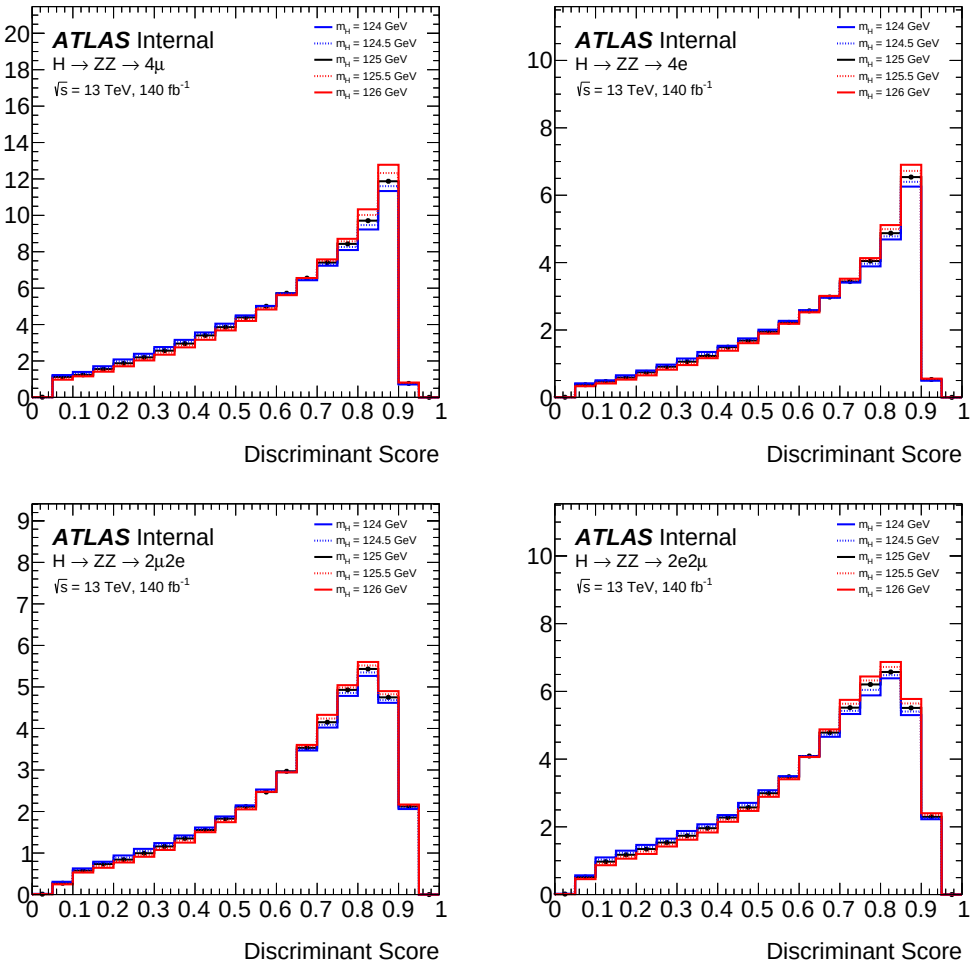

FIGURE 4.60: The original and interpolated $P_s(D_{4l}|m_H)$ PDFs for the different mass points, in the 4μ (top left), $4e$ (top right), $2\mu 2e$ (bottom left), and $2e2\mu$ (bottom right) final states.

4.9 Systematic uncertainties for the mass measurement

On top of the statistical uncertainties governed by the size of the data, all relevant theoretical and experimental systematic uncertainties are taken in account, which originate from choices and assumptions made for the measurement, which reflect the limitations of the strategy. Typical sources of systematics are from theoretical assumptions in MC, reconstruction and calibration of physics objects, data-driven and prediction methods to adjust shape variables, but also models used to describe signal and background distributions. For the likelihood model, two systematic sources can be distinguished; a category impacting the expected number of events, and another affecting the shape of the signal and background PDFs.

In this analysis, normalisation systematics have a negligible impact on the measurement, since the parameter of interest is the mass of the Higgs boson, as opposed to a cross section measurement. These are included in the model where the systematics on the normalisation weights of each MC number of events are varied up and down by one σ_{sys} in each decay channel. Similarly, two models are obtained from varying the shape systematics of the MC distributions. In the case of the signal PDF $P_s(m_{4l}|D_{4l}, \sigma_{4l}, m_H)$, the nominal DCB is refitted to the varied signal MC distributions, allowing the mean and the width of the DCB to float, while the other parameters are fixed to their nominal values. For $P_s(D_{4l}|m_H)$ in the signal likelihood and the background PDF $P_b(m_{4l}, D_{4l})$, all systematics affecting the shape are included and taken into account in the morphing procedure of the PDFs.

The main sources of systematics in this analysis come from those of the leptons. Systematic uncertainties associated to the muon momentum scale and resolution are taken into account [82], which originate from the calibration of their tracks. These affect the shape of the signal and background models. Figure 4.61 shows the impact of the muon momentum scale on the m_{4l} and D_{4l} distribution for signal and ZZ background including all channels. For the signal m_{4l} distribution, the difference in the mean is of the order of 11-16 MeV, while changes in the flat background distribution are negligible. Changes on the D_{4l} distributions of both signal and background are negligible. Analogously, the electron energy scale and resolution systematic uncertainties are also taken in account [50], which are mainly from the calibration of EM energy clusters and correction to the data resolution. Figure 4.62 shows the impact of this on the m_{4l} and D_{4l} distributions for signal and ZZ background including all channels. Similarly to muon systematics, the background distributions are negligible, while a shift of 22 MeV in the signal m_{4l} mean is observed.

Other experimental sources of systematic uncertainties originating from the integrated luminosity recorded by ATLAS [41], pile-up reweighing [41], and the lepton reconstruction, identification and isolation efficiencies [82] [50] are also considered,

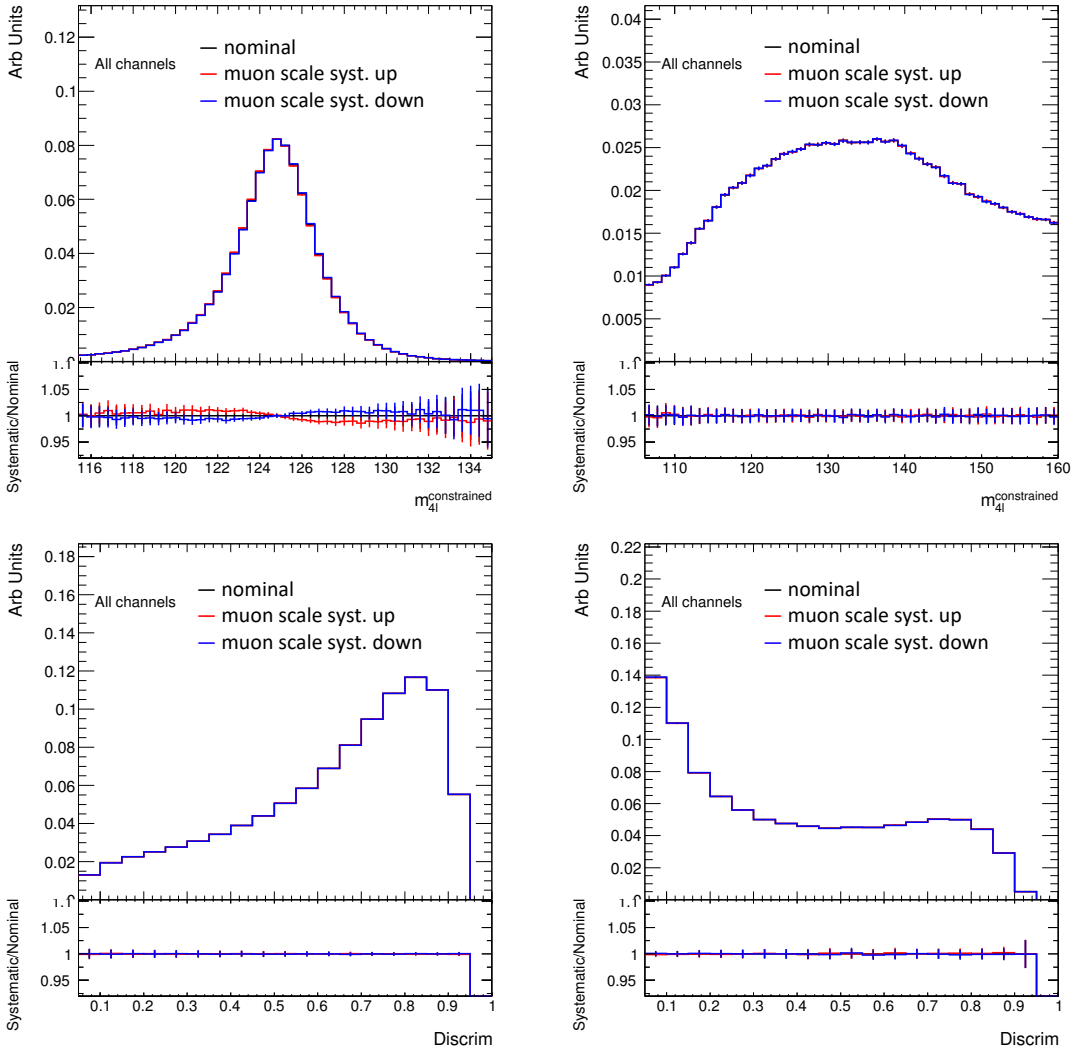

FIGURE 4.61: The impact of the muon momentum scale systematics on the m_{4l} and D_{4l} distributions for signal and ZZ background including all channels. The ratio plots show the deviation from the nominal distributions after varying the systematics with $\pm 1\sigma$.

however, these are found to have a limited effect overall, with a negligible impact on the signal model. Typically, theoretical uncertainties affect predominantly the normalisation and expected yield of the different MC processes. Given the accuracy at which the cross section of each process in MC is calculated (mentioned in section 4.3.2), an uncertainty is attributed to account for the next leading order not included in the calculation. In this analysis, theoretical uncertainties have a slightly larger impact on the D_{4l} than the m_{4l} distribution. Furthermore, additional theoretical uncertainties are assigned to the dominant $q\bar{q} \rightarrow ZZ$ MC. These are obtained from comparing different generators, where their difference is taken as a systematic variation. Table 4.2 shows the leading sources of systematic uncertainties and their impact on the uncertainty of the mass measurement.

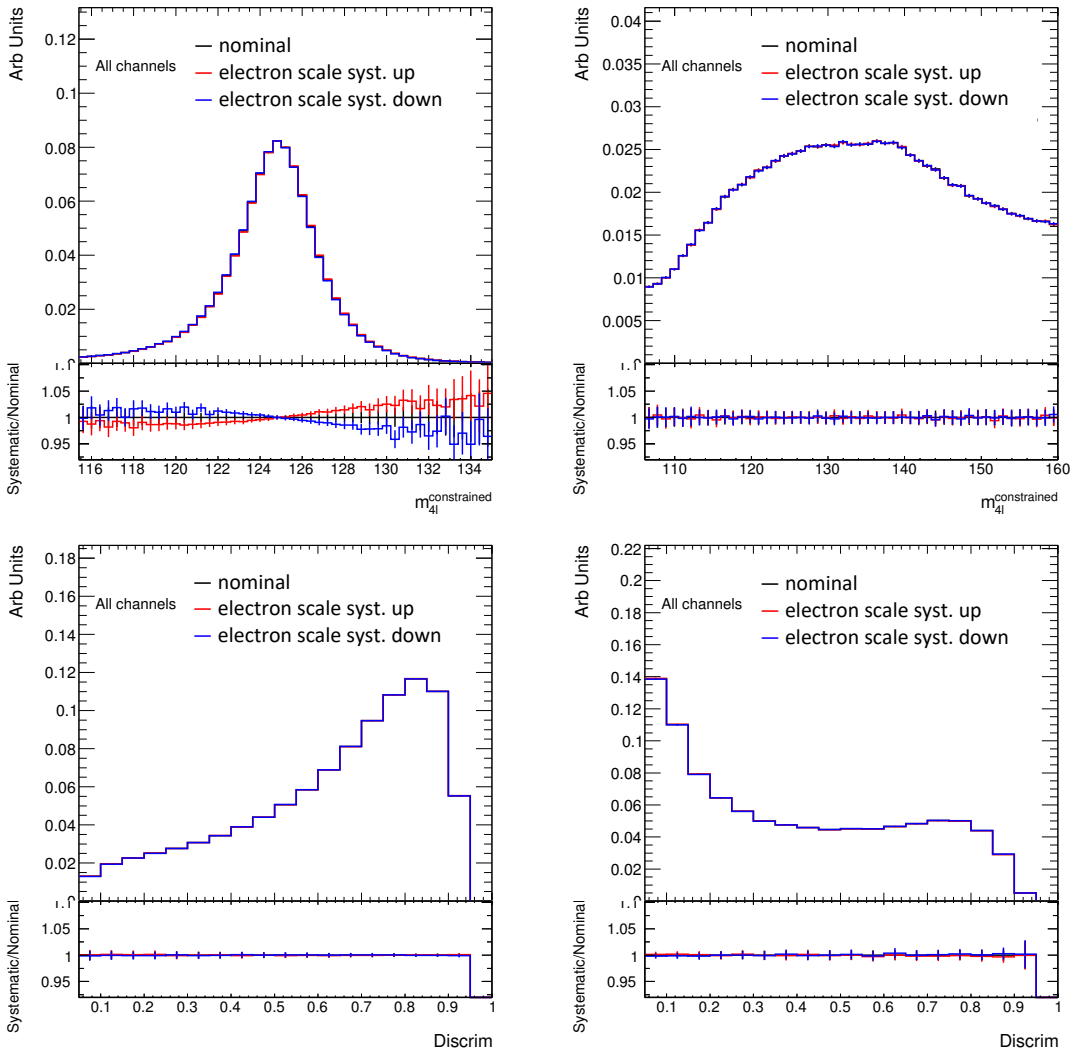

FIGURE 4.62: The impact of the electron energy scale systematics on the m_{4l} and D_{4l} distributions for signal and ZZ background including all channels. The ratio plots show the deviation from the nominal distributions after varying the systematics with $\pm 1\sigma$.

TABLE 4.2: Impact of the leading systematic uncertainties on the mass measurement.

Systematic Uncertainty	Impact (MeV)
Muon momentum scale	28
Electron energy scale	19
Theoretical	14

4.10 Measurement of the Higgs boson mass

4.10.1 Data and MC comparisons in the signal region

After performing the same event selection in data, Table 4.3 shows the number of observed events in data compared to the expected MC events for the previously discussed processes. The observed results are overall in agreement with the expectations. Figure 4.63 shows the all channel inclusive measured m_{4l} distribution in data compared to the expected distributions from MC simulation for signal, ZZ^*, and tXX and VVV, and the data-driven estimated Z+jets and $t\bar{t}$. The uncertainty band includes the statistical and systematic uncertainties on the expectation. Figure 4.64 shows the same comparison in the four individual decay channels. In Appendix B.5, D_{4l} and σ_{4l} distributions in data are shown compared to those from MC.

TABLE 4.3: The expected contribution of the different processes and observed number of events in the SR for $m_{4l} \in [105, 160]$ GeV range.

Final state	Higgs ($m_H = 125$ GeV)	$qqZZ$	$ggZZ$	Reducible background	tXX VVV	Total	Observed
4μ	81 ± 5	119 ± 6	5.1 ± 3.3	7.4 ± 0.5	3.4 ± 0.4	215 ± 9	217
$2e2\mu$	56.0 ± 3.3	80 ± 4	3.4 ± 2.2	8.8 ± 0.6	2.40 ± 0.22	151 ± 6	169
$2\mu 2e$	43.1 ± 3.1	61 ± 4	2.9 ± 1.8	9.3 ± 1.6	2.27 ± 0.29	119 ± 6	115
$4e$	38.9 ± 2.9	53 ± 5	2.7 ± 1.7	7.5 ± 1.0	2.11 ± 0.25	104 ± 6	103
Total	219 ± 13	313 ± 19	14 ± 9	33.5 ± 2.9	10.2 ± 1.0	589 ± 25	604

4.10.2 The Higgs boson mass fit

As mentioned in section 4.8, the extended likelihood is used to perform the measurement of m_H. Given the observed number of events in each decay channel, the nuisance parameters describing the shape and normalisation systematic uncertainties and the previously described PDFs for the signal and background likelihoods, the extended likelihood used for the Higgs boson mass m_H fit is constructed as,

$$
\begin{aligned}
L\left(m_H|\boldsymbol{x},\theta\right) = \prod_c \text{Pois}\left(N_c^{obs}|N_c^{exp}\left(m_H,\mu_c,\theta\right)\right) \quad \times \\
\{\prod_i^{events} \mu_c \cdot N_{S,c}^{exp}\left(m_H,\theta\right) P_{S,c}(m_{4l}|D,\sigma,m_H,\theta) \cdot P_{s,c}(D|m_H,\theta) \quad + \\
\sum_c^{bkgs} N_{B,c}^{exp}\left(\theta\right) P_{B,c}\left(m_{4l},D|\theta\right) \qquad \},
\end{aligned} \tag{4.42}
$$

with N_c^{obs} the number of observed events in decay channel c, θ represents the nuisance parameters for the systematic uncertainties, $N_{s,c}^{exp}$ and $N_{b,c}^{exp}$ the expected number of events in signal and background in decay channel c, which is given by the

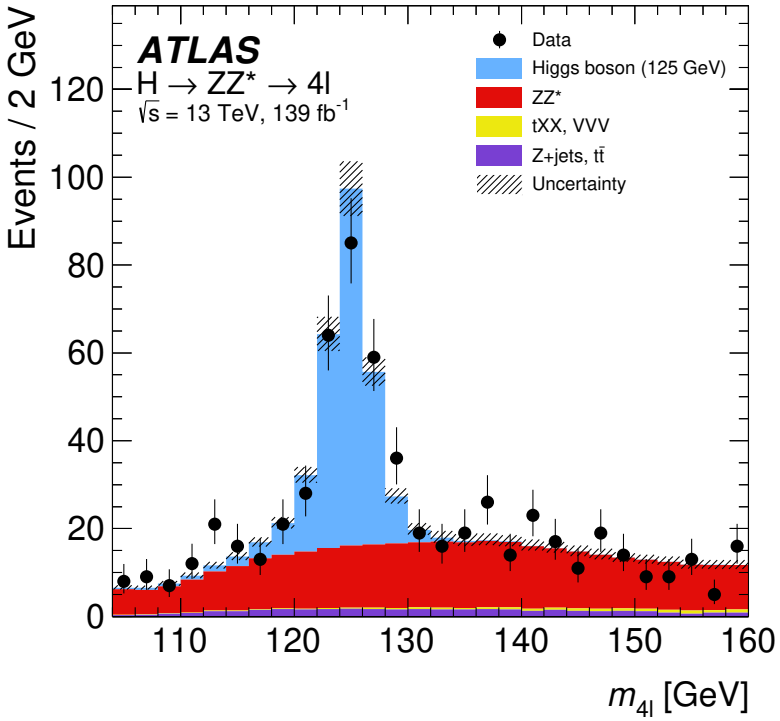

FIGURE 4.63: The measured m_{4l} distribution in data (black points) is shown compared to the expectation, taken from MC simulation for signal, ZZ^*, and tXX and VVV, and from the data-driven estimate for Z+jets and $t\bar{t}$. The uncertainty band includes the statistical and systematic uncertainties on the expectation [1].

sum of the number of events in each of the individual processes,

$$N_c^{exp}\left(m_H, \mu_c, \theta\right) = \mu_c \cdot N_{S,c}^{exp}\left(m_H, \theta\right) + \sum_b^{bkgs} N_{b,c}^{exp}\left(\theta\right), \tag{4.43}$$

with *bkgs* denoting all background processes and μ_c the signal strength in the corresponding decay channel. The best estimate of the Higgs boson mass can be fitted by maximising the following profile likelihood ratio,

$$\lambda(m_H) = \frac{L\left(m_H, \hat{\hat{\theta}}(m_H)\right)}{L\left(\hat{m}_H, \hat{\theta}\right)}. \tag{4.44}$$

where $\hat{\hat{\theta}}$ represents the values of θ that maximises L for a given fixed value of m_H, referred to as the conditional maximum-likelihood estimator of θ. On the other hand, $\hat{m}_H$ and $\hat{\theta}$ are the estimates of the parameters m_H and θ that maximise the likelihood unconditionally. Equivalently, for convenience the test statistic $q(\lambda) = -2ln\lambda$ is used instead to find the best estimate of m_H that minimises this function. The extraction of the m_H estimate is obtained from a simultaneous profile likelihood fit in the four decay channels in the m_{4l} spectrum, corresponding to a range from 105 to 160 GeV. In each of these fits, the m_H, the signal and background normalisation, and

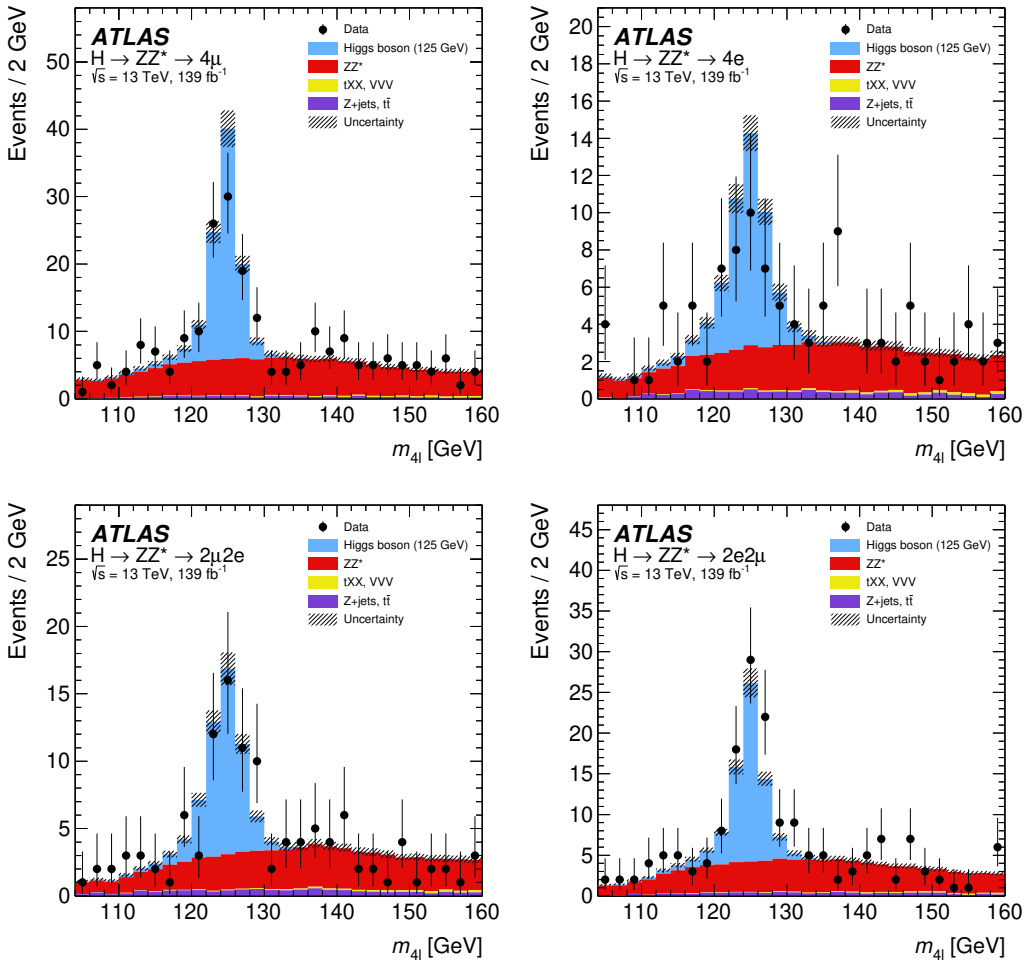

FIGURE 4.64: The measured m_{4l} distribution in data is shown compared to the expectation for each final state channel, taken from MC simulation for signal, ZZ^*, and tXX and VVV, and from the data-driven estimate for Z+jets and $t\bar{t}$. The uncertainty band includes the statistical and systematic uncertainties on the expectation [1].

the nuisance parameters associated to the systematics are free parameters.

4.10.3 The Higgs boson mass results

Finally, after performing a simultaneous maximum-likelihood fit in the four $H \to ZZ \to 4l^{\pm}$ final states in the $m_{4l} \in [105, 160]$ GeV range, the resulting m_H estimate reads,

$$\boxed{m_H = 124.99 \pm 0.18\,(\text{stat.}) \pm 0.04\,(\text{syst.})\ \text{GeV},} \tag{4.45}$$

where the estimation of the statistical uncertainty is obtained by constraining the nuisance parameters to their best-values, while keeping the other parameters unconstrained. Given the total uncertainty, an upper bound on the systematic uncertainty

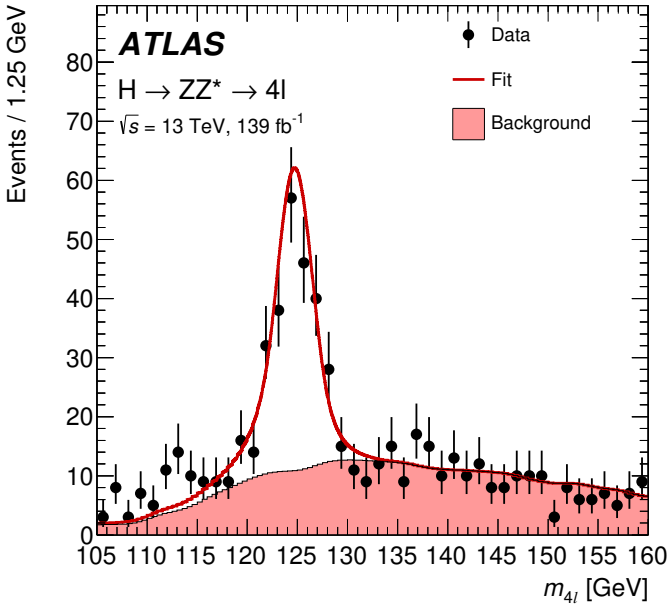

FIGURE 4.65: The m_{4l} data distribution from all decay channels combined (black points) along with the fit result (red curve). The background component of the fit result is shown separately with the red-shaded area [1].

is calculated by subtracting the statistical uncertainty as follows,

$$\sigma_{sys}^{m_H} = \sqrt{(\sigma_{total}^{m_H})^2 - (\sigma_{stat}^{m_H})^2}. \tag{4.46}$$

The total uncertainty measured is found to be 0.19 GeV, and is dominated by the statistical uncertainty. Figure 4.65 shows the m_{4l} data distribution from all decay channels combined, along with the resulting fitted curve. The background contribution from the fit result is also shown separately with the red-shaded area. The fitted normalisation factors are all found compatible with predictions from the SM. Furthermore, m_H is also fitted in the individual final states. The latter comparison for the individual decay channels is shown in Figure 4.66, where a relatively good agreement is observed despite the low number of events. Figure 4.67 (A) shows the profile likelihood functions of each decay channel along with the combined-fit profile likelihood. The horizontal dashed line indicates the location of the 1-σ uncertainty. The fit results obtained in each final state are shown in Figure 4.67 (B) together with the combined result. The total statistical and systematic uncertainty is also given for each measurement, where channels are ordered in decreasing uncertainty. The vertical dashed line indicates the combined result, with the grey band corresponding to its total uncertainty. The fit results on the m_H value from the individual decay channels are all found to be in agreement and consistent with the combined results.

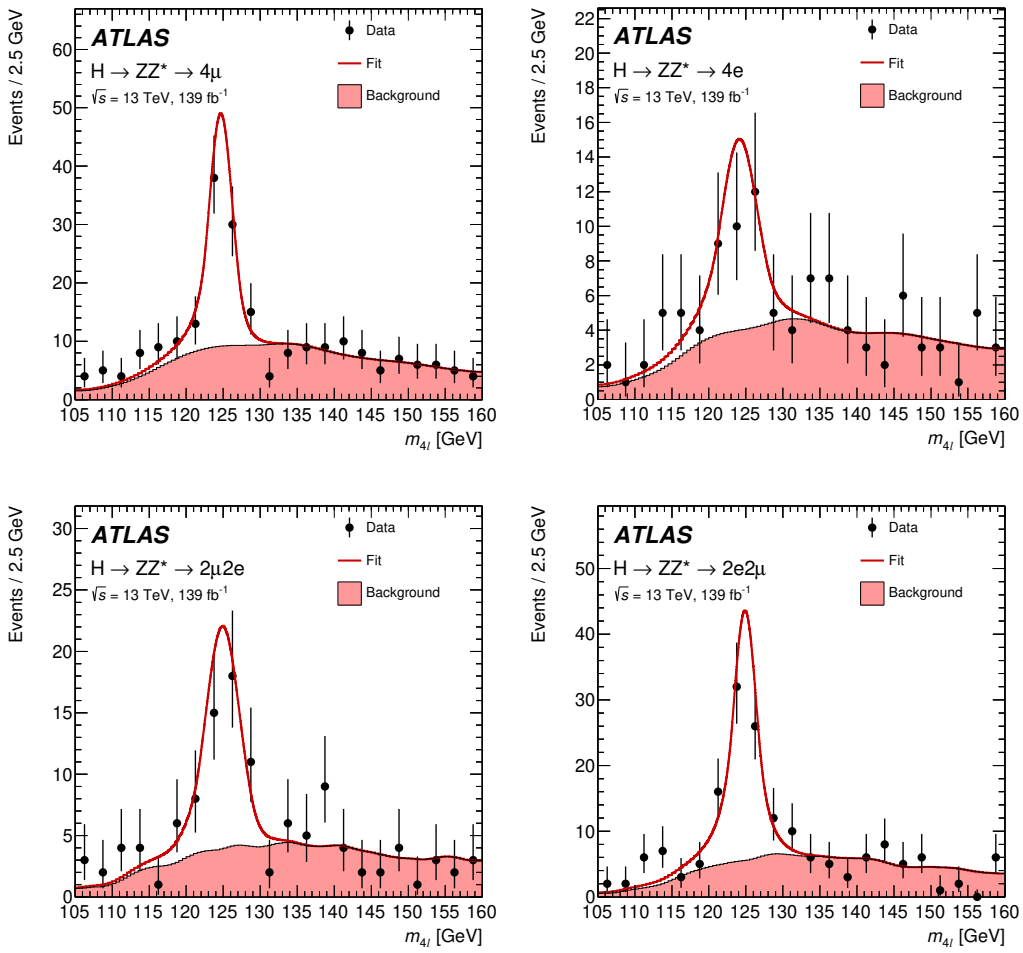

FIGURE 4.66: The m_{4l} data distribution in each decay channel (black points) along with the fit results (red curve). The background component of the fit result is shown separately with the red-shaded area [1].

4.10.4 Run-1 & Run-2 combined results of the Higgs boson mass

Having the measured Higgs boson mass using the Run-2 dataset at 139 fb^{-1} eq. 4.11, and the previously measured Higgs boson mass using the Run-1 dataset at 25 fb^{-1} in the same final states, a combined measurement is performed to obtain a more precise result. Systematic uncertainties in the two measurements are assumed to be uncorrelated, given differences in the centre-of-mass energy of the datasets, improved techniques of estimation and theoretical predictions for the Run-2 measurement. The combined Higgs boson mass result is measured to be,

$$\boxed{m_H = 124.94 \pm 0.17\,(\text{stat.}) \pm 0.03\,(\text{syst.})\ \text{GeV},} \tag{4.47}$$

where a reduction of 10 MeV is observed in both the systematic and statistical uncertainties. The value is consistent with all measurements across the four decay channels and the inclusive measurement shown in Figure 4.67 (B). The observed

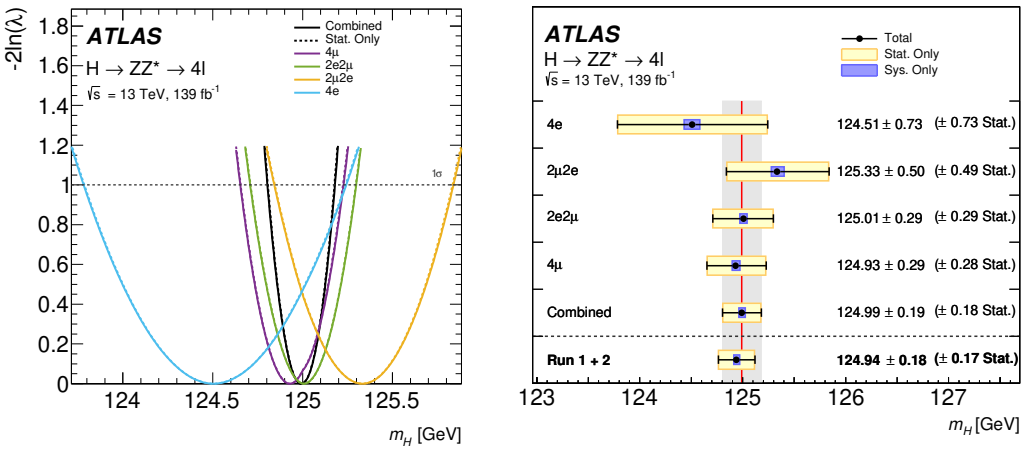

(A) (B)

FIGURE 4.67: (A) The negative log-likelihood function for the fit in each final state, and the combined-measurement (black). The solid curves include the systematic uncertainties, in contrast to the dashed curves. The horizontal dashed line indicates the location of the 1-σ uncertainty. (B) The fitted m_H results obtained in each final state together with the combined result. The vertical dashed line indicates the combined result, and the grey band its total uncertainty [1].

negative log-likelihood function for the Run-1, Run-2 and combined measurement is shown in Figure 4.68.

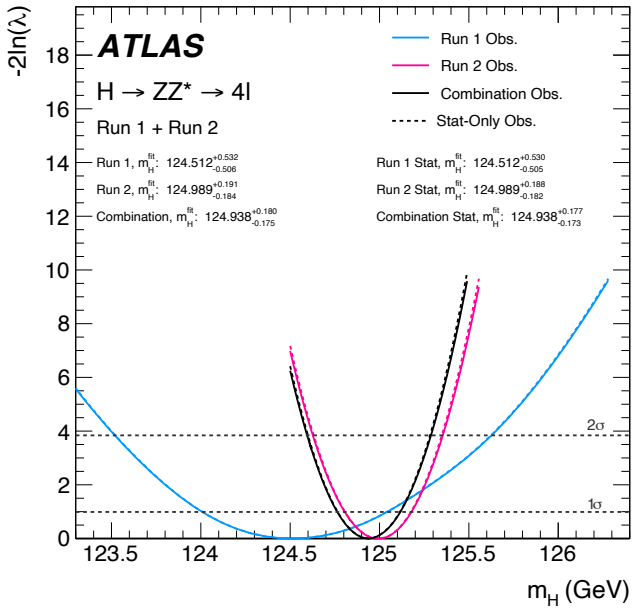

FIGURE 4.68: The observed negative log-likelihood functions for the Run-1, Run-2 and combined measurement. The solid curves include the systematic uncertainties, in contrast to the dashed curves. The horizontal dashed lines indicate the location of the 1- and 2-σ uncertainties [1].

4.11 Summary & Conclusion

As demonstrated in section 1.2.4, the introduction of the Higgs field is crucial to explain the mass acquisition of the massive Standard Model particles. This could be explained through the Higgs mechanism with spontaneous symmetry breaking, from which the existence of a massive scalar boson is predicted, a.k.a. the Higgs boson. The discovery of the latter boson in 2012 by the ATLAS and CMS collaborations has been a key step in the understanding of the electroweak symmetry breaking, and another firm confirmation of the Standard Model theory. As mentioned in section 1.4, the Higgs boson mass is one of the free parameters of the theory, which to the best of available knowledge has to be measured empirically. Furthermore, it is an essential parameter to predict its production cross sections and decay branching ratios to Standard Model particles.

In this thesis, a measurement of the mass of the Higgs boson, m_H, is presented using proton-proton collision data from the Large Hadron Collider at a centre-of-mass energy of $\sqrt{s}$ = 13 TeV recorded by the ATLAS detector. The dataset corresponds to the 2015-2018 period of data-taking, and has an integrated luminosity of 139 fb^{-1}. The mass measurement was performed in the $H \to ZZ \to 4l^{\pm}$ final states, a.k.a the golden decay channels, including muons and/or electrons. As mentioned in section 4.2, despite the relatively low branching ratio, the $H \to ZZ \to 4l^{\pm}$ decay channels are excellent for the mass measurement, due to the high signal over background ratio and the fully reconstructed final states. In ATLAS, electrons and muons are reconstructed and identified with high efficiency and precision, resulting in a good mass resolution and a clean signal signature from these latter final states.

The Higgs boson mass measurement was performed using an unbinned maximum likelihood fit on the invariant mass of the four reconstructed leptons m_{4l}, passing the event and object selection 4.4. The signal m_{4l} distribution was analytically modelled using a double-sided Crystal Ball function, within the range $m_{4l} \in [105, 160]$ GeV. On top of an efficient event selection of Higgs boson candidates and an optimal background estimation, techniques to reduce the uncertainty on m_H were exploited, with the kinematic Z-mass constraint fit providing the largest gain of up to 19% in the reduction of the m_H uncertainty, followed by the final state radiation recovery, the use of neural networks for an additional discrimination between signal and background events, and a event-based estimation of the uncertainty on m_H.

For this measurement, a number of challenges were encountered, namely the underestimation of the m_H uncertainty and the disagreement between data and simulation in the di-muon invariant mass spectrum after the Z-mass constraint fit. After investigation, the uncertainties of the muon track parameters were found mismodelled in simulation compared to data, which were at the origin of the latter contradictions.

Moreover, the most prominent impact was found to originate from the muon track momentum uncertainties $\sigma_{q/p}$, since the latter quantity is directly propagated for the estimation of the m_H uncertainty and is crucial for the Z-mass constraint fit. The calibration of these quantities was found to be a difficult task due to the complex geometry of the Muon Spectrometer, which disabled the use of trivial correction methods. This was finally solved by developing a non-parametric bias-correction method based on quantile mapping. After the calibration of the muon track momentum uncertainties, the constrained di-muon invariant mass was restored and the estimation of the m_H uncertainty was improved, which was initially underestimated.

Finally, the Higgs boson mass using the ATLAS Run-2 dataset in the $H \to ZZ \to 4l^{\pm}$ was measured to be,

$$\boxed{m_H = 124.99 \pm 0.18 \text{ (stat.)} \pm 0.04 \text{ (syst.) GeV},}$$

with on top of this result, a combined measurement using the the ATLAS Run-1 and Run-2 datasets being performed, resulting in the best measurement of the Higgs boson mass performed by the ATLAS experiment,

$$\boxed{m_H = 124.94 \pm 0.17 \text{ (stat.)} \pm 0.03 \text{ (syst.) GeV}.}$$

Both measurements are consistent with all previously measured values, summarised in section 4.1. These results were published and can be found in [1]. Furthermore, the latest measurement of the Higgs boson cross section times the branching ratio for the $H \to ZZ \to 4l^{\pm}$ decays was found to be 1.34 ± 0.12 pb [108], which is consistent with the Standard Model predicted value of 1.33 ± 0.08 pb [25], assuming m_H = 125 GeV. As the latter assumption is consistent with the mass measurements in this thesis, both results provide a confirmation of the Standard Model prediction.

Chapter 5

Study of Effective Field Theory operators modifying electroweak quartic gauge couplings in $\gamma\gamma \to 4\ell$ events using $\sqrt{s} = 13$ TeV proton-proton collision events recorded by the ATLAS detector

5.1 Introduction to photon-induced physics at the LHC

The Standard Model electroweak sector is rich in phenomenology of gauge-boson interactions. Many of these predicted processes have been observed, however, a number are still undiscovered. These are often rare processes which are difficult to produce in the current experimental facilities. Among others, photon-induced processes, where two initial photons interact with each other, are extremely rare due to their small cross section in combination with the associated experimental challenges. Since there are no efficient ways to produce beams of photons with a high enough energy (the most powerful current lasers typically produce photons at the MeV scale) to probe the electroweak scale, such processes can be only measured in lepton and hadron colliders, in events where the accelerated charged particles emit high energy photons. Using the Equivalent Photon Approximation [90], where the Lorentz contracted electromagnetic field of an ultrarelativistic charged particle is approximated by photons moving in parallel with the latter particle, it is possible to predict the cross section of photon-induced processes using charged particle colliders such as the LHC. In the SM, di-photon vertices are not allowed in QED interactions, and thus photons do not interact directly. Nevertheless, the interaction can happen indirectly, e.g. through a virtual fermion loop.

There is one electroweak interaction where photons do interact directly. Recently, the observation of photon-induced production of a W boson pair, $\gamma\gamma \to WW$, was reported [99], using 139 fb^{-1} of LHC proton-proton collision data taken at $\sqrt{s}$ = 13 TeV recorded by the ATLAS experiment during the years 2015-2018. The measurement was performed in the leptonic channels of the W bosons, $WW \to e\nu\mu\nu$, where only events with an electron and a muon of opposite electric charge were selected (the same lepton-flavour channels are dominated by the $\gamma\gamma \to l^+l^-$ process). To suppress the quark and gluon-induced WW production, which is by far the most dominant process for the latter production, the measurement is performed by selecting events where the interaction vertex is free from additional charged particle tracks. Within a fiducial volume corresponding to the acceptance of the ATLAS detector and the analysis event selection, the cross section was measured to be 3.13 $\pm$ 0.31 (stat.) $\pm$ 0.28 (syst.) fb. This value was found to be in agreement with the SM prediction.

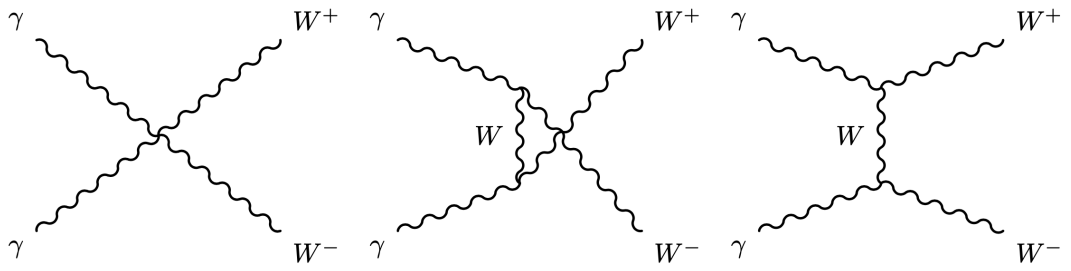

FIGURE 5.1: The leading order Feynman diagrams of the $\gamma\gamma \to WW$ process through triple and quartic self-interactions.

In fact, photon-induced processes offer a unique way to probe the electroweak sector. For instance, the $\gamma\gamma \to WW$ process involves triple and quartic self-interactions of the electroweak bosons at leading order, and is a direct test of the electroweak gauge structure of the SM. Figure 5.1 shows the Feynman diagrams of the $\gamma\gamma \to WW$ process through triple and quartic self-interactions. Such processes are sensitive to anomalous gauge-boson interactions, which can serve as a basis for interpretations of BSM trilinear and quartic gauge couplings. After a successful measurement of the $\gamma\gamma \to WW$ process, one can explore other photon-induced processes sensitive to anomalous gauge-boson interactions, or putting a stronger affirmation on the SM predictions. In this chapter, a MC simulation study based on Run 2 data is presented, where possible BSM contributions from the photon-induced four lepton production (discussed in the next section) are investigated in the context of the SMEFT.

5.2 The photon-induced four-lepton production.

Another possible photon-induced process is the production of four leptons, $\gamma\gamma \to 4l^{\pm}$, with the same final state signature as the $H \to ZZ \to 4l^{\pm}$ process discussed

in the previous chapter . It is tempting to think that the four leptons would originate from a pair of Z/γ^* bosons, however, neutral gauge boson self-interaction couplings are not predicted in the SM. Figure 5.2 shows Feynman diagrams of the SM photon-induced four lepton production through QED vertices. In BSM scenarios, there could be additional diagrams where the production proceeds through neutral gauge couplings. Therefore, measuring the $\gamma\gamma \to 4l^{\pm}$ process, can serve as a direct test of the SM. Figure 5.3 shows possible tree-level BSM contributions to the $\gamma\gamma \to 4l^{\pm}$ process through triple and quartic neutral gauge-boson vertices. The grey circles represent anomalous gauge couplings in which new heavy particles can contribute in the interaction. In the next section, the strategy for measuring the photon-induced $\gamma\gamma \to 4l^{\pm}$ process is briefly discussed.

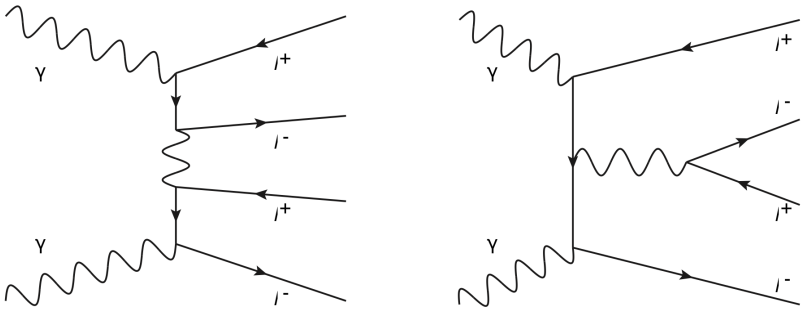

FIGURE 5.2: The tree-level Feynman diagram of the SM photon-induced four lepton production process.

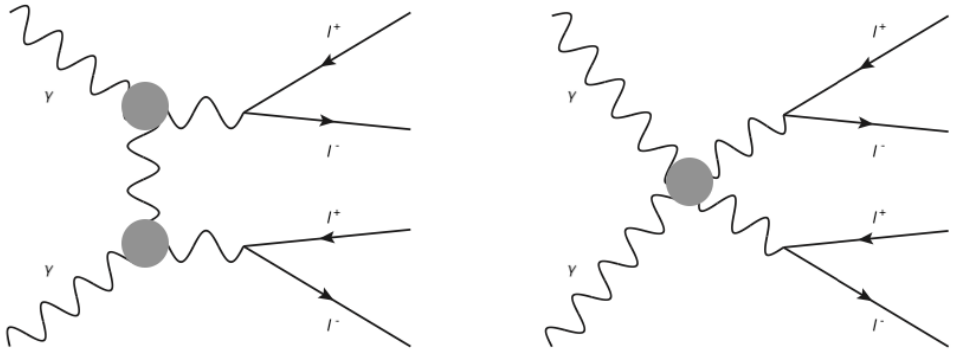

FIGURE 5.3: Feynman diagrams of possible BSM triple and quartic neutral gauge-boson interactions involved in the photon-induced four lepton production.

5.2.1 Event selection of the $\gamma\gamma \to 4l^{\pm}$ process.

In general, the $\gamma\gamma \to 4l^{\pm}$ event selection follows the exact same strategy used in the $\gamma\gamma \to WW$ analysis [99]. The main differences are in the lepton kinematic requirements and the vertex calculation, which is based on four leptons instead of two. Moreover, the four lepton quadruplet selection is very similar to the $H \to ZZ \to 4l^{\pm}$

analysis (described in section 4.4). Similarly, the final state particles considered are electrons and muons. There are three decay channels corresponding to the combination of all the SFOS leptons, defining the quadruplet. Four-lepton events are triggered by a list of di-, and tri-lepton triggers, which can found in Appendix B. Both leptons are required to pass the loose identification criteria and the isolation requirements discussed in section 4.4. Given the rarity of the process, a very low p_T-threshold is used, muons and electrons are preselected if their p_T exceeds, respectively, 3 GeV and 4.5 GeV. For the η range considered, electrons are selected within $|\eta| < 2.47$ and muons within $|\eta| < 2.7$.

The major difference with the $H \to ZZ \to 4l^{\pm}$ analysis is the so-called *exclusivity requirement*, where events are required to have no additional reconstructed charged particle tracks in addition to those from the four leptons in vicinity of the quadruplet vertex. Moreover, using the primary vertex selection from section 1.4 results in a significant loss of events. Therefore, the definition of the vertex is customised such that only tracks associated to reconstructed leptons are used, while selecting only vertices associated to the latter tracks. The weighted average position of the leptons is calculated as,

$$z_{vtx}^{4l} = \frac{z_{l_1}\sin^2\theta_1 + z_{l_2}\sin^2\theta_2 + z_{l_3}\sin^2\theta_3 + z_{l_4}\sin^2\theta_4}{\sin^2\theta_1 + \sin^2\theta_2 + \sin^2\theta_3 + \sin^2\theta_4} \tag{5.1}$$

with θ the angle between the lepton and the beam axis. The $\sin\theta$ is used as an approximation of the z resolution of the lepton. After an MC study, an optimal window size of $\Delta z = \pm 1$ mm, centred at z_{vtx}^{4l} is chosen where zero additional tracks are required.

Candidate events from the $\gamma\gamma \to 4l^{\pm}$ process are identified by the presence of at least four leptons passing the preselection described above. Events are then selected if at least two SFOS pairs can be formed given the preselected leptons. If there are more than two pairs, the pair with an invariant mass closest to the Z-boson mass are chosen. Consequently, the closest pair to the Z mass is tagged as the leading pair, and the second the subleading pair. In order to veto J/ψ events, the invariant mass of all possible SFOS pairs is required to have $m_{ll} > 5$ GeV. Given the two SFOS pairs, a quadruplet is formed. Analogously to the $H \to ZZ \to 4l^{\pm}$ analysis, there are four possible quadruplets when discriminating the pairs based on their invariant mass, namely $4e$, 4μ, $2e2\mu$ and $2\mu2e$. In addition to the previous kinematic cuts, the leading lepton in p_T in the leading pair is required to have a $p_T > 15$ GeV, and the second leading lepton in p_T (not necessarily from the leading pair) $p_T > 10$ GeV.

Background processes to the $\gamma\gamma \to 4l^{\pm}$ process are the same as those of the $H \to ZZ \to 4l^{\pm}$ process, where the latter is also a background process to the former. In contrast with the $H \to ZZ \to 4l^{\pm}$ measurement, the irreducible and reducible background contributions are all estimated from the MC simulation. Figure 5.4 shows the

distribution of the number of reconstructed tracks excluding those from the quadruplet, n_{trk}, within a $\pm$1mm range around the vertex, in data and MC. The $n_{trk} = 0$ bin is the SR for $\gamma\gamma \rightarrow 4l^{\pm}$ measurement and is therefore blinded. Analogously to the $H \rightarrow ZZ \rightarrow 4l^{\pm}$ measurement, the ZZ continuum is by far the most dominant process, while other background sources have very small contributions. Good agreement between data and MC is observed in the $n_{trk} > 0$ bins. From the SR including all final states, 8.9 ± 3.0 (statistical uncertainties only) SM signal events are expected from MC, and 8.2 ± 2.9 background events. Figure 5.5 shows the invariant masses of the quadruplet m_{4l} and the leading pair m_{01} in the $n_{trk} > 0$ CR for data and MC. Despite a very low number of events, the agreement is relatively stable, reflecting a relatively good background modelling. Figures 5.6 and 5.7 show, respectively, the MC distribution of the same kinematic variables (and the sub-leading pair invariant mass) and the p_T distributions of the four individual leptons in the SR. In general, one can conclude that the photon-induced signal has a non-resonant behaviour, which follows the background distribution closely. From the individual p_T distributions of the four leptons, it is clear that keeping the p_T threshold low has the benefit of increasing the signal acceptance. Finally, the measurement of the $\gamma\gamma \rightarrow 4l^{\pm}$ process is still a work in progress, with as its main goal the optimisation of the event selection and the increase of the signal over background ratio. Therefore, data events in the SR remain blinded for the rest of this chapter.

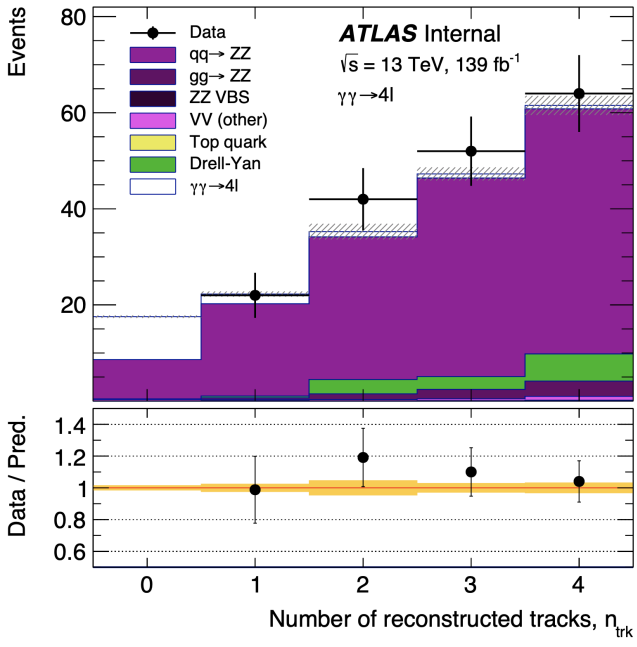

FIGURE 5.4: The number of reconstructed track distribution, n_{trk}, in data and MC. The $n_{trk} = 0$ is the SR and is therefore blinded. Good agreement between data and MC is observed in the $n_{trk} > 0$ bins.

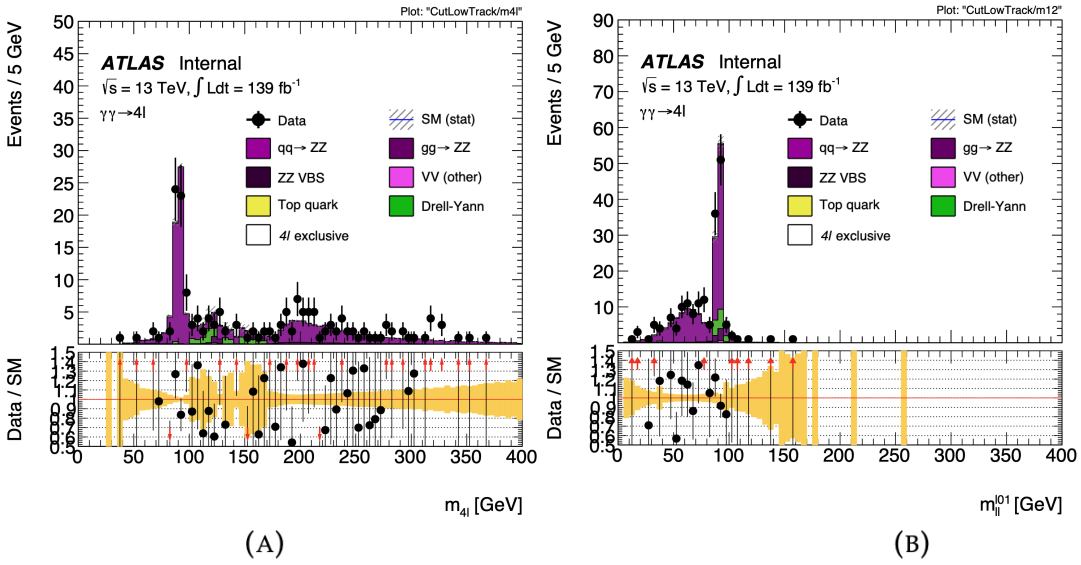

(A) (B)

FIGURE 5.5: The invariant mass distribution of the quadruplet (A) and leading pair (B) in the $0 < n_{trk} < 5$ CR for data and MC.

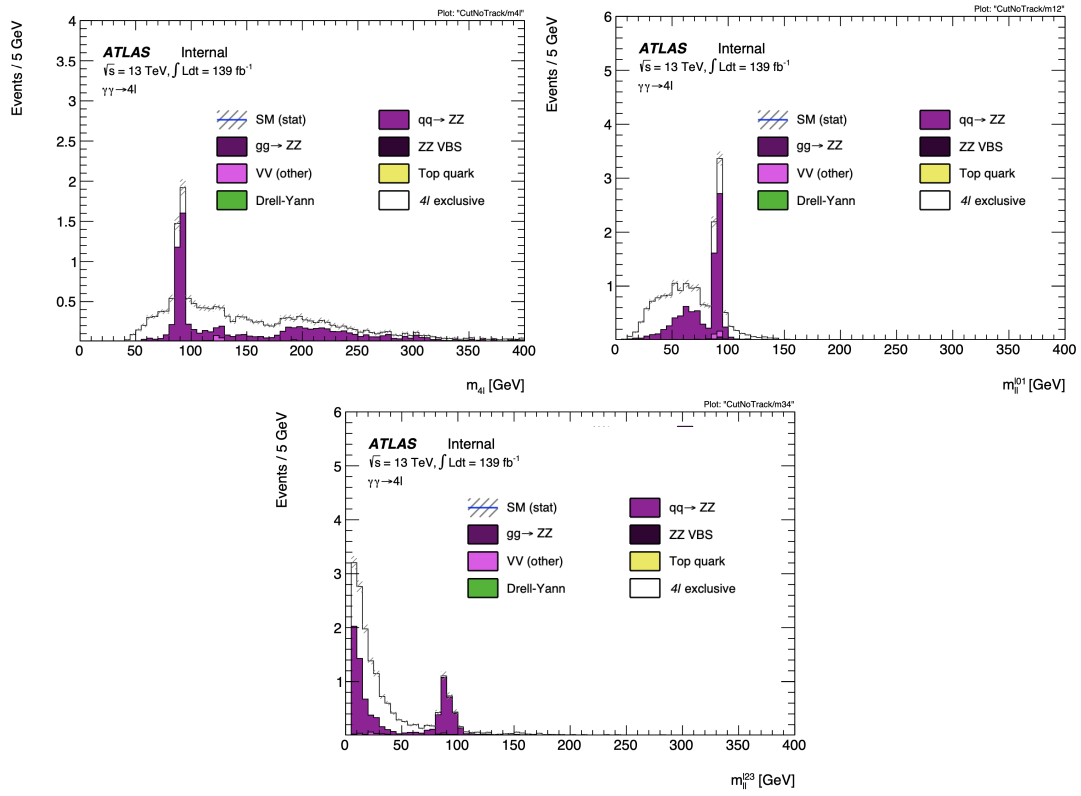

FIGURE 5.6: The signal and background MC invariant mass distribution of the quadruplet (A) and leading pair (B) and sub-leading pair (C) in the $n_{trk} = 0$ SR.

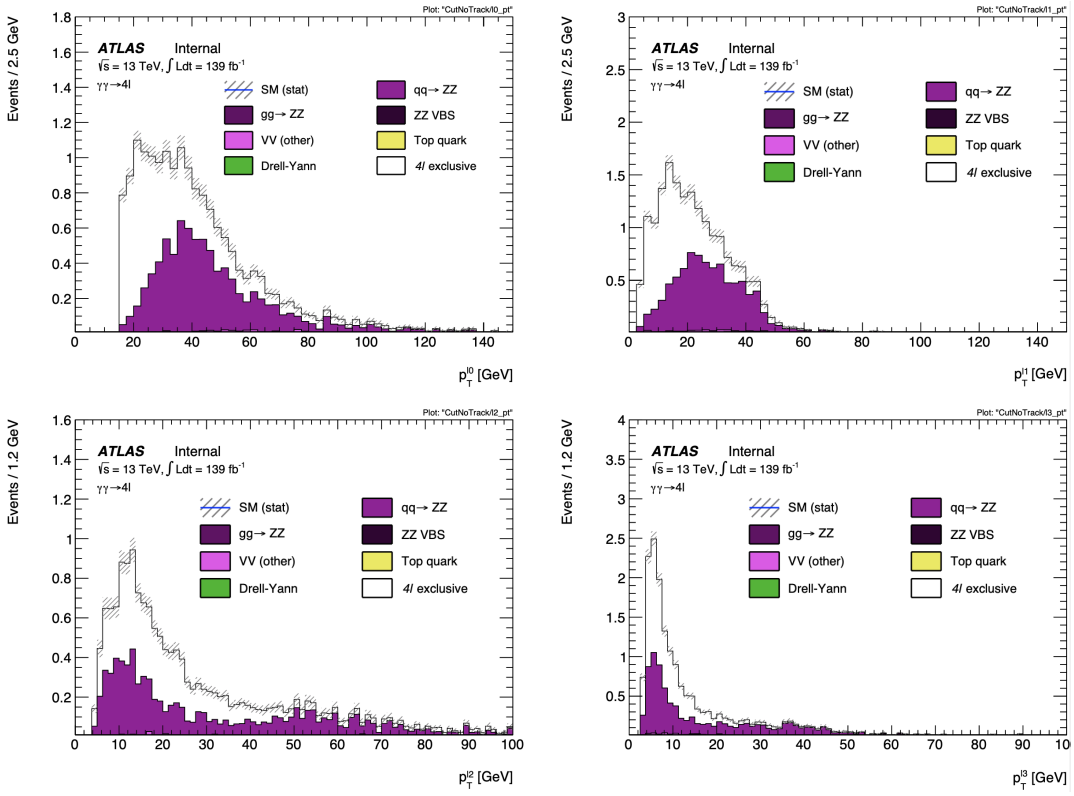

FIGURE 5.7: The signal and background MC p_T distribution of the individual leptons in the $n_{trk} = 0$ SR.

5.3 Effective Field Theory study of anomalous quartic gauge-couplings using the $\gamma\gamma \to 4l^{\pm}$ process.

In this MC simulation study, BSM contributions from anomalous quartic gauge-couplings to the $\gamma\gamma \to 4l^{\pm}$ production are investigated in the framework of the Standard Model Effective Field Theory (SMEFT). As mentioned in section 1.5, one can write the effective Lagrangian parametrising in higher dimension operators $\mathcal{O}_i$ (d > 4) effects of some unknown BSM physics at mass scale Λ characterising the energy scale at which the new physics is expected to be relevant,

$$\mathscr{L}_{EFT} = \mathscr{L}_{SM} + \sum_{d=5}^{\infty} \sum_{i} \frac{c_i^{(d)}}{\Lambda_i^{d-4}} \mathcal{O}_i^{(d)}, \tag{5.2}$$

where BSM effects are encoded in the expansion of $1/\Lambda$, and a Wilson coefficient c_i is associated to each operator. Odd dimension operators involve couplings that do not preserve the lepton and baryon number conservation. Therefore, in this study these operators are neglected. Consequently, the leading terms in the SMEFT after the SM Lagrangian have operators of dimension 6 (and of the order $\mathcal{O}(\Lambda^{-2})$),

$$\mathscr{L}'_{EFT} = \mathscr{L}_{SM} + \sum_{i} \frac{c_i^{(6)}}{\Lambda^2} \mathcal{O}_i^{(6)} + \sum_{j} \frac{c_j^{(8)}}{\Lambda^4} \mathcal{O}_j^{(8)} + \ \dots\ , \tag{5.3}$$

while the associated cross section contribution of each term can be expressed as,

$$\begin{aligned} \sigma'_{EFT} = \sigma_{SM} &+ \sum_{i} \left(\frac{c_i^{(6)}}{\Lambda^2} a_i^{(6\times SM)} + h.c. \right) + \sum_{ij} \frac{c_i^{(6)} c_j^{(6)*}}{\Lambda^4} b_{ij}^{(6\times 6)} \\ &+ \sum_{i} \left(\frac{c_i^{(8)}}{\Lambda^4} a_i^{(8\times SM)} + h.c. \right) + \sum_{ij} \frac{c_i^{(8)} c_j^{(8)*}}{\Lambda^8} b_{ij}^{(8\times 8)} + \dots\ , \end{aligned} \tag{5.4}$$

with the first and third sum including terms with contributions from the interference between SM and higher dimension BSM operators, while pure BSM terms are included in the second and the fourth sum. The former and the latter terms are, respectively, linear and quadratic in the Wilson coefficients. Moreover, in this study one is only interested in operators affecting quartic vertices without interference from di- and triple gauge couplings. The lowest dimension operators satisfying this condition are of dimension 8 and of the order $\mathcal{O}(\Lambda^{-4})$ in the expansion. These operators are relevant to interactions including the Higgs boson and the gauge bosons at tree level, and conserve charge-conjugation and parity. Based on the number of gauge boson field strength tensors the operators contain, these are classified into three groups, namely M-, T- and S-operators. The expression of all operators (18 in total) in terms of the gauge bosons field strength tensors and/or the covariant derivatives of the Higgs field can be found in Appendix C.1. Since photons do not

couple directly to the Higgs boson and S-operators contain only covariant derivatives of the Higgs field, the $\gamma\gamma \to 4l^{\pm}$ process is not sensitive to this class of operators which are therefore omitted in this study. Table 5.1 shows the different operators, and which of the different quartic electroweak gauge-boson vertices they affect. For example, $ZZAA$ refers to a quartic vertex including the interaction of two Z bosons and two photons, represented with A. Comparing the two classes, the T-operators appear to be sensitive to more neutral gauge-boson vertices. It should be noted that the T_8 and T_9 exclusively affect neutral gauge-boson vertices, to which the $\gamma\gamma \to 4l^{\pm}$ topology is the most sensitive.

TABLE 5.1: The different EFT dimension 8 operators and which of the different quartic EW gauge-boson vertices they impact. A represents a photon

	WWWW	WWZZ	ZZZZ	WWAZ	WWAA	ZZZA	ZZAA	ZAAA	AAAA
S_0, S_1, S_2	✓	✓	✓	-	-	-	-	-	-
M_0, M_1 , M_7	✓	✓	✓	✓	✓	✓	✓	-	-
M_2, M_3, M_4, M_5	-	✓	✓	✓	✓	✓	✓	-	-
T_0, T_1, T_2	✓	✓	✓	✓	✓	✓	✓	✓	✓
T_5, T_6, T_7	-	✓	✓	✓	✓	✓	✓	✓	✓
T_8, T_9	-	-	✓	-	-	✓	✓	✓	✓

Following this classification, while taking into account the sensitivity of the $\gamma\gamma \to 4l^{\pm}$ process, eq. 5.3 can be written as a function of the relevant M- and T-operators[1],

$$\mathscr{L}_{EFT}^{\gamma\gamma\to 4l^{\pm}} = \mathscr{L}_{SM} + \sum_{i=0,i\neq 6}^{7} \frac{f_{M_i}}{\Lambda^4}\mathscr{O}_{M_i} + \sum_{j=0,j\neq 3,4}^{9} \frac{f_{T_j}}{\Lambda^4}\mathscr{O}_{T_j}. \tag{5.5}$$

The total EFT cross section can be then expressed as a linear combination of the SM cross section, the linear BSM-SM interference terms and quadratic BSM terms,

$$\sigma_{EFT}^{\gamma\gamma\to 4l^{\pm}} = \sigma_{SM} + \sum_i \frac{c_i^{(8)}}{\Lambda^4} a_i + \sum_{ij} \frac{c_i^{(8)} c_j^{(8)}}{\Lambda^8} b_{ij}, \tag{5.6}$$

where c_i the Wilson coefficients corresponding to the M- or T-operators, which are assumed to be real. In the SMEFT, the Wilson coefficients as well as the new physics energy scale Λ are both free parameters that have to be determined. Therefore, in the next sections the value of the c_i/Λ^4 ratio is considered as one fit parameter. In this analysis, the contribution to each operator is investigated separately without interference, i.e. one coefficient is considered at a time while terms with $i \neq j$ in eq. 5.6 are set to zero. In this case, the total EFT cross section is simplified to the computation of the SM, the linear and quadratic term of a specific operator. Using the generator MADGRAPH5_AMC@NLO [70, 71], one can compute for the $\gamma\gamma \to 4l^{\pm}$ process the linear and quadratic terms separately of the total cross section for a given value of c_i/Λ^4, from which the coefficients a_i and b_{ii} can be derived from the generator to determine the quadratic function $\sigma_{EFT}(c_i/\Lambda^4)$. Moreover the derivation

[1]The Wilson coefficient c_i of a specific operator is always denoted with $f_{operator}$.

of these coefficients can be found in Appendix C.2. The coefficients a_i and b_{ii} for all M- and T-operators calculated for the $2e2\mu$ final state can be found in Table C.2. For the BSM contribution, the EFT model used to generate the linear and quadratic contributions can be found in [100]. As an example, Figure C.2 shows the value of linear and quadratic terms of the effective cross section (eq. 5.6) as a function of f_{T8}/Λ^4.

5.3.1 Expected exclusion limits on the Wilson coefficients.

In general, searches for new phenomena can lead to two scenarios: a discovery, where the SM only hypothesis is falsified by the disagreement with data, and therefore some new physics has to be taken in account to explain the difference; or, if the data is found to agree with the SM predictions, one can use this result for exclusion limits. This information can serve as a roadmap for theorists and experimentalists to avoid in their new physics searches regions (e.g. in some phase space) that have already been explored and excluded. These results are typically quantified with *upper* and *lower exclusion limits*. For example, an upper exclusion limit can be interpreted as; If new unknown physics affects the considered topology, the resulting rate must be below the estimated exclusion limit for the given phase space (e.g. the centre-of-mass energy).

Given the total effective cross section $\sigma_{EFT}(c_i/\Lambda^4)$, one can estimate exclusion limits on the various dimension-8 operators. This can be achieved by predicting the SM signal and background yield for the $\gamma\gamma \to 4l^{\pm}$ process. Given the uncertainties, one can estimate the maximum number of BSM yield that would still be compatible with an SM only hypothesis. Considering eq. 4.2 relating the number of expected events, N_{exp}, to the cross section $\sigma_{BSM}(c_i/\Lambda^4)$, given a value of c_i/Λ^4,

$$N_{exp} = \sigma(c_i/\Lambda^4)\mathcal{L}A\epsilon, \tag{5.7}$$

one can derive expected exclusion limits on the c_i/Λ^4 values given N_{exp} that would be still consistent with SM only hypothesis. From this estimation, the most sensitive operators to the $\gamma\gamma \to 4l^{\pm}$ process can be identified. Combining eq. 5.6 and eq. 5.7, c_i/Λ^4 is related to the number of expected BSM events N_{BSM} as,

$$c_i/\Lambda^4 = \frac{-a_i \pm \sqrt{a_i^2 + 4b_{ii}N_{BSM}/\mathcal{L}A\epsilon}}{2b_{ii}}. \tag{5.8}$$

In this study, MC samples with reconstructed events for the BSM contribution are lacking. As a consequence, the event selection efficiencies ϵ cannot be measured, only MC samples with generator level information are used as input. In combination with the calculated BSM cross sections using MADGRAPH5_AMC@NLO [70, 71], generator-level events are simulated using PYTHIA8 [74]. Assuming an equivalent reconstruction of SM and BSM events, the event selection efficiencies ϵ are taken

from SM to approximate the expected number of reconstructed BSM events. Based on this assumption and the predicted number of SM events, expected exclusion limits on the c_i/Λ^4 values are estimated using a profile likelihood fit. The likelihood is built from the Poisson PDFs of the expected BSM signal and events predicted in the SM[2] events, and instead of the observed number of data events, the total estimated SM yield is input. The following likelihood is constructed for each operator,

$$L(N_{SM}|c_i/\Lambda^4) = Pois(N_{SM}|N_{SM} + N_{BSM}(c_i/\Lambda^4)), \tag{5.9}$$

where no systematic uncertainties are taken into account. The exclusion limits on the c_i/Λ^4 value are obtained using the so-called *p-value*, which represents the probability of measuring a result that is of equal or greater incompatibility with the BSM hypothesis. A conventional p-value of 0.05 is used in BSM searches to exclude the signal hypothesis which corresponds to a statistical significance level of 95%. Results for the c_i/Λ^4 expected limits of each operator, corresponding to the latter confidence level, are shown in Figure 5.8, where the negative log-likelihood scan of the profile likelihood test statistic is plotted as a function of c_i/Λ^4. The first (lowest) and second horizontal lines indicate the exclusion limits at, respectively, 68% and 95% confidence level. Table 5.2 summarises the values for each operator. Comparing the exclusion limits of the two classes, the T-operators are clearly the best constrained using the $\gamma\gamma \to 4l^{\pm}$ process. This is expected from Table 5.1, where the T-operators modify more neutral gauge-bosons couplings, to which the $\gamma\gamma \to 4l^{\pm}$ topology is the most sensitive. Furthermore, considering the order of magnitude of the exclusion limits, and the corresponding a_i and b_{ii} coefficients in eq. 5.6 in Table C.2, one can conclude that the BSM contribution to the effective cross section is completely dominated by the quadratic terms, where the contribution from the linear terms is negligible.

[2]The SM $\gamma\gamma \to 4l^{\pm}$ process is also considered as background to the BSM signal.

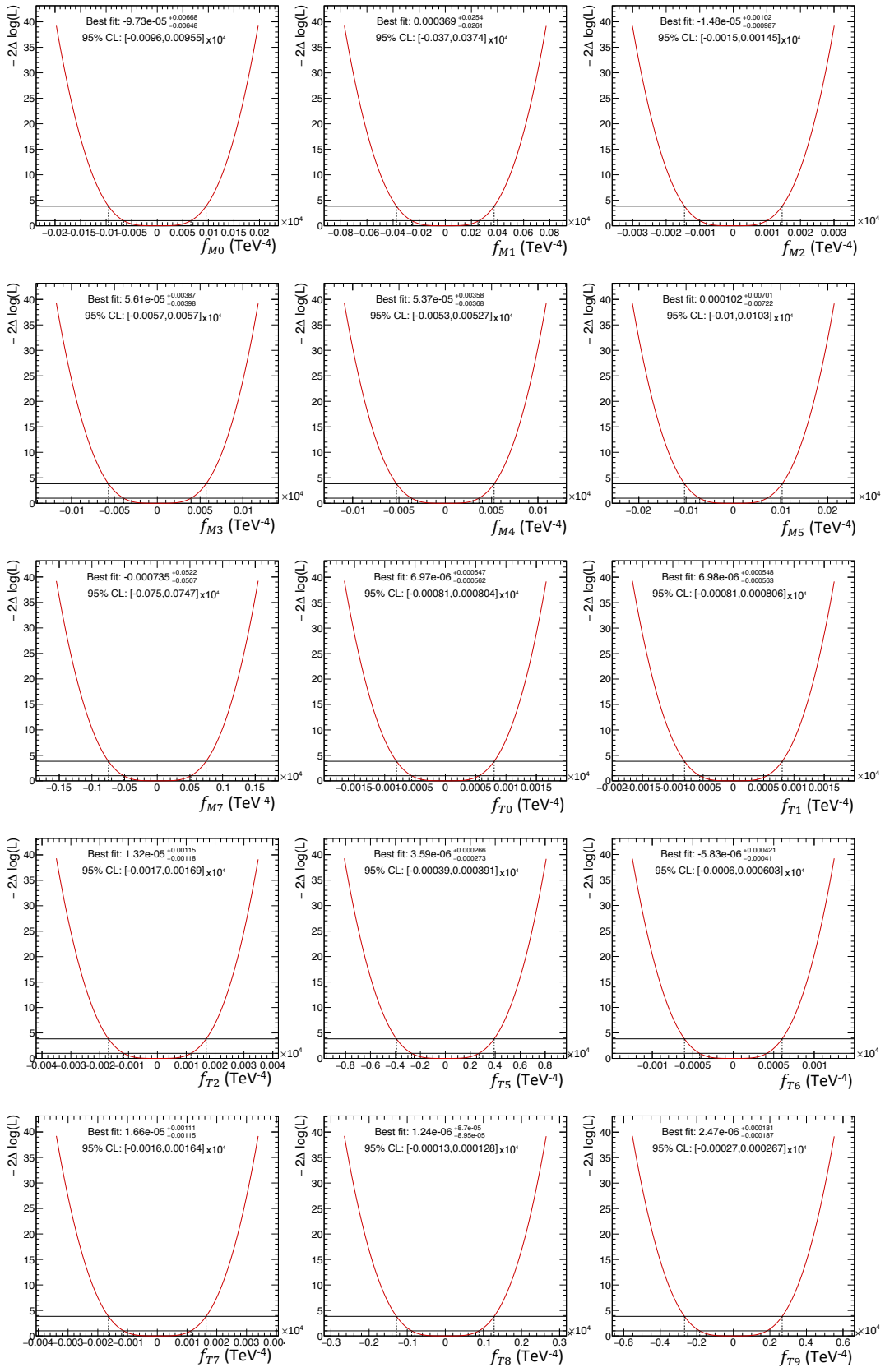

FIGURE 5.8: The negative log-likelihood scan of the profile likelihood test statistic as a function of c_i/Λ^4. The first (lowest) and second horizontal line indicates the exclusion limits at, respectively, 68% and 95% confidence level.

TABLE 5.2: Expected lower and upper limits on c_i/Λ^4 values of the various EFT operators corresponding to those shown in Figure 5.8.

	Exclusion limits on c_i/Λ^4 (TeV^{-4})
f_{M0}/Λ^4	[-96 , 95.5]
f_{M1}/Λ^4	[-370 , 374]
f_{M2}/Λ^4	[-15 , 14.5]
f_{M3}/Λ^4	[-57 , 57.0]
f_{M4}/Λ^4	[-53 , 52.7]
f_{M5}/Λ^4	[-100 , 103]
f_{M7}/Λ^4	[-750, 747]
f_{T0}/Λ^4	[-8.1, 8.04]
f_{T1}/Λ^4	[-8.1 , 8.06]
f_{T2}/Λ^4	[-17 , 16.9]
f_{T5}/Λ^4	[-3.9 , 3.91]
f_{T6}/Λ^4	[-6 , 6.03]
f_{T7}/Λ^4	[-16 , 16.4]
f_{T8}/Λ^4	[-1.3 , 1.28]
f_{T9}/Λ^4	[-2.7 , 2.67]

5.3.2 Comparison of kinematic distributions between Standard Model and effective operators

Results from Table 5.2 were computed using the overall number of expected events. However, binning these events as a function of some quantity can improve the signal sensitivity. Similarly to section 3.2.4, differences in distributions of discriminating kinematic variables between SM and BSM can be used to improve exclusion limits. Therefore, potential discriminating variables are studied in SM and BSM distributions. First, kinematic variables of the leptons, namely p_T, η and ϕ, are compared between the SM and BSM contributions from a specific operator. Figures 5.9 and 5.10 show a comparison of these latter quantities for each of the four leptons at generator-level, for the SM $\gamma\gamma \to 4l^{\pm}$ and the corresponding BSM contribution from the M_0 and T_0 operators as an example. The latter distributions are normalised to correspond to an integral of 6.7 events, corresponding to the maximum number of BSM events that would still be compatible with an SM only hypotheses, while the SM signal distribution is normalised 8.9 events (the expected number of events from reconstructed events). From Figures 5.9 and 5.10, the p_T distribution of leptons from BSM events is stretched over a larger spectrum while SM events are limited to approximately 200 GeV leptons. Also leptons from BSM events tend to have more forward leptons with high $|\eta|$ values, whereas SM leptons are slightly more central with small $|\eta|$ values. In the $|\phi|$ spectrum, SM and BSM are relatively similar and isotropically distributed. Moreover, a comparison in the latter quantities of all operators in the two classes are compared in Figure 5.11. The M-operators are represented in blue histograms and the T-operators in red. The distributions are normalised to the same integral value for the shape comparison. In general, the M-operators show clear peaks in the forward region with high $|\eta|$ values, while the T-operators show a relatively flatter η distribution falling toward the extrema. The p_T distributions are also clearly different in both operators. In the M-operators, the distribution is more shifted toward higher values, and falls off more rapidly compared to the T-operators, which also differ in the shape of the spectra. The ϕ distributions are similar overall. Furthermore, variables of the four-lepton system are also compared, which are defined as,

- $\cos\theta^*_{12}$, a variable sensitive to the polarisation of the decaying particle, with θ^*_{12} the angle between the negatively charged lepton in the leading di-lepton rest frame, and the leading lepton pair in the lab frame,
- similarly, $\cos\theta^*_{34}$, with θ^*_{34} the angle between the negative lepton in the sub-leading dilepton rest frame, and the sub-leading lepton pair in the lab frame,
- $|\Delta\phi_{l1,l2}|$, the difference in the azimuthal angle between the leading and sub-leading lepton (in p_T) of the quadruplet,
- $|\Delta y_{Z1,Z2}|$, the absolute rapidity difference between the leading and subleading pair,

- m_{Z1}, the invariant mass of the leading lepton pair in the quadruplet (closest to the Z mass),
- m_{Z2}, the invariant mass of the subleading lepton pair in the quadruplet,
- m_{4l}, the invariant mass of the quadruplet.

Figures 5.12 - 5.13 show the generator-level kinematic distributions of the latter variables, for the SM and BSM photon-induced signal, for the M_0 and T_0 operators as an example. Following the discussion in section 3.2.4, angular variables appear to have different shapes comparing SM and BSM distributions, however, they do overlap for most of the spectra. On the other hand, SM and BSM distributions of invariant mass variables m_{Z1}, m_{Z2} and m_{4l} show a high discriminating power, where the overlap between SM and BSM PDFs is minimal. Moreover, a resonant behaviour is observed in BSM distributions of the di-lepton invariant mass spectra, which enhances the signal over background ratio. This latter effect is expected to improve the constraint on the c_i/Λ^4 values; the larger the signal over background ratio, the higher the statistical power to reject the BSM contribution assuming a measurement in agreement with the SM predictions. Moreover, the comparison of all operators in the M- and T-operators is also shown in Figure 5.14 for the latter variables. From this comparison, the distribution of angular variables is more or less similar, except for the $|\Delta y_{Z1,Z2}|$ distributions which are different in both classes of operators, with the M-operators having an obvious second peak at higher values. In the di-lepton invariant masses, T-operators appear to have larger tails in their distributions, while M-operators have a more pronounced peak around the Z mass. The m_{4l} spectrum is also different, the T-operators show a more smeared distribution with a shifted peak at higher values compared to the M-operators.

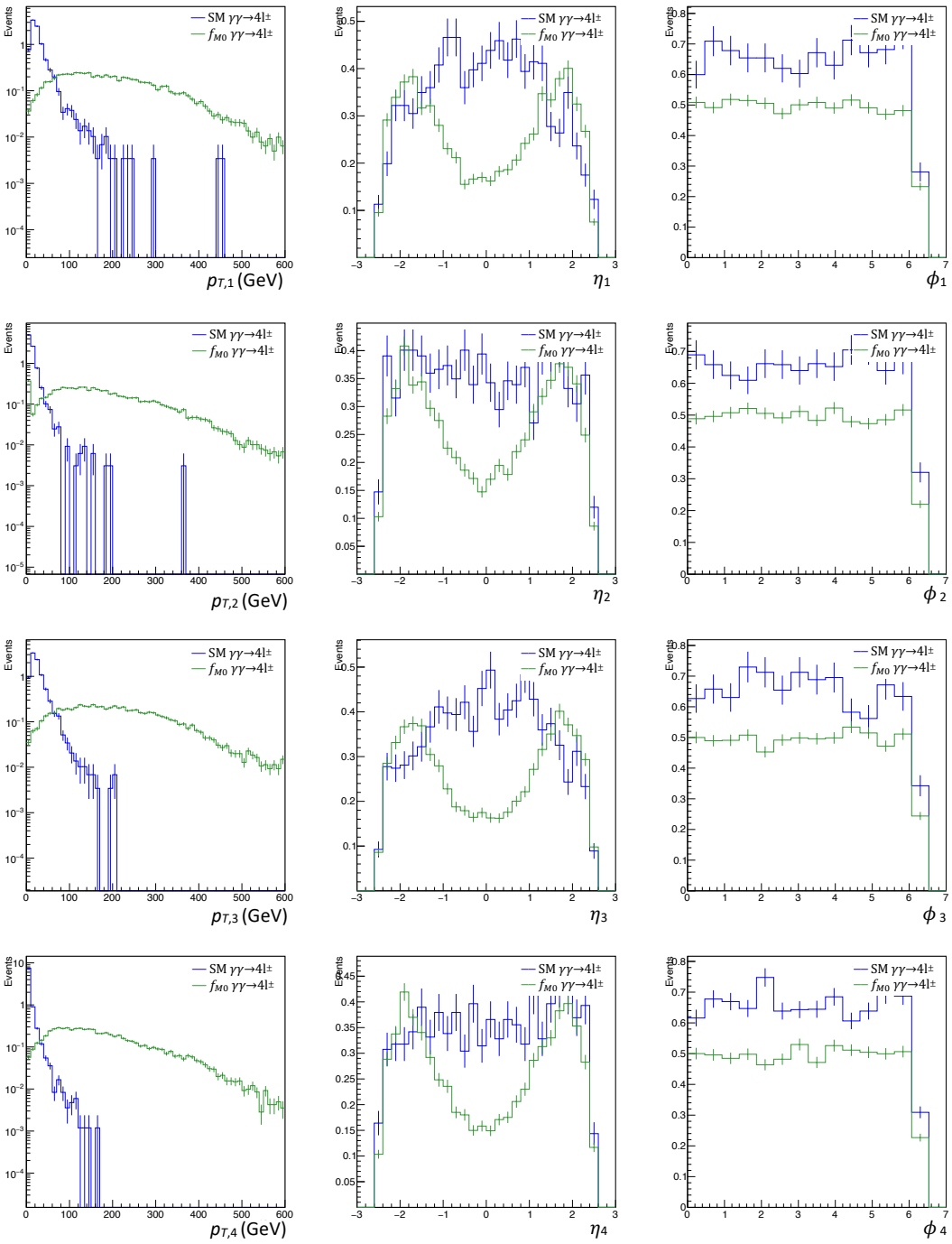

FIGURE 5.9: A comparison of the kinematic distributions for each of the four leptons at generator-level, for the SM $\gamma\gamma \to 4l^{\pm}$ and the corresponding BSM contribution from the M_0 operator.

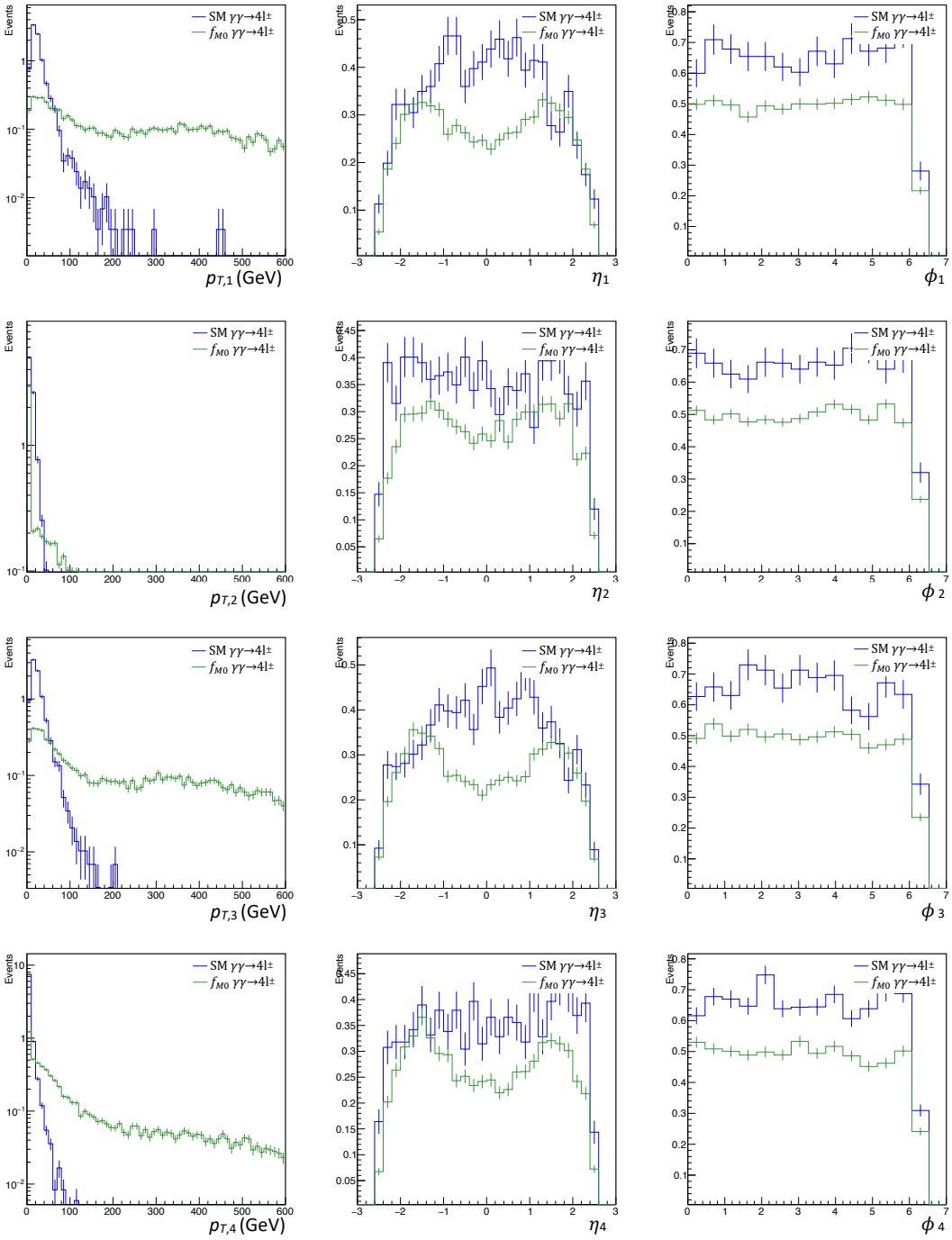

FIGURE 5.10: A comparison of the kinematic distributions for each of the four leptons at generator-level, for the SM $\gamma\gamma \to 4l^{\pm}$ and the corresponding BSM contribution from the T_0 operator.

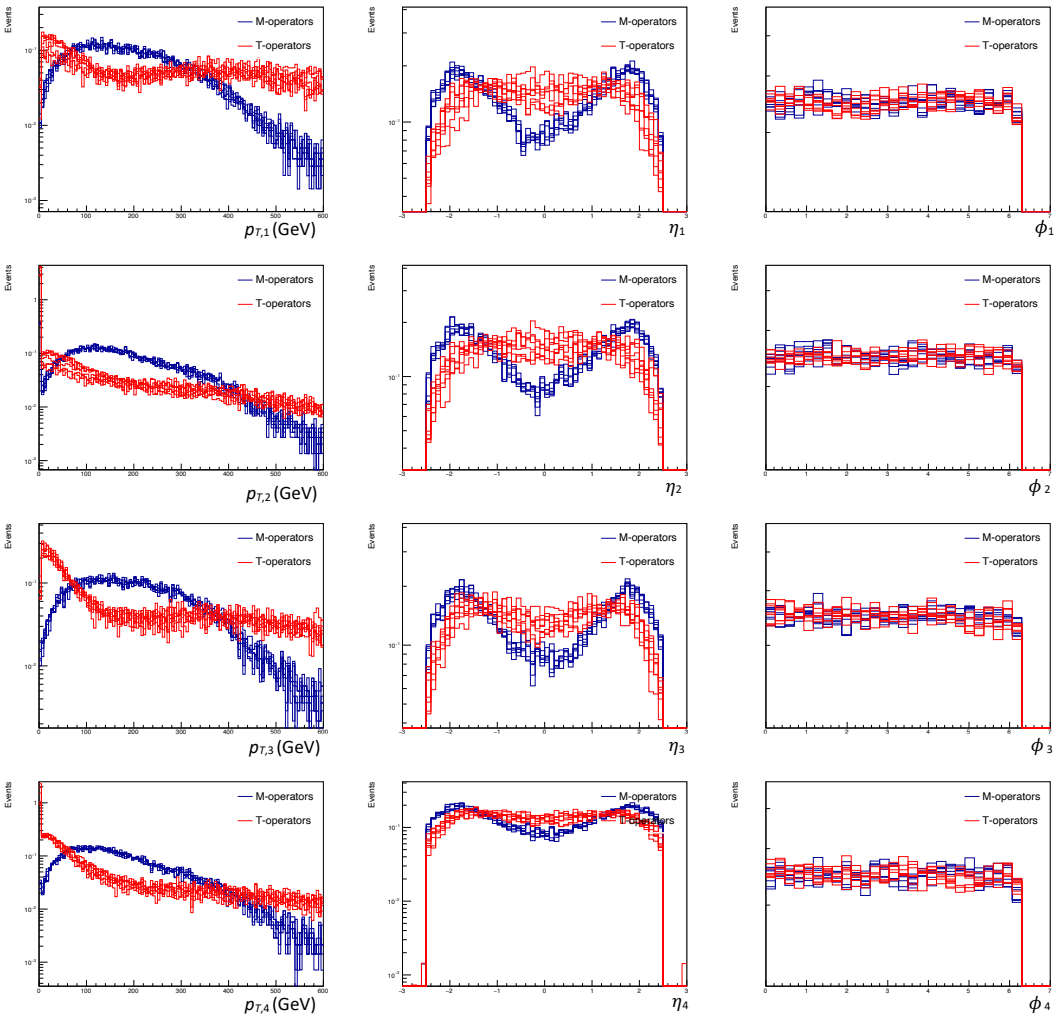

FIGURE 5.11: A comparison of the kinematic distributions for each of the four leptons at generator-level in all M- and T-operators.

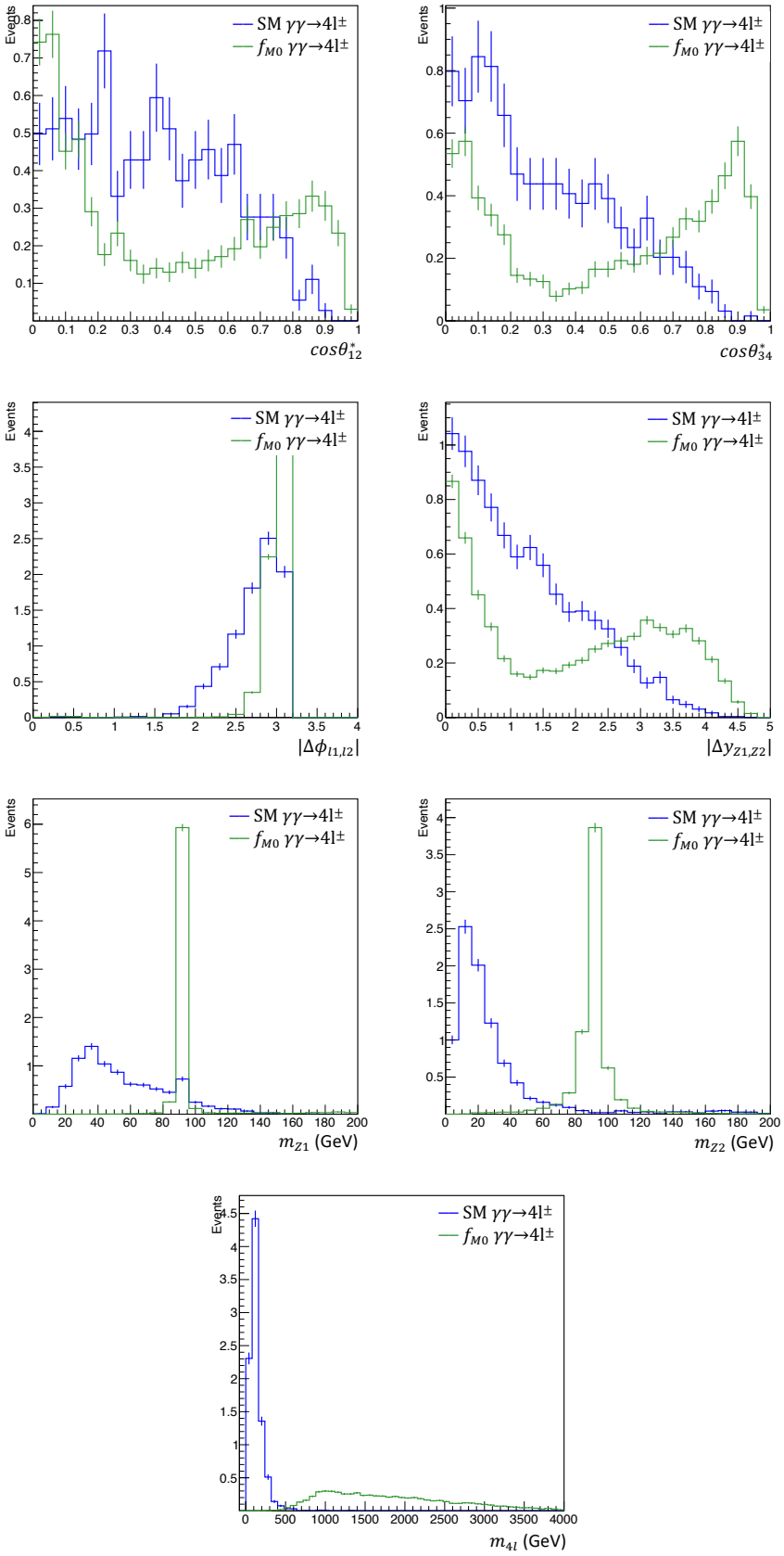

FIGURE 5.12: A comparison of the distributions of four-lepton kinematic variables at generator-level, for the SM $\gamma\gamma \to 4l^{\pm}$ and the corresponding BSM contribution from the M_0 operator.

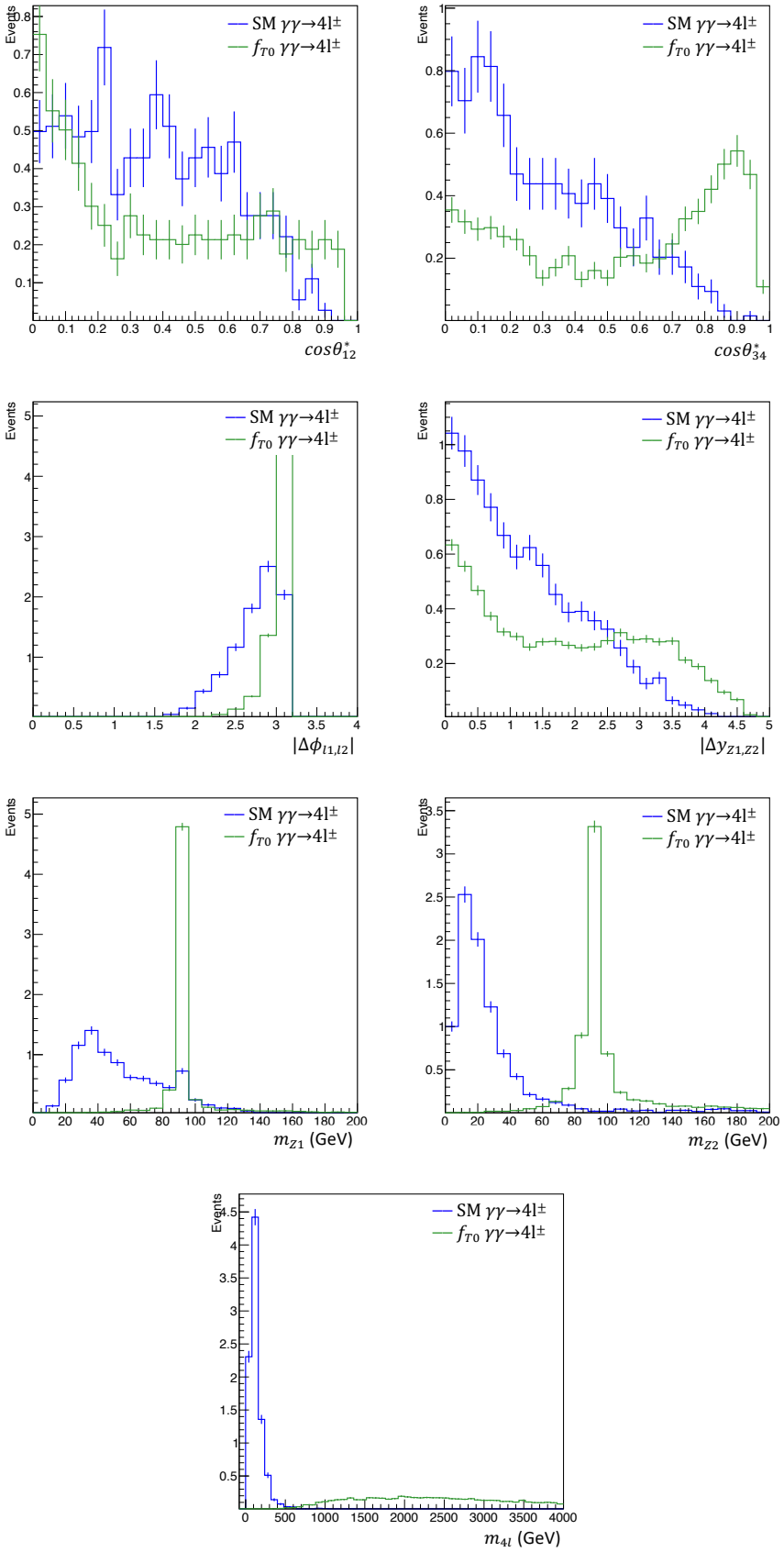

FIGURE 5.13: A comparison of the distributions of four-lepton kinematic variables at generator-level, for the SM $\gamma\gamma \to 4l^{\pm}$ and the corresponding BSM contribution from the T_0 operator.

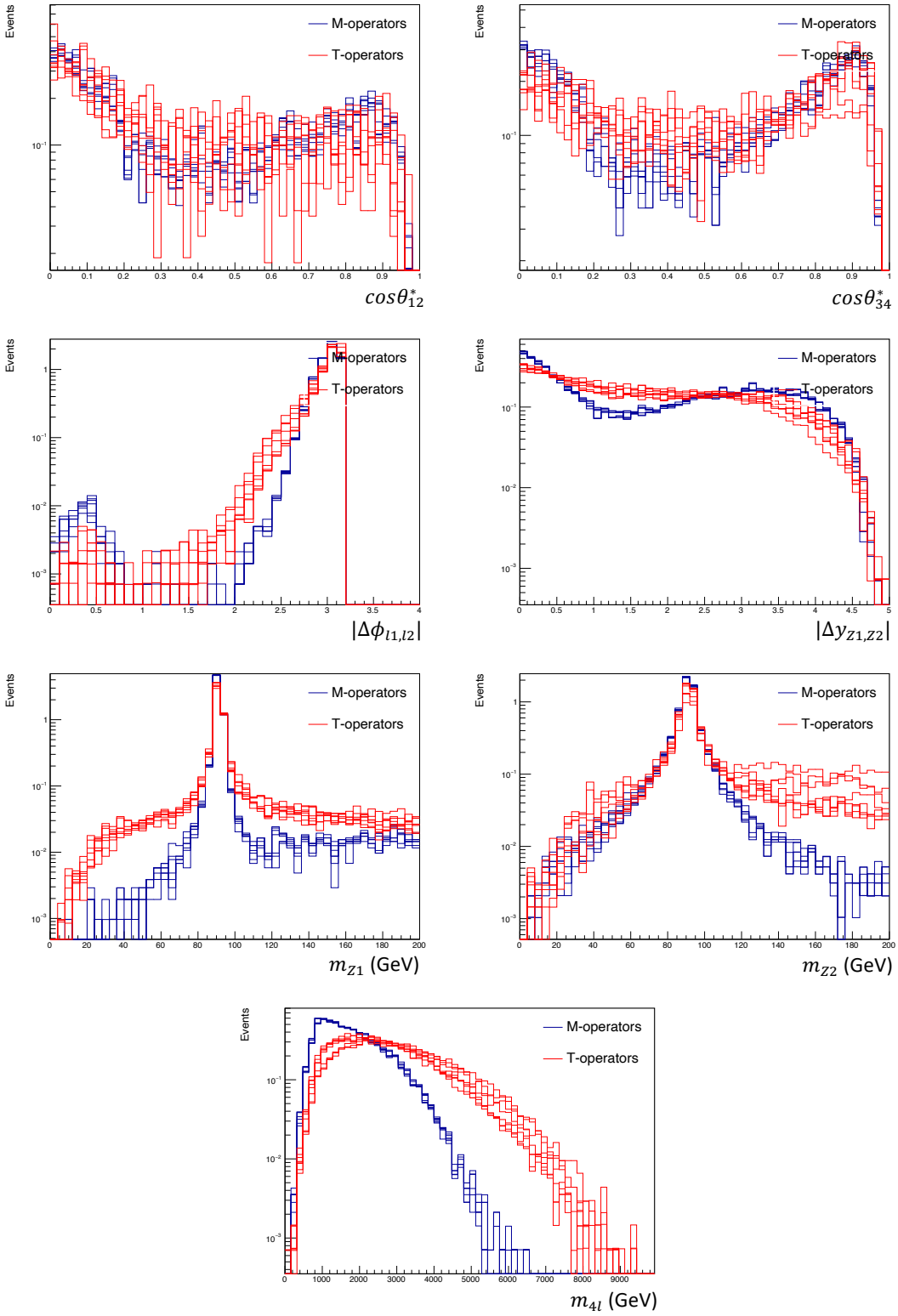

FIGURE 5.14: A comparison of the distributions of four-lepton kinematic variables at generator-level in all M- and T-operators.

5.3.3 Exclusion limits on EFT operators using kinematic distributions

After the SM and BSM comparison of the various kinematic PDFs, the most promising variables in terms of discriminating power are m_{Z2} and m_{4l}, which are chosen for the estimation of the c_i/Λ^4 exclusion limits. In section 5.3.1, the Poisson likelihood was constructed from the overall number of expected events for the SM and BSM contribution. Using the differential distributions in m_{Z2} and m_{4l}, a binned Poisson likelihood is used, where the number of events in each bin are Poisson distributed, thus,

$$L(N^{SM}|c_i/\Lambda^4) = \prod_k Pois(N_k^{SM}|N_k^{SM} + N_k^{BSM}(c_i/\Lambda^4)), \tag{5.10}$$

with the index k running over the bins of the m_{Z2} or m_{4l} histogram. Similarly to section 5.3.1, expected exclusion limits are obtained assuming an SM only hypothesis, where the number of events per bin are obtained from MC of SM reconstructed events. Due to the lack of BSM MC at reconstruction-level, the number of events per bin are approximated by,

$$N_k^{BSM,reco} = N_k^{BSM,gen} \times \frac{N_k^{SM,reco}}{N_k^{SM,gen}}, \tag{5.11}$$

assuming equivalent efficiency for reconstructed SM and BSM events. Given the previously estimated low SM number of events, $N_{SM} = 17.1 \pm 5.9$, using the number of bins shown in Figures 5.12 - 5.13 would result in a negligible number of events per bin, leading to large statistical uncertainties. Therefore, the binning is reduced to have a reasonable number of events per bin in the m_{Z2} and m_{4l} distributions. Exclusion limits calculated in section 5.3.1 can be regarded as results from a single binned histogram.

As an example, the m_{Z2} distribution is divided into two bins, i.e. m_{Z2} = [0, 100, 200] GeV. For the same p-value used in the exclusion limits shown in Figure 5.8, the results for the c_i/Λ^4 value of each operator, corresponding to a 95% confidence level are shown in Figure 5.15 using the m_{Z2} spectrum. Compared to the exclusion limits calculated in Figure 5.8, equivalent to those calculated from a single binned histogram, results from the two-bins histograms show clearly improved exclusion limits as expected.

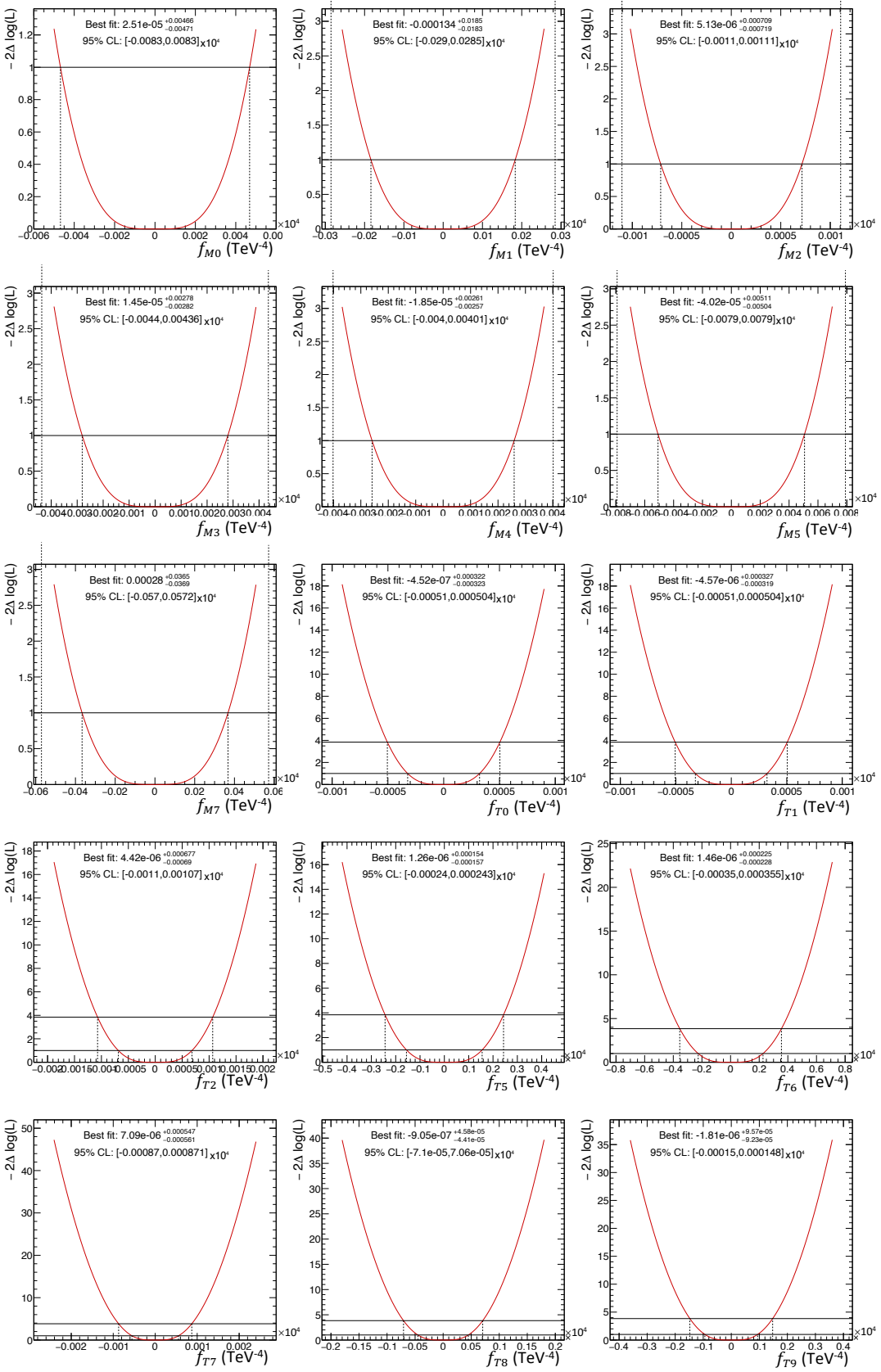

FIGURE 5.15: The negative log-likelihood scan of the profile likelihood test statistic as a function of c_i/Λ^4. The first (lowest) and second horizontal line indicates the exclusion limits at, respectively, 68% and 95% confidence level.

5.3.4 Bin optimisation for exclusion limits estimation

In the previous section, kinematic distributions with a significant discriminating power between SM and BSM events were selected that can be used to improve the constraint on c_i/Λ^4 values. An example was shown using the m_{Z2} spectrum in a binned likelihood to calculate the exclusion limits, where the limits compared to results obtained in section 5.3.1 were clearly more stringent. In fact, the binning chosen in the latter example was arbitrary, where the spectrum was simply divided into two equal-sized bins. In order to improve the exclusion limits even further, one can optimise the binning such that the discriminating power is maximised. For example, in the case of the m_{Z2} distribution (Figure 5.14), it is trivial to see that opting for two bins is not the optimal choice to exploit the resonant peak at the Z mass value. Therefore, there are two important parameters to tweak, namely the number of bins and the bin boundaries, in order to find the optimal configuration which maximises the constraint of c_i/Λ^4 values. However, as mentioned in the previous section, it is important to keep a threshold of number of events per bin, to avoid large statistical uncertainties. In the two-bins case, Figure 5.16 shows the bin content of the m_{Z2} (left plot) and m_{4l} (right plot) bins, as a function of the bin boundary choice, i.e.,

$$m_{Z2} = [0, i, 200] \text{ GeV},$$

$$m_{4l} = [0, i, 1200] \text{ GeV},$$

with i the bin boundary. Also, the statistical uncertainties per bin and the one-event threshold are shown. The blue-shaded area corresponds to the case where at least one event is found per bin. Figure 5.17 shows the upper[3] exclusion limits for the M_0 and T_0 operators estimated using the m_{Z2} and m_{4l} distributions in the two-bins case, as a function of the bin boundary choice. The yellow horizontal line corresponds to the best exclusion limit from all two-bins configurations, while the green line for the best exclusion limit given at least one event per bin. As expected, varying the bin boundaries has clearly an impact on the estimated exclusion limits. Comparing the m_{Z2} (left) and m_{4l} results, the latter shows tighter exclusion limits, however, as discussed before, the m_{Z2} case necessitates more than two bins to exploit the resonant behaviour in the BSM case. Having the optimal binning for each spectrum and operator corresponding to the best exclusion limits in Figure 5.17, a further attempt to improve the constraint is to consider three-bins spectra, while repeating the previously mentioned steps. Figure 5.18 shows the upper exclusion limit estimated for the m_{Z2} (left plot) and m_{4l} (right plot) distribution in the three-bins case, as a function of the second bin boundary choice, while fixing the first bin boundary to the one corresponding to the best exclusion limits in the two-bins case. The top and bottom plots correspond respectively to the M_0 and T_0 operators. As expected, the m_{Z2} results improved after adding a third bin around the Z peak, while in the case of the

[3] In this study, the difference in absolute value of the lower and upper exclusion limits are negligible across all operators.

m_{4l}, a third bin has no effect. In summary, the latter variable in the two-bins case, taking in account at least the one event per bin, provides the best exclusion limits, which are shown in Figure 5.19 and summarised in Table 5.3.

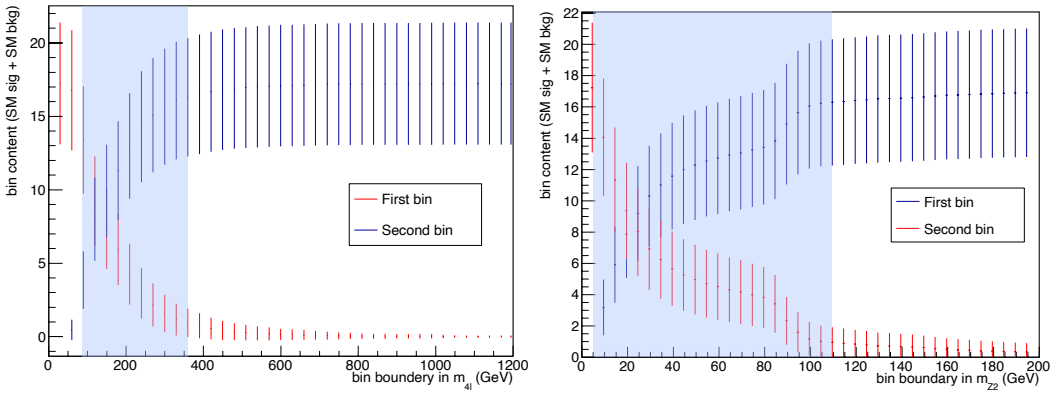

FIGURE 5.16: The m_{4l} (left) and m_{Z2} (right) bin content distribution in the two-bins case as a function of the bin boundary choice. In the blue-shaded area each bin has at least one event.

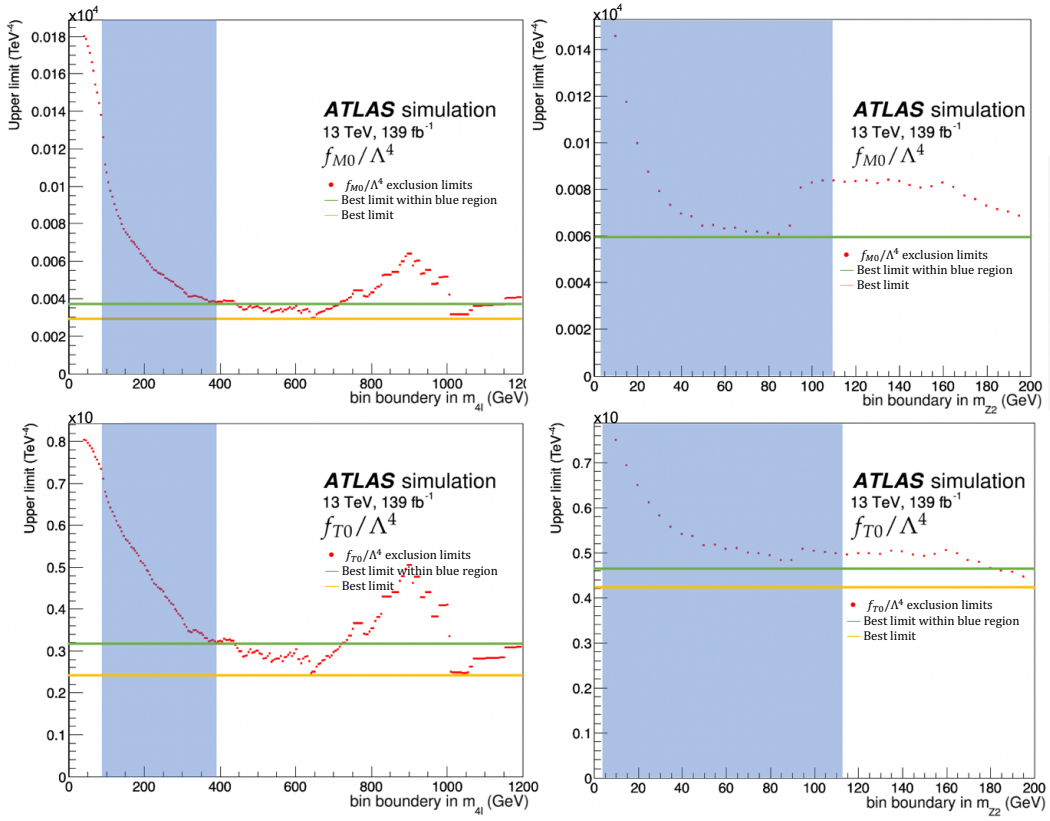

FIGURE 5.17: The upper exclusion limits estimated from the m_{4l} (left) and m_{Z2} (right) two-bins distribution, as a function of the bin boundary choice. The top and bottom plots correspond respectively to the M_0 and T_0 operators. The yellow horizontal line corresponds to the best exclusion limit from all two-bins configuration, while the green line for the best exclusion limit given at least one event per bin.

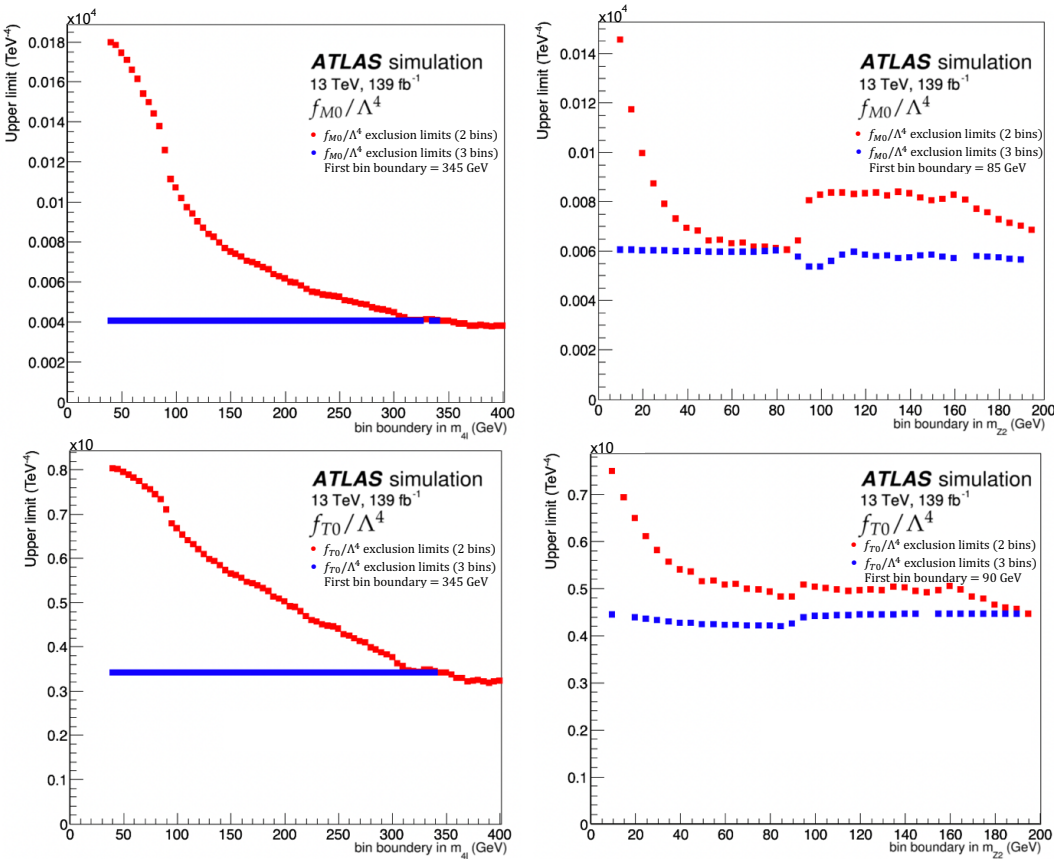

FIGURE 5.18: The positive upper exclusion limit estimated for the m_{4l} (left) and m_{Z2} (right) distribution in the three-bins case, as a function of the second bin boundary choice, while fixing the first bin boundary to the one corresponding to the best exclusion limits in the two-bins case. The top and bottom plots correspond respectively to the M_0 and T_0 operators.

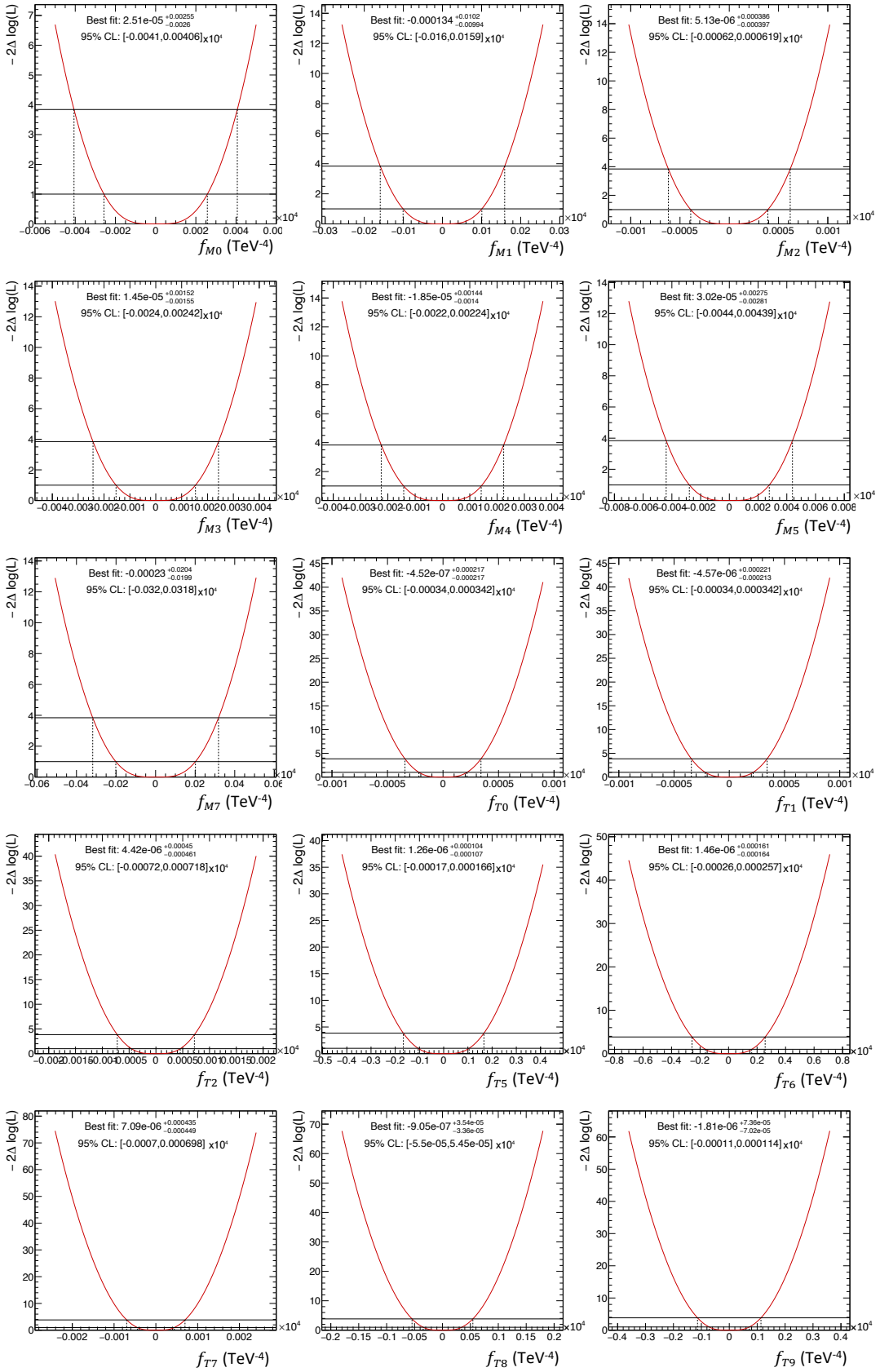

FIGURE 5.19: The negative log-likelihood scan of the profile likelihood test statistic as a function of c_i/Λ^4. The first (lowest) and second horizontal line indicates the exclusion limits at, respectively, 68% and 95% confidence level.

TABLE 5.3: Expected lower and upper limits on c_i/Λ^4 values of the various EFT operators corresponding to those shown in Figure 5.19.

	Exclusion limits on c_i/Λ^4 (TeV^{-4})
f_{M0}/Λ^4	[-41 , 40.6]
f_{M1}/Λ^4	[-160 , 159]
f_{M2}/Λ^4	[-6.2 , 6.19]
f_{M3}/Λ^4	[-24 , 24.2]
f_{M4}/Λ^4	[-22 , 22.4]
f_{M5}/Λ^4	[-44 , 43.9]
f_{M7}/Λ^4	[-320, 318]
f_{T0}/Λ^4	[-3.4, 3.42]
f_{T1}/Λ^4	[-3.4, 3.42]
f_{T2}/Λ^4	[-7.2 , 7.18]
f_{T5}/Λ^4	[-1.7 , 1.66]
f_{T6}/Λ^4	[-2.6 , 2.57]
f_{T7}/Λ^4	[-7, 6.98]
f_{T8}/Λ^4	[-0.55, 0.545]
f_{T9}/Λ^4	[-1.1 , 1.14]

5.3.5 Unitarity conserving exclusion limits

As mentioned in section 1.6, an effective field theory is constructed on the basis that the relevance of some unknown physics is at much larger energies than the considered scale, such that higher dimension operators are suppressed by factors of $1/\Lambda$. In the case where the probed energy scale is large enough such that these latter operators are not suppressed, their corresponding couplings become significant and the additional content of the UV theory can no longer be neglected. In fact, this can lead to the violation of the quantum mechanical unitarity. As a consequence, the probabilities associated to interactions are no longer conserved, leading to unphysical predictions. An example is found in the SM, where the cross section of producing a pair of W-bosons from an e^-e^+ annihilation is found to increase with the centre-of-mass energy without a limit, and consequently violates unitarity at some energy scale. This issue was successfully solved by introducing the neutral gauge Z boson, where the latter cross section converges asymptotically at high energies [5]. Analogously, one expects the existence of some BSM particle(s) that would fix the unitarity when considered in the EFT predictions.

At the LHC, the energy scale at which physics processes are probed can reach the TeV scale, where BSM effects could be manifested. Since the total BSM contribution leads to an increase in the cross section of the $\gamma\gamma \to 4l^{\pm}$ process, one has to determine constraints on the c_i/Λ^4 values below which unitarity is conserved given the probed energy scale $\sqrt{\hat{s}}$. For the $\gamma\gamma \to 4l^{\pm}$ process, the m_{4l} variable is used as the probed characteristic scattering energy scale. The procedure for obtaining these constrained limits is achieved by applying a cut-off on the integrated m_{4l} spectrum for the BSM contribution on generator-level, i.e. all events above the m_{4l} cut-off are not considered. On the other hand, unitarity bounds on the c_i/Λ^4 values are calculated by evaluating the maximum centre-of-mass energy allowed by unitarity, which is obtained from [91]. Therefore, limits are compared to the unitarity bound as a function of the centre-of-mass energy, where the limits at each $\sqrt{\hat{s}}$ are calculated with a cut-off on $m_{4l} = \sqrt{\hat{s}}$. Figures 5.20 and 5.21 show in red the unitarity bound curve of M- and T-operators as a function of $\sqrt{\hat{s}}$, while the black dots correspond to the expected exclusion limits given a cut-off at $\sqrt{\hat{s}}$. Values of c_i/Λ^4 above the unitarity bound curve, at a given $\sqrt{\hat{s}}$ value, violate unitarity. From the results in all operators, it is clear that exclusion limits at low cut-off values violate unitarity, while in some operators (mainly M-operators) limits in small parts of the high mass range are found below the unitarity bound. As limits in the low $\sqrt{\hat{s}}$ range exceed the unitarity bounds, it is not sufficient to guarantee the validity of the EFT. Consequently, with the expected data it is not possible, yet, to obtain limits on c_i/Λ^4 within the boundaries of the unitarity requirement, and hence within the validity of the EFT. This is mainly due to the relatively low number of expected events that would be compatible with the SM given the cut-off values.

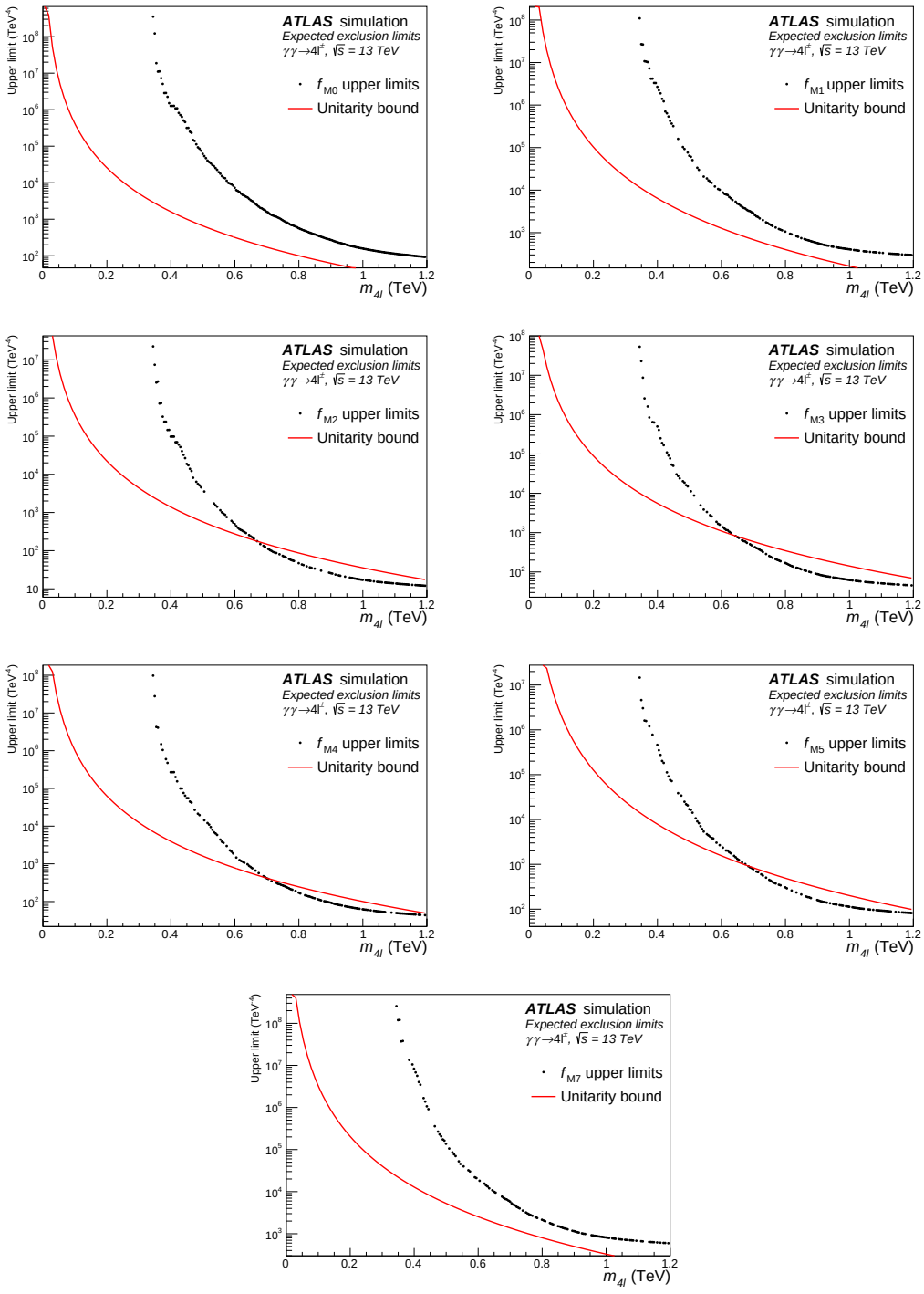

FIGURE 5.20: A comparison of the unitarity bound of M-operators as a function of $\sqrt{\hat{s}}$, and the expected exclusion limits given a cut-off at $\sqrt{\hat{s}}$. Values of c_i/Λ^4 above the unitarity bound curve, at a given $\sqrt{\hat{s}}$ value, violate unitarity.

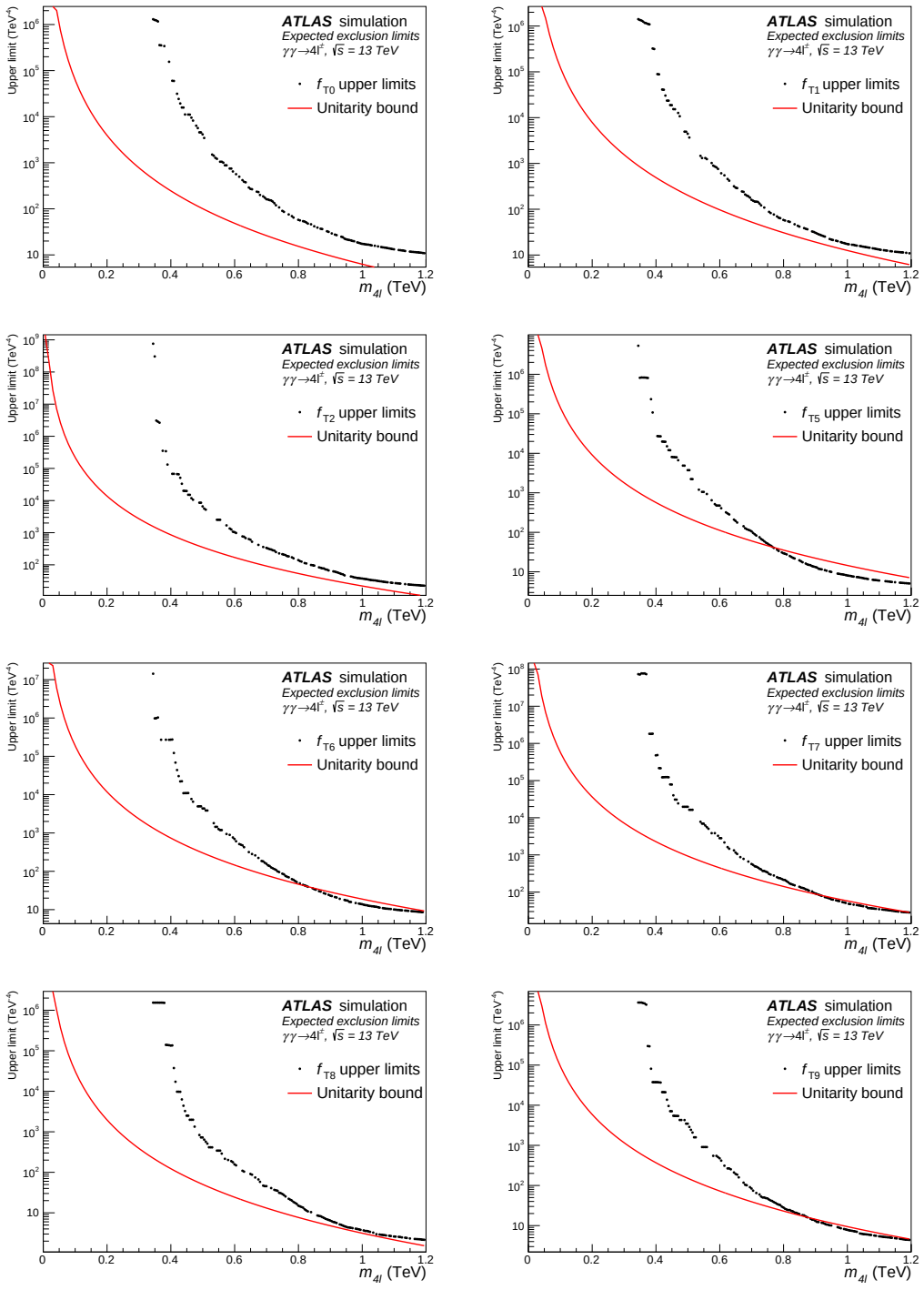

FIGURE 5.21: A comparison of the unitarity bound of T-operators as a function of $\sqrt{\hat{s}}$, and the expected exclusion limits given a cut-off at $\sqrt{\hat{s}}$. Values of c_i/Λ^4 above the unitarity bound curve, at a given $\sqrt{\hat{s}}$ value, violate unitarity.

5.4 Summary & conclusion

As mentioned in section 5.1, the Standard Model electroweak sector is abundant in phenomenology of boson interaction processes, where many have been experimentally confirmed, while a number still remain unobserved. As the SM is more likely to be an effective theory, expected to be a good approximation at low energy scales (typically at Λ_{EW}) of some fundamental UV theory valid at all scales, probing further the electroweak sector can lead to the first fissure of the SM, where any deviation from its predictions would constitute a smoking gun for new BSM physics. In section 5.3, the search for the $\gamma\gamma \to 4l^{\pm}$ process was introduced, where its Feynman diagram in the SM were shown in Figure 5.2. This process can provide sensitivity to BSM anomalous quartic neutral gauge-boson vertices, where possible BSM processes were shown in Figure 5.3. As discussed in section 1.6, a model independent approach for capturing the low-energy impact of new physics is formulated in the Standard Model Effective Field Theory framework. In this formalism, an extension of the SM is realised by constructing an effective Lagrangian as a series of a complete set of higher dimensional operators, preserving the SM gauge invariance in which new physics contributions are encoded. Terms of such operators are proportional to Wilson coefficients c_i suppressed by inverse powers of a typical mass scale Λ of the new physics extension (eq. 5.2).

In this chapter, an EFT study was presented in the context of the search for the $\gamma\gamma \to 4l^{\pm}$ process, where BSM contributions from anomalous quartic gauge-couplings were investigated. Following the theoretical framework presented in [91], only operators preserving lepton number conservation, and affecting only quartic vertices without interference from di- and triple gauge couplings, were considered. The lowest order relevant operators are of dimension 8, corresponding to a set of 15 operators, which can be distinguished in two classes, namely M and T-operators, where their difference is manifested in the number of gauge boson field strength tensors they contain. The contribution of each operator was investigated separately, without the interference of others BSM operators. From the effective Lagrangian eq. 5.3, the associated effective cross section eq. 5.6 is derived, which is expressed as a linear combination of the SM cross section, an SM-BSM interference term linearly proportional to c_i/Λ^4, and a pure BSM term quadratic in c_i/Λ^4. In the SMEFT, these quantities are free parameters that have to be measured empirically. Assuming an SM only hypothesis. the aim was to estimate expected exclusion limits on the c_i/Λ^4 values. Using eq. 5.8 relating c_i/Λ^4 and the number of expected SM events, a first estimate of upper exclusion limits (Table 5.2) on the c_i/Λ^4 of each operator, corresponding to a statistical significance level of 95%, were calculated using a profile likelihood fit, assuming Poisson distributed number of expected events. In this preliminary study, only statistical uncertainties were taken into account. In general, comparing the exclusion limits of the two classes, T-operators are the best constrained, which as expected

were the most sensitive to neutral quartic gauge-boson couplings.

In an attempt to improve the previously mentioned exclusion limits by exploiting differential distributions with the aim to maximise the BSM signal over the SM background ratio, potential discriminating variables were studied. After investigation of various SM and BSM kinematic distributions, the m_{4l} and m_{Z2} spectra were found to have the largest discriminating power. Consequently, expected exclusion limits corresponding to 95% confidence level were calculated using a binned Poisson likelihood fit in bins of the latter quantities. Compared to the first estimates, results using the m_{Z2} distribution shown in Figure 5.15 were significantly improved. In a second attempt to improve the results by optimising the binning of the m_{4l} and m_{Z2} distributions used in the binned likelihood fit, exclusion limits were calculated for different configurations. The best configuration maximising the exclusion limits was found using the m_{4l} distribution. From these results shown in Table 5.3, the T_8 and T_9 operators were clearly the best constrained, which was expected since they exclusively modify neutral quartic gauge-boson couplings (Table 5.1). The latter expected exclusion limits can be compared to those published by the CMS collaboration [114], where a similar study was performed using the leptonic final states of ZZ electroweak production in association with two jets. In this measurement, limits on five T-operators are reported, namely,

$$
\begin{aligned}
-0.37 < f_{T_0}/\Lambda^4 < 0.35,\\
-0.49 < f_{T_1}/\Lambda^4 < 0.49,\\
-0.98 < f_{T_2}/\Lambda^4 < 0.98,\\
-0.68 < f_{T_8}/\Lambda^4 < 0.68,\\
-1.46 < f_{T_9}/\Lambda^4 < 1.46.
\end{aligned}
$$

Compared to results in Table 5.3, the three first limits are better constrained in the latter study, while the T_8 and T_9 expected limits in this thesis are more stringent. Finally, as mentioned in section 5.3.5, the validity of an EFT is limited to a scale where the new physics is sufficiently suppressed, while beyond a certain threshold where the new physics content is no longer suppressed, quantum mechanical unitarity can be violated, leading to unphysical predictions. Therefore, in section 5.3.5 exclusion limits on c_i/Λ^4 were recalculated given a cut-off on the m_{4l} spectrum of the BSM MC at generator-level, where the latter variable characterises the probed energy scale. Finally, in Figures 5.20 and 5.21 the constrained limits on, respectively, the M- and T-operators were compared to theoretical unitarity bounds [91] on the c_i/Λ^4 values corresponding to the maximum centre-of-mass energy below which unitarity is conserved. From these results, one concludes that, given the expected number of $\gamma\gamma \to 4l^{\pm}$ SM events, it is not possible to obtain limits on the c_i/Λ^4 values within the boundaries of the unitarity requirement, and hence within the validity of the effective field theory.

Appendix A

Electron reconstruction and identification rejection study

A.1 Background rejection in $Z \rightarrow e^{-}e^{+}$ events per category per identification menu

Investigating the individual identification efficiencies of the various backgrounds (Figures A.1, A.2 and A.3), this difference is mainly coming from photon conversions (Figure A.1) and light-flavour background rejections (Figure A.2), which have different shapes in the p_T spectrum. Moreover, the rejection in both spectra tends to decrease after ∼50 GeV in the $Z \rightarrow e^{-}e^{+}$ case. This effect is not yet understood. In the case of the heavy-flavour background, the p_T an η distributions are relatively similar for both samples (Figure A.3).

Furthermore, The identification efficiency curves for the *medium* identification menu (Figure A.4) are showing fairly similar shapes and rejections, with a slightly higher light-flavour rejection below ∼40 GeV for the $Z \rightarrow e^{-}e^{+}$ sample.

A.2 Closure test: generator-level vs. reconstruction-based selection

Having the efficiency/rejection results in Z(ee)+jets MC, one can verify the background purity in the results using generator truth information of the simulated events. This can be achieved by performing a closure test, where the rejection measurements will be calculated using this time truth level event selection. Since it is possible in MC to retrieve details of the simulated events, one can use the type and origin of the reconstructed electrons to polarise between the prompt and the background fake electrons.

The closure test will be performed by replacing, in the Z mass window selection, the ID and track isolation requirements with truth type and origin of the reconstructed electrons, i.e. the Z electrons are well known, and so is the event selection of Z+jets

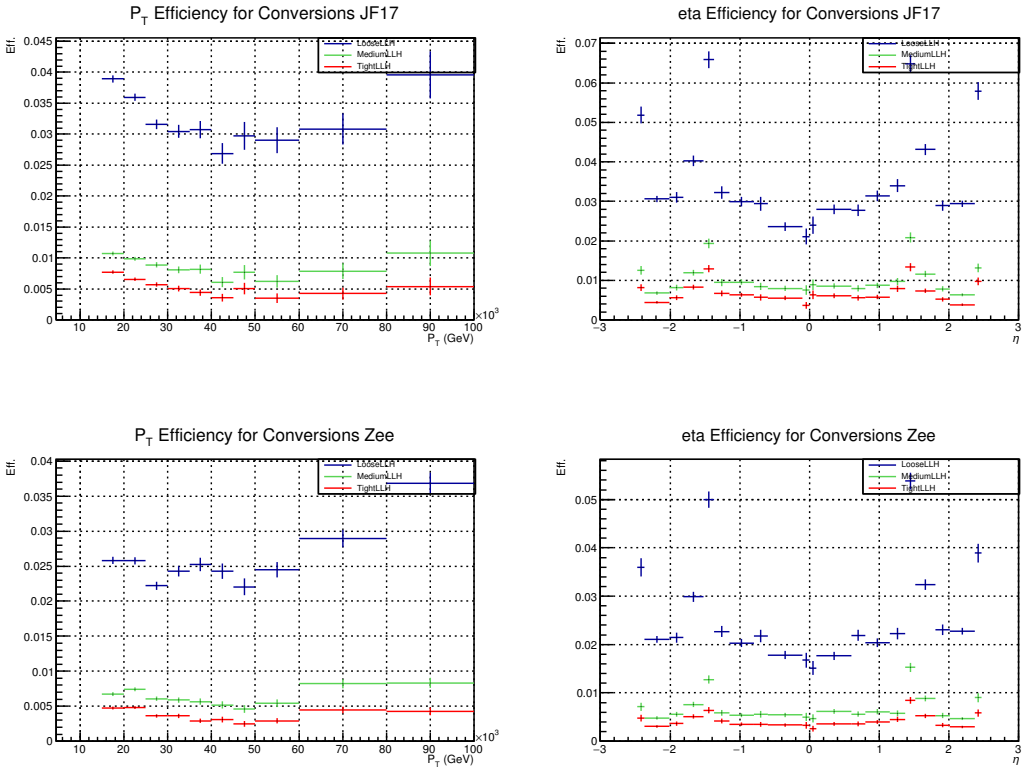

FIGURE A.1: The photon conversions background identification efficiency as a function of η and p_T for the different ID-menus. The two top plots correspond to the background enriched sample, while the other two plots on the bottom correspond to the $Z \rightarrow e^- + e^+$ sample.

events and the removal of the Z prompt electrons in the efficiency calculation. Figure A.5 and A.6 show a comparison of the efficiencies in jet p_T and η, Figure A.7 and A.8 in electron p_T and η, calculated with the truth based and the ID and track isolation based Z electrons selection.

In the jet and electron η spectrum (Figure A.6 and A.8), the agreement is relatively good, given only statistical uncertainties, with a very small deviation for higher η values. As for the p_T spectra (Figure A.5 and A.7), the agreement is different in both cases. For the jet p_T comparison, the agreement is bad around 40-60 GeV, which is not the case in electron p_T. The red distribution in jet p_T has a higher efficiency in this specific region, which is with high probability where Z electrons would belong. Therefore, this might suggest a signal contamination in the efficiency calculation using the medium ID and the track isolation. Furthermore, the efficiency in jet p_T in the low p_T region falls off much lower than in electron p_T (approximately a factor of 10^3 difference), which might justify why the effect is negligible in the electron p_T agreement.

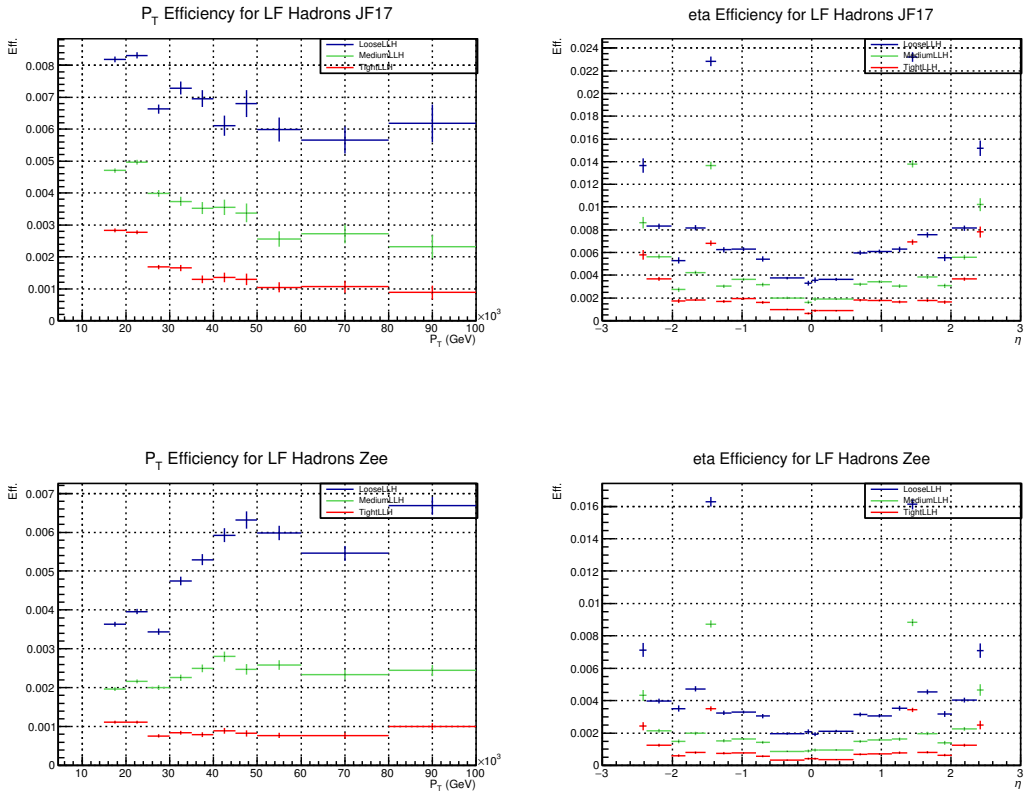

FIGURE A.2: The light-flavour background identification efficiency as a function of η and p_T for the different ID-menus. The two top plots correspond to the background enriched sample, while the other two plots on the bottom correspond to the $Z \rightarrow e^- + e^+$ sample.

Since the events are MC generated, one can also investigate in the truth information of the ID and track isolation selected events. In Figure A.9 and A.10, the type versus the origin of respectively the fake reconstructed electrons and the prompt Z electrons are plotted. From both plots, it is clear that the background is not negligible. In the fake electrons plot, signal contamination from Z prompt electrons represents approximately 4% of the total fake electrons collection, which is not negligible. Also the selection of Z electrons has background, but jets represent a tiny contribution (approximately 0.4 %). Finally, the overall efficiency and rejection based on truth event selection is respectively $\epsilon_{reco\ bkg}$ = 2.730 $\pm$ 0.002 % and $R_{reco\ bkg}$ = 36.62 $\pm$ 0.03. Given only statistical uncertainties, these results are relatively close to those calculated in section 3.4.2.

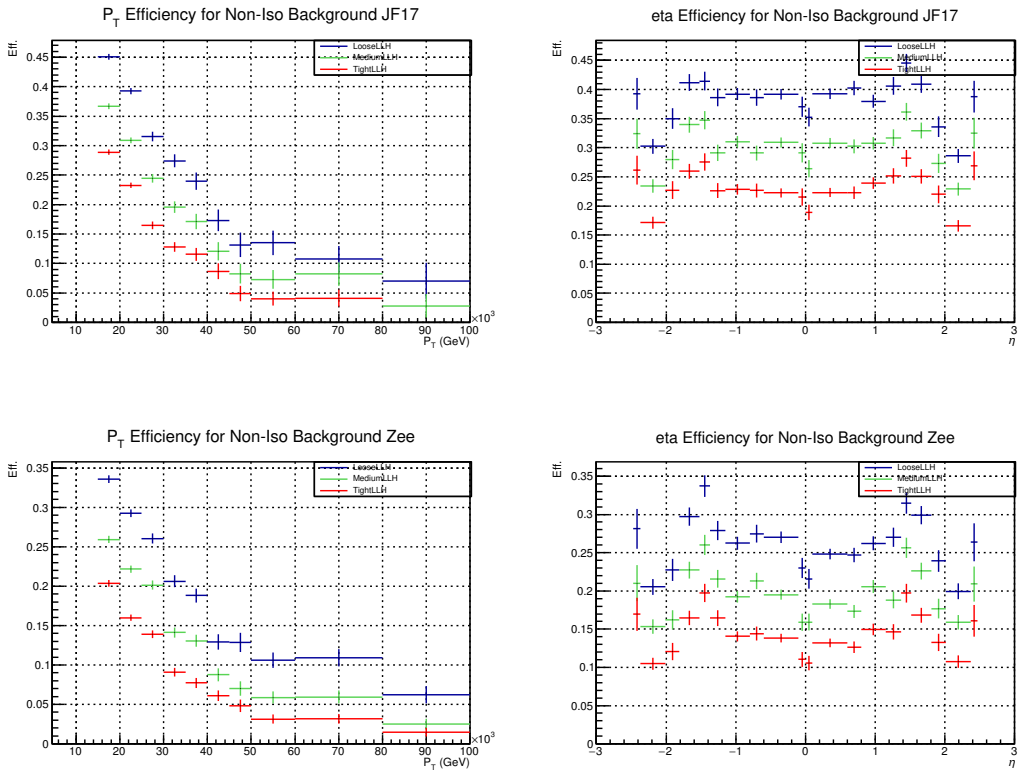

FIGURE A.3: The heavy-flavour background identification efficiency as a function of η and p_T for the different ID-menus. The two top plots correspond to the background enriched sample, while the other two plots on the bottom correspond to the $Z \rightarrow e^- + e^+$ sample.

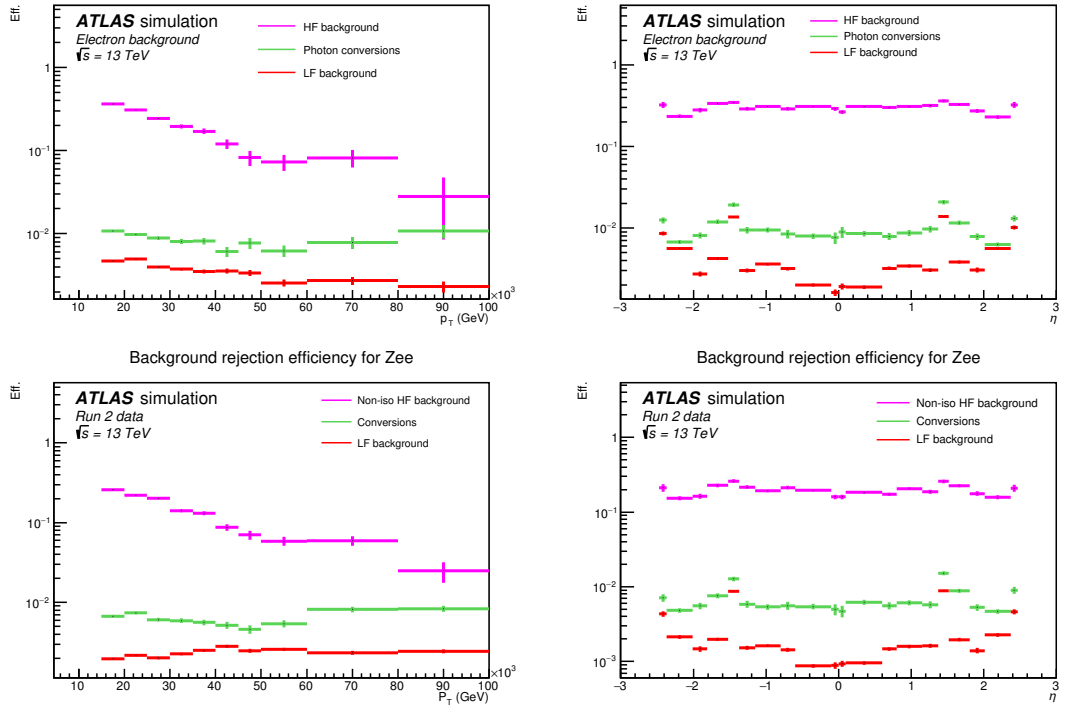

FIGURE A.4: The background identification efficiency for the *medium* ID-menu for the various background sources as a function of η and p_T. The two top plots correspond to the background enriched sample, while the other two plots on the bottom correspond to the $Z \to e^- + e^+$ sample.

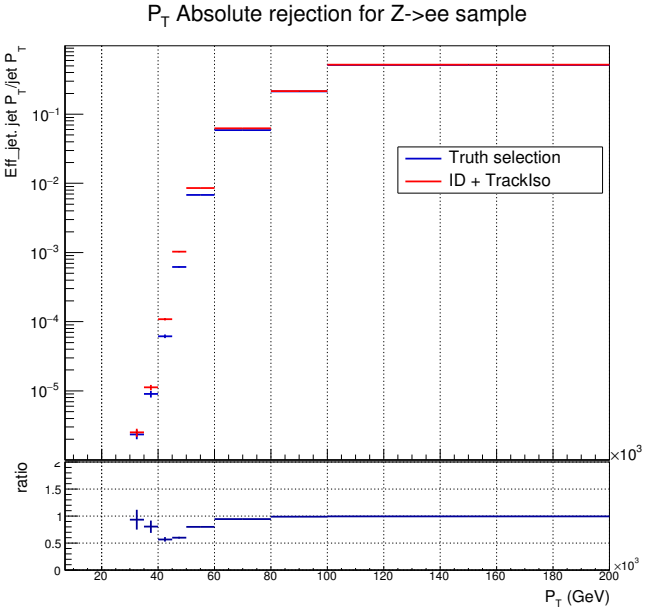

FIGURE A.5: The reconstruction efficiency of jets as electrons in jet p_T bins. The blue distribution corresponds to the efficiency calculated based on truth information while the red distribution is based on the ID and track isolation.

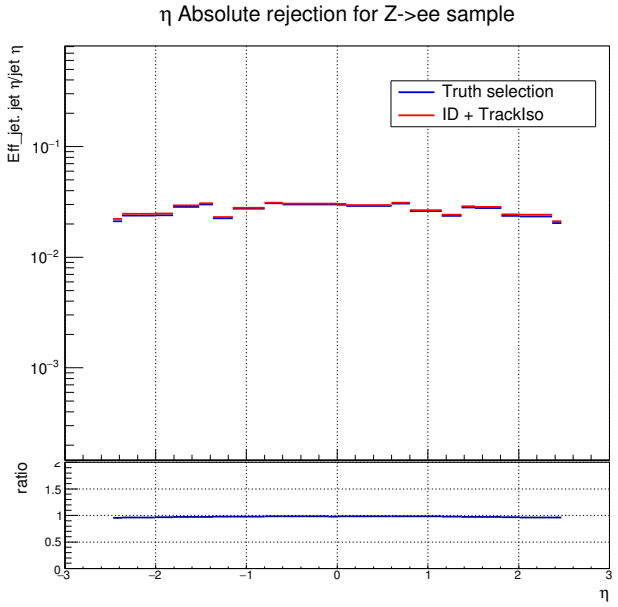

FIGURE A.6: The reconstruction efficiency of jets as electrons in jet η bins. The blue distribution corresponds to the efficiency calculated based on truth information while the red distribution is based on the ID and track isolation.

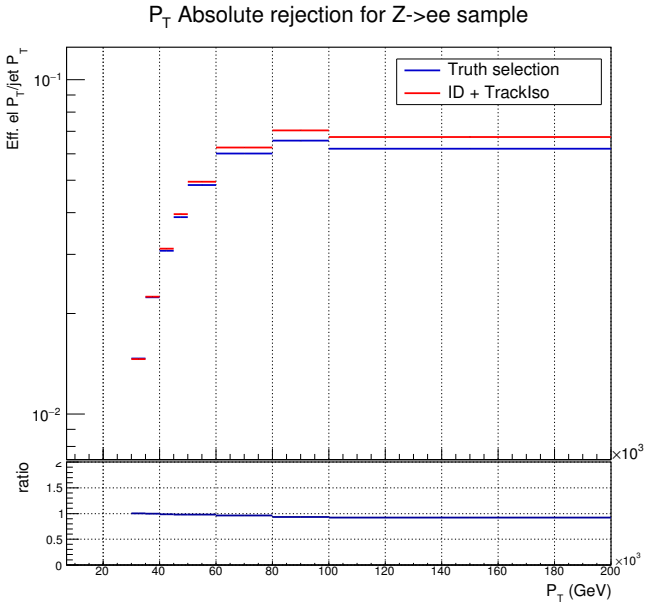

FIGURE A.7: The reconstruction efficiency of jets as electrons in electron p_T bins. The blue distribution corresponds to the efficiency calculated based on truth information while the red distribution is based on the ID and track isolation.

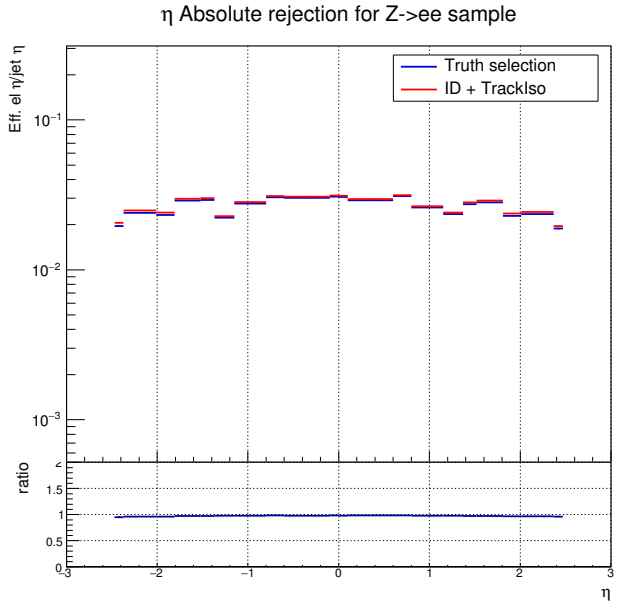

FIGURE A.8: The reconstruction efficiency of jets as electrons in electron η bins. The blue distribution corresponds to the efficiency calculated based on truth information while the red distribution is based on the ID and track isolation.

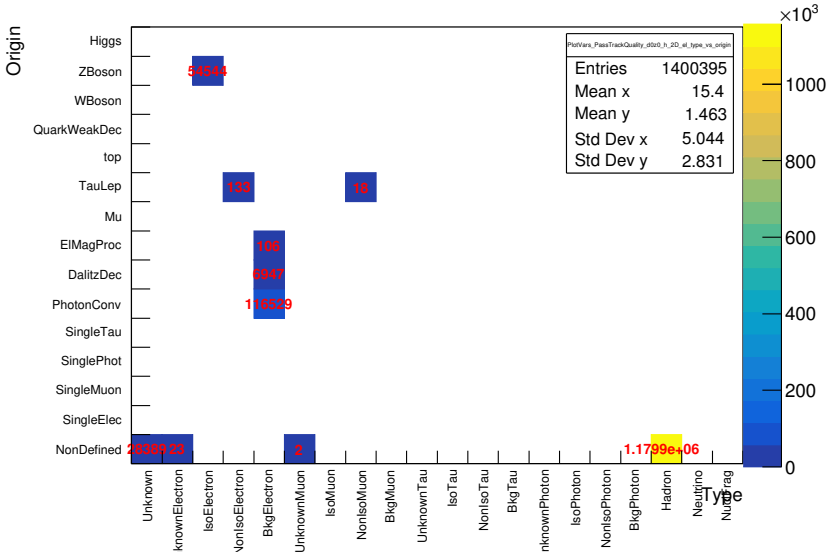

FIGURE A.9: The truth type and origin of the reconstructed fake electrons using the ID and track isolation in the Z mass window selection. Not all fake electrons are displayed in the plot, only significant contributions are shown.

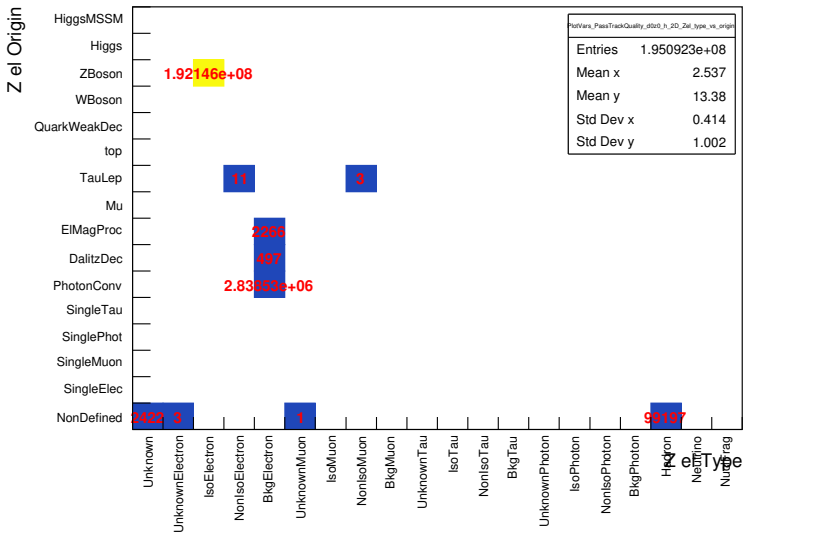

FIGURE A.10: The truth type and origin of the Z prompt electrons using the ID and track isolation in the Z mass window event selection. Not all fake electrons are displayed in the plot, only significant contributions are shown.

Appendix B

Measurement of the Higgs boson mass in $H \to ZZ^* \to 4\ell$

B.1 Single, di- and tri-lepton triggers

Channel	Single-lepton	Di-lepton	Tri-lepton
$4e$	e24_lhmedium_L1EM18VH (Period D) e24_lhmedium_L1EM20VH (Period E-J) e60_lhmedium e120_lhloose	2e12_lhloose_L12EM10VH	e17_lhloose_2e9_lhloose
4μ	mu20_iloose_L1MU15 mu40 mu60_0eta105_msonly	2mu10 mu18_mu8noL1	3mu6 3mu6_msonly mu18_2mu4noL1
$2e2\mu$	$4e$ OR 4μ	$4e$ OR 4μ OR e17_lhloose_mu14 e24_medium_L1EM20VHI_mu8noL1 e7_medium_mu24	$4e$ OR 4μ OR 2e12_lhloose_mu10 e12_lhloose_2mu10

TABLE B.1: Summary of the 2015 triggers used for the $H \to ZZ \to 4l^{\pm}$ event candidates and the corresponding p_T thresholds given the lepton type. In the case where more than one trigger is listed, the *or-statement* is intended.

Channel	Single-lepton	Di-lepton	Tri-lepton
$4e$	e24_lhmedium_ivarloose (Period A-D3) e26_lhtight_nod0_ivarloose (Period D4-F) e60_lhmedium_nod0 e60_lhmedium e140_lhloose_nod0 e300_etcut (Period A-D3)	2e15_lhvloose_nod0_L12EM13VH (Period A-D3) 2e17_lhvloose_nod0 (Period D4-F)	e17_lhloose_nod0_2e9_lhloose_nod0 (Period A-D3) replaced by HLT_e17_lhloose_nod0_2e10_lhloose_nod0_L1EM15VH_3EM8VH when instantaneous luminosity > $1.2 \cdot 10^{34}$cm^{-2}s^{-1}
4μ	mu24_ivarloose_L1MU15 (Period A) mu24_iloose_L1MU15 (Period A) mu24_ivarmedium (Period B-E) mu24_imedium (Period B-E) mu26_ivarmedium (Period D4-) mu26_imedium (Period D4-E2) mu40 (Period A) mu50	2mu10 (Period A) 2mu10_nomucomb (Period A) 2mu14 (Period B-) 2mu14_nomucomb (B-D3) mu20_mu8noL1 (Period A-E) mu20_nomucomb_mu6noL1_nscan03 (Period A-D3) mu22_mu8noL1 (Period D4-F)	3mu4 (Period A, I4-) 3mu6 (Period B-D3) 3mu6_msonly (Period D4-F) mu11_nomucomb_2mu4noL1_nscan03_L1MU11_2MU6 (Period A-D3) mu20_2mu4noL1 mu20_nomucomb_mu6noL1_nscan03 mu20_msonly_mu10noL1_msonly_nscan05_noComb (Period A-D3)
$2e2\mu$	$4e$ OR 4μ	$4e$ OR 4μ OR e17_lhloose_nod0_mu14 (Period A-D3) e24_lhmedium_nod0_L1EM20VHI_mu8noL1 (Period A-D3) e7_lhmedium_nod0_mu24 (Period A-D3) e17_lhloose_mu14 (Period D4-F) e24_lhmedium_L1EM20VHI_mu8noL1 (Period D4-F) e7_lhmedium_mu24 (Period D4-F)	$4e$ OR 4μ OR HLT_e17_lhloose_nod0_mu14 HLT_e24_lhmedium_nod0_L1EM20VHI_mu8noL1 (Period A-D3) HLT_e26_lhmedium_nod0_L1EM22VHI_mu8noL1 (Period D4-) HLT_e7_lhmedium_nod0_mu24 HLT_e12_lhloose_nod0_2mu10 HLT_2e12_lhloose_nod0_mu10

TABLE B.2: Summary of the 2016 triggers used for the $H \to ZZ \to 4l^{\pm}$ event candidates and the corresponding p_T thresholds given the lepton type. In the case where more than one trigger is listed, the *or-statement* is intended.

Channel	Single-lepton	Di-lepton	Tri-lepton
$4e$	HLT_e26_lhtight_nod0_ivarloose HLT_e60_lhmedium_nod0 HLT_e140_lhloose_nod0 HLT_e300_etcut	HLT_2e17_lhvloose_nod0_L12EM15VHI[3] HLT_2e24_lhvloose_nod0	HLT_e24_lhvloose_nod0_2e12_lhvloose_nod0_L1EM20VH_3EM10VH
4μ	HLT_mu26_ivarmedium HLT_mu50 HLT_mu60_0eta105_msonly	HLT_2mu14 HLT_mu22_mu8noL1 HLT_mu22_mu8noL1_calotag_0eta010	HLT_mu20_2mu4noL1 HLT_3mu6_msonly HLT_3mu4 (below 1.2e34) HLT_3mu6 HLT_4mu4
$2e2\mu$	$4e$ OR 4μ	$4e$ OR 4μ OR HLT_e17_lhloose_nod0_mu14 HLT_e26_lhmedium_nod0_mu8noL1 HLT_e7_lhmedium_nod0_mu24	$4e$ OR 4μ OR HLT_e12_lhloose_nod0_2mu10 HLT_2e12_lhloose_nod0_mu10

TABLE B.3: Summary of the 2017 triggers used for the $H \to ZZ \to 4l^{\pm}$ event candidates and the corresponding p_T thresholds given the lepton type. In the case where more than one trigger is listed, the *or-statement* is intended.

Channel	Single-lepton	Di-lepton	Tri-lepton
$4e$	HLT_e26_lhtight_nod0_ivarloose HLT_e26_lhtight_nod0[4] HLT_e60_lhmedium_nod0 HLT_e140_lhloose_nod0 HLT_e300_etcut	HLT_2e17_lhvloose_nod0_L12EM15VHI HLT_2e24_lhvloose_nod0 (L1_2EM20VH)	HLT_e24_lhvloose_nod0_2e12_lhvloose_nod0_L1EM20VH_3EM10VH
4μ	HLT_mu26_ivarmedium HLT_mu50 HLT_mu60_0eta105_msonly	HLT_2mu14 (L1_2MU10) HLT_mu22_mu8noL1 (L1_MU20)	HLT_mu20_2mu4noL1 (L1_MU20) HLT_3mu6 (L1_3MU6)
$2e2\mu$	$4e$ OR 4μ	$4e$ OR 4μ OR HLT_e17_lhloose_nod0_mu14 HLT_e26_lhmedium_nod0_mu8noL1 HLT_e7_lhmedium_nod0_mu24	$4e$ OR 4μ OR HLT_e12_lhloose_nod0_2mu10 HLT_2e12_lhloose_nod0_mu10

TABLE B.4: Summary of the 2018 triggers used for the $H \to ZZ \to 4l^{\pm}$ event candidates and the corresponding p_T thresholds given the lepton type. In the case where more than one trigger is listed, the *or-statement* is intended.

B.2 Generator comparison study of electron reducible background in Z+jets events

In this section, a comparison of the estimated reducible background electrons using two different MC generators is studied. The goal is to test the dependency on generators, which have different methods of simulating the physics processes though the ATLAS detector. The generators are SHERPA, which is the nominal choice, and MADGRAPH is the alternative option. A comparison is performed using one of the most prominent background sources for fake electrons, Z bosons production in association with jets. Simulation samples of this process contain two genuine prompt electrons from the Z boson decay, and fake reconstructed electrons from different background sources, mainly those listed in section 3.2. Using these samples, a MC generator background classification is performed between Z+jets SHERPA and Z+jets MADGRAPH MC. Figure B.5 shows a comparison of the electron type obtained from generator-level information between Z+jets SHERPA and Z+jets MADGRAPH MC. In the $Z + X$ CR, MADGRAPH has about 10% more heavy-flavour background and photon conversions than SHERPA. Also, a factor of 2 difference in isolated electrons but their contribution is very low.

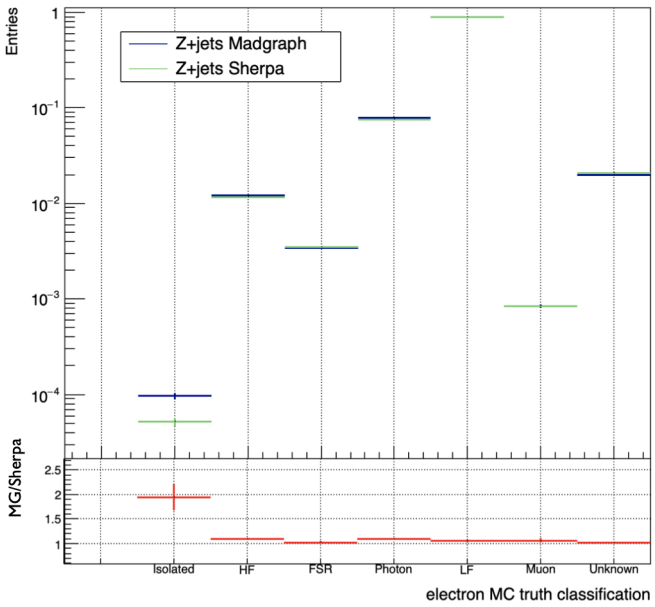

TABLE B.5: Electron type classification comparison between Z+jets Sherpa vs Z+jets Madgraph

As discussed in section 4.5.2.2, for estimating the light-flavour and photon conversions background, a fit is performed in the $3l + X$ CR. The fit is on the expected number of pixel hits in the innermost layers of the ID. The templates of the backgrounds are taken from both MC samples in the $Z + X$ CR. Using an unfolding tool, referred to as the *sPlot method*, the light-flavour and photon conversions background is determined in terms of electron p_T and the number of associated reconstructed jets. Transfer factors, which are the efficiencies of the background passing the analysis selections, are also calculated for both backgrounds in the $Z + X$ CR, which are corrected to match data using scale factors. The final step is the extrapolation of the backgrounds contribution to the SR, using the transfer factors, which calculated from the $Z + X$ CR.

Figure B.6 shows the ratio between SHERPA and MADGRAPH of the fit yields, transfer factors and scale factors as a function of the number of jets per event and electron p_T, within the $3l + X$ CR. The plots on the left side correspond to the photon conversions background, and the light-flavour jets on right side. Regarding the fit yields, the agreement is overall relatively good. This is expected from the similar templates in both event samples. The transfer factors are clearly different in both generators. The difference is mainly expected from different ways of simulating the energy distribution around reconstructed object, which results in a different calibration for the isolation requirements. The last two bottom plots show the ratio of the scale factors used to correct MC to data. From the difference in the transfer factors, it is no surprise that the scale factors are also different.

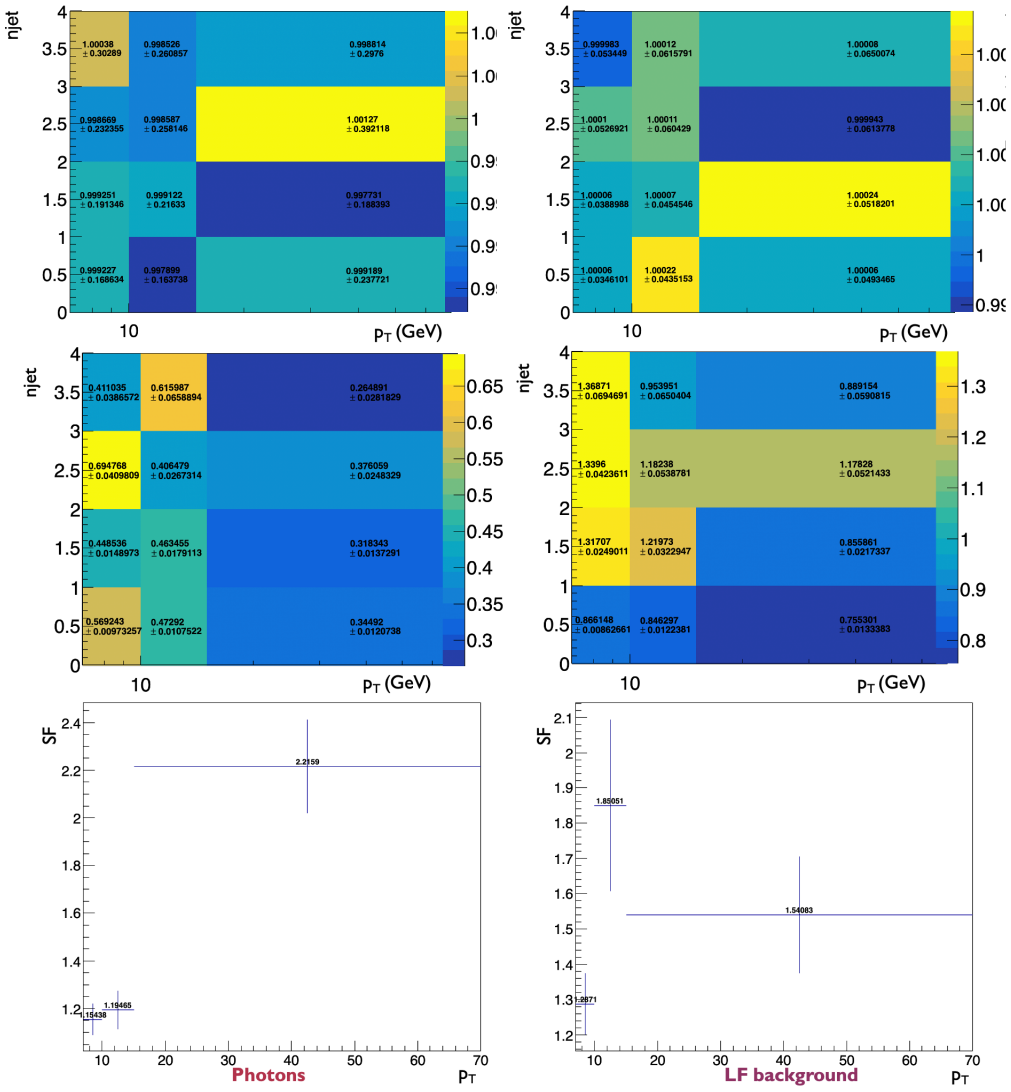

TABLE B.6: Fit yield, transfer factors and scale factors ratio between SHERPA and MADGRAPH as a function of the number of jets per event and electron p_T within the $3l + X$ CR. The plots on the left side correspond to the photon conversions background, and the light-flavour jets on right side.

Finally, using both generators the fit results for the different electron background sources in the SR are compared in Table B.7. For the light-flavour and photon conversions background, the results are within the total uncertainties (statistical and systematic). For the heavy-flavour background the results are also in agreement, However, MADGRAPH has a large total uncertainty, which is mainly statistical dominated due to a small number of simulated events in the SR.

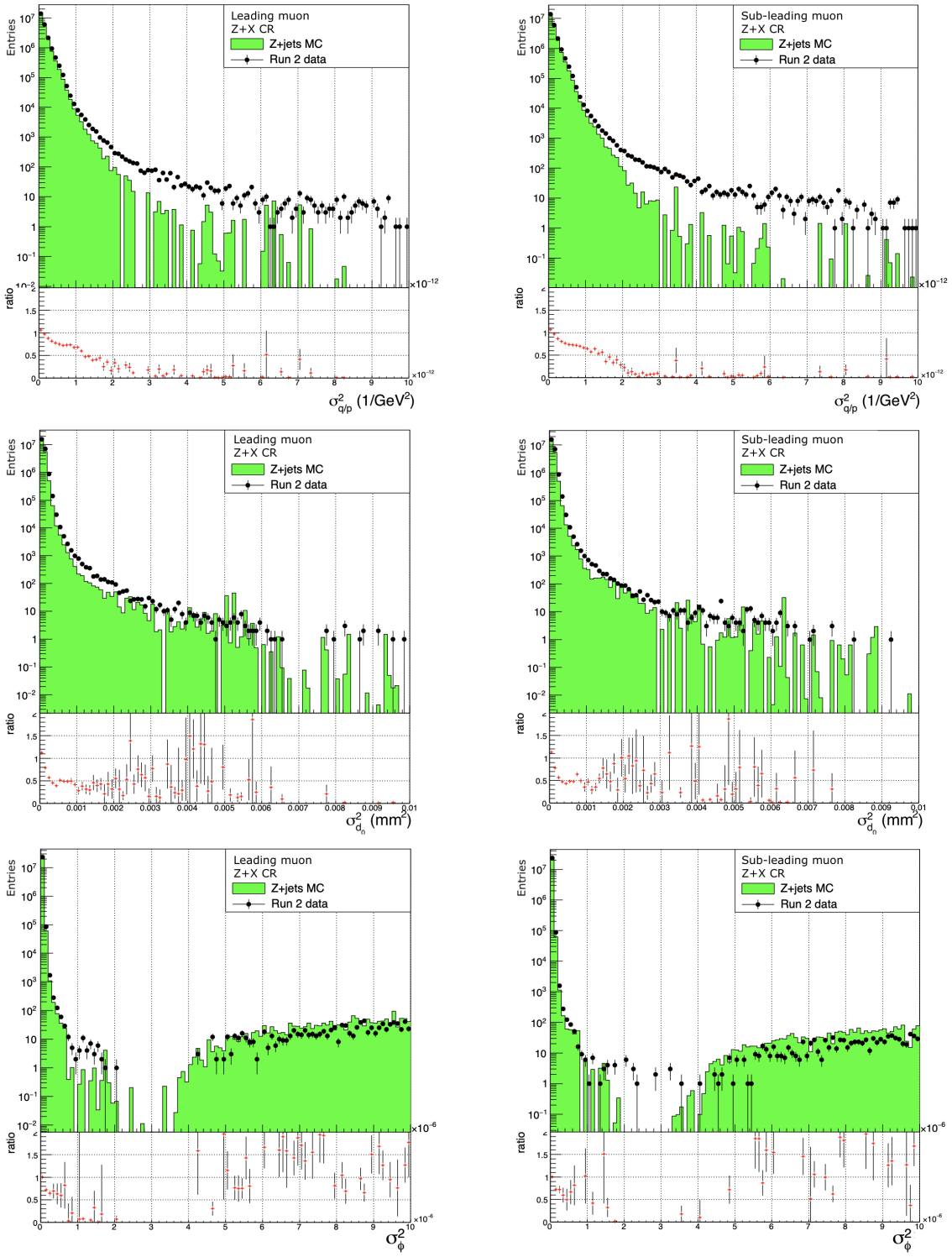

FIGURE B.1: The leading leptons covariance matrix elements distribution in data and MC.

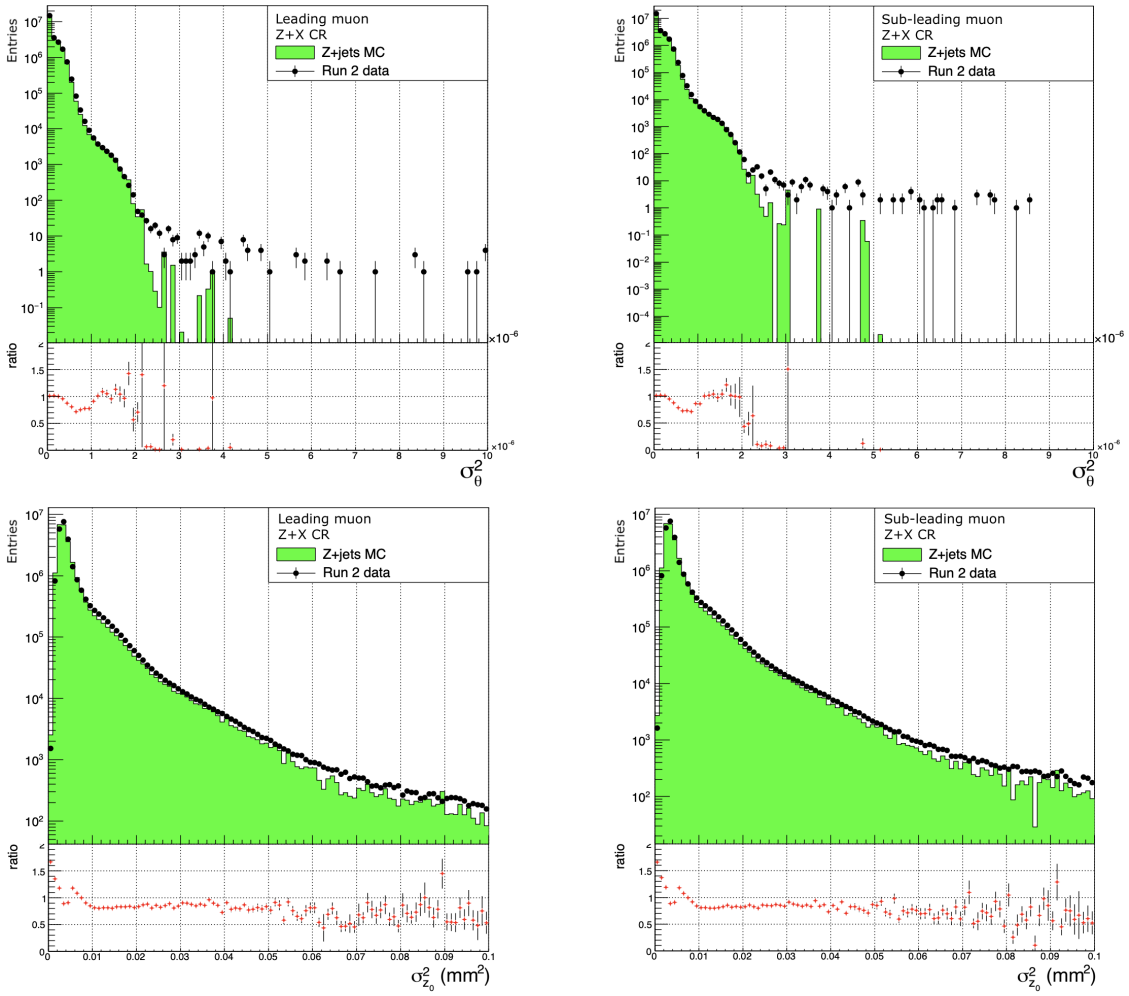

FIGURE B.2: The leading leptons covariance matrix elements distribution in data and MC.

Fit results in SR using Z+jets			
Type of background	Light-flavour jets	Misidentified photons	Heavy-flavour jets
SR yield in Sherpa	15.05±0.54(stat.)±2.37(sys.)	4.25±0.70(stat.)±0.85(sys.)	12.14±3.66 (stats.+sys.)
SR yield in MadGraph	10.41±0.36(stat.)±3.20(sys.)	6.96±1.14(stat.)±1.40(sys.)	22.65±11.77 (stats.+sys.)

TABLE B.7: Comparison of the fit results using SHERPA and MADGRAPH for the different electron background sources in the SR.

B.3 Data/MC comparison of the muon covariant matrix element

B.4 QM correction maps derived from the $Z + X$ CR

In Figure B.3, a comparison is shown between the QM correction maps (discussed in section 4.7.3.2) derived from the inclusive calibration samples containing $Z \to \mu^-\mu^+$ events and maps from di-muon events from the $Z + X$ CR. The curves are overall relatively in good agreement.

B.5 Additional data and MC comparisons in the signal region

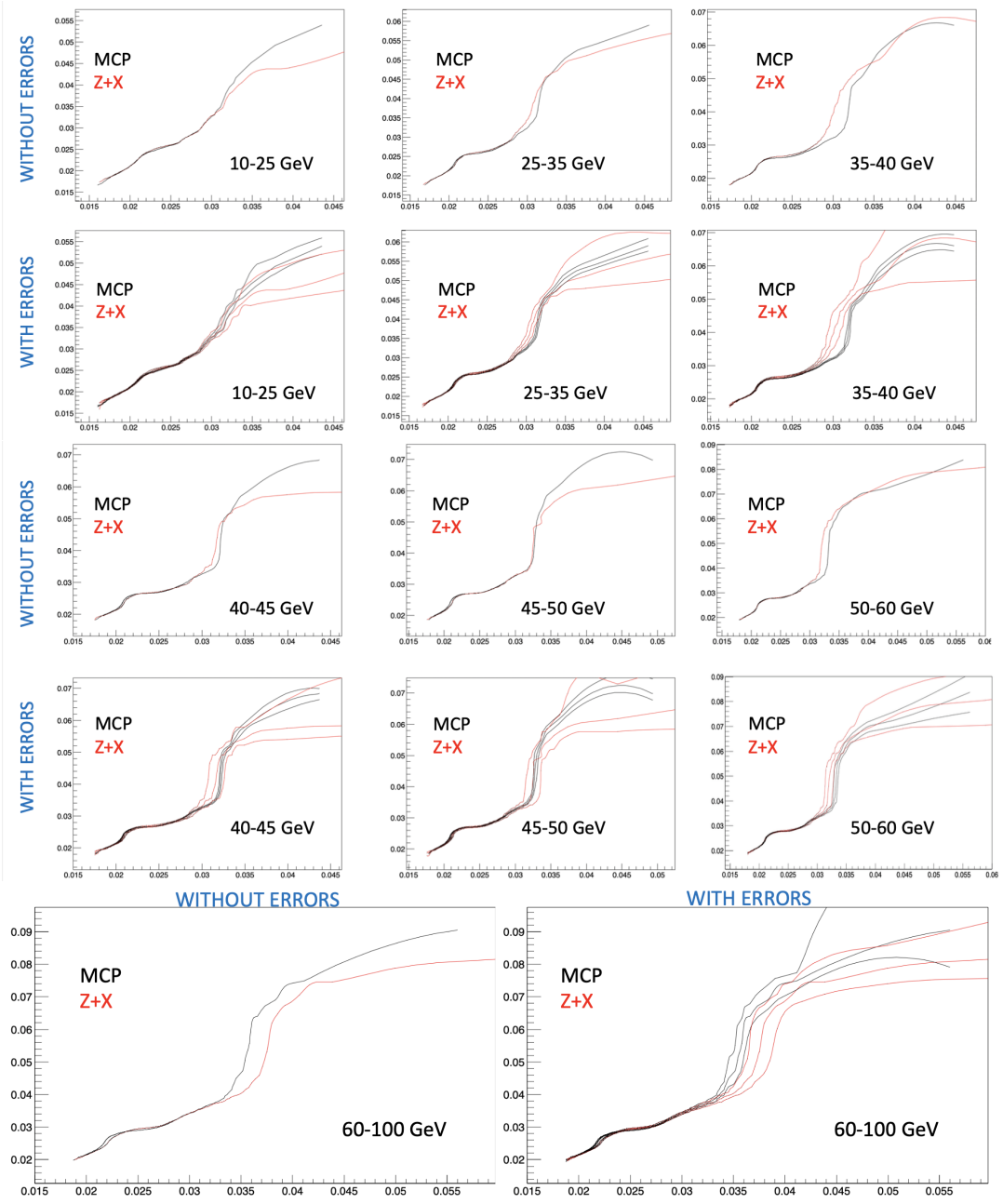

FIGURE B.3: A comparison is shown between the QM correction maps (discussed in section 4.7.3.2) derived from the inclusive calibration samples containing $Z \to \mu^-\mu^+$ events and maps from di-muon events from the $Z + X$ CR.

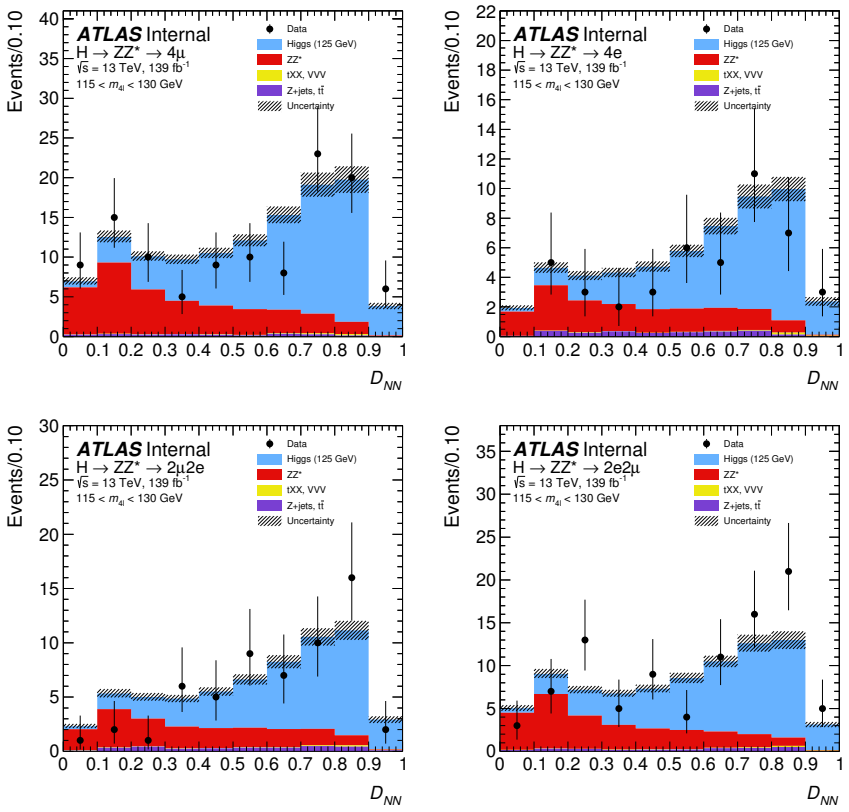

FIGURE B.4: The pre-fit inclusive D_{4l} distribution for each of the decay channels.

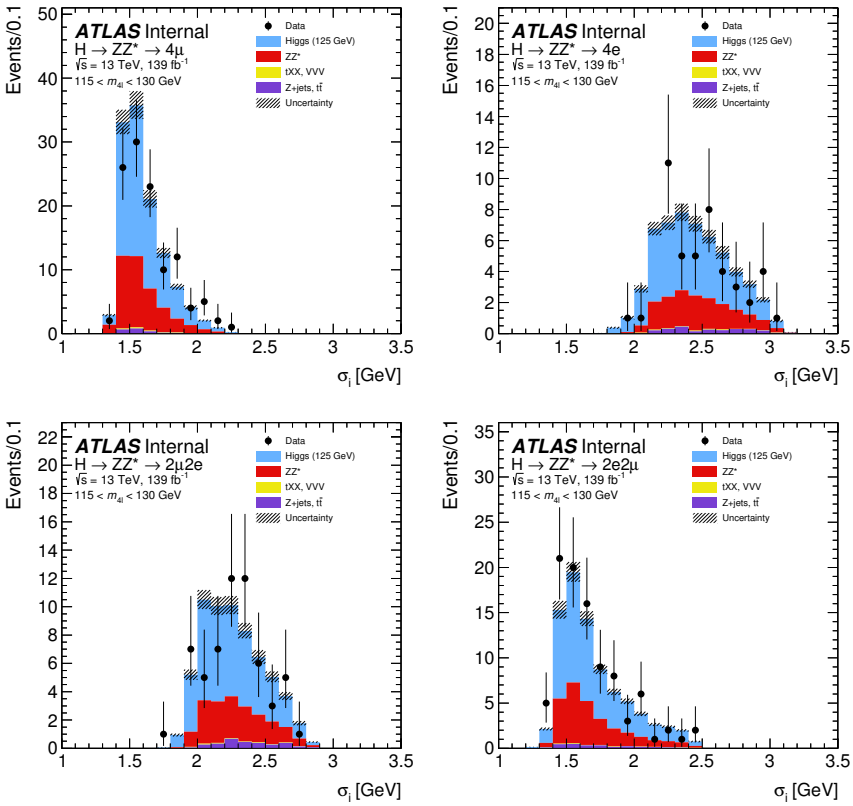

FIGURE B.5: The pre-fit inclusive σ_{4l} distribution for each of the decay channels.

Appendix C

EFT study of operator sensitive to EW quartic vertices in $\gamma\gamma \to 4\ell$

C.1 Definition of the dimension 8 relevant to quartic gauge couplings

Following the notation in this reference [paper], there are three classes of dimension 8 operators that affect electroweak quartic couplings. Figure C.1 shows the different dimension 8 EFT operators that leads to BSM neutral gauge-boson quartic interactions. The first class of operators, the *M*-operators, contains two covariant derivatives of the Higgs field, and two field strength tensors. The *T*-operators have four covariant derivatives of the Higgs field, and the *S*-operators have four field strength tensors. Table 5.1 shows the different operators, and which of the different quartic electroweak gauge-boson vertices they affect.

$$\mathcal{O}_{M,0} = \mathrm{Tr}\left[\widehat{W}_{\mu\nu}\widehat{W}^{\mu\nu}\right] \times \left[(D_\beta\Phi)^\dagger D^\beta\Phi\right] \ , \quad \mathcal{O}_{M,1} = \mathrm{Tr}\left[\widehat{W}_{\mu\nu}\widehat{W}^{\nu\beta}\right] \times \left[(D_\beta\Phi)^\dagger D^\mu\Phi\right] \ ,$$
$$\mathcal{O}_{M,2} = \left[B_{\mu\nu}B^{\mu\nu}\right] \times \left[(D_\beta\Phi)^\dagger D^\beta\Phi\right] \ , \quad \mathcal{O}_{M,3} = \left[B_{\mu\nu}B^{\nu\beta}\right] \times \left[(D_\beta\Phi)^\dagger D^\mu\Phi\right] \ ,$$
$$\mathcal{O}_{M,4} = \left[(D_\mu\Phi)^\dagger \widehat{W}_{\beta\nu}D^\mu\Phi\right] \times B^{\beta\nu} \ , \quad \mathcal{O}_{M,5} = \left[(D_\mu\Phi)^\dagger \widehat{W}_{\beta\nu}D^\nu\Phi\right] \times B^{\beta\mu} + \mathrm{h.c.} \ ,$$
$$\mathcal{O}_{M,7} = \left[(D_\mu\Phi)^\dagger \widehat{W}_{\beta\nu}\widehat{W}^{\beta\mu}D^\nu\Phi\right] \ .$$

$$\mathcal{O}_{T,0} = \mathrm{Tr}\left[\widehat{W}_{\mu\nu}\widehat{W}^{\mu\nu}\right] \times \mathrm{Tr}\left[\widehat{W}_{\alpha\beta}\widehat{W}^{\alpha\beta}\right] \ , \quad \mathcal{O}_{T,1} = \mathrm{Tr}\left[\widehat{W}_{\alpha\nu}\widehat{W}^{\mu\beta}\right] \times \mathrm{Tr}\left[\widehat{W}_{\mu\beta}\widehat{W}^{\alpha\nu}\right]$$
$$\mathcal{O}_{T,2} = \mathrm{Tr}\left[\widehat{W}_{\alpha\mu}\widehat{W}^{\mu\beta}\right] \times \mathrm{Tr}\left[\widehat{W}_{\beta\nu}\widehat{W}^{\nu\alpha}\right] \ , \quad \mathcal{O}_{T,5} = \mathrm{Tr}\left[\widehat{W}_{\mu\nu}\widehat{W}^{\mu\nu}\right] \times B_{\alpha\beta}B^{\alpha\beta}$$
$$\mathcal{O}_{T,6} = \mathrm{Tr}\left[\widehat{W}_{\alpha\nu}\widehat{W}^{\mu\beta}\right] \times B_{\mu\beta}B^{\alpha\nu} \ , \quad \mathcal{O}_{T,7} = \mathrm{Tr}\left[\widehat{W}_{\alpha\mu}\widehat{W}^{\mu\beta}\right] \times B_{\beta\nu}B^{\nu\alpha}$$
$$\mathcal{O}_{T,8} = B_{\mu\nu}B^{\mu\nu}B_{\alpha\beta}B^{\alpha\beta} \ , \quad \mathcal{O}_{T,9} = B_{\alpha\mu}B^{\mu\beta}B_{\beta\nu}B^{\nu\alpha} \ .$$

$$\mathcal{O}_{S,0} = \left[(D_\mu\Phi)^\dagger D_\nu\Phi\right] \times \left[(D^\mu\Phi)^\dagger D^\nu\Phi\right]$$
$$\mathcal{O}_{S,1} = \left[(D_\mu\Phi)^\dagger D^\mu\Phi\right] \times \left[(D_\nu\Phi)^\dagger D^\nu\Phi\right]$$
$$\mathcal{O}_{S,2} = \left[(D_\mu\Phi)^\dagger D_\nu\Phi\right] \times \left[(D^\nu\Phi)^\dagger D^\mu\Phi\right]$$

FIGURE C.1: The dimension 8 operators that leads to BSM EW gauge-boson quartic interactions.

EFT operators	Quadratic term (pb)	Linear term (pb)
M0	0.91 ± 0.0032	$-2.17\times 10^{-6} \pm 6.17\times10^{-8}$
M1	0.060 ± 0.00017	$-1.42\times10^{-5} \pm 4.05\times10^{-7}$
M2	39.19 ± 0.14	$9.92\times10^{-7} \pm 7.49\times10^{-8}$
M3	$1.19\times10^{-5} \pm 3.28\times10^{-8}$	$6.50\times10^{-6} \pm 4.91\times10^{-7}$
M4	2.99 ± 0.010	$4.11\times10^{-6} \pm 4.06\times10^{-7}$
M5	0.79 ± 0.0022	$3.59\times10^{-6} \pm 2.71\times10^{-7}$
M7	$0.015 \pm 4.15\times10^{-5}$	$-5.74\times10^{-7} \pm 1.36\times10^{-8}$
T0	129.6 ± 0.26	$0.00015 \pm 1.75\times10^{-6}$
T1	129.6 ± 0.26	$0.00015 \pm 1.75\times10^{-6}$
T2	29.74 ± 0.083	$0.00011 \pm 3.03\times10^{-6}$
T5	612.9 ± 0.97	$0.00024 \pm 1.11\times10^{-5}$
T6	321.5 ± 0.86	$4.37 \times 10^{-5} \pm 4.45\times10^{-6}$
T7	51.33 ± 0.11	$8.43\times 10^{-5} \pm 3.00\times 10^{-6}$
T8	8179 ± 15.79	$0.0010 \pm 2.40\times10^{-5}$
T9	1887 ± 3.73	$0.00082 \pm 3.88\times10^{-5}$

TABLE C.1: The values of the linear and quadratic terms of the effective cross section (eq. 5.6) in the $2e2\mu$ final state channel, where each $c_i/\Lambda = 10^{-8}$ GeV^{-4}, while the others are set to zero.

C.2 Cross section of the SM and BSM $\gamma\gamma \to 4l^{\pm}$ process

Using MADGRAPH5_AMC@NLO [70,71], one can generate the $\gamma\gamma \to 4l^{\pm}$ process in the SM and BSM scenario, while calculating the corresponding cross sections. In the case of BSM, the EFT model [100] is used, where the value c_i/Λ^4 of the different operators can be set to calculate the BSM contribution to the process. From eq. 5.6, the last two terms form the total contribution from the dimension-8 operators listed in Table 5.1. These terms can be separately computed given a value of c_i/Λ^4. Table C.1 shows the values of the linear and quadratic terms of the effective cross section (eq. 5.6) in the $2e2\mu$ final state channel as an example, where each $c_i/\Lambda = 10^{-8}$ GeV^{-4}, while the others are set to zero. It should be noted that for this c_i/Λ^4 value the quadratic term is orders of magnitude higher, while the linear contribution is for some operators negative, since the latter represents an interference term between the SM and the BSM operators, which can lead to constructive or destructive interference. From these generated values using MADGRAPH5_AMC@NLO [70,71], one can predict the value of the linear and quadratic terms given any c_i/Λ^4 value by determining the proportionality constants a_i and b_{ii} in eq. 5.6. These are listed in Table C.2 for each M- and T-operator in the $2e2\mu$ final state. Figure C.2 shows in blue dots the cross section values generated using MADGRAPH5_AMC@NLO [70,71] for different values of c_{T8}/Λ^4, while the red curve corresponds to the function determined from the fitted a_i and b_{ii} coefficients. The agreement is clearly spot on. The same closure test is performed for the other operators and final states, where the same closure is observed. The proportionality constants a_i and b_{ii} can be used to estimate the quadratic and linear terms of the effective cross section for any c_i/Λ^4, value.

	Linear coefficient (pb/GeV^{-4})	Quadratic coefficient pb/GeV^{-8}
M0	-211+/-8	(9.088+/-0.026)e+15
M1	114.1+/-2.4	(5.967+/-0.024)e+14
M2	(-1.39+/-0.05)e+03	(3.909+/-0.011)e+17
M3	748+/-16	(2.566+/-0.010)e+16
M4	383+/-15	(2.980+/-0.009)e+16
M5	413+/-9	(7.826+/-0.031)e+15
M7	-57.0+/-1.2	(1.492+/-0.006)e+14
T0	(1.467+/-0.009)e+04	(1.1370+/-0.0021)e+18
T1	(1.467+/-0.009)e+04	(1.1370+/-0.0021)e+18
T2	(1.096+/-0.007)e+04	(2.614+/-0.005)e+17
T5	(2.400+/-0.028)e+04	(5.440+/-0.011)e+18
T6	(2.67+/-0.22)e+03	(2.906+/-0.008)e+18
T7	(7.33+/-0.12)e+03	(4.705+/-0.013)e+17
T8	(1.019+/-0.010)e+05	(7.499+/-0.022)e+19
T9	(2.106+/-0.018)e+14	(1.730+/-0.005)e+19

TABLE C.2: The fitted a_i and b_{ii} coefficients (from eq. 5.6) for each M- and T-operator in the $2e2\mu$ final state.

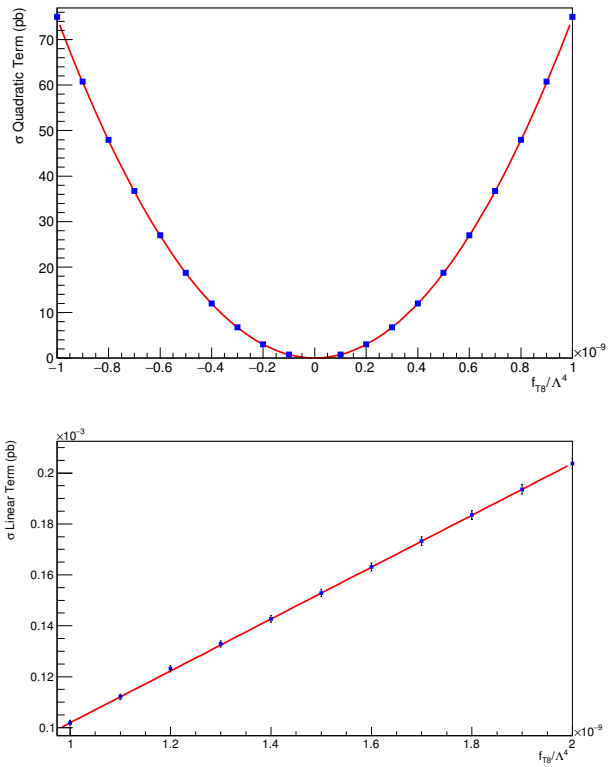

FIGURE C.2: The quadratic (A) and linear (B) term value (from eq. 5.6) as a function of c_{T8}/Λ^4. The values in blue dots were generated using MADGRAPH5_AMC@NLO [70, 71] for different values of c_{T8}/Λ^4, and the red curve corresponds the function determined from the fitted a_i and b_{ii} coefficients.

Bibliography

[1] ATLAS Collaboration. (2022). Measurement of the Higgs boson mass in the $H \to ZZ^* \to 4\ell$ decay channel using 139 fb $^{-1}$ of $\sqrt{s} = 13$ TeV pp collisions recorded by the ATLAS detector at the LHC. arXiv preprint arXiv:2207.00320.

[2] Griffiths, D., & Schroeter, D. (2018). Introduction to Quantum Mechanics (3rd ed.). Cambridge: Cambridge University Press. doi:10.1017/9781316995433.

[3] O. S. Brning, P. Collier, P Lebrun, S. Myers, R. Ostojic, J. Poole, and P. Proudlock, LHC Design Report. Geneva: CERN, 2004.

[4] I. Falconer, "J J Thomson and the discovery of the electron," Physics Education, vol. 32, pp. 226–231, jul 1997. 10.1088/0031-9120/32/4/015.

[5] Mark Thomson. Modern Particle Physics. Cambridge University Press, 2013.

[6] Francis Halzen and Alan D. Martin. Quarks and Leptons: An Introductory Course in Modern Particle Physics. John Wiley and Sons, 1984.

[7] Konstantinidis, N. et al. Lecture notes for the 2017 HEP School for Experimental High Energy Physics Students. Tech. rep. Science and Technology Facilities Council, 2017. url: http://purl.org/net/epubs/manifestation/34993301/RAL-TR-2017-009.pdf.

[8] Abdelhak Djouadi. "The anatomy of electroweak symmetry breaking". In: Physics Reports 457.1-4 (Feb. 2008), pp. 1–216. issn: 0370-1573. doi: 10.1016/j.physrep. 2007.10.004. url: http://dx.doi.org/10.1016/j.physrep.2007.10.004.

[9] Peter W. Higgs. "Broken Symmetries and the Masses of Gauge Bosons". In: Phys. Rev. Lett. 13 (16 Oct. 1964), pp. 508–509. doi: 10.1103/PhysRevLett.13.508. url: https://link.aps.org/doi/10.1103/PhysRevLett.13.508.

[10] F. Englert and R. Brout. "Broken Symmetry and the Mass of Gauge Vector Mesons". In: Phys. Rev. Lett. 13 (9 Aug. 1964), pp. 321–323. doi: 10.1103/ PhysRevLett.13.321. url: https://link.aps.org/doi/10.1103/PhysRevLett.13.321.

[11] G. S. Guralnik, C. R. Hagen, and T. W. B. Kibble. "Global Conservation Laws and Massless Particles". In: Phys. Rev. Lett. 13 (20 Nov. 1964), pp. 585–587. doi: 10.1103/PhysRevLett.13.585. url: https://link.aps.org/doi/10.1103/ PhysRevLett.13.585.

[12] M. Roos, “Dark Matter: The evidence from astronomy, astrophysics and cosmology,” 2010. arXiv: 1001.0316 [astro-ph.CO].

[13] T. Lee and H. Park, Graviton and Massive Symmetric Rank-Two Tensor in String Theory, Acta Phys. Polon. Supp. **13** (2020), 303 doi:10.5506/APhysPolBSupp.13.303 [arXiv:1909.08516 [hep-th]].

[14] S. M. Carroll, "Lecture notes on general relativity,” [arXiv:gr-qc/9712019 [gr-qc]].

[15] S. P. Martin, Adv. Ser. Direct. High Energy Phys. **18** (1998), 1-98 doi:10.1142/9789812839657_0001 [arXiv:hep-ph/9709356 [hep-ph]].

[16] Polchinski, J. (1998). String Theory (Cambridge Monographs on Mathematical Physics). Cambridge: Cambridge University Press. doi:10.1017/CBO9780511816079

[17] Escultura, E.E.. (2008). The grand unified theory. Nonlinear Analysis: Theory, Methods & Applications. 69. 823-831.

[18] 10.1016/j.na.2008.02.043. Mazumdar, A. (1999). Extra dimensions and inflation. Physics Letters B, 469(1-4), 55-60.

[19] Hanneke, D., Fogwell, S., & Gabrielse, G. (2008). New measurement of the electron magnetic moment and the fine structure constant. Physical Review Letters, 100(12), 120801.

[20] Weinberg, S. (2021). On the development of effective field theory. The European Physical Journal H, 46(1), 1-6.

[21] Månsson, A. (2009). Understanding the special theory of relativity. arXiv preprint arXiv:0901.4690.

[22] Young, Thomas (1804). "The Bakerian lecture. Experiments and calculation relative to physical optics". Philosophical Transactions of the Royal Society of London. 94: 1–16. doi:10.1098/rstl.1804.0001. S2CID 110408369. Retrieved 14 July 2021.

[23] "X-Ray Data Booklet". xdb.lbl.gov. Retrieved 2020-06-20.

[24] Griffiths, D. "Introduction to Elementary particles. 2. enl. and rev." (2008).

[25] LHC Higgs Cross Section Working Group. Handbook of LHC Higgs Cross Sections: 4. Deciphering the Nature of the Higgs Sector. CERN Yellow Reports: Monographs. Oct. 2016. doi: 10.23731/CYRM-2017-002. url: https://cds.cern.ch/record/ 2227475.

[26] Mangano, M.L., Ortona, G. & Selvaggi, M. Measuring the Higgs self-coupling via Higgs-pair production at a 100 TeV p–p collider. Eur. Phys. J. C 80, 1030 (2020). https://doi.org/10.1140/epjc/s10052-020-08595-3

[27] "Review of Particle Physics," Progress of Theoretical and Experimental Physics, vol. 2020, 08 2020. 10.1093/ptep/ptaa104.

[28] The ATLAS Collaboration, "Summary plots from the ATLAS standard model physics group," 2018. https://atlas.web.cern.ch/Atlas/GROUPS/PHYSICS/CombinedSummaryPlots/SM/.

[29] Ellis, J. (2021). SMEFT Constraints on New Physics Beyond the Standard Model. arXiv preprint arXiv:2105.14942.

[30] E.P. Wigner, Group Theory and its Application to the Quantum Mechanics of Atomic Spec- tra, Academic Press (1959).

[31] The ATLAS Collaboration, "The ATLAS experiment at the cern large hadron collider," Journal of Instrumentation, vol. 3, pp. S08003–S08003, aug 2008. 10.1088/1748-0221/3/08/s08003.

[32] The CMS Collaboration JINST, vol. 3, pp. S08004–S08004, aug 2008. 10.1088/1748- 0221/3/08/s08004.

[33] View of the LHC tunnel. (Image: Maximilien Brice/CERN), https://cds.cern.ch/record/1998498

[34] DiGiovine, B., Henderson, D., Holt, R. J., Raut, R., Rehm, K. E., Robinson, A., ... & Ugalde, C. (2015). Bubble chambers for experiments in nuclear astrophysics. Nuclear Instruments and Methods in Physics Research Section A: Accelerators, Spectrometers, Detectors and Associated Equipment, 781, 96-104.

[35] I. C. MacNeill, "Measurement of top quark-antiquark pair production in association with a Z boson with a trilepton final state in pp collisions at 8 TeV center of mass energy,"

[36] Saldin, E. (2018). Relativity and synchrotron radiation: critical reexamination of existing theory. arXiv preprint arXiv:1808.07808.

[37] Larmor J (1897). "LXIII.On the theory of the magnetic influence on spectra; and on the radiation from moving ions". Philosophical Magazine. 5. 44 (271): 503–512. doi:10.1080/14786449708621095. Formula is mentioned in the text on the last page.

[38] E. Mobs, "The CERN accelerator complex. complexe des accélérateurs du cern," Jul 2016. https://cds.cern.ch/record/2197559.

[39] AC Team, "Computer-generated diagram of an LHC dipole.", Sep 1998. https://cds.cern.ch/record/39731

[40] L. Evans and P. Bryant, "LHC Machine," JINST **3** (2008), S08001 doi:10.1088/1748-0221/3/08/S08001

[41] The ATLAS Collaboration, “ATLAS data quality operations and performance for 2015–2018 data-taking,” Journal of Instrumentation, vol. 15, p. P04003–P04003, Apr 2020. 10.1088/1748-0221/15/04/p04003.

[42] ATLAS Collaboration. “Performance of the ATLAS Trigger System in 2015”. In: The European Physical Journal C 77.5 (May 2017). issn: 1434-6052. doi: 10.1140/epjc/s10052-017-4852-3. arXiv: 1611.09661 [hep-ex]. url: http://dx.doi.org/10.1140/epjc/s10052-017-4852-3.

[43] Holzer, B.J.. (2016). Introduction to Particle Accelerators and their Limitations. 10.5170/CERN-2016-001.29.

[44] S. Chatrchyan *et al.* [CMS], "The CMS Experiment at the CERN LHC,” JINST **3** (2008), S08004 doi:10.1088/1748-0221/3/08/S08004

[45] LHCb Collaboration, T. (2008). "The LHCb detector at the LHC.", doi: 10.1088/1748-0221/3/08/S08005

[46] ALICE collaboration Letter of intent for a large ion collider experiment, CERN-LHCC-93-016, http://cdsweb.cern.ch/record/290825

[47] Reuven Y. Rubinstein and Dirk P. Kroese. 2016. Simulation and the Monte Carlo Method (3rd. ed.). Wiley Publishing.

[48] The ATLAS movie, "From Virtual World to Real World", Jun 2007, http://atlas.ch/dvds.html

[49] The ATLAS Collaboration, “Electron reconstruction and identification in the ATLAS experiment using the 2015 and 2016 lhc proton–proton collision data at $\sqrt{s}$ = 13 TeV,” The European Physical Journal C, vol. 79, p. 639, Aug 2019. 10.1140/ep jc/s10052-019-7140-6.

[50] Aad, Georges, et al. "Electron and photon performance measurements with the ATLAS detector using the 2015–2017 LHC proton-proton collision data." (2019).

[51] “Electron efficiency measurements with the ATLAS detector using 2012 LHC proton–proton collision data”. In: The European Physical Journal C 77.3 (2017). ISSN: 1434-6052. DOI: 10.1140/epjc/s10052-017-4756-2. URL: http://dx.doi.org/10.1140/epjc/s10052-017-4756-2.

[52] Aad, Georges, et al. "Observation of a new particle in the search for the Standard Model Higgs boson with the ATLAS detector at the LHC." Physics Letters B 716.1 (2012): 1-29.

[53] Chatrchyan, Serguei, et al. "Observation of a new boson at a mass of 125 GeV with the CMS experiment at the LHC." Physics Letters B 716.1 (2012): 30-61.

[54] Aad, Georges, et al. "Combined Measurement of the Higgs Boson Mass in p p Collisions at s= 7 and 8 TeV with the ATLAS and CMS Experiments." Physical review letters 114.19 (2015): 191803.

[55] Collaboration, ATLAS. (2018). Measurement of the Higgs boson mass in the $H \to ZZ \to 4l^{\pm}$ and $H \to \gamma\gamma$ channels with $\sqrt{s}$ = 13 TeV pp collisions using the ATLAS detector. Physics Letters B. 784.

[56] ATLAS collaboration. (2018). Measurement of the Higgs boson mass in the $H \to ZZ^* \to 4\ell$ and $H \to \gamma\gamma$ channels with $\sqrt{s} = 13$ TeV pp collisions using the ATLAS detector. arXiv preprint arXiv:1806.00242.

[57] ATLAS Collaboration, Higgs boson production cross-section measurements and their EFT interpretation in the 4l decay channel at $\sqrt{s}$ = 13 TeV with the ATLAS detector, Eur. Phys. J. C 80 (2020) 957, arXiv: 2004.03447 [hep-ex] (cit. on pp. 3–8, 13), Erratum: Eur. Phys. J. C 81 (2021) 29.

[58] ATLAS Collaboration, Measurements of the Higgs boson inclusive and differential fiducial cross sections in the 4l decay channel at $\sqrt{s}$ = 13 TeV, Eur. Phys. J. C 80 (2020) 942, arXiv: 2004.03969 [hep-ex] (cit. on p. 4).

[59] K. Hamilton, P. Nason, E. Re and G. Zanderighi, NNLOPS simulation of Higgs boson production, JHEP 10 (2013) 222, arXiv: 1309.0017 [hep-ph] (cit. on p. 4).

[60] S. Catani and M. Grazzini, Next-to-Next-to-Leading-Order Subtraction Formalism in Hadron Collisions and its Application to Higgs-Boson Production at the Large Hadron Collider, Phys. Rev. Lett. 98 (2007) 222002, arXiv: hep-ph/0703012 [hep-ph] (cit. on p. 4).

[61] J. Butterworth et al., PDF4LHC recommendations for LHC Run II, J. Phys. G 43 (2016) 023001, arXiv: 1510.03865 [hep-ph] (cit. on p. 4).

[62] K. Hamilton, P. Nason and G. Zanderighi, Finite quark-mass effects in the NNLOPS POWHEG+MiNLO Higgs generator, JHEP 05 (2015) 140, arXiv: 1501.04637 [hep-ph] (cit. on p. 4).

[63] S. Alioli, P. Nason, C. Oleari and E. Re, A general framework for implementing NLO calculations in shower Monte Carlo programs: the POWHEG BOX, JHEP 06 (2010) 043, arXiv: 1002.2581 [hep-ph] (cit. on p. 4).

[64] P. Nason, A new method for combining NLO QCD with shower Monte Carlo algorithms, JHEP 11 (2004) 040, arXiv: hep-ph/0409146 (cit. on p. 4).

[65] S. Frixione, P. Nason and C. Oleari, Matching NLO QCD computations with parton shower simulations: the POWHEG method, JHEP 11 (2007) 070, arXiv: 0709.2092 [hep-ph] (cit. on p. 4).

[66] K. Hamilton, P. Nason and G. Zanderighi, MINLO: Multi-Scale Improved NLO, JHEP 10 (2012) 155, arXiv: 1206.3572 [hep-ph] (cit. on p. 4).

[67] J. M. Campbell et al., NLO Higgs Boson Production Plus One and Two Jets Using the POWHEG BOX, MadGraph4 and MCFM, JHEP 07 (2012) 092, arXiv: 1202.5475 [hep-ph] (cit. on p. 4).

[68] K. Hamilton, P. Nason, C. Oleari and G. Zanderighi, Merging H/W/Z + 0 and 1 jet at NLO with no merging scale: a path to parton shower + NNLO matching, JHEP 05 (2013) 082, arXiv: 1212.4504 [hep-ph] (cit. on p. 4).

[69] S. Catani and M. Grazzini, Next-to-Next-to-Leading-Order Subtraction Formalism in Hadron Collisions and its Application to Higgs-Boson Production at the Large Hadron Collider, Phys. Rev. Lett. 98 (2007) 222002, arXiv: hep-ph/0703012 [hep-ph] (cit. on p. 4).

[70] J. Alwall et al., The automated computation of tree-level and next-to-leading order differential cross sections, and their matching to parton shower simulations, JHEP 07 (2014) 079, arXiv: 1405.0301 [hep-ph] (cit. on pp. 4, 8).

[71] M. Wiesemann et al., Higgs production in association with bottom quarks, JHEP 02 (2015) 132, arXiv: 1409.5301 [hep-ph] (cit. on p. 4).

[72] R. D. Ball et al., Parton distributions for the LHC run II, JHEP 04 (2015) 040, arXiv: 1410.8849 [hep-ph] (cit. on p. 4).

[73] D. J. Lange, The EvtGen particle decay simulation package, Nucl. Instrum. Meth. A 462 (2001) 152 (cit. on p. 4).

[74] T. Sjöstrand, S. Mrenna and P. Skands, A brief introduction to PYTHIA 8.1, Comput. Phys. Commun. 178 (2008) 852, arXiv: 0710.3820 [hep-ph] (cit. on pp. 4, 5).

[75] D. de Florian et al., Handbook of LHC Higgs Cross Sections: 4. Deciphering the Nature of the Higgs Sector, (2016), arXiv: 1610.07922 [hep-ph] (cit. on pp. 2, 4, 12).

[76] T. Gleisberg et al., Event generation with SHERPA 1.1, JHEP 02 (2009) 007, arXiv: 0811.4622 [hep-ph] (cit. on p. 4).

[77] T. Gleisberg and S. Höche, Comix, a new matrix element generator, JHEP 12 (2008) 039, arXiv: 0808.3674 [hep-ph] (cit. on p. 4).

[78] F. Cascioli, P. Maierhöfer and S. Pozzorini, Scattering Amplitudes with Open Loops, Phys. Rev. Lett. 108 (2012) 111601, arXiv: 1111.5206 [hep-ph] (cit. on p. 4).

[79] E. Bothmann et al., Event generation with Sherpa 2.2, SciPost Phys. 7 (2019) 034, arXiv: 1905.09127 [hep-ph] (cit. on p. 4).

[80] GEANT4 Collaboration, S. Agostinelli et al., Geant4 – a simulation toolkit, Nucl. Instrum. Meth. A 506 (2003) 250 (cit. on p. 5).

[81] R. D. Ball et al., Parton distributions with LHC data, Nucl. Phys. B 867 (2013) 244, arXiv: 1207.1303 [hep-ph] (cit. on p. 5).

[82] G. Aad et al. "Muon reconstruction performance of the ATLAS detector in proton– proton collision data at $\sqrt{s}$ = 13 TeV". In: The European Physical Journal C 76.5 (May 2016). issn: 1434-6052. doi: 10.1140/epjc/s10052-016-4120-y. arXiv: 1603.05598 [hep-ex]. url: http://dx.doi.org/10.1140/epjc/s10052-016-4120-y.

[83] CMS collaboration. (2015). Limits on the Higgs boson lifetime and width from its decay to four charged leptons. arXiv preprint arXiv:1507.06656.

[84] Schramm, Steven. (2018). ATLAS Jet Reconstruction, Calibration, and Tagging of Lorentzboosted Objects. EPJ Web of Conferences. 182. 02113. 10.1051/epjconf/201818202113.

[85] Abada, A., Abbrescia, M., AbdusSalam, S.S. et al. FCC Physics Opportunities. Eur. Phys. J. C 79, 474 (2019). https://doi.org/10.1140/epjc/s10052-019-6904-3

[86] Malley, Marjorie C. (25 August 2011). Radioactivity: A History of a Mysterious Science. Oxford University Press. pp. 78–79. ISBN 9780199766413.

[87] Romão, J., Andringa, S. Vector boson decays of the Higgs boson. Eur. Phys. J. C 7, 631–642 (1999). https://doi.org/10.1007/s100529801038

[88] Einan Gardi, Nigel Glover, Aidan Robson, "LHC Phenomenology", eBook ISBN 978-3-319-05362-2, url: https://doi.org/10.1007/978-3-319-05362-2

[89] Deur, A., Brodsky, S. J., & de Téramond, G. F. (2016). The QCD running coupling. Progress in Particle and Nuclear Physics, 90, 1-74.

[90] E. Fermi, "On the theory of collisions between atoms and electrically charged particles," Nuovo Cimento, vol. 2, pp. 143–158, 1925. https://doi.org/10.1142/97898127042140 026.

[91] da Silva Almeida, E., Éboli, O. J. P., & Gonzalez–Garcia, M. C. (2020). Unitarity constraints on anomalous quartic couplings. Physical Review D, 101(11), 113003.

[92] Jueid, A. (2021, December). Studying QCD modeling of uncertainties in particle spectra from dark-matter annihilation into jets. In Journal of Physics: Conference Series (Vol. 2156, No. 1, p. 012057). IOP Publishing.

[93] F. Chollet et al., Keras, https://keras.io, 2015 (cit. on p. 41).

[94] Martin Abadi et al., TensorFlow: Large-Scale Machine Learning on Heterogeneous Systems, Software available from tensorflow.org, 2015, url: https://www.tensorflow.org/ (cit. on p. 41).

[95] Aad, G., Abbott, B., Abbott, D. C., Abed Abud, A., Abeling, K., Abhayasinghe, D. K., ... & Balli, F. (2021). Measurement of light-by-light scattering and search for axion-like particles with 2.2 nb- 1 of Pb+ Pb data with the ATLAS detector. Journal of High Energy Physics, 2021(3), 1-45.

[96] ATLAS Collaboration, Measurement of exclusive $\gamma\gamma \to l^+l^-$ production in proton–proton collisions $\sqrt{s}$ = 7 TeV with the ATLAS detector, Phys. Lett. B 749 (2015) 242, arXiv: 1506.07098 [hep-ex].

[97] ATLAS Collaboration, Measurement of the exclusive $\gamma\gamma \to \mu^+\mu^-$ process in proton–proton at $\sqrt{s}$ = 13 TeV with the ATLAS detector, Phys. Lett. B 777 (2018) 303, arXiv: 1708.04053 [hep-ex].

[98] CMS Collaboration, Search for exclusive or semi-exclusive $\gamma\gamma$ production and observation of exclusive and semi-exclusive e^+e^- production in pp collisions at $\sqrt{s}$ = 7 TeV, JHEP 11 (2012) 080, arXiv: 1209.1666 [hep-ex].

[99] The ATLAS Collaboration, "Observation of photon-induced W+W production in pp collisions at $\sqrt{s}$ = 13 TeV using the ATLAS detector," Physics Letters B, p. 136190, 2021. https://doi.org/10.1016/j.physletb.2021.136190.

[100] O. Eboli and M. Gonzalez–Garcia, "Classifying the bosonic quartic couplings," Physical Review D, vol. 93, May 2016. 10.1103/physrevd.93.093013.

[101] B. Richter, Very high energy electron-positron colliding beams for the study of the weak Interactions, Nucl. Instr. & Meth. 136, 47 (1976), and SLAC-PUB-1738.

[102] Riemann, T. (1997). Study of the Z Boson at LEP. arXiv preprint hep-ph/9712435.

[103] Breit, G.; Wigner, E. (1936). "Capture of Slow Neutrons". Physical Review. 49 (7): 519. Bibcode:1936PhRv...49..519B. doi:10.1103/PhysRev.49.519.

[104] Rene Brun and Fons Rademakers, ROOT - An Object Oriented Data Analysis Framework, Proceedings AIHENP'96 Workshop, Lausanne, Sep. 1996, Nucl. Inst. & Meth. in Phys. Res. A 389 (1997) 81-86.

[105] Cranmer, K. (2015). Practical Statistics for the LHC. arXiv preprint arXiv:1503.07622.

[106] M. Oreglia. "A Study of the Reactions $\Psi' \to \gamma\gamma\Psi$". PhD thesis. SLAC, 1980. url: http://www-public.slac.stanford.edu/sciDoc/docMeta.aspx?slacPubNumber=slac-r-236.html.

[107] Aaboud, M., Aad, G., Abbott, B., Abdallah, J., Abeloos, B., ... & Baroncelli, A. (2017). Identification and rejection of pile-up jets at high pseudorapidity with the ATLAS detector. The European Physical Journal C, 77(9), 1-32.

[108] ATLAS Collaboration. Higgs boson production cross-section measurements and their EFT interpretation in the 4l decay channel at $\sqrt{s}$ = 13 TeV with the ATLAS detector. 2020. arXiv: 2004.03447 [hep-ex].

[109] T. G. Cornelissen et al., Concepts, design and implementation of the ATLAS New Tracking (NEWT), ATL-SOFT-PUB-2007-007, 2007, url: https://cds.cern.ch/record/1020106.

[110] T. G. Cornelissen et al., The global Ξ^2 track fitter in ATLAS, J. Phys. Conf. Ser. 119 (2008) 032013.

[111] ATLAS Collaboration, Improved electron reconstruction in ATLAS using the Gaussian Sum Filter- based model for bremsstrahlung, ATLAS-CONF-2012-047, 2012, url: https://cds.cern.ch/ record/1449796.

[112] Amsler, C.; et al. (Particle Data Group) (2010). "PL B667, 1 (2008), and 2009 partial update for the 2010 edition" (PDF). Archived (PDF) from the original on 2011-06-05. Retrieved 2010-05-19.

[113] Soyez, G. (2008). The SISCone and anti-kt jet algorithms. arXiv preprint arXiv:0807.0021.

[114] CMS collaboration. (2017). Evidence for vector boson scattering in events with four leptons and two jets in proton-proton collisions at $\sqrt{s}$ = 13 TeV. CMS-PAS-SMP-20-001.

[115] Track and Vertex reconstruction, R. Fruhwirth and A. Strandlie, Rev.Mod.Phys 82 1419 (2010) http://rmp.aps.org/abstract/RMP/v82/i2/p1419_1